Lawrence Berkeley National Laboratory
LBL Publications

Title

The Kinetics of Laser Pulse Vaporization of Uranium Dioxide by Mass Spectrometry

Permalink

https://escholarship.org/uc/item/8182b353

Author

Tsai, Chuen-Horng

Publication Date

1981-11-01

eScholarship.org Powered by the California Digital Library
University of California

UC-41
LBL-13679
c.2 repl.

Lawrence Berkeley Laboratory
UNIVERSITY OF CALIFORNIA

Materials & Molecular Research Division

RECEIVED
LAWRENCE
BERKELEY LABORATORY

JAN 20 1982

LIBRARY AND
DOCUMENTS SECTION

THE KINETICS OF LASER PULSE VAPORIZATION OF URANIUM DIOXIDE BY MASS SPECTROMETRY

Chuen-horng Tsai
(Ph.D. thesis)

November 1981

TWO-WEEK LOAN COPY
For Reference
This is a Library Circulating Copy
which may be borrowed for two weeks
Not to be taken from this room

LBL-13679
c.2 repl.

Prepared for the U.S. Department of Energy under Contract W-7405-ENG-48

DISCLAIMER

This document was prepared as an account of work sponsored by the United States Government. While this document is believed to contain correct information, neither the United States Government nor any agency thereof, nor the Regents of the University of California, nor any of their employees, makes any warranty, express or implied, or assumes any legal responsibility for the accuracy, completeness, or usefulness of any information, apparatus, product, or process disclosed, or represents that its use would not infringe privately owned rights. Reference herein to any specific commercial product, process, or service by its trade name, trademark, manufacturer, or otherwise, does not necessarily constitute or imply its endorsement, recommendation, or favoring by the United States Government or any agency thereof, or the Regents of the University of California. The views and opinions of authors expressed herein do not necessarily state or reflect those of the United States Government or any agency thereof or the Regents of the University of California.

The Kinetics of Laser Pulse Vaporization of Uranium Dioxide by Mass Spectrometry

Chuen-horng Tsai
Ph.D. Thesis

Materials & Molecular Research Division
Lawrence Berkeley Laboratory
University of California
Berkeley, CA 94720

This work has been supported by the Director, Office of Energy Research, Office of Basic Energy Science, Materials Science Division of the U.S. Department of Energy under contract No. W-7405-ENG-48.

The Kinetics of Laser Pulse Vaporization of Uranium Dioxide by Mass Spectrometry

Chuen-horng Tsai

Ph.D. *Nuclear Engineering Dept.*

Sponsor: *Materials Science Division*
U.S. Department of Energy

Prof. D. R. Olander
Chairman of Committee

ABSTRACT

Safety analyses of nuclear reactors require knowledge of the evaporation behavior of UO_2 at temperatures well above the melting point of 3140 K. In this study, rapid transient heating of a small spot on a UO_2 specimen was accomplished by a laser pulse, which generates a surface temperature excursion. This in turn vaporizes the target surface and the gas expands into vacuum.

The surface temperature transient was monitored by a fast-response automatic optical pyrometer. The maximum surface temperatures investigated range from ~3700 K to ~4300 K. A computer program was developed to simulate the laser heating process and calculate the surface temperature evolution. The effect of the uncertainties of the high temperature material properties on the calculation was included in a sensitivity study for UO_2 vaporization. The measured surface temperatures were in satisfactory agreements.

A quadrupole mass spectrometer was used to identify and analyze the major vapor species in the vaporizing flow, and to measure the rate of evaporation from the target

surface. The information yielded the partial vapor pressure of each species and the composition in the vapor jet. For the partial pressure of UO_2, the pressure-temperature relation $\log p(atm) = 26.81 - 26089/T(K) - 5.594\log T(K)$ best fits to the experimental results. This p-T relation falls inside the confidence limits recommended in the literature assessment report.

The degree of ionization in the hot vapor was estimated from the mass spectrometer measurement of thermonic ions compared with the neutral molecules. The result was in good agreement with the calculation based on Sha's equation and effective "unisolated" ionization potential.

No dimer signal of any vapor molecule was measured, indicating the absence of condensation in the highly supersaturated vapor leaving the surface.

A shock wave structure is developed by laser pulsing on a UO_2 target in an ambient inert gas. This structure was photographed during the laser pulse. By applying the Mack disk formula, the total vapor pressure corresponding to maximum temperature was obtained. The resulting low vapor pressure and low heat of vaporization deduced from this measurement is attributed to excessively high surface temperature measured due to nonequilibrium radiation from the hot vapor.

Additional diagnostics of the phenomenum included collection of the vapor blowoff on disks followed by neutron activation to determine the angular distribution of the vaporization process. The extent of droplet production was also investigated by disk collection. Liquid droplets are observed, but the quantity of UO_2 they contained was insignificant compared to the total mass evaporated.

TABLE OF CONTENTS

APPENDICES

The Kinetics of Laser Pulse Vaporization of Uranium Dioxide by Mass Spectrometry

Chuen-horng Tsai

Department of Nuclear Engineering
University of California

Materials & Molecular Research Division
Lawrence Berkeley Laboratory
Berkeley, CA 94720

ABSTRACT

Safety analyses of nuclear reactors require knowledge of the evaporation behavior of UO_2 at temperatures well above the melting point of 3140 K. In this study, rapid transient heating of a small spot on a UO_2 specimen was accomplished by a laser pulse, which generates a surface temperature excursion. This in turn vaporizes the target surface and the gas expands into vacuum.

The surface temperature transient was monitored by a fast-response automatic optical pyrometer. The maximum surface temperatures investigated range from ~3700 K to ~4300 K. A computer program was developed to simulate the laser heating process and calculate the surface temperature evolution. The effect of the uncertainties of the high temperature material properties on the calculation was included in a sensitivity study for UO_2 vaporization. The measured surface temperatures were in satisfactory agreements.

A quadrupole mass spectrometer was used to identify and analyze the major vapor species in the vaporizing flow, and to measure the rate of evaporation from the target surface. The information yielded the partial vapor pressure of each species and the composition in the vapor jet. For the partial pressure of UO_2, the pressure-temperature relation $\log p(\text{atm}) = 26.81 - 26089/T(\text{K}) - 5.594 \log T(\text{K})$ best fits to the experimental results. This p-T relation falls inside the confidence limits recommended in the literature assessment report.

The degree of ionization in the hot vapor was estimated from the mass spectrometer measurement of thermonic ions compared with the neutral molecules. The result was in good agreement with the calculation based on Sha's equation and effective "un-isolated" ionization

potential.

No dimer signal of any vapor molecule was measured, indicating the absence of condensation in the highly supersaturated vapor leaving the surface.

A shock wave structure is developed by laser pulsing on a UO_2 target in an ambient inert gas. This structure was photographed during the laser pulse. By applying the Mack disk formula, the total vapor pressure corresponding to maximum temperature was obtained. The resulting low vapor pressure and low heat of vaporization deduced from this measurement is attributed to excessively high surface temperature measured due to nonequilibrium radiation from the hot vapor.

Additional diagnostics of the phenomenum included collection of the vapor blow-off on disks followed by neutron activation to determine the angular distribution of the vaporization process. The extent of droplet production was also investigated by disk collection. Liquid droplets are observed, but the quantity of UO_2 they contained was insignificant compared to the total mass evaporated.

ACKNOWLEDGEMENTS

I would like to express my deep gratitude to Professor Donald R. Olander of the Department of Nuclear Engineering, University of California at Berkeley for his constant, patient guidance and fruitful suggestions on designing the experiments and analyzing the data.

I would like to thank Dr. Alan Covington of the Ames Research Center of National Aeronautics and Space Administration for the opportunity of using their facilities and his informing me useful references.

I would also like to thank Dan Winterbauer and John Souza in the machine shop and Jack Harrell in the electronic shop for their prompt and good services of parts fabrication.

I wish to express my appreciation to my colleague, former and present, in the Nuclear Materials Group: Dr. Albert Machiels, Dr. Medhi Balooch, Dr. Rosa Yang, Dr. Kee Kim, and Doug Dooley for their constant inspirations and valuable experiences on the experimental work.

This work has been supported by the Director, Office of Energy Research, Office of Basic Energy Science, Materials Science Division of the U. S. Department of Energy under contract #W-7405-ENG-48.

I. INTRODUCTION

The analysis of a hypothetical core disassembly accident (HCDA) plays an important role in liquid metal fast breeder reactor (LMFBR) safety analysis. Most theoretical analyses originate from a two-dimensional coupled neutronics-hydrodynamics computer code "VENUS" developed by Sha and Hughes*[1]* or the modified version of it*[2,3]*, in which the termination of a power excursion is assumed to be due to heating and to the negative temperature coefficient of reactivity (due to the Doppler effect) and due to the core expansion driven mainly by the fuel vapor pressure. The analysis of such excursions generally consists of three phases*[3]*: accident initiation (voiding, meltdown etc.), reactor disassembly (hydrodynamic effects) and containment evaluation (energy-work conversion). The equation of state of the fuel material, which contributes to the last two phases, incorporates the hydrodynamic calculation as the driving force for neutronic disassembly and the conversion of thermal to mechanical energy resulting in the release of deposited energy after termination of the excursion. The peak fuel temperatures in these calculations range from 4000 K to 5000 K, a temperature range where limited knowledge of fuel vapor properties exists to support such analysis.

Currently used in the analysis are the extrapolations from the static measurements performed well below the temperature range of interest*[4-10]*, based upon a few thermophysical or thermochemical models (see Appendix A for the assessment of these models). Fig. 1.1 and Table 1.1 summarize some of the low temperature static measurements. They agree fairly well in magnitude up to ~2500 K, but differ considerably in the enthalpy of vaporization ΔH_{vap}.

Measurements in the temperature range of 4000 K to 5000 K are desirable because

(i) the present scatter of the input data in the variance analysis leads to an uncertainty of about one order of magnitude (see Appendix A),

(ii) the conventional measurement techniques, such as the Knudsen effusion and transpiration methods, fail not only because of a lack of high melting crucible materials, but because of a departure from molecular evaporation*[11]*,

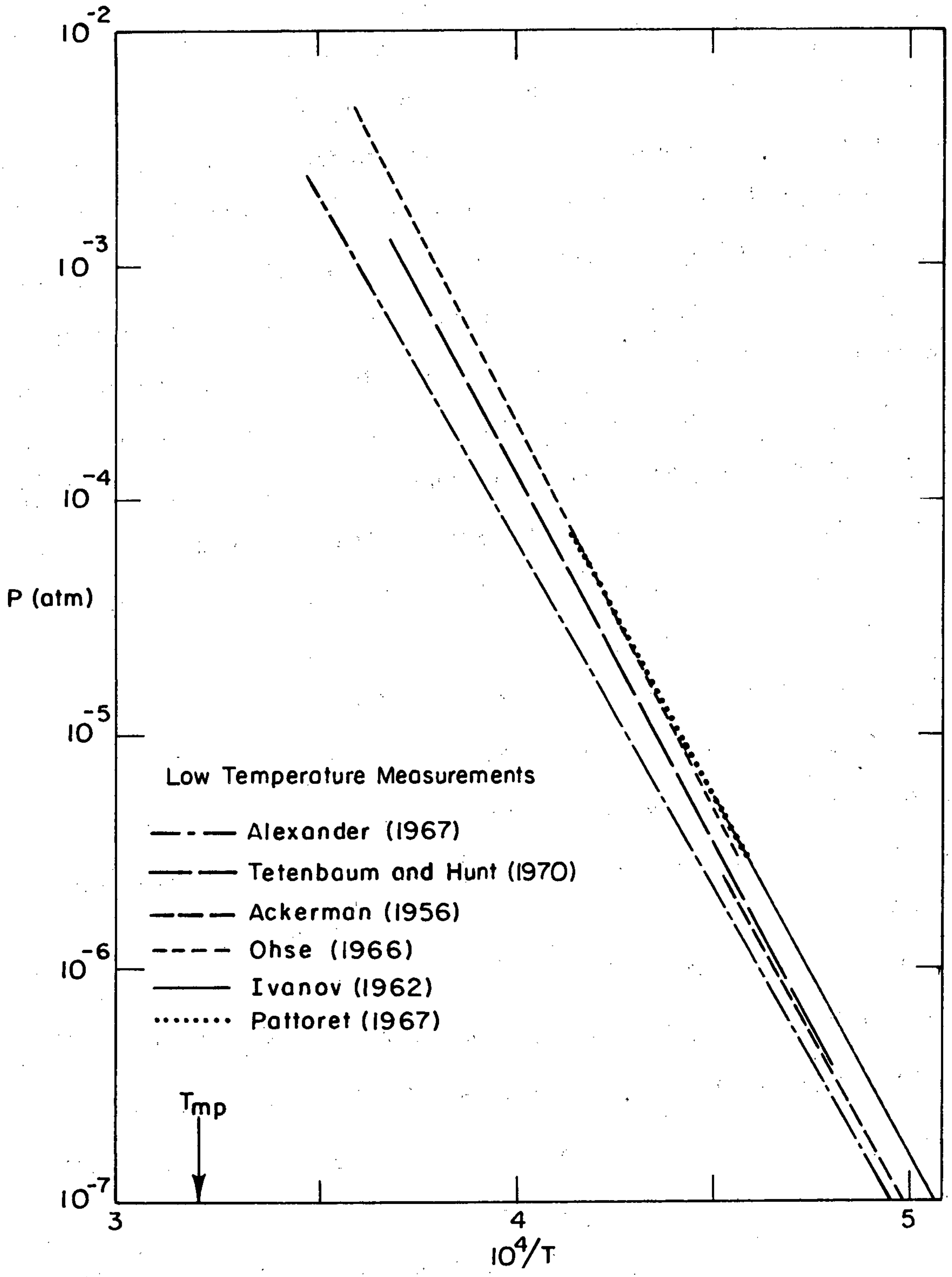

XBL 784-4859

Fig.1.1 Low Temperature Measurements of UO_2 Vapor Pressure

TABLE 1.1

Saturation Vapor Pressure - Temperature Relation of UO_2 at Low Temperature Region

Vapor Pressure $\log P(\mathrm{atm}) = -A/T(K) + B$		Sublimation		Temperature Range (K)	Reference
A	B	ΔH^0 kcal/mol	ΔS^0 cal/mol-K		
29305	7.539	134.1	34.5	2000 - 2940	Alexander*[4]*
31284	8.610	143.1	39.4	2080 - 2705	Tetenbaum & Hunt*[5]*
29961	7.955	137.1	36.4	1600 - 2200	Ackermann*[6]*
33180	9.545	151.8	43.7	2200 - 2800	Ohse*[7]*
32146	9.222	147.1	42.2	1920 - 2220	Ivanov*[8]*
30850	8.60	141.2	39.3	1890 - 2420	Pattoret*[9]*
27426	7.373			3175 - 3390	Reedy & Chasanov*[10]*

(iii) equilibrium saturation data may not well represent the transient behavior in HCDA,

(iv) direct measurements can help establish a reliable theoretical model for eventual HCDA analysis,

(v) measurements in the temperature range up to 5000 K can improve further extrapolation to the critical region when it is needed, and

There have been proposed several dynamic pulse heating techniques: electrical resistive*[12,13]*, electron beam*[14-16]*, neutron pulse*[17,18]* and laser beam*[19-27]*. Reviews and discussions of various techniques can be found in Refs. 21 and 28. All the dynamic heating techniques are characterized by:

——— a temperature range between 4000 K and 5000 K

——— evaporation times in the order of millisecond range

——— surface recession velocities between 1 and 100 cm/sec.

With the conventional (low-rate) methods, the composition of the evaporating surface is constant during the evaporation process. In the laser pulsing techniques, however, the high evaporation rates and the incongruency of UO_2 vaporization causes the composition of the evaporating surface to change with time, giving vapor pressures which are different from the equilibrium pressures corresponding to the bulk composition. A computer program was developed to simulate the laser heating process and the surface temperature evolution. This program also considers solid-state diffusion coupled with the heat conduction process. A sample calculation for UO_2 is given in Section II.3. A sensitivity study of the effect of the uncertainties of the high temperature material properties on the calculation is also presented.

In the experimental portion of the study, laser surface heating is adopted to attain UO_2 peak surface temperatures from just above the melting temperature (3600 K) up to ~4300 K. The surface temperature transient is monitored by a fast-response automatic optical pyrometer. Under ultra-high vacuum, the evaporated molecules are ejected from the surface and form a collision-free Knudsen flow. A quadrupole mass spectrometer is used to identify and analyze the various vapor species in the flow, and to measure the vaporization rate of each species from the surface. This information yields the partial vapor pressure and the composition in the vapor jet. From the double-peaked mass spectrometer signals, one from high energy ions and the other from neutral molecules, the degree of ionization in the hot vapor is estimated. The formation of polymers (especially dimers) in the ejected vapor is investigated.

Because laser-induced vaporization under an ambient atmosphere is analogous to a free-jet from a sonic orifice, a shock structure is developed by laser pulsing on a solid in an ambient inert gas. This luminous shock can be photographed by a conventional camera. Applying the Mach disc formula, the total vapor pressure corresponding to the maximum surface temperature is obtained.

Additional diagnostics of the phenomenum include collection of the vapor blow-off to determine the extent of droplet production (either by direct emission from the molten surface or by condensation in the rapidly cooling vapor plume) and examination of ion emission from the surface.

II. MATHEMATICAL SIMULATION OF TRANSIENT LASER HEATING AND VAPORIZATION OF SOLIDS

II.1. INTRODUCTION

When laser radiation is incident on an absorbing material, all of the resulting effects, such as phase changes (melting and vaporization), thermal stress, thermal radiation and shock waves from the surface and mass transport in the bulk, are associated with the surface temperatures, temperature gradients and composition gradients generated by the transient energy input. The laser energy absorption and conduction is considered as a macroscopic heat transfer process because the laser pulse/material heating time (msec) is far longer than the time for electronic relaxation and transfer of energy to the lattice phonons ($\sim 10^{-13}$ sec). In addition to the heat conduction problem, the composition redistribution during the transient due to the incongruent evaporation has to be considered when the target material is a compound.

Although laser surface heating technique has been applied for years*[29-27]* to thermophysical property investigation of liquid phase urania, there has been no attempt to calculate the thermal evolution of a solid urania subject to intense laser impingement.

Ohse et al*[22]* relied mainly on the pyrometric measurement of surface temperature and surface oxygen depletion was not considered. Their only temperature profile calculation*[23]* was an adaptation of the Dabby and Paek*[29]* model. This model assumes a prior (known) steady state surface temperature, called the "evaporation temperature", for the purpose of investigating the influence of the sub-surface temperature profile on the pyrometric measurement of surface temperatures (i.e. the difference in emitted thermal radiation intensity between a uniformly heated sample and the one with non-uniform temperature profile).

At first, Bober et al relied on the gasdynamic model to interpret vapor temperature*[19]*, then switched to the pyrometric measurement*[30]*. The surface oxygen depletion and oxygen-to-uranium ratio profile was calculated based on the "forced congruent evaporation" model by Breitung*[31]* assuming a prior steady state, followed by a step temperature change which rapidly develops a steady state composition profile near the evaporating surface. The basic requirements for the forced congruent evaporation model are the steady state temperature and sufficient time for oxygen diffusion in the solid to reach steady state. These conditions are not met in ~msec transient heating because the characteristic time for oxygen diffusion process is in the same order as the temperature evolution; consequently the asymptotic stationary "congruent" evaporation condition is not obtainable.

In this study, a mathematical model of heat and mass transfer in uranum oxide subject to laser irradiaton is developed and solved numerically. It can easily be modified for other surface or near-surface heat sources or/and other solid materials. In the uranium-oxygen system, oxygen is the preferentially vaporizing component, and as a result of the limited mobility of oxygen in the solid, an oxygen deficiency is set up near the surface. Because of the bivariant behavior of near-stoichiometric uranium oxide, the heat transfer problem and the oxygen diffusion problem are coupled and a numerical method of simultaneously solving the two problems in a semi-infinite solid is studied. The temperature dependence of the thermal properties and oxygen diffusivity, as well as the effect of surface ablation, leads to considerable non-linearities in both the governing differential equations and the boundary conditions. The method is based on the earlier analysis by Olstad and Olander *[32,33]*, but the generality of the problem is expanded and the efficiency of the numerical scheme is improved.

II.2. MATHEMATICAL MODEL

Consider a semi-infinite slab occupying the region $z \geqslant 0$, which is irradiated by a laser pulse. One-dimensional heat conduction, one-dimensional ablation (no radial liquid movement), a planar melting front beneath the surface, and one-dimensional oxygen diffusion are assumed. Melting is treated implicitly via the heat capacity term and heat of vaporization term (see Appendix D section 2). Although the laser spot size on the surface is usually small (~5mm diameter), it is still orders of magnitude larger than the characteristic penetration depth of heat conduction and component depletion by diffusion in most materials, especially refractory materials such as uranium oxide. Transient vaporization due to laser heating is based on the Hertz-Langmiur vacuum vaporization formula because the decrease in surface stoichiometry and the ablation rate can only be quantified based on this assumption. However, allowance is made for backscattering of vaporized molecules by collisions in the vapor adjacent to the surface. The vapor plume created by vaporization is assumed to be transparent to the incident laser radiation.

Either penetration of laser radiation (near-surface volumetric heating) or surface heating is allowed. This option is designed not only to accomodate different optical properties of the materials subject to laser radiation, but also for application of the calculation scheme to other heating techniques, such as exploding wires, electron beam bombardment, energetic ion impingement heating and neutron and gamma ray pulse heating, which have been proposed for the acquisition of thermochemical data or which drive often transient heating phenomena, such as those in pulsed fusion reactors.

II.2.1 Mass Balance Equation

Due to the low diffusion coefficient of uranium ions in UO_2 compared with the diffusion coefficient of oxygen ions, the uranium ions are considered to form an immobile lattice through which oxygen can migrate.

The mass balance equation of oxygen in the solid phase is:

$$\frac{\partial C_o}{\partial t} = -\frac{\partial}{\partial z} j_o^d \tag{2-1}$$

where C_o = mass concentration of oxygen atom in the solid, g/cm^3

j_o^d = oxygen diffusive flux in the solid, g/cm^2-sec.

To account for the possibility of significant ablation from the interphase boundary, we make the following coordinate transformation:

$$x = z - vt \tag{2-2}$$

where x is the distance from the moving boundary, z is the coordinate from the original surface, and v is the ablation (surface recession) velocity.

After the coordinate transformation, the balance equation of oxygen becomes:

$$\frac{\partial C_o}{\partial t} - v\frac{\partial C_o}{\partial x} = -\frac{\partial}{\partial x} j_o^d \tag{2-3}$$

Rearranging this equation, we have:

$$\frac{\partial C_o}{\partial t} = -\frac{\partial}{\partial x} j_o^d + v\frac{\partial C_o}{\partial x} \tag{2-4}$$

II.2.2 Energy Balance Equation

The general energy balance equation for the solid, assuming that oxygen is the only mobile component, is:

$$\rho\frac{\partial \hat{U}}{\partial t} = -\frac{\partial q}{\partial z} - \frac{\partial}{\partial z}(j_o^d \bar{h}_o) + Q_v \tag{2-5}$$

where ρ = mass density, g/cm^3

$\hat{U}$ = specific internal energy, J/g

q = heat flux, W/cm^2

$\bar{h}_o$ = partial specific enthalpy of oxygen, J/g

Q_v = volumetric heat source, W/cm^3.

For the heat conduction through a condensed, incompressible medium with mobile oxygen and immobile uranium, the specific internal energy $\hat{U}$ is a function of temperature T and concentration C_o only. Therefore,

$$\frac{\partial \hat{U}}{\partial t} = \left(\frac{\partial \hat{U}}{\partial C_o}\right)_T\left(\frac{\partial C_o}{\partial t}\right) + \left(\frac{\partial \hat{U}}{\partial T}\right)_{C_o}\left(\frac{\partial T}{\partial t}\right) \tag{2-6}$$

Assuming no mechanical work is done,

$$\hat{U} = \hat{H} = (\bar{h}_o C_o + \bar{h}_U C_U)/\rho \tag{2-7}$$

where $\bar{h}_U$ = partial specific enthalpy of uranium, J/g

C_U = mass concentration of uranium atom in the solid, g/cm^3

Since $\bar{h}_U$ and C_U are independent of C_o (because of the assumption that uranium atoms are immobile),

$$\left(\frac{\partial \hat{U}}{\partial C_o}\right)_T = \bar{h}_o/\rho \tag{2-8}$$

Similarly,

$$\left(\frac{\partial \hat{U}}{\partial T}\right)_{C_o} = \left(\frac{\partial \hat{H}}{\partial T}\right)_{C_o} = C_p \tag{2-9}$$

where C_p is the constant pressure specific heat in J/g-K. Therefore, equation (2-6) becomes:

$$\frac{\partial \hat{U}}{\partial t} = \frac{\bar{h}_o}{\rho}\frac{\partial C_o}{\partial t} + C_p \frac{\partial T}{\partial t} \tag{2-10}$$

Substituting Eq. (2-10) into Eq. (2-5) and using the coordinate transformation of Eq. (2-2), we have:

$$\rho C_p \frac{\partial T}{\partial t} - \rho C_p v \frac{\partial T}{\partial x} + \bar{h}_o \frac{\partial C_o}{\partial t} - \bar{h}_o v \frac{\partial C_o}{\partial x} = -\frac{\partial q}{\partial x} - \frac{\partial}{\partial x}(j_o^d \bar{h}_o) + Q_v \tag{2-11}$$

Multiplying Eq. (2-4) by $\bar{h}_o$ and substituting the result into Eq. (2-11) yields:

$$\rho C_p \frac{\partial T}{\partial t} - \rho C_p v \frac{\partial T}{\partial x} = -\frac{\partial q}{\partial x} - j_o^d \frac{\partial}{\partial x}\bar{h}_o + Q_v \tag{2-12}$$

II.2.3 Oxygen Diffusive Flux and Heat Flux

Taking into account the Soret and Dufour effects, the mass and heat fluxes are given by:

$$j_o^d = -D_o \frac{\partial C_o}{\partial x} - \frac{D_o Q^* C_o}{RT^2}\frac{\partial T}{\partial x} \tag{2-13}$$

$$q = -\frac{D_o Q^*}{M_o}\frac{\partial C_o}{\partial x} - k\frac{\partial T}{\partial x} \tag{2-14}$$

where D_o = diffusion coefficient of oxygen in uranium oxide, cm^2/sec

Q^* = heat of transport of oxygen in uranium oxide, J/mole

R = gas constant = 8.314 J/K-mole

M_o = atomic weight of oxygen = 16 g/g-atom

k = thermal conductivity, W/cm-K

II.2.4 Initial and Boundary Conditions

The two balance equations (2-4) and (2-12) are coupled through the two fluxes j_o^d and q. In order to solve those two partial differential equations, we need two initial conditions and four boundary conditions.

The initial conditions are:

$$T(x,0) = T_o \text{ and } C_o(x,0) = C_o^o \quad @\ t=0 \tag{2-15}$$

where T_o is the initial temperature before laser impingement

and C_o^o is the initial mass concentration of oxygen.

The boundary conditions are:

(i) at the moving interphase boundary, x = 0:

As a result of preferential vaporization and the finite supply rate from the bulk, oxygen is depleted at the surface and a concentration gradient is set up inside of the oxide which drives a flux of oxygen atoms towards the surface. The diffusion flux at the surface is given in Eq. (2-13) except all the quantities are evaluated at x=0.

The mass balance for oxygen atoms at the interphase boundary gives:

$$j_o^d = j_o^g + vC_o^s \quad @\ x=0 \tag{2-16}$$

where C_o^s is the mass concentration of oxygen atom of the solid at the surface, j_o^g is the total vaporization mass flux of oxygen in the gas phase. The latter is:

$$j_o^g = -\ (3\Phi_{UO_3}+2\Phi_{UO_2}+\Phi_{UO}+\Phi_O+2\Phi_{O_2})M_o \tag{2-17}$$

The surface recession velocity, v, is the ratio of the evaporation mass flux of uranium-bearing species j_U^g and the mass concentration of uranium atom in the solid C_U,

$$v = -\ j_U^g/C_U = (\Phi_{UO_3}+\Phi_{UO_2}+\Phi_{UO}+\Phi_U)M_U/C_U \tag{2-18}$$

The sign convention is that a flux (mass or heat) is positive if it is in the positive x direction. The fluxes are relative to the moving boundary.

The Hertz-Langmuir vaporization rate of species i, $[\Phi_i]_L$ is:

$$[\Phi_i]_L = \frac{P_i}{\sqrt{2\pi M_i R T_s}} \quad \text{mole/cm}^2\text{–sec} \tag{2-19}$$

where T_s is the surface temperature and P_i is the equilibrium pressure of species i over the solid at the surface composition and temperature. The vaporization coefficient is assumed to be unity. The vacuum vaporization formula of Eq. (2-19) is strictly valid only if the vapor plume in front of the solid is collisionless. However, many theoretical investigations*[34-36]* have shown that even in a collision-dominated vapor plume, the net vaporization rate is at least 82% of that given by Eq. (2-19) (i.e. the fraction of the forward vaporization flux backscattered to the surface is <18%). Thus, the vaporization rates are given by:

$$\Phi_i = (1-\beta)\,[\Phi_i]_L \tag{2-19a}$$

where β is the backscattering coefficient, 0.18.

Combining Eqs. (2-13) and (2-16), we have:

$$- D_o \frac{\partial C_o}{\partial x}\Big|_{x=0} - \frac{D_o Q^* C_o}{RT^2}\frac{\partial T}{\partial x}\Big|_{x=0} = j_o^g + vC_o^s \tag{2-20}$$

The heat flux in the solid at the interphase boundary is balanced by the heat loss carried by the vaporizing species (ablation), the radiation heat loss and the heat flux input from the laser (for surface absorption only), i.e.,

$$(q)_{x=0} = - \sum_i M_i \Phi_i \Delta H_i^v - \epsilon_t \sigma (T_s^4 - T_b^4) + Q_s \tag{2-21}$$

where ΔH_i^v = heat of vaorization of species i, J/g

T_b = the ambient temperature (usually room temperature), K

ϵ_t = total hemispherical optical emissivity

σ = Stefan-Boltzmann constant = 5.6686×10^{-12} J/cm^2-sec-K^4

and Q_s = surface heat source, W/cm^2.

If the heat source incident on the surface is considered to penetrate into the solid, the volumetric heat source term Q_v in the energy equation is nonzero and the surface heat source term Q_s in the boundary condition is zero. Conversely, if the heat source is considered as a surface source, Q_s is nonzero and Q_v is zero.

Combining Eqs. (2-14) and (2-21), we have:

$$-\frac{D_oQ^*}{M_o}\frac{\partial C_o}{\partial x}\Big|_{x=0} - k\frac{\partial T}{\partial x}\Big|_{x=0} = -\sum_i M_i\Phi_i\Delta H_i^v - \epsilon_t\sigma(T_s^4 - T_b^4) + Q_s \qquad (2\text{-}22)$$

The boundary condition Eqs. (2-20) and (2-22) can be solved for $\partial C_o/\partial x$ and $\partial T/\partial x$ explicitly:

$$\left(\frac{\partial T}{\partial x}\right)_{x=0} = \frac{\sum_i M_i\Phi_i\Delta H_i^v + \epsilon_t\sigma(T_s^4 - T_b^4) - Q_s + \frac{Q^*}{M_o}(j_o^g + vC_o^s)}{k - \frac{D_o(Q^*)^2C_o^s}{M_oRT_s^2}} \qquad (2\text{-}23)$$

$$(i = UO_3, UO_2, UO, U, O, O_2)$$

$$\left(\frac{\partial C_o}{\partial x}\right)_{x=0} = \frac{-\frac{k}{D_o}(j_o^g + vC_o^s) - \frac{Q^*C_o^s}{RT_s^2}\left[\sum_i M_i\Phi_i\Delta H_i^v + \epsilon_t\sigma(T_s^4 - T_b^4) - Q_s\right]}{k - \frac{D_o(Q^*)^2C_o^s}{M_oRT_s^2}} \qquad (2\text{-}24)$$

(ii) far from the evaporating surface in the solid ($x = \infty$):

$$T(\infty,t) = T_o \text{ and } C_o(\infty,t) = C_o^o \qquad (2\text{-}25)$$

II.2.5 Oxygen Diffusion and Heat Conduction Equations

Substituting the fluxes, Eqs. (2-13) and (2-14), into the partial differential equations (2-4) and (2-12), we obtain the two boundary value problems to be solved for T and C_o:

$$\frac{\partial C_o}{\partial t} = \frac{\partial}{\partial x}\left(D_o\frac{\partial C_o}{\partial x} + \frac{D_oQ^*C_o}{RT^2}\frac{\partial T}{\partial x}\right) + v\frac{\partial C_o}{\partial x} \qquad (2\text{-}26)$$

$$\frac{\partial T}{\partial t} = \frac{1}{\rho C_p}\frac{\partial}{\partial x}\left(\frac{D_oQ^*}{M_o}\frac{\partial C_o}{\partial x} + k\frac{\partial T}{\partial x}\right) + \left(\frac{D_o}{\rho C_p}\frac{\partial C_o}{\partial x} + \frac{D_oQ^*C_o}{\rho C_pRT_2}\frac{\partial T}{\partial x}\right)\frac{\partial \bar{h}_o}{\partial x} + v\frac{\partial T}{\partial x} + \frac{Q_v}{\rho C_p} \qquad (2\text{-}27)$$

$$\text{I.C.: } T(x,0) = T_o \text{ and } C_o(x,0) = C_o^o \text{ @ } t=0 \qquad (2\text{-}28)$$

$$\text{B.C.: } \left(\frac{\partial T}{\partial x}\right)_{x=0} = \frac{\sum_i M_i\Phi_i\Delta H_i^v + \epsilon_t\sigma(T_s^4 - T_b^4) - Q_s + \frac{Q^*}{M_o}(j_o^g + vC_o^s)}{k - \frac{D_o(Q^*)^2C_o^s}{M_oRT_s^2}} \qquad (2\text{-}29)$$

$$\left(\frac{\partial C_o}{\partial x}\right)_{x=0} = \frac{-\frac{k}{D_o}(j_o^g + vC_o^s) - \frac{Q^*C_o^s}{RT_s^2}\left[\sum_i M_i\Phi_i\Delta H_i^v + \epsilon_t\sigma(T_s^4 - T_b^4) - Q_s\right]}{k - \frac{D_o(Q^*)^2C_o^s}{M_oRT_s^2}} \qquad (2\text{-}30)$$

$$T(\infty,t) = T_o \text{ and } C_o(\infty,t) = C_o^o \text{ @ } x=\infty \qquad (2\text{-}31)$$

II.2.6 Approximate Conservation Equations

In this study, an approximate solution is obtained by assuming that Q^* and $\partial \bar{h}_o/\partial x$ are zero; in other words, the thermal diffusion (Soret and Dufour effects) of oxygen is neglected and the oxygen diffusion does not transport any energy. Dependence of the physical properties of the solid or liquid on oxygen concentration is neglected, but their temperature dependence is accounted for. Also, the ablation heat term $\sum_i M_i \Phi_i \Delta H_i^v$ is approximated by $j_{tot} \Delta H_{vap}$, where ΔH_{vap} is the heat of vaporization from P_{tot}-T relation (P_{tot} is the total vapor pressure of UO_2) and j_{tot} is the total vaporization flux.

$$j_{tot} = \sum_i M_i \Phi_i \tag{2-32}$$

The validity of these approximations has been tested and found to be acceptable.

In reality, it is the oxygen-to-uranium ratio, O/U, in which we are interested rather than the oxygen concentration C_o. Let us define the oxygen-to-uranium ratio $r = \frac{C_o/M_o}{C_U/M_U}$. Since the concentration of uranium C_U is assumed constant, we can obtain equations for r simply multiplying the equations involving C_o by $\frac{M_U}{M_o C_U}$. Also, the optical absorbtivity can be increased by a preheating technique (see section III.1.3) which eliminates sub-surface heating, so that we can drop the volumetric heat source term Q_v. For laser surface heating, Q_s in the boundary condition can be expressed as $(1-R)q_p(t)$, where R is the reflectivity of solid surface to the laser light and $q_p(t)$ is the laser power density on the surface at time t.

With the above simplifications and variable change, the governing equations become:

$$\frac{\partial r}{\partial t} = \frac{\partial}{\partial x}(D_o \frac{\partial r}{\partial x}) + v \frac{\partial r}{\partial x} \tag{2-33}$$

$$\frac{\partial T}{\partial t} = \frac{1}{\rho C_p} \frac{\partial}{\partial x}(k \frac{\partial T}{\partial x}) + v \frac{\partial T}{\partial x} \tag{2-34}$$

$$\text{I.C.: } T(x,0) = T_o \text{ and } r(x,0) = r_o \tag{2-35}$$

$$\text{B.C.: } (\frac{\partial T}{\partial x})_{x=0} = \frac{1}{k_s}[j_{tot} \Delta H_{vap} + \epsilon_t \sigma (T_s^4 - T_b^4) - (1-R) q_p(t)] \tag{2-36}$$

$$(\frac{\partial r}{\partial x})_{x=0} = -\frac{1}{D_o^s}(\frac{j_o^g M_U}{C_U M_o} + v r_s) \tag{2-37}$$

$$T(\infty,t) = T_o \text{ and } r(\infty,t) = r_o \tag{2-38}$$

where r_s and r_o are the oxygen-to-uranium ratios of the solid at the surface and in the bulk, respectively.

The species evaporation rates Φ_i which contribute to the total ablation rate j_{tot} are obtainable from Eqs. (2-19) and (2-19a) if the partial vapor pressures of all gaseous species are known functions of surface temperature and surface O/U ratio. The Φ_i also determine the ablation velocity v by Eq. (2-18) and the oxygen vaporization flux by Eq. (2-17). The vaporization terms in the boundary conditions couple the heat conduction and oxygen diffusion problems. The objective of the calculation is the Φ_i which are related to the signals detected by the mass spectrometer in the vacuum experiment. In addition, the calculation produces the temperature of the surface T_s which is also measured by the optical pyrometer. Both Φ_i and T_s are functions of time, and are measured from the time of impingement of the laser on the surface.

The standard classical reference on the conduction heat transfer analysis is the book by Carslaw and Jaeger*[37]*, in which a number of exact solutions are given for semi-infinite solids that are subjected to a variety of initial and surface conditions. In almost all of the problems for which an exact solution is possible, the thermal properties k, ρ and C_p are taken to be constant. In addition, the problems amenable to analytic solutions have linear initial and boundary conditions. However, in our case, the considerable nonlinearities resulting from the temperature-dependent thermal properties, the convectivelike term appearing from coordinate transformation, and the nonlinear boundary conditions containing the strong temperature-dependent ablative and radiation heat loss terms, make exact solution impossible.

The system of Eqs. (2-33) - (2-38) is solved numerically by the method described in Appendix B. The most commonly used numerical method for solving this kind of problem is the finite difference method*[38-42]*. Although it has been found that the finite difference method is not very efficient for highly nonlinear problems, it turns out to work quite well with a smoothly-varying heat source which drives the transient, with a predictor-corrector scheme for constructing a good initial guess for the iterations and by the use of varying time and space increments.

The material properties of UO_2 required in the analysis are given in Appendix D. They are permitted to vary with temperature but not with oxygen-to-uranium ratio. The overall effect of the vaporization process is to make the surface of the urania hypostoichiometric. Although the diffusivity of oxygen in solid UO_{2-x} has not yet been measured, it is almost certainly composition-dependent and larger than that in UO_2. However, the surface is melted very shortly at the initiation of a high energy laser pulse, and the diffusivity of oxygen in liquid UO_{2-x} is the important quantity. Its value is completely unknown but it is doubtful that concentration effects are as important as temperature effects in the liquid range.

II.3 SAMPLE ANALYSES FOR UO_2 VAPORIZATION

Two computer programs have been developed in this study. The program "STAR" (Surface Temperature And composition Ratio calculation) is for the materials which vaporize incongruently, so that the surface composition changes are coupled with a temperature transient. In this program, one-dimensional time-dependent heat conduction and diffusion equations are solved considering melting, the moving boundary, ablation, and radiation heat losses. The program "SURFT" (SURFace Temperature calculation) is for the materials which vaporize congruently so that no diffusion process is involved and only one-dimensional heat conduction equation with the moving boundary and ablation and radiation heat losses is solved.

Depending on the laser high voltage used to achieve different energy levels, the laser output has different pulse shape. These are shown in Fig. 2.1 for 10 joules and 30 joules pulses. The power density for use in Eq. (2-36) is determined from the pulse energy and the normalized laser pulse shape by the method described in Section III.2.1. Table C.1 of Appendix C shows an example of the input deck of the program "STAR" with total laser energy of 10 joules and the pulse shape shown by the solid line in Fig. 2.1.

Fig. 2.2 shows the results of the "STAR" computer run for 10 joules. The initial temperature (T_o) is 1600 K. The surface composition depletion is about 1.95 at 10 joules and as low as 1.75 at 30 joules. The maximum surface temperature from "STAR" is 3954 K for 10 joules and 4607 K for 30 joules. Corresponding to these surface temperatures, the "forced congruent" model*[31]* gives surface compositions of about 1.89 at 3954 K and about 1.57 at 4607 K. Fig. 2.3 shows the temperature and O/U distribution in the UO_2 at the time that the maximum temperature is achieved. The oxygen-depleted zone is seen to extent to a depth of ~5 μm.

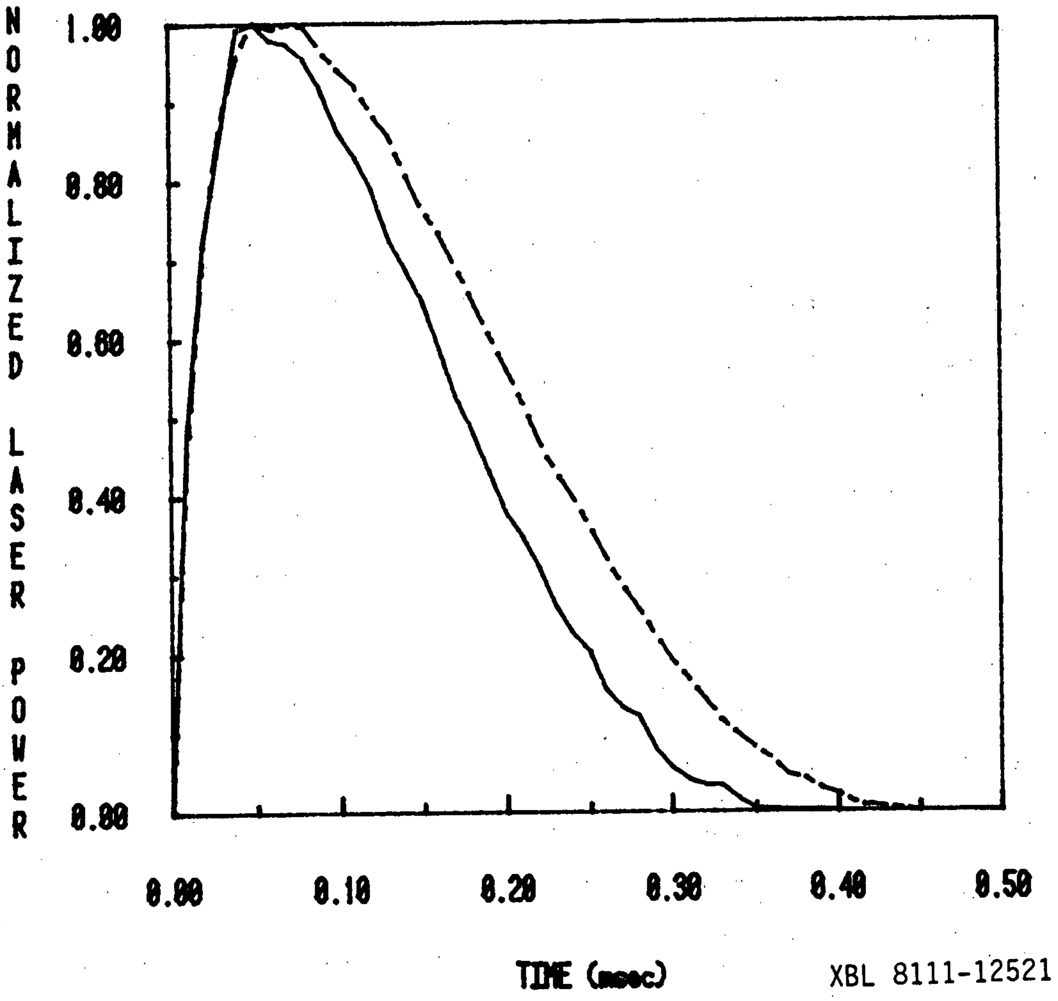

XBL 8111-12521

Fig. 2.1 Normalized Laser Temporal Shape

——— $7.32 < E < 10.6$ joules

–·–·– $11.4 < E < 16.8$ joules

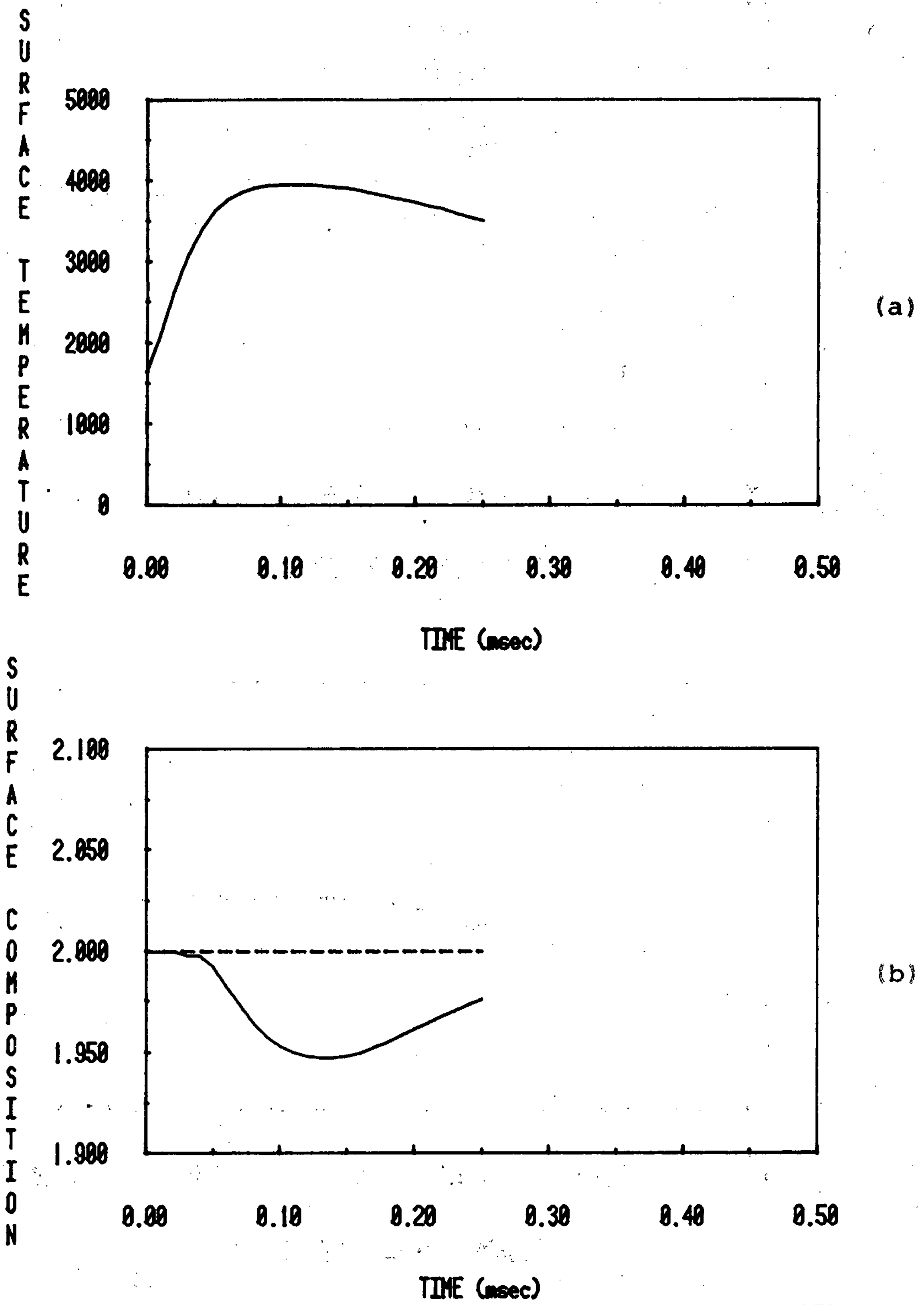

XBL 8110-12279

Fig. 2.2 (a) The Surface Temperature Transient and (b) The Surface Composition Transient for a 10 J Laser Pulse on UO_2

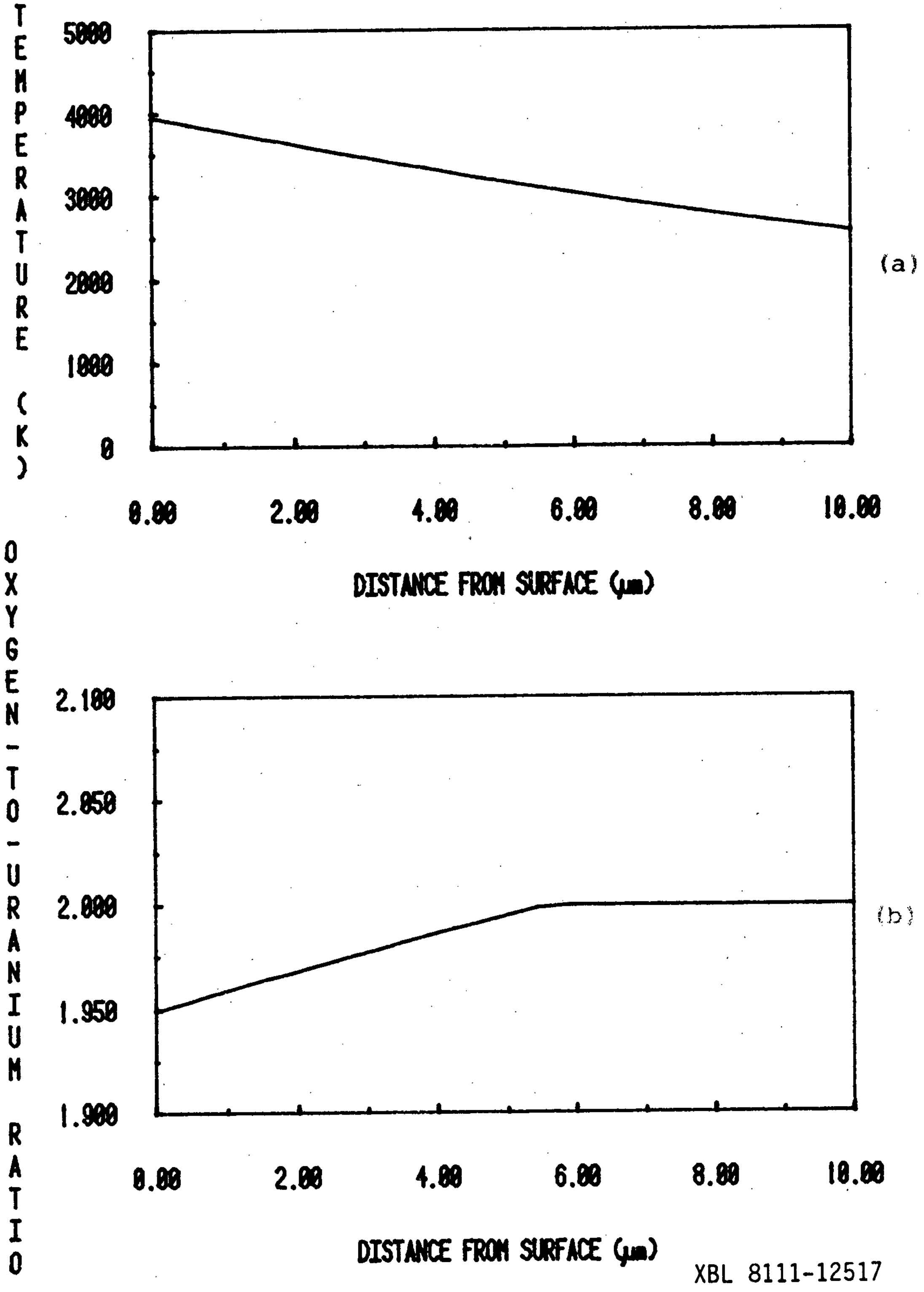

XBL 8111-12517

Fig. 2.3 (a) Temperature Distribution and (b) Oxygen-to-Uranium Ratio Profile in UO_2 Subject to a 10 J Laser Pulse (at Maximum Surface Temperature)

II.4 SENSITIVITY ANALYSIS OF THE PROPERTY UNCERTAINTIES

Some of the material properties of liquid UO_2 provided in Appendix D have not been precisely measured. A sensitivity study is to investigate the effect of these property uncertainties on the calculation described in the previous sections. The method of uncertainty analysis selected for use with STAR code is the Response Surface Method (RSM) *[107,108].*

II.4.1 Background of Response Surface Method

Any of the output variables of a computer code may be termed a "response". The response of the output variables to the input variables defines a surface termed "response surface". The response surface method of uncertainty analysis is based on a systematic sampling of the true response surface which is then approximated by a polynomial equation in the input variables.

Let $Y(z_i)$ denote the code response as a function of $z = z_1, z_2, \cdots z_k$ input variables. The Taylor's series expansion about any point μ_i is then given by:

$$\begin{aligned} Y(z_i) = Y(\mu_i) + \sum_{i=1}^{k} \frac{\partial Y(\mu_i)}{\partial z_i}(z_i - \mu_i) + \frac{1}{2}\sum_{i=1}^{k} \frac{\partial^2 Y(\mu_i)}{\partial z_i^2}(z_i - \mu_i)^2 \\ + \sum_{i,j>i}^{k} \frac{\partial^2 Y(\mu_i)}{\partial z_i \partial z_j}(z_i - \mu_i)(z_j - \mu_j) + \text{higher order terms} \end{aligned} \qquad (2\text{-}39)$$

It has been shown that a range of plus and minus one standard deviation ($\pm 1\sigma$) in the input variable uncertainties permit construction of a sample surface small enough so that the true response surface can be reasonably approximated by a second order polynomial. Furthermore, multiplying and dividing each term of Eq. (2-39) by one standard deviation, σ_i, of the appropriate variable leads to the following form of the equation:

$$\begin{aligned} \underset{\sim}{Y}(z_i) = Y(\mu_i) + \sum_{i=1}^{k} \frac{\partial Y(\mu_i)\sigma_i}{\partial z_i}\frac{(z_i - \mu_i)}{\sigma_i} + \frac{1}{2}\sum_{i=1}^{k} \frac{\partial^2 Y(\mu_i)\sigma_i^2}{\partial z_i^2}\frac{(z_i - \mu_i)^2}{\sigma_i^2} \\ + \sum_{i,j>i}^{k} \frac{\partial^2 Y(\mu_i)}{\partial z_i \partial z_j}\sigma_i\sigma_j\frac{(z_i - \mu_i)(z_j - \mu_j)}{\sigma_i\sigma_j} \end{aligned} \qquad (2\text{-}40)$$

Now, let us define the response parameters as follows:

$$C_o = Y(\mu_i)$$

$$C_i = \frac{\partial Y(\mu_i)}{\partial z_i}\sigma_i$$
$$C_{ii} = \frac{1}{2}\frac{\partial^2 Y(\mu_i)}{\partial z_i^2}\sigma_i^2 \qquad (2\text{-}41)$$
$$C_{ij} = \frac{\partial^2 Y(\mu_i)}{\partial z_i \partial z_j}\sigma_i\sigma_j$$
$$x_i = \frac{z_i - \mu_i}{\sigma_i}$$

Then Eq. (2-40) is simplified to a normal form:

$$Y(x_i) = C_o + \sum_{i=1}^{k} C_i x_i + \sum_{i=1}^{k} C_{ii} x_i^2 + \sum_{i,j>i}^{k} C_{ij} x_i x_j \qquad (2\text{-}42)$$

where x_i are dimensionless standard deviations.

The procedures of the analysis then come as follows:

(1) Select a base case problem.

(2) Make a choice of the ouput responses to be investigated and input variables to be perturbed.

(3) Design a pattern of input variable perturbation (to be described in the next section); run the problem as many times as the design dictates, each time varying the input variables according to the pattern.

(4) Generate the response surface equations from the results of the runs.

(5) Solve the response surface equations for the response parameters C's; estimate the mean and variances of the responses (second order mean $\mu = C_o + \sum_{i=1}^{k} C_{ii}$ and variance $\sigma_y^2 = \sum_{i=1}^{k} C_i^2 + \sum_{i,j>i}^{k} C_{ij}^2$).

(6) Estimate the fractional contributions of the input variables to the response variance ($FC_i = C_i^2 / \sum_{i=1}^{k} C_i^2$).

II.4.2 Input Variables Perturbation Pattern

The design of the perturbation pattern chosen for this study is called Two Level Factorial design*[108]*. "Two level" refers to the fact that each factor (input variable) is evaluated at two different values (e.g. plus and minus one standard deviation). "Factorial" means that factor will be perturbed simultaneously, rather than the usually used "one-at-a-time" perturbation, with permutations of the original pattern used to obtain a sufficient number of runs. Each run generates one point on the response surface Y, and if n runs are required, a set of n equations with the form of Eq. (2-42) and coefficients either +1 or -1 is constructed to solve for the C's.

II.4.3 Sensitivity Study for UO_2 Vaporization

The material properties chosen as uncertain input variables for sensitivity study are chosen as the thermal conductivity, the oxygen diffusion coefficient and the heat of vaporization for liquid phase UO_2. All the other properties are considered relatively accurate compared to these three factors. The output variables to be investigated are the maximum surface temperature and the surface composition at the time when surface temperature is maximum. Table 2.1 lists the value of the input variables used in the computer runs and the response of each run.

The next step is to generate the response surface equations for the perturbation pattern shown in Table 2.1:

$$\begin{aligned}
y_1 &= C_o+C_1+C_2+C_3+C_{11}+C_{22}+C_{33}+C_{12}+C_{23}+C_{13}\\
y_2 &= C_o-C_1+C_2-C_3+C_{11}+C_{22}+C_{33}-C_{12}-C_{23}+C_{13}\\
y_3 &= C_o+C_1-C_2+C_3+C_{11}+C_{22}+C_{33}-C_{12}-C_{23}+C_{13}\\
y_4 &= C_o-C_1+C_2+C_3+C_{11}+C_{22}+C_{33}-C_{12}+C_{23}-C_{13}\\
y_5 &= C_o-C_1-C_2-C_3+C_{11}+C_{22}+C_{33}+C_{12}+C_{23}+C_{13}\\
y_6 &= C_o-C_1-C_2+C_3+C_{11}+C_{22}+C_{33}+C_{12}-C_{23}-C_{13}\\
y_7 &= C_o+C_1+C_2-C_3+C_{11}+C_{22}+C_{33}+C_{12}-C_{23}-C_{13}
\end{aligned} \tag{2-43}$$

where subscript 1 denotes thermal conductivity, 2 denotes oxygen diffusion coefficient, and 3 denotes heat of vaporization.

Letting $\mu = C_o+C_{11}+C_{22}+C_{33}$, which is equal to the mean, Eq. (2-43) can be expressed as a matrix equation:

$$\begin{bmatrix} y_1 \\ y_2 \\ y_3 \\ y_4 \\ y_5 \\ y_6 \\ y_7 \end{bmatrix} = \begin{bmatrix} 1 & 1 & 1 & 1 & 1 & 1 & 1 \\ 1 & -1 & 1 & -1 & -1 & -1 & 1 \\ 1 & 1 & -1 & 1 & -1 & -1 & 1 \\ 1 & -1 & 1 & 1 & -1 & 1 & -1 \\ 1 & -1 & -1 & -1 & 1 & 1 & 1 \\ 1 & -1 & -1 & 1 & 1 & -1 & -1 \\ 1 & 1 & 1 & -1 & 1 & -1 & -1 \end{bmatrix} \begin{bmatrix} \mu \\ C_1 \\ C_2 \\ C_3 \\ C_{12} \\ C_{23} \\ C_{13} \end{bmatrix} \tag{2-44}$$

After Gaussian elimination, Eq. (2-44) becomes

$$\begin{bmatrix} 1 & 1 & 1 & 1 & 1 & 1 & 1 \\ 0 & 1 & 0 & 1 & 1 & 1 & 0 \\ 0 & 0 & 1 & 0 & 1 & 1 & 0 \\ 0 & 0 & 0 & 1 & 0 & 1 & -1 \\ 0 & 0 & 0 & 0 & 1 & 1 & 0 \\ 0 & 0 & 0 & 0 & 0 & 1 & 0 \\ 0 & 0 & 0 & 0 & 0 & 0 & 1 \end{bmatrix} \begin{bmatrix} \mu \\ C_1 \\ C_2 \\ C_3 \\ C_{12} \\ C_{23} \\ C_{13} \end{bmatrix} = \begin{bmatrix} y_1 \\ \frac{1}{2}(y_1-y_2) \\ \frac{1}{2}(y_1-y_3) \\ \frac{1}{2}(y_4-y_2) \\ \frac{1}{4}(y_1+y_5-y_2-y_3) \\ \frac{1}{4}(y_4+y_5-y_2-y_6) \\ \frac{1}{4}(y_1+y_2-y_4-y_7) \end{bmatrix} \tag{2-45}$$

Therefore, the coefficients μ, C_i's can be solved:

$$\begin{aligned} C_{13} &= \frac{1}{4}(y_1 + y_2 - y_4 - y_7) \\ C_{23} &= \frac{1}{4}(y_4 + y_5 - y_2 - y_6) \\ C_{12} &= \frac{1}{4}(y_1 + y_6 - y_3 - y_4) \\ C_3 &= \frac{y_4-y_2}{2} - C_{23} + C_{13} \\ C_2 &= \frac{y_1-y_3}{2} - C_{12} - C_{13} \\ C_1 &= \frac{y_1-y_2}{2} - C_3 - C_{12} - C_{13} \\ \mu &= y_1 - C_1 - C_2 - C_3 - C_{12} - C_{13} - C_{23} \end{aligned} \tag{2-46}$$

Applying Eq. (2-46) to the responses maximum surface temperature and surface composition at this temperature respectively can yield the response mean and the coefficient C's, from which the variances and the fractional contributions of the three input variables to the variance can be calculated. The result is shown in Table 2.2. Fig. 2.4 Shows a mean and variance of a surface temperature with time for 10 joules laser energy. Fig. 2.5a & b plot the theoretical means of maximum surface temperature and surface composition at this temperature against laser incident energy respectively, with a band of variances estimated. As expected, uncertainties in k and ΔH_v have the greatest effect on the thermal response while the uncertainty in D_o affects principally the O/U ratio.

TABLE 2.1

Input and Output Variables (Responses) of Sensitivity Study for Laser Evaporation of UO_2

Run#	E_i (joules)	Input Variable			Response	
		x_1*	x_2**	x_3***	T_s^{max} (K)	$(O/U)_{T_s^{max}}$
I-1	10	+1	+1	+1	3865	1.9691
I-2		-1	+1	-1	4155	1.9290
I-3		+1	-1	+1	3895	1.9020
I-4		-1	+1	+1	4016	1.9531
I-5		-1	-1	-1	4195	1.7997
I-6		-1	-1	+1	4052	1.8658
I-7		+1	+1	-1	3973	1.9549
II-1	16.8	+1	+1	+1	4159	1.9206
II-2		-1	+1	-1	4430	1.8468
II-3		+1	-1	+1	4206	1.7966
II-4		-1	+1	+1	4260	1.8979
II-5		-1	-1	-1	4502	1.6547
II-6		-1	-1	+1	4320	1.7421
II-7		+1	+1	-1	4308	1.8829
III-1	30	+1	+1	+1	4550	1.8069
III-2		-1	+1	-1	4827	1.6969
III-3		+1	-1	+1	4639	1.5954
III-4		-1	+1	+1	4623	1.7860
III-5		-1	-1	-1	4952	1.4638
III-6		-1	-1	+1	4732	1.5559
III-7		+1	+1	-1	4737	1.7283

* $x_1=+1$: $k = 0.044$ W/cm-K; $x_1=-1$: $k = 0.031$ W/cm-K

** $x_2=+1$: $D_o = 1.59\times10^{-2}\, e^{-2516/T}$; $x_2=-1$: $D_o = 3.03\times10^{-1}\, e^{-24800/T}$ cm^2/sec

*** $x_3=+1$: $\Delta H_v = 1959$ J/g; $\Delta H_v = 979.5$ J/g

TABLE 2.2

Measured Variances of the Responses from STAR Code

Energy (joules)	Maximum Surface Temperature (K)					Oxygen-to-Uranium Ratio				
	mean	variance	% contribution			mean	variance	% contribution		
			k	D_o	ΔH_v			k	D_o	ΔH_v
10	4018	107	65	2	33	1.9185	0.0463	2	79	19
16.8	4318	105	32	7	61	1.8195	0.0832	20	78	2
30	4738	124	14	19	67	1.6396	0.1224	3	85	12

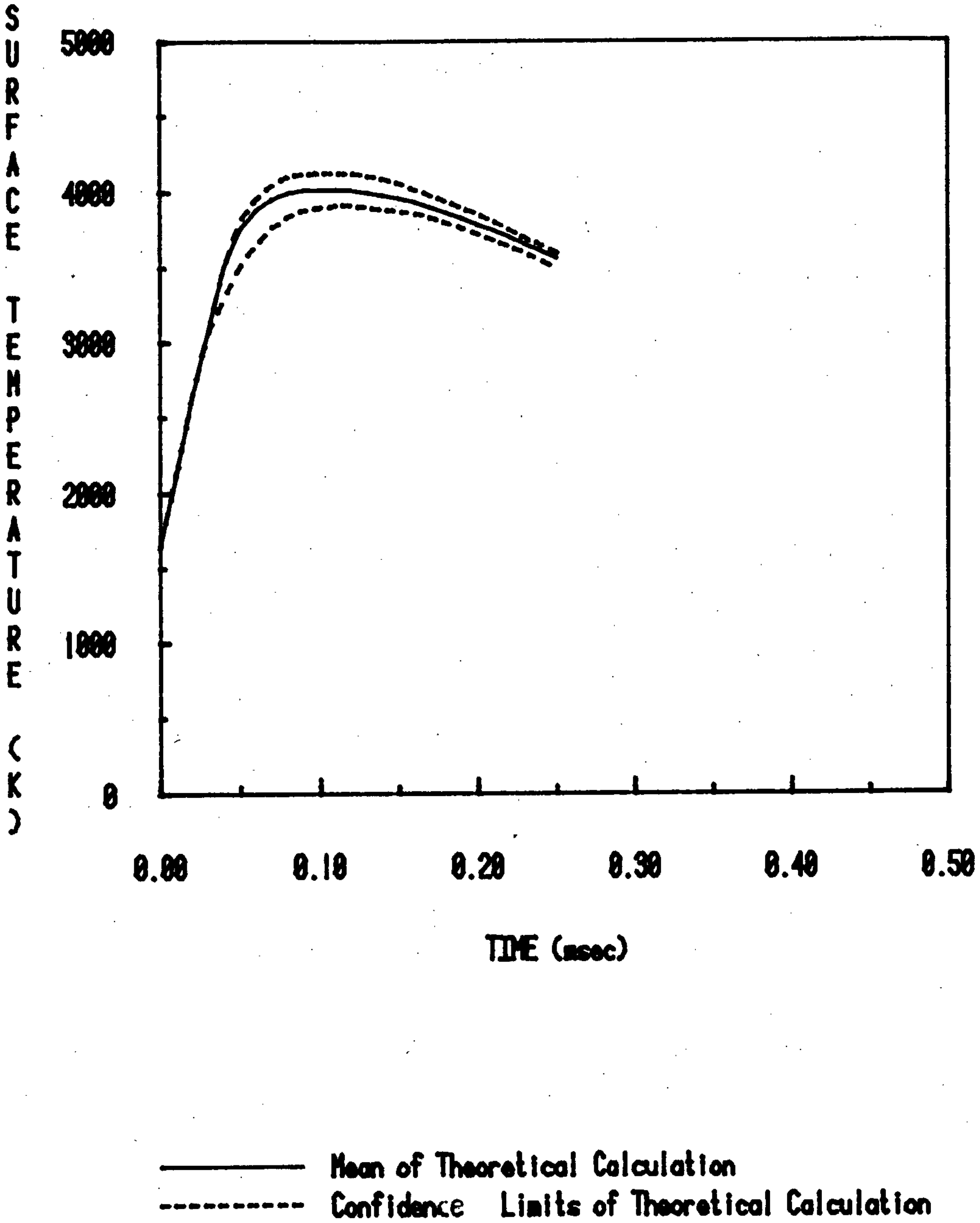

XBL 8111-12510

Fig. 2.4 Mean and Variance of Surface Temperature Transient for a 10 J Laser Pulse from Sensitivity Analysis

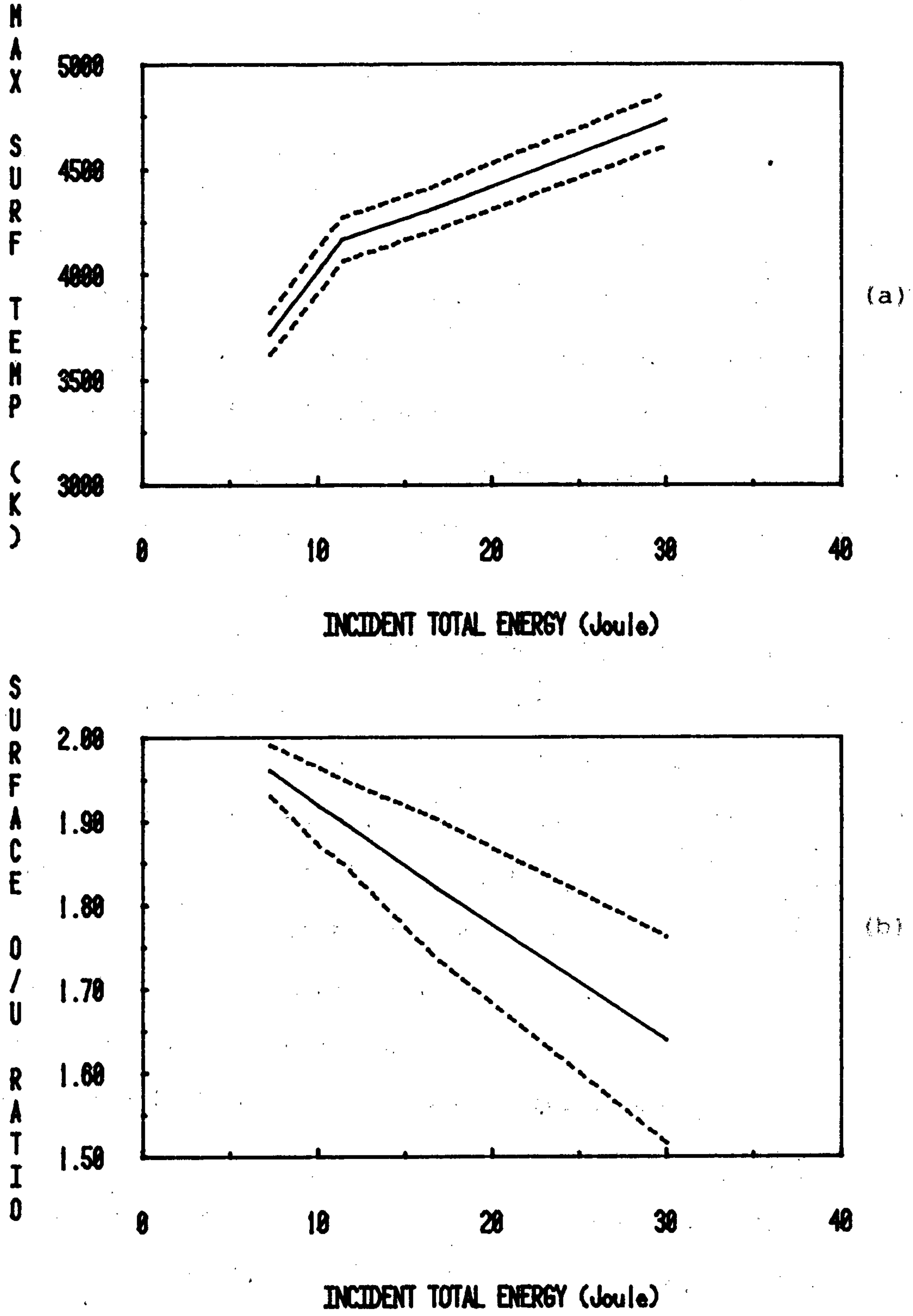

XBL 8111-12511

Fig. 2.5 Theoretical Mean of (a) Maximum Surface Temperature and (b) Surface Composition at Maximum Surface Temperature versus Incident Laser Energy

III. EXPERIMENTAL

III.1. APPARATUS

III.1.1 Overall

The overall system can be divided into five parts: the laser system, the target vacuum chamber, the detector vacuum chamber, the optical pyrometer and the transient data recording device. Each part of the system will be described in detail in subsequent sections. Fig. 3.1 shows a sketch of the system set-up and Fig. 3.2 is an overall view.

The whole system is aligned with the help of three He-Ne CW gas lasers. Their functions are:

(#1) positions the electron bombardment heater holding the UO_2 target by shooting from the window in the end of the mass spectrometer chamber through the ionizer, the two collimating apertures and onto the target.

(#2) aligns the 100% rear mirror reflector and the plane output reflector (~8% reflection) in the Nd-glass laser cavity for efficient pumping by shooting from the front end of the Nd-glass laser cavity (for the complete alignment procedure see Ref. 43).

(#3) aligns the Nd-glass laser on the target by shooting from the rear end of the Nd-glass laser, through the laser rod, the optical components, and hitting the same spot as gas laser #1. The optical pyrometer is aligned by focusing it on the same spot illuminated by gas lasers #1 and #3.

Since the three He-Ne gas lasers and the optical pyrometer are sitting on very stable and precisely adjustable Hercules tripods respectively, the alignment procedure, although tedious and time consuming, could be done very accurately.

III.1.2 Laser System

The laser system is composed of an American Optical 1.06 μm Nd-glass laser with rod replaced by an Owens-Illinois ED-2-3 silicate glass rod doped with 3% Nd^{+3} ions (concentration

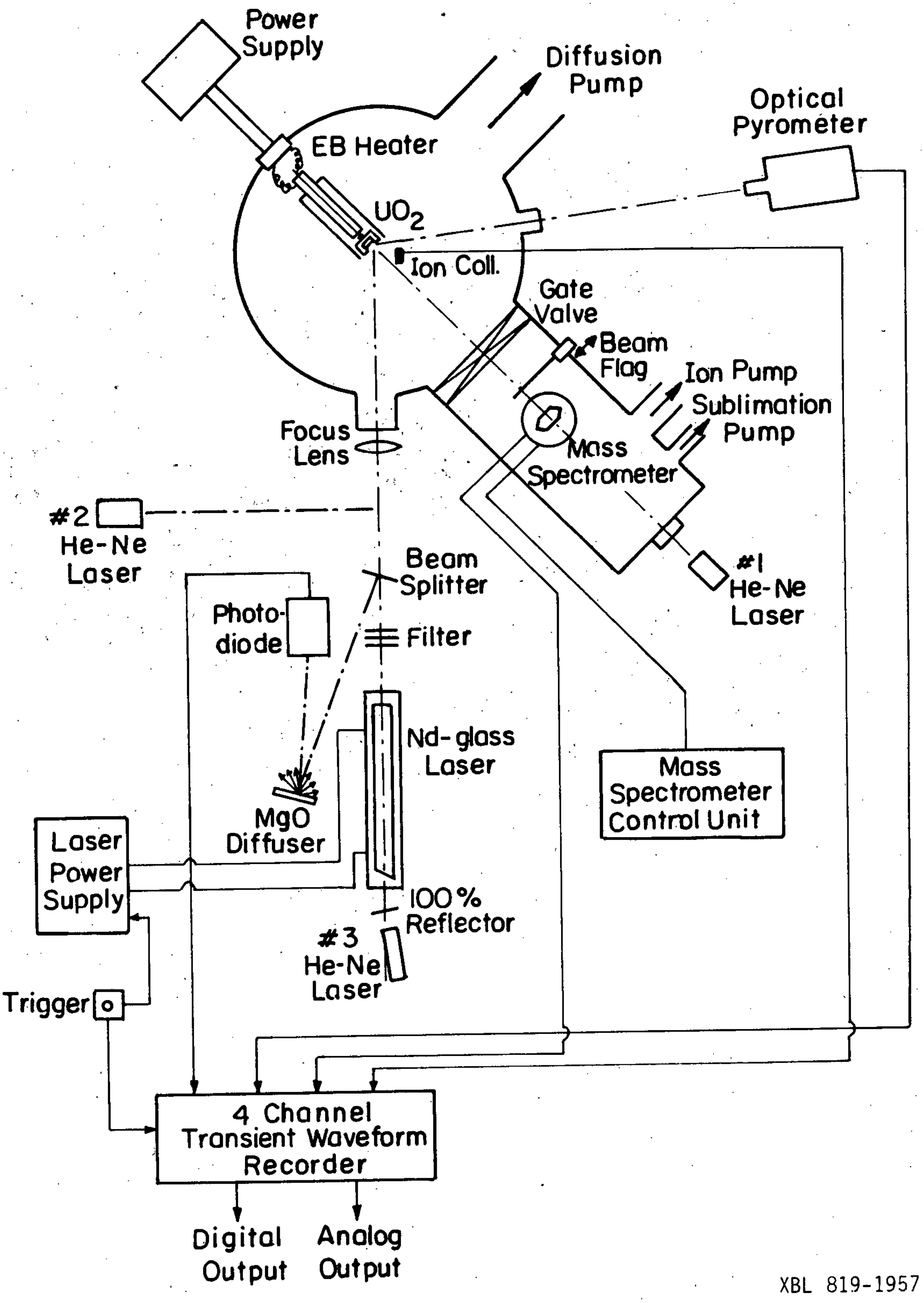

Fig. 3.1 The Apparatus Setup of the Laser-Induced Vaporization Study by Mass Spectrometry

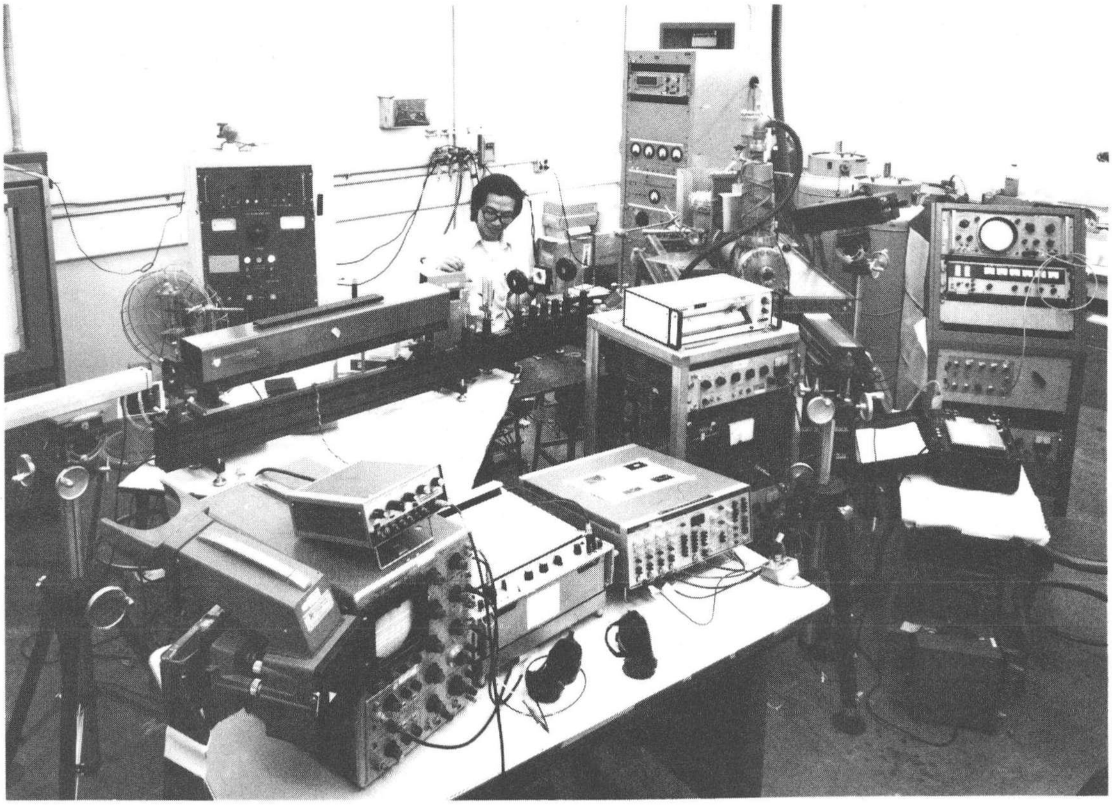

CBB 818-7826

Fig. 3.2 Photograph of the Experimental Apparatus.
(From left to right: He-Ne Laser, Nd-glass Laser, Laser Power Supply on the back, Photodiode, Vacuum System, Electron Beam Heater Power Supply on the back, Optical Pyrometer, Mass Spectrometer Controller. On the front table are Scope, X-Y Plotter, and Transient Waveform Recorder.)

of $0.91\times10^{20}/cm^3$). The rod diameter is 1/2 inches and total length is about 20 inches so that the rod length-to-diameter ratio is optimized at 40 for maximum efficiency*[43,44]*. The rod is distilled-water-cooled on the outside as are the ends. The laser is optically pumped by two linear xenon flashtubes closely coupled to the laser rod with a highly reflective silver reflector. "Conventional" mode is used in this experiment, which means that the laser pulse width is governed by the flash discharge duration (~200 μsec). The laser output energy used is about 20 joules and the energy incident on the target can be varied by a set of neutral density filters right following the output reflector. The measured beam divergence is around 12 milliradians and the spot size on the target, after passing through a 100 cm beam correcting lens and a 20 cm focusing lens, is an ellipse with minor and major radii of 3.3 and 4.7 mm. The laser beam is partially split to a MgO diffuser and detected by a calibrated Korad KD-1 photodiode, the signal from which is recorded by the first channel of Biomation 1015 transient recorder (to be described later). This gives the laser energy trace and the power as a function of time (normalized power shape as well).

III.1.3 Target Chamber

The target chamber is pumped to 10^{-7} torr by a 500 liters/sec, 6-inch NRC vacuum diffusion pump with a Granville-Phillips liquid nitrogen cold trap. The UO_2 target is mounted on a tungsten cap on the head of a electron bombardment heater. UO_2 sample is a 1.18 cm diameter, 1 mm thickness wafer, cut from the pellets provided by General Electric Co., and the surface exposed to laser is polished by silicon carbide abrasives and diamond paste to ~6 μm roughness. The tungsten holder is heated from a heated tungsten filament, and the UO_2 sample is then heated by thermal conduction. The electron bombardment heater as shown in Fig. 3.3 is mounted on a rotary feed-through fixed on the vacuum flange so that the target could be rotated after each shot to provide fresh areas for subsequent laser pulses. The heater served to (i) heat UO_2 up to ~2400°C for mass spectrometer calibration and (ii) preheat the sample to ~1400°C, the ductile-to-brittle transition temperature of UO_2*[45]*, in order to avoid sample cracking resulting from the large thermal stress induced by laser heating; at this

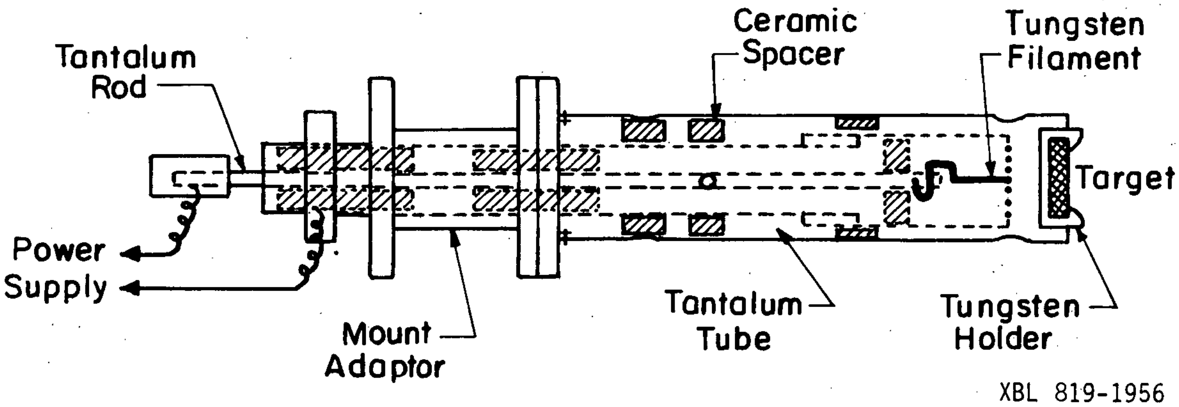

XBL 819-1956

Fig. 3.3 Electron Beam Bombardment Heater temperature, the light absorption cut-off of UO_2 is also shifted to a wavelength of 1.3 μm *[46]* (longer than that of Nd-glass laser 1.06 μm) which avoids in-depth heating by laser radiation penetration into the sample. A pair of collimating apertures, one of 1 mm diameter located at 4" from the target and one of 3.2 mm diameter at 8" from the target, is mounted along the molecular beam axis to ensure that the ionizer only "sees" a ~1 mm diameter spot on the target in both calibration and laser experiments. A Farady-cup ion detector consisting of a copper plate, a -90 volt battery and a 10 MΩ resistor in parallel with a 2μf capacitor and a 50Ω resistor is used to detect the ion signals from the partialy ionized gas ejected from the laser heated target. The ion current is recorded by the fourth channel of the waveform recorder. Two shield plates are mounted on feed-throughs of each side of the chamber to protect the glass windows for laser beam entry and for temperature measurement from being coated during calibration. They are removed by feed-throughs prior laser pulsing.

III.1.4 Detector Chamber

The detector chamber is pumped by a 200 liters/sec ULTEK ion pump and a Varian titanium sublimation pump. With the gate valve closed, the detector chamber is kept under vacuum of ~10^{-10} torr. During experimental runs with the gate valve open, the pressure increases to 10^{-8} torr range. The mass spectrometer ionizer is located 40 cm from the target. A beam flag mounted on a linear feed-through is positioned between the collimating aperture and the ionizer for blocking the molecules emitted from the target during mass spectrometer calibration (to be described in the later section) in order to measure the background signals. The detector is an EAI Quad 250 quadrupole mass spectrometer (see Fig. 3.9) with its axis perpendicular to the molecular beam path (i.e. perpendicular to the normal to the target surface), so that the detector is molecular-beam-density sensitive. A small percentage of the molecules passing through the ionizer is ionized by the electrons emitted from one of the dual tungsten filaments. Some of the ions are then accelerated by the ion potential at the entry of the quadrupole structure and focused by an electrostatic focusing lens into the quadrupole section. The quadrupole as a "mass filter" has applied R.F. and D.C. fields which allows only those ions within a specific range of charge-to-mass ratios with stable orbits to reach the end of the structure and be detected by a Bendix electron multiplier. The current signal produced at the electron multiplier output, which is spread out to much longer pulse width than the laser pulse due to the time of flight and the velocity distribution of the molecules and shifted a time delay due to the transit time of the ions through the quadrupole, is recorded in the third channel of the transient waveform recorder.

III.1.5 Optical Pyrometer

The target surface temperature is measured by a PYRO "Photomatic" I automatic optical pyrometer manufactured by Pyrometer Instrument Company, Inc. The instrument is divided into two parts: (1) The optical unit which consists of a high sensitivity photo multiplier tube, an interference filter for wavelength of 6500±100 Å, a high voltage power supply and preamplifier, a set of three range filters, an objective lens, a reference standard lamp and a modulating oscillator, (2) The electronic unit which consists of a temperature indicating meter, scale range selector and indicator lights, function switch knob, a null balance control, a recorder jack and a controller jack *[47]*. The two units are connected by a cable.

The pyrometer has two modes of operation: automatic and transient. The automatic mode was used for preheating and mass spectrometer calibration when steady state temperatures were measured. In this mode, it operates on the same principle as the disappearing filament pyrometer except an auto-adjusting feedback electronic null-balance system replaces the human eye in comparing the target source radiation with the internal reference lamp.

The transient mode bypasses the internal lamp and operates as an optical system coupled directly to a photo multiplier. Since the power supply in the as-received optical unit was not regulated, an external regulated, high stability FLUKE power supply was used in transient mode operation. In this mode, the unit has a response on the order of nanoseconds, thus allowing measurements of temperature transients in the range of milliseconds. These are recorded by the second channel of the transient waveform recorder. The target focusing is adjustable from 8" to infinity. The target size-to-focal distance relationship is governed by the equation:

$$D = \frac{x}{400} \qquad (3\text{-}1)$$

where D = target diameter in inches

x = distance in inches between target and objective lens.

In this experiment, corresponding to x of 19.25 inches, the target diameter was about 0.048 inches or 1.22 mm. After taking into account the 45° incidence, the major axis of the pyrometric viewing spot on the target was about 1.73 mm.

III.1.6 Transient Data Recording

A 4-channel transient waveform recorder manufactured by Gould Inc., the Biomation Model 1015, is used to capture the signals from the laser power photodiode, the optical pyrometer, the mass spectrometer and the ion detector. It has four input channels each with 1024 words memory capacity so that it can record four different signals simultaneously. The fastest sampling rate of this device is 10 μsec/sample (or 100 kHz). The recorder is triggered by the same signal which triggers the laser flashtubes. It then samples and digitizes the input signals by A/D converters, and stores the counts in the memory. The signals are then retrieved later through built-in D/A converters by a X-Y plotter at a slower rate. A unique capability of this device is its ability to record the signal preceding the trigger time. This "pretrigger recording" feature ensures recording of the leading baseline and rise of a signal. This device also greatly reduces the systematic error inherent in analyzing the photographed signals monitored by an oscilloscope *[48]*.

III.2. SYSTEM CALIBRATION

III.2.1 Laser Parameters

The laser parameters characterizing the process of laser-material interactions normally include (i) temporal pulse shape (ii) radial power intensity distribution and (iii) pulse energy. These parameters are part of the input to the computer code described in Chapter 2 and need to be known in each experiment.

III.2.1.1 Temporal Laser Pulse Shape:

The time variation of the laser power during each shot is measured by a Korad KD-1 photodiode. This device was calibrated with a Korad K-J2 calorimeter, which was pre-calibrated by the manufacturer. The photodiode output gives a voltage V(t) from which the laser power as a function of time can be obtained from the following effective pulse width:

$$t_{pul} = \frac{E}{P_{max}} = \int \frac{P(t)}{P_{max}} dt = \int \frac{V(t)}{V_{max}} dt \tag{3-2}$$

where E = the incident total energy of the pulse in joules,

$P(t)$ = the incident power at time t in watts,

P_{max} = the incident maximum power in watts,

$V(t)$ = the voltage output of the photodiode at time t in volts,

and V_{max} = the maximum voltage output of the photodiode.

The relation is valid as long as the responsivity of the photodiode is linear. The integration $\int V(t)/V_{max} dt$ over the pulse can be obtained from the photodiode and E from the calorimeter (after correcting for window transmission), then the Eq. (3-2) yields P_{max}. For the normalized laser pulse shapes shown in Fig. 2.1, t_{pul} = 0.1685 msec and 0.2067 msec; For a laser shots of 10 and 30 joules, P_{max} is 60 kW and 150 kW respectively. The incident power at any time can be obtained from the linear relation of P and V:

$$P(t) = V(t) \frac{P_{max}}{V_{max}} \tag{3-3}$$

III.2.1.2 Radial Laser Power Intensity Distribution in the Beam:

The laser beam intensity profile across the radius must be known to determine the peak power density at the center of the beam spot where the surface temperature is measured and the signal measured by the mass spectrometer arises. In the measurements on iron and zirconium hydride*[48]* and the preliminary measurements on UO_2*[49]*, a low energy Ruby laser was used; a Gaussian shape of the beam was assumed and the manufactuer's value of divergence angle was accepted. However, it is believed that the intensity distribution from a high power Nd-glass laser has broader wings than a Gaussian because the beam is composed of several components of different divergence angles*[50]*. Therefore the focal spot calculation after a single-element aspheric lens that assumes a single divergence angle can be misleading. Consequently, the focal spot intensity distribution has to be determined experimentally.

The conventional way of obtaining this information from measurement of an exposed spot on film is not adequate because this technique needs preliminary densitometry of the film and the method by which it is developed. In addition, at high exposures the film saturates in the center of the spot, giving an artificially flattened profile. Another method of determining the radial power profile is by measuring the energy passing through pinholes of various sizes. This technique yields good results on the focal spot size but it is limited by the diffraction limit. In the present work, a knife-edge technique has been used for this measurement*[51,52]*. In this procedure a sharp-edge razor blade is moved across the focal plane by a micrometer at an angle of 45 degrees and the transmitted energy as a function of blade-edge position is measured with the laser calorimeter (Fig. 3.4). The transmitted energy curve is then differentiated and fitted to a parabolic distribution, assuming axial symmetry. Fig. 3.5 shows the computer fit of the normalized intensty profile $I(r)/I_p$, where $I(r)$ is the energy density at radius r, $I(r)=\int q(r,t)dt$, $q(r,t)$ being the power density at radius r and time t, and I_p is the energy density at center $r=0$, $I_p=\int q_p(t)dt$, $q_p(t)$ being the central power density at time t.

Since E = total energy of one pulse = $\int I(r)2\pi r dr$,

$$\frac{E}{I_p} = \int \frac{I(r)}{I_p} 2\pi r dr = A_{eff} \qquad (3\text{-}4)$$

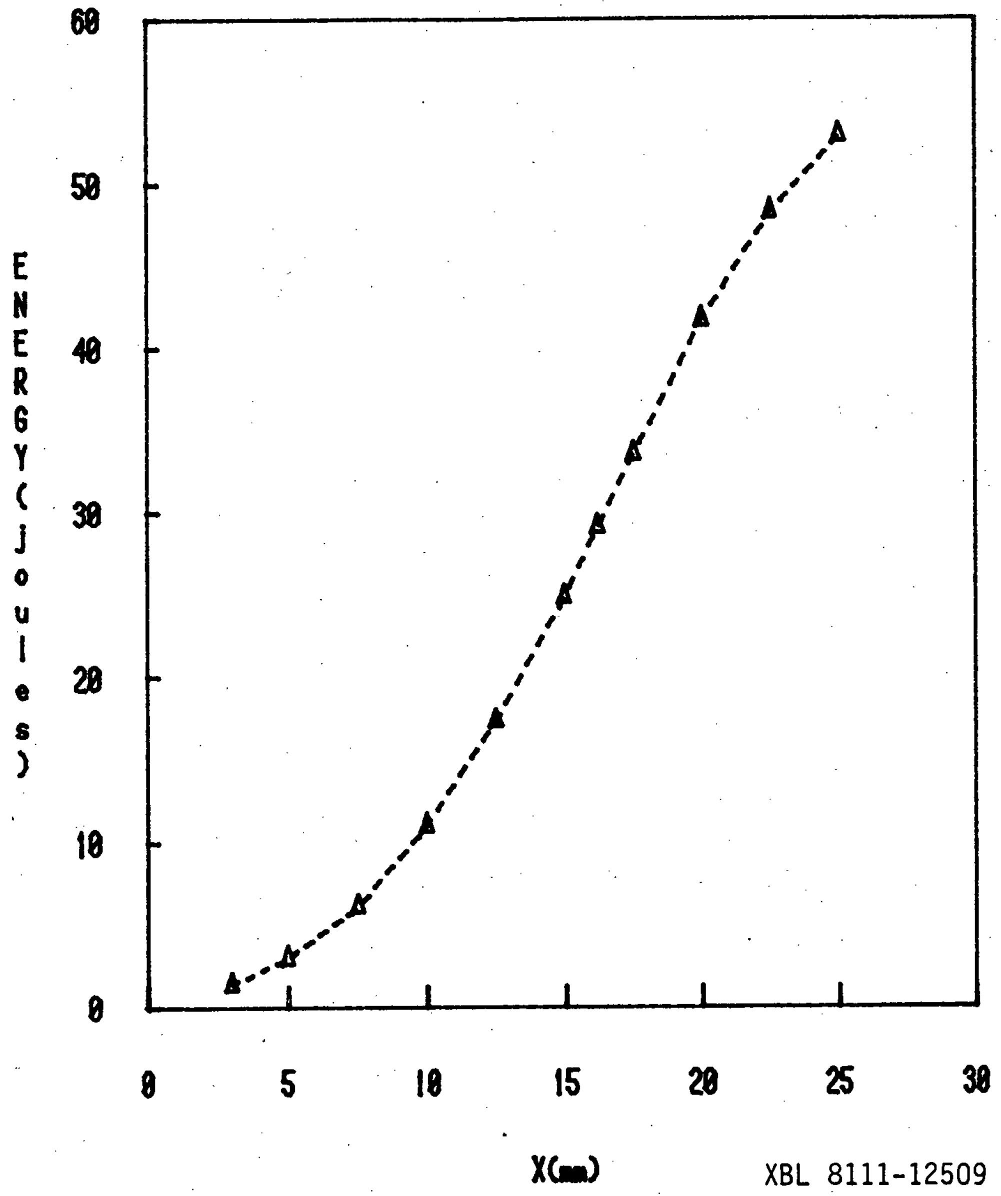

Fig. 3.4 Transmitted Energy versus Knife-edge Position in Laser Radial Power Distribution Measurment (x is the knife-edge position in the direction of micrometer motion at 45° to the laser beam path.)

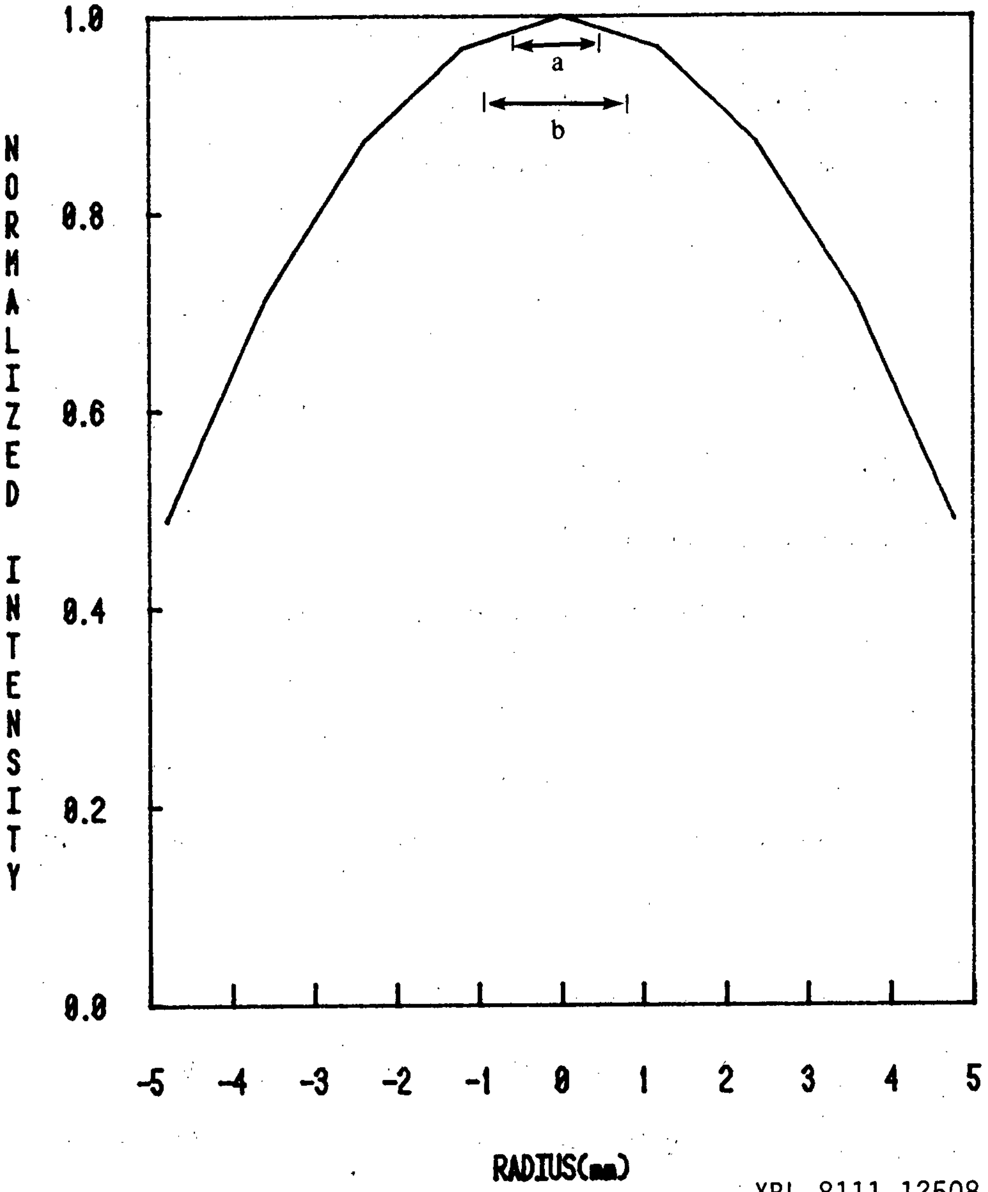

XBL 8111-12508

Fig. 3.5 Normalized Laser Radial Power Intensity Distribution from Knife-edge Measurement (along major axis)

a: mass spectrometer viewing spot (~1 mm diameter)

b: optical pyrometer viewing spot (~1.73 mm diameter) where A_{eff}, the "effective" area defined above can be obtained by integrating the normalized intensity profile. For the focused laser spot shown in Fig. 3.5, in which 45° angle of incidence is already taken into account, A_{eff} is equal to 0.4964 cm^2. This is the area which would be illuminated by a spatially uniform laser pulse of power density $q_p(t)$ and give the total energy in the real pulse. The mass spectrometer and optical pyrometer viewing spots are also indicated in Fig. 3.5.

Then the central energy density is equal to the ratio of total energy to the effective area, or E/A_{eff}. Since $I_p = \int q_p(t)dt$,

$$\frac{I_p}{q_p^{max}} = \int \frac{q_p(t)}{q_p^{max}} dt = \int \frac{P(t)}{P_{max}} dt = t_{pul} \tag{3-5}$$

where q_p^{max} is the maximum (in t) central power density in W/cm^2.

Combining Eqs. (3-4) and (3-5), the central maximum power density is:

$$q_p^{max} = \frac{E}{A_{eff} t_{pul}} \tag{3-6}$$

This quantity serves as the scale factor for the normalized laser power pulse shapes shown in Fig. 2.1 and thereby gives the power density source $q_p(t)$ for the theoretical calculation based on Eq. (2-36).

III.2.1.3 Incident Laser Total Energy:

The total energy output of each pulse from the Nd-glass laser can be determined from the measured photodiode voltage signal of each shot with the aid of a calibration relation. Let E_o be the laser pulse energy after the filters and the beam splitter. To calculate the energy incident on the target, corrections for absorption by the optical components such as the lenses and the glass windows have to be made. The neutral density filters are placed between the laser output reflector mirror and the beam splitter so that the energy measured from the photodiode output has already accounted for this attenuation factor. If the transmissivity of the lens is τ_{lens} and the transmissivity of the window is τ_{window}. Then the energy incident on the target is

$$E = E_o \tau_{lens} \tau_{window} \tag{3-7}$$

Fig. 3.6 shows such a calibration, which relates the maximum voltage from the photodiode (V_{max}) and the incident laser energy (E).

III.2.2 Optical Pyrometer Calibration

A THERMOGAGE dual pyrolytic graphite cavity at NASA-Ames Research Center was used as a black body source for calibration of the automatic optical pyrometer used in the experiments. The "true" temperatures were read by a manual optical pyrometer calibrated by the National Bureau of Standards. Both pyrometers were focused on the same spot in the black body cavity. At each cavity current setting, the "true" temperature was marked and, when the range switch was on the second and third scales, the voltages from the transient output jack on the optical unit was recorded by a digital voltmeter. The procedure was repeated for temperatures up to ~3000 K, the limit of the black body source. Above 3000 K, an extrapolation procedure was established by using the absorbing glass formula:

$$A_{lh} = \frac{1}{T_l} - \frac{1}{T_h} \tag{3-8}$$

where T_l is the temperature reading at lower scale, T_h is the temperature reading at higher scale for the same voltage reading and A_{lh} is the relative "A-value" of lower scale absorbing glass to that of higher scale. An average value of A_{lh} was obtained over the voltage range where the temperature readings in scales 2 and 3 were both available. Then the "mean A_{lh} value" was used to determine T_h for the higher voltage range from measured T_l in scale 2 by solving Eq. (3-8).

Fig. 3.7 shows the result from which one can obtain the "brightness" temperature of the target for a particular measured voltage. The calibration curve was fitted to the following formula:

$$\log V_T = \log \frac{C}{e^{a/T}-1} = \log C - \log (e^{a/T}-1) \tag{3-9}$$

The value a = 21994 K was determined, which has good agreement with the Plank equation:

$$\log N_\lambda = \log \frac{C_1\lambda^{-5}/\pi}{e^{C_2/\lambda T}-1} = \log (C_1\lambda^{-5}/\pi) - \log (e^{C_2/\lambda T}-1) \tag{3-10}$$

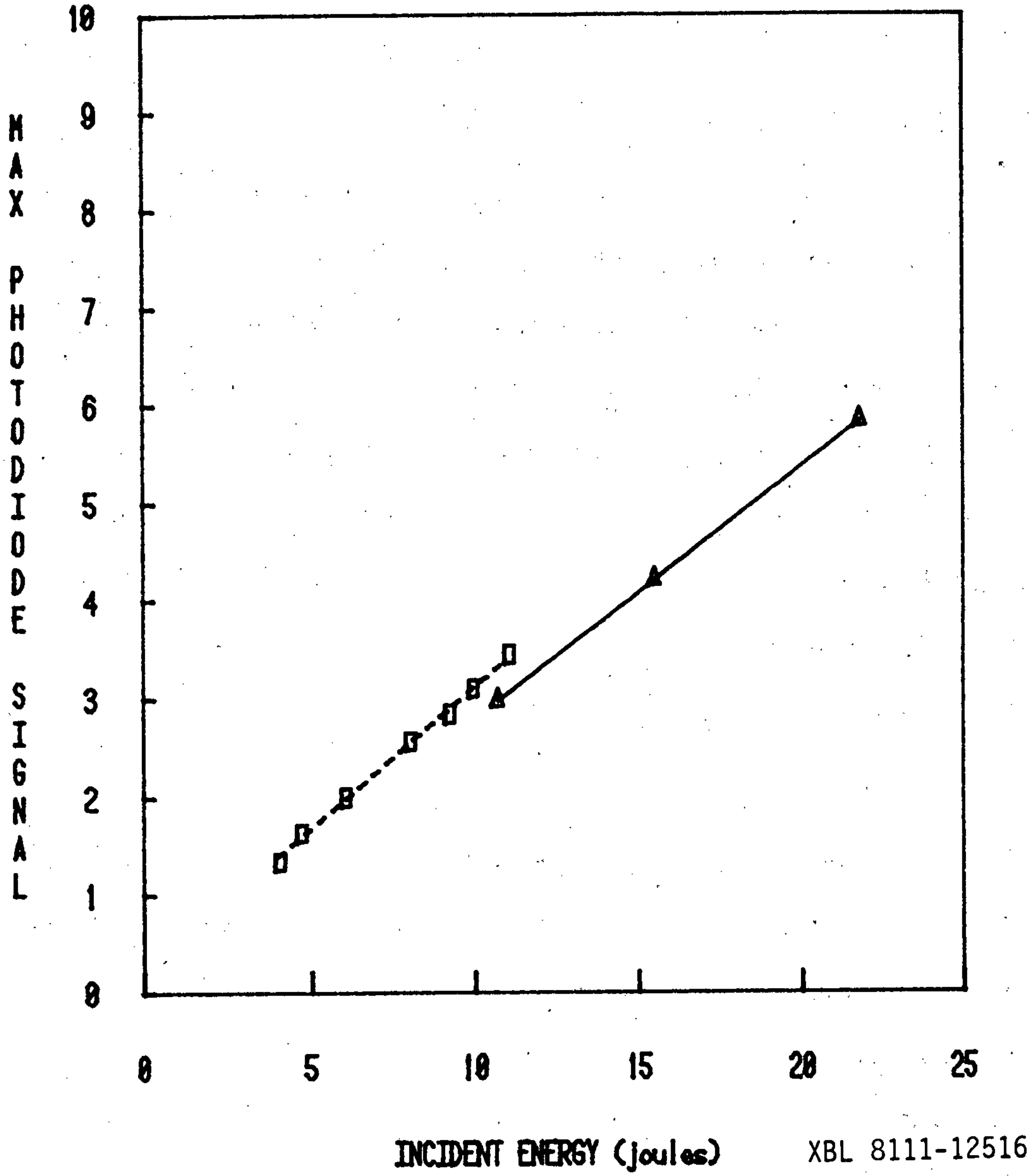

Fig.3.6 Photodiode Calibration for Laser Energy Measurement

□ Laser Voltage = 3000 volts

Δ Laser Voltage = 3500 volts

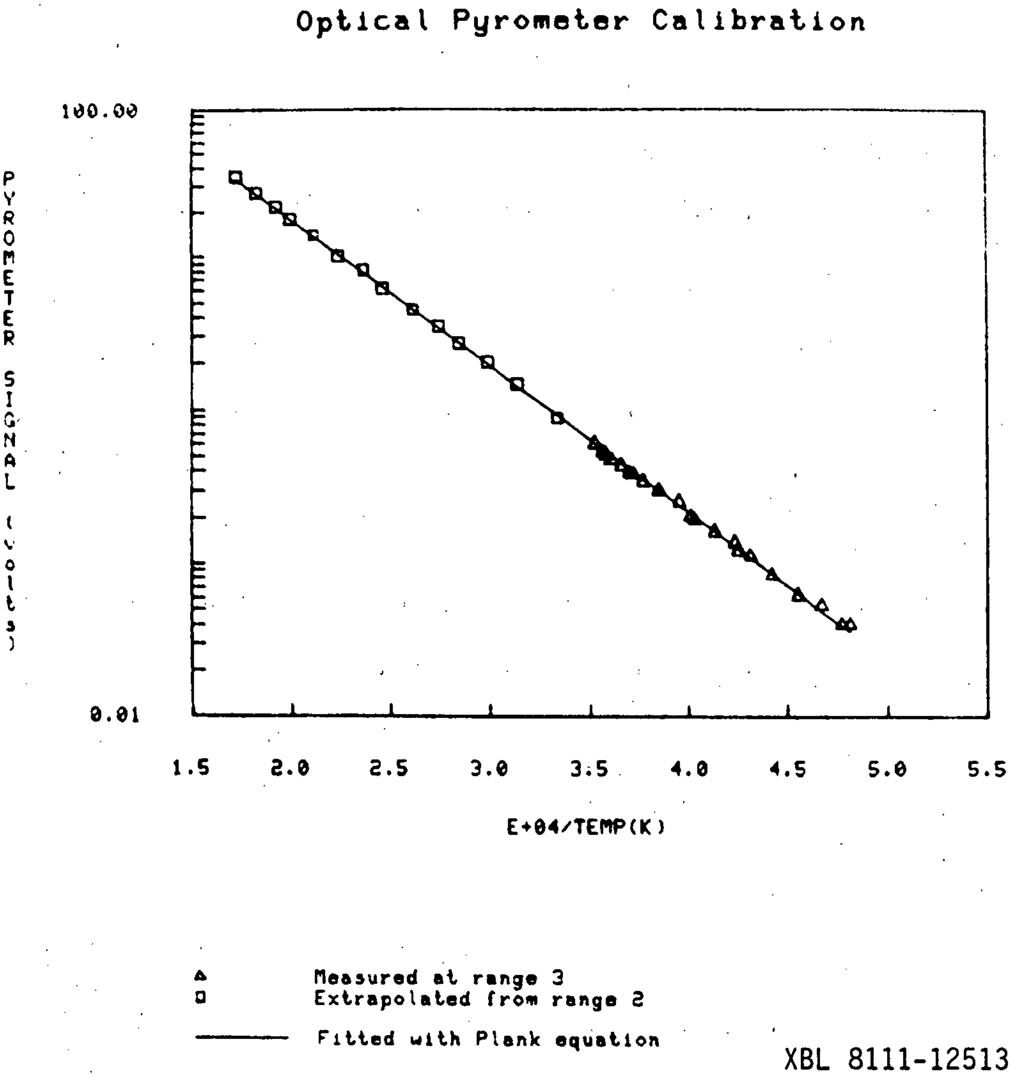

XBL 8111-12513

Fig. 3.7 Optical Pyrometer Calibration for Temperature Measurement in which $C_2/\lambda = 1.438/6500\times10^{-8} = 22100$ K. In order to account for the non-unity emissivity from non-black body radiation, the correction to "real" temperature is made with the formula:

$$\frac{1}{T_o} = \frac{1}{T_b} + \frac{\lambda}{C_2}\ln\epsilon_\lambda \tag{3-11}$$

where T_o is the black body temperature, T_b is the "brightness" temperature, λ is the wavelength of the thermal radiation detected (6500 Å), C_2 is a constant (1.438 cm-K) and ϵ_λ is the optical emissivity at wavelength λ (see Appendix D).

There has been only one attempt to measure the optical emissivity at a wavelength of 6500 Å*[53]*. To estimate the uncertainty in the temperature measurement arising from an uncertainty in the optical emissivity, a 10% error in ϵ_λ will lead to a 43.5 K error in T at 3000 K and 122 K error at 5000 K.

The optical pyrometer is sighted into the target vacuum chamber through a glass window. A correction for absorption by this component can be made by measuring the radiation from a tungsten strip lamp with and without the glass window. The "A-value" of the glass can be obtained through the equation:

$$\frac{1}{T_1} = \frac{1}{T_2} + A \tag{3-12}$$

where T_1 is the temperature reading without the glass, T_2 is the temperature reading with the glass and A is a constant of the glass. Having a series of T_1's and T_2's the average value of constant A can be obtained as -3.6325×10^{-6}. Then, in the real measurement, the true temperature T_t can be obtained from the black body temperature T_o from the optical pyrometer after correcting for non-unity emissivity by:

$$\frac{1}{T_t} = \frac{1}{T_o} + A \tag{3-13}$$

Combining Eqs. (3-11) and (3-13), if T_b is the temperature "read" from the optical pyrometer, the "true" temperature after correcting for emissivity and glass window is

$$\frac{1}{T_t} = \frac{1}{T_b} + \frac{\lambda}{C_2}\ln\epsilon_\lambda + A \tag{3-14}$$

III.2.3 Mass Spectrometer Calibration

The vapor emitted by the hot target was detected by a quadrupole mass spectrometer, which accepted the vapor flow of a molecular beam. The mass spectrometer is shown in Fig. 3.8. An electron beam gun (Fig. 3.3) was used to heat up a UO_2 wafer under vacuum to generate a steady state molecular beam for both mass location and intensity calibration. The hot calibration was used instead of a UO_2-filled Knudsen cell calibration performed before the laser experiments*[49]* for the following reasons: (i) The alignment of the system was not disturbed (ii) the same sample surface condition prevailed (iii) the mass spectrometer drift was eliminated because the mass peaks could be tuned just before the laser shot (iv) the dependence of the signal on the surface area was eliminated.

The UO_2 surface temperature was quite uniform spatially during the calibration (±10 K), and was varied from 1760°C to 2045°C as measured by the automatic optical pyrometer (in the Auto mode). The mass spectrometer signal during calibration was meaured by a Keithley 410 Micro-microammeter. The system was tuned to mass numbers 286 (UO_3), 270 (UO_2), 254 (UO), 238 (U) and 32(O_2). For each data point, the net signal from vaporization was determined from the difference in signals without and with the beam flag in the detector chamber blocking the beam.

The mass spectrometer settings used for calibration as well as for the laser runs were:

$V_{electron}$ = 70 v = electron potential
V_{ion} = 11 v = ion potential relative to the ionizer
V_{focus} = 27 v = ion focusing potential
$V_{multiplier}$ = -2500 v = electron multiplier potential
$V_{extractor}$ = 40 v = electron extraction potential
$I_{extractor}$ = 0 mA = collected electron current
$I_{emission}$ = 1 mA = ionizer emitted electron current

The resolution was adjusted so that the valley between adjacent mass peaks for 270, 254 and 238 just touched the base line. The ion potential was adjusted to avoid mass peak splitting

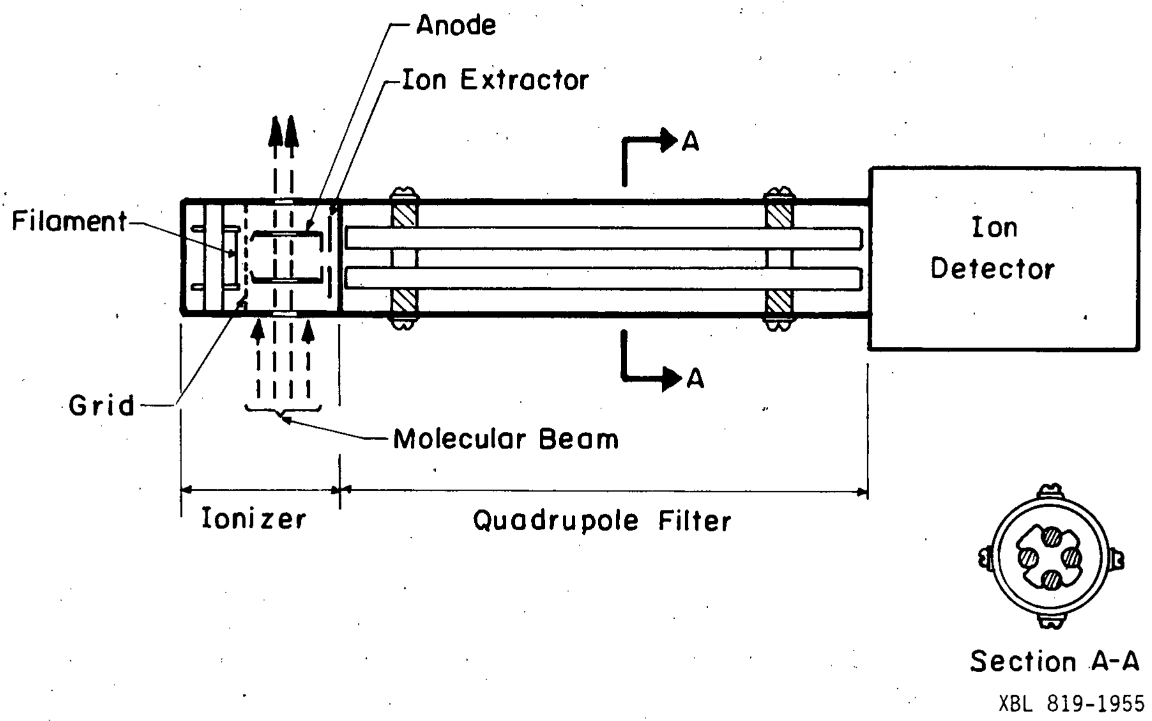

Fig. 3.8 Quadrupole Mass Spectrometer

and the rest of the voltage settings were chosen to obtain the biggest signals. The result plotted as log(ST) versus 1/T are shown in Fig. 3.9. From the slopes of the curves in Fig. 3.9, the heats of sublimation of 182.5 kcal/mol for UO_3, and 144 kcal/mol for UO_2 were obtained; the literature gives 143 kcal/mol for UO_2*[5]*. Since the slopes of the UO and U lines are close to that of UO_2, it is believed that they both represent the fragments of dissociative ionization (cracking) of UO_2.

For a steady state source and free molecular flow, the average molecular density of the beam reaching the ionizer n (in molecules/cm^3) is proportional to the ratio of the pressure (in atm) and the temperature (in K) on the sample surface:

$$n = K_g K_u \frac{P}{T} \tag{3-15}$$

where the proportionality constant consists of a unit conversion factor K_u (from atm/K to molecules/cm^3), and a geometric constant $K_g (= \frac{A_s}{4\pi l^2})$, in which A_s is the surface area of the source, and l is the distance between the source and the detector.

The output current signal from the mass spectrometer S (in amps) is proportional to the molecular density of the species detected:

$$S = K_{MS}\sigma\gamma n \tag{3-16}$$

where K_{MS}(amp-cm) consists of the characteristic parameters of the mass spectrometer ($=I_e L F_q G$, I_e being the emission electron current of ionizer filament (in amps), L being the length of the electron sheet (in cm), F_q being the fraction of the ions actually reaching the electron multiplier through the quadrupole compared to the toal ions produced in the ionizer, and G being the electron multiplier gain*[54]*), σ is the ionization cross section (in cm^2/molecule) and γ is the average number of secondary electrons emitted at the first dynode for each ion collected (in electrons/ion).*

The vapor in equilibrium with UO_2(s) is composed of six species, namely UO_3, UO_2, UO,

---

*In order to make the units consistent, a factor of magnitude unity with units of ions/electron has to be applied because one ion is produced once a molecule is ionized by an electron.

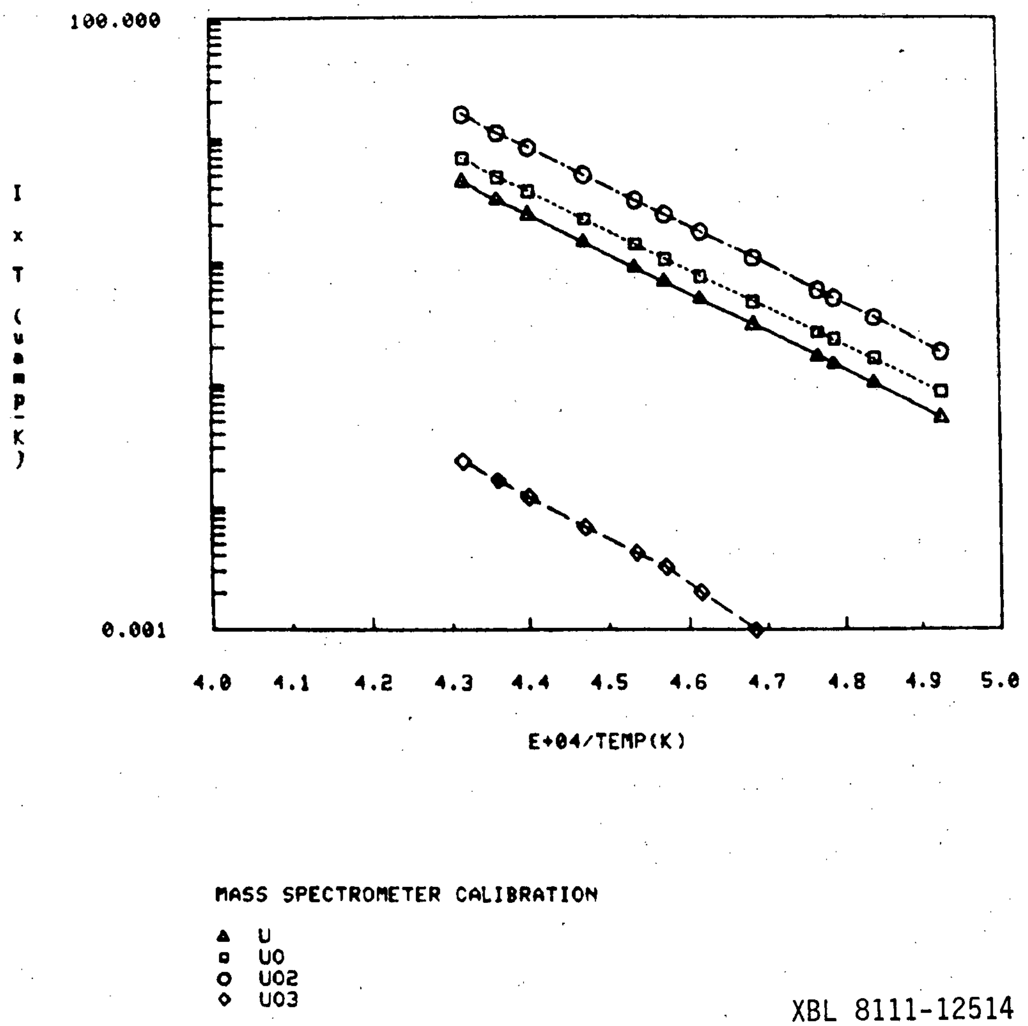

XBL 8111-12514

Fig. 3.9 Mass Spectrometer Calibration

U, O and O_2. Of these, UO_3, UO_2 and UO are the most abundant. Upon impact by high energy electrons in the ionizer, UO_3 neutral molecules may fragment and produce lower mass ions, such as UO_2^+, UO^+, U^+; Similarly UO_2 molecules may fragment and produce UO^+, U^+; finally UO can crack to U^+. The ions produced from the same mass of neutral species (e.g. UO_3^+ from UO_3) are called "parent ions", while those produced from higher mass neutrals (e.g. UO_2^+ from UO_3) are called "fragment ions". The measured current of some mass is the sum of the parent ions and fragment ions from higher mass.

The contribution of i^+ ions from ionization of i neutral $= [n_i\sigma_i\gamma_i F_{ii}]\ K_{MS}$

The contribution of i^+ ions from ionization and fragments of k neutral $= [n_k\sigma_k\gamma_i F_{ki}]\ K_{MS}$

where F_{ii} = fraction of i^+ ions from ionization of i neutral

F_{ki} = fraction of i^+ ions from ionization of k neutral $(m_k > m_i)$

$n_i(n_k)$ = molecular density of i(k) neutral in the ionizer, cm^{-3}

$\sigma_i(\sigma_k)$ = total ionization cross section of i(k) neutral

γ_i = first dynode efficiency for i^+ ion.

The signal of i^+ ions measured will be the sum of the parent ions and fragments from higher mass neutrals. Using the notations: 3 = UO_3, 2 = UO_2, 1 = UO and 0 = U, the signal of i^+ is:

$$S_{i^+} = K_{MS}\,[n_i\sigma_i\gamma_i F_{ii} + \sum_{k>i}^{3} n_k\sigma_k\gamma_i F_{ki}] \qquad (3\text{-}17)$$

$i = 3, 2, 1, 0$

Applying Eq. (3-15) to each species i, we have:

$$n_i = K_g K_u \frac{P_i}{T} \qquad (3\text{-}18)$$

Therefore

$$S_{i^+} = K_{MS}K_gK_u\gamma_i\,[\frac{P_i}{T}\sigma_i F_{ii} + \sum_{k>i}\frac{P_k}{T}\sigma_k F_{ki}] \qquad (3\text{-}19)$$

Multiplied by $\frac{T}{\sigma_2\gamma_i}$ where σ_2 is the σ for UO_2, Eq. (3-19) becomes

$$S_{i+}T = K\sigma_2\gamma_i\,[P_iC_iF_{ii}+\sum_{k>i} P_kC_kF_{ki}] \qquad (3\text{-}20)$$

where $K = K_{MS}K_gK_u$ and C_i = relative total ionization cross section of neutral i to that of UO_2 ($= \sigma_i/\sigma_2$)

For the uranium bearing species produced by UO_2 vaporization:

$$S_3T = K\sigma_2\gamma_3P_3C_3F_{33} \qquad (3\text{-}21)$$

$$S_2T = K\sigma_2\gamma_2[P_2C_2F_{22}+P_3C_3F_{32}] \qquad (3\text{-}22)$$

$$S_1T = K\sigma_2\gamma_1[P_1C_1F_{11}+P_2C_2F_{21}+P_3C_3F_{31}] \qquad (3\text{-}23)$$

$$S_0T = K\sigma_2\gamma_0[P_0C_0F_{00}+P_1C_1F_{10}+P_2C_2F_{20}+P_3C_3F_{30}] \qquad (3\text{-}24)$$

By dividing Eqs. (3-21), (3-23) and (3-24) by Eq. (3-22), the ratios of the signals can be expressed as:

$$\frac{S_3}{S_2} = \frac{\gamma_3}{\gamma_2}\,\frac{(\frac{P_3}{P_2})C_3F_{33}}{C_2F_{22}+(\frac{P_3}{P_2})C_3F_{33}} \qquad (3\text{-}25)$$

$$\frac{S_1}{S_2} = \frac{\gamma_1}{\gamma_2}\,\frac{[(\frac{P_1}{P_2})C_1F_{11}+C_2F_{21}+(\frac{P_3}{P_2})C_3F_{31}]}{C_2F_{22}+(\frac{P_3}{P_2})C_3F_{32}} \qquad (3\text{-}26)$$

$$\frac{S_0}{S_2} = \frac{\gamma_0}{\gamma_2}\,\frac{[(\frac{P_0}{P_2})C_0F_{00}+(\frac{P_1}{P_2})C_1F_{10}+C_2F_{20}+(\frac{P_3}{P_2})C_3F_{30}]}{C_2F_{22}+(\frac{P_3}{P_2})C_3F_{32}} \qquad (3\text{-}27)$$

The current ratios S_3/S_2, S_1/S_2, S_0/S_2 for different temperatures can be obtained from the calibration curves in Fig. 3.9. The pressure ratios P_3/P_2, P_1/P_2, P_0/P_2 can be obtained from the thermophysical calculations for the congruently vaporizing compositions for different temperatures. The C's are from Pattoret*[55]*:

$$(\sigma\gamma)_0/(\sigma\gamma)_1/(\sigma\gamma)_2/(\sigma\gamma)_3 = 1.15 : 0.80 : 0.55 : 0.38 \qquad (3\text{-}28)$$

The relative electron multiplier gain is expected to be inversely proportional to the square root of the ion mass*[54]*, that is:

$$\gamma_0 : \gamma_1 : \gamma_2 : \gamma_3 = 1.065 : 1.031 : 1 : 0.972 \qquad (3\text{-}29)$$

Therefore,

$$C_3 = 0.710,\ C_2 = 1,\ C_1 = 1.406,\ C_0 = 1.962 \qquad (3\text{-}30)$$

An optimal set of F_{ij}'s can be obtained by fitting Eqs. (3-25)-(3-27) to the data in Fig. 3.9, which yields:

$F_{33} = 0.080$

$F_{32} = 0.600$

$F_{31} = 0.220$

$F_{30} = 0.100$

$F_{22} = 0.610$

$F_{21} = 0.232$

$F_{20} = 0.158$

$F_{11} = 0.900$

$F_{10} = 0.100$

and the constant $K\sigma_2\gamma_2 = 1.6 \pm 0.5$ amp-K/atm.

For the geometry we have with 1 mm diameter cell orifice, 40 cm cell-to-ionizer distance, we have $K_g = 3.9\times10^{-5}$. The unit conversion factor $K_u = 7.32\times10^{21}$ molecules/cm^3-K/atm. Therefore, the mass spectrometer instrumental constant is $K_{MS}\sigma_2\gamma_2 = 5.5\times10^{-18}$ amp-cm^3.

Table 3.1 shows the comparison of this work with the fragmentation fractions measured by Blackburn*[56]* and Pattoret*[55]*. Our result agree quite well with those of Pattoret*[55]*.

TABLE 3.1

The Fragmentation Fractions of U-O System

	Blackburn	Pattoret	This work
F_{33}	0.104	0.200	0.080
F_{32}	0.438	0.600	0.600
F_{31}	0.458	0.160	0.220
F_{30}	0.000	0.040	0.100
F_{22}	0.500	0.625	0.610
F_{21}	0.500	0.281	0.232
F_{20}	0.000	0.094	0.158
F_{11}	0.667	0.880	0.900
F_{10}	0.333	0.120	0.100

III.3 EXPERIMENTAL PROCEDURE

The experiments are performed in the following manner:

(1) Polish the target as described in section III.1.3.

(2) Mount the target on the electron bombardment heater and install in the target chamber.

(3) Evacuate the target chamber.

(4) Open the gate valve to the detector chamber (which is always kept under vacuum).

(5) Align the system and the Nd-glass laser as described in section III.1.1.

(6) Turn on the Nd-glass laser power supply and set voltage.

(7) Check the alignment by shooting the Nd-glass laser through an aperture and on a polaroid film. Shoot #3 gas laser through the same path. Adjust the optical components and shoot the Nd-glass laser until the two lasers illuminate on the same spot.

(8) Align and focus the optical pyrometer on the target with the #3 gas laser shooting on the target, so that the optical pyrometer will measure the surface temperature of the center of the Nd-glass laser focal spot.

(9) Preheat the target with the electron bombardment heater. Measure the target temperature with the auto mode of the optical pyrometer. Stablize the temperature at 1600 K, which is the initial specimen temperature for temperature transient calculation.

(10) Set the optical pyrometer to the transient operate mode.

(11) Connect the photodiode, the optical pyrometer, the mass spectrometer and the ion collector to the transient waveform recorder.

(12) Install the neutral density filters between the Nd-glass laser and the beam splitter as the laser energy is desired.

(13) Tune the mass spectrometer control to the mass of the species to be measured.

(14) Estimate the voltage of each signal to be measured and set the full scale of each channel of the transient recorder to attain highest sensitivity.

(15) "Arm" the transient recorder at the "Ready" mode for data recording.

(16) Trigger the Nd-glass laser.

(17) The transient recorder should record 4 signals for the experiment and stop recording after receiving a pre-set delayed triggering signal.

(18) Switch the mass spectrometer control to monitor another species.

(19) Repeat step (14) to (18) for all the vapor species of interest thus completing the run for one laser energy.

(20) Install different numbers of filter or change the laser power supply voltage to get another laser energy and repeat steps (13) to (19).

IV. RESULTS AND DISCUSSIONS

IV.1 SURFACE MORPHOLOGY

IV.1.1 Melting

The laser-irradiated UO_2 sample surface was examined by scanning electron microscope. Fig. 4.1a shows a typical laser-irradiated area (produced by a 28 Joules pulse). A ring structure on the sample surface is observed within the previously molten area. The ring structure is attributed to the radial propagation of a central disturbance on the liquid surface in the form of capillary waves*[57]*. The discontinuous quasi-periodic liquid displacement from the center of the "pool" due to the recoil forces of the evaporating material is believed to be the driving mechamism of this disturbance.

Melting out to an ellipse of major radius 3.8 mm and minor radius 2.4 mm is measured with lower magnification optical microscope. According to one-dimensional thermal analysis computer code "STAR" (see chapter II), the maximum surface temperatures at the observed major and minor ellipse boundaries, corresponding to the measured laser radial intensity distribution (section III.2.1), are 4160 K and 4270 K respectively. The fact that they are much higher than the melting temperature of UO_2 is believed to be due to the requirement of some in-depth melting for visual characteristics of a previously molten surface.

IV.1.2 Surface Stoichiometry

Figs. 4.1b and 4.1c show the UO_2 surface under higher magnification by SEM inside and outside of the previously molten zone, respectively. Both surfaces have been thermally etched by the laser irradiation and show distinct grain structures. Various surface analyses were used to determine the nature of the white dots appearing mostly along the grain boundaries in the laser irradiated area (Fig. 4.1b). The surface concentration of the aggregates decreases with radius from the center of the ellipse, showing that they are associated with the surface temperature distribution. Such precipitates might be expected from the surface depletion of oxygen due to the preferential evaporation of this element (as UO_3, see chapter II). However,

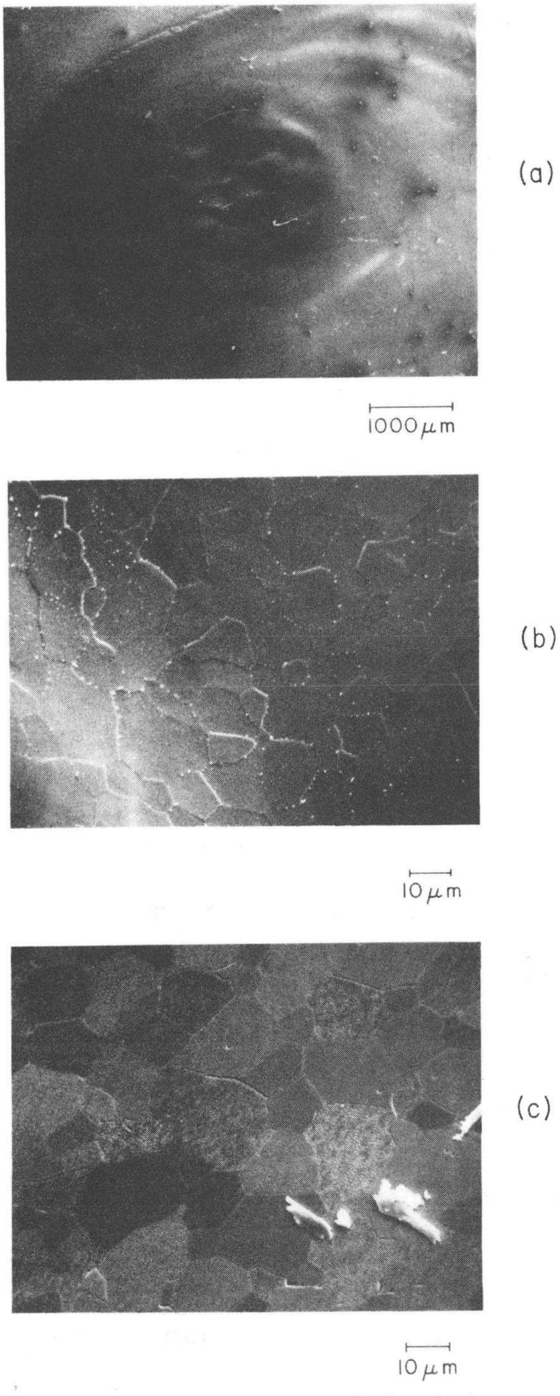

XBB 792-1498

Fig. 4.1 Scanning Electron Microphotographs of (a) & (b) previously molten and (c) non-molten UO_2 Surface following bombardment by a 28 J Laser Pulse computer simulation of the surface temperature and composition evolution during the laser power transient shows that, the surface stoichiometry decreases to 1.78. However, the O/U ratio is predicted to remain in the single phase UO_{2-x} region, so precipitation of uranium metal should be thermodynamically impossible.

SEM-EDAX elemental analysis was not capable of distinguishing the white particles from the matrix, because (i) SEM-EDAX is not sensitive to oxygen, and (ii) the particles are in sub-micron range while SEM electron beam size is tens of microns. Scanning Auger microscope (SAM) circumvented these two difficulties; in addition, another advantage of SAM is the shorter Auger electron penetration (10 - 30 Å) compared to about 1 - 10 μm x-ray penetration from EDAX, which permits measurement of the "surface" stoichiometry. The shallow Auger penetration depth is small in comparison to the ~15 μm oxygen depletion depth during the vaporization transient.

Figs. 4.2a and 4.2b show the Auger electron spectra from the matrix and the particle, respectively, after ion sputtering sufficient to remove all carbon peaks. Comparing the two spectra suggests that the particles are not pure uranium metal because they show no difference in the relative peaks of uranium and oxygen. This observation is consistent with the calculation of the surface O/U relative to the lower phase boundary of the oxygen-uranium system; there remains, however, the question of what the particles are.

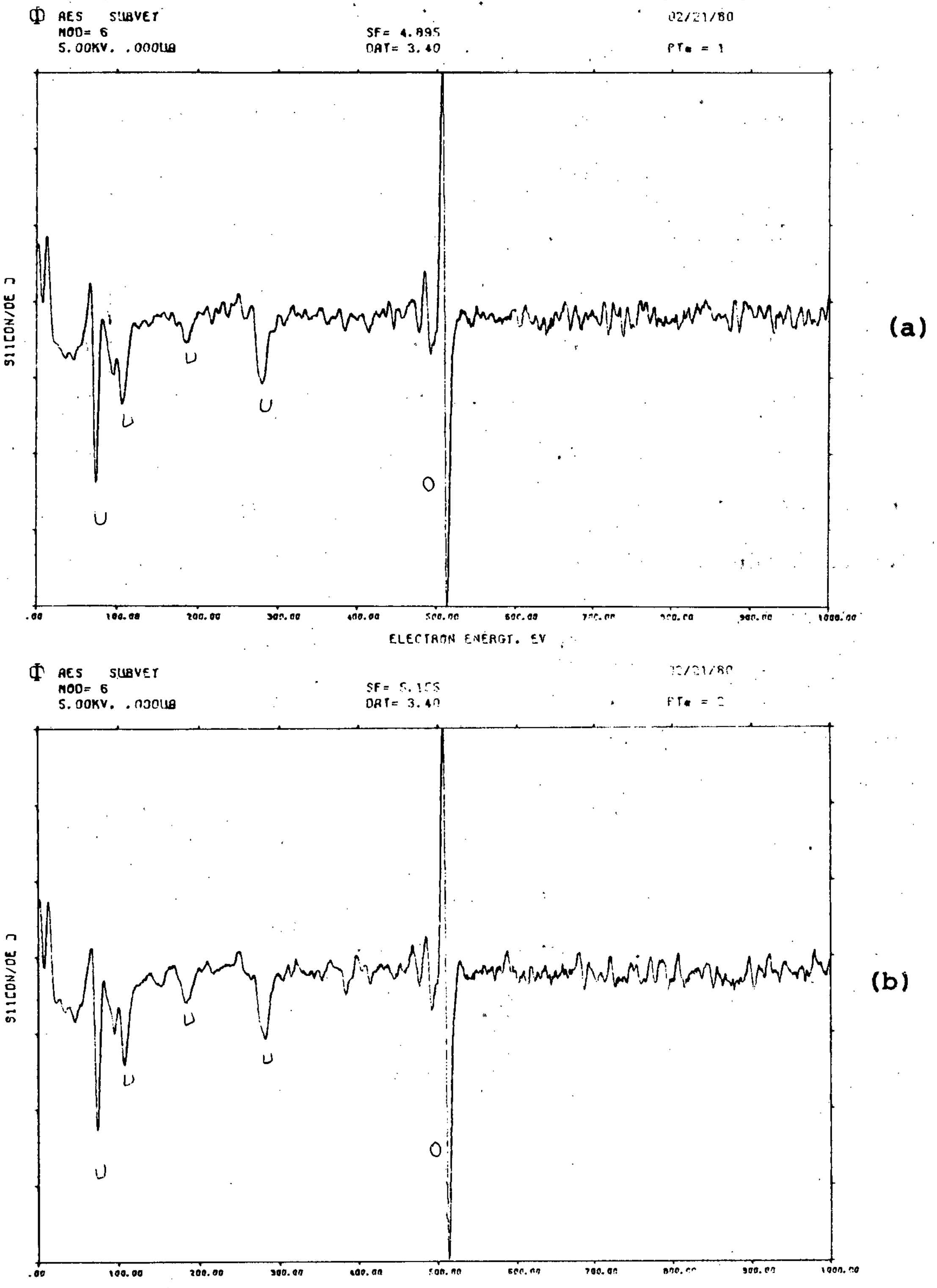

XBL 819-1958

Fig. 4.2 Auger Electron Spectra from (a) the Matrix and (b) the Particals in Laser irradiated area (Fig. 4.1(b))

IV.2 CRATER DEPTH MEASUREMENT

The removal of the target material by high power laser creates a crater at the focal spot as seen from Fig. 4.1. Ready*[58]* has experimentally determined the depths of this kind of crater and related these measurements to the surface temperatures. Ohse*[22]* also adopted this measurement technique, correlating the peak central surface temperature measured by an optical pyrometer with the central depth measured by inductive sensor tip scanning across the crater profile.

In this study, the crater profile was also measured by an inductive sensor along the axes of the elliptical shape of crater. Figs. 4.3 and 4.4 show this measurement along the major and minor axis respectively for a sequence of five shots of 28 joules each. The total amount of UO_2 evaporated computed by integrating the crater profile was about 55 mg; this is a factor of 7 higher than the figure from the theoretical calculation (7.9 mg) for the five shot sequence, based upon Langmuir vaporization incorporating the calculated surface temperatures.

The liquid movement, which is seen microscopically in Fig. 4.1 and confirmed by the raised rim on the edge of the crater in Figs. 4.3 and 4.4, is probably one of the reasons for this discrepancy. Chunk sputtering due to the high power laser bombardment*[65]* or microexplosions beneath the surface due to high porosity sample*[22]* may also be explanations.

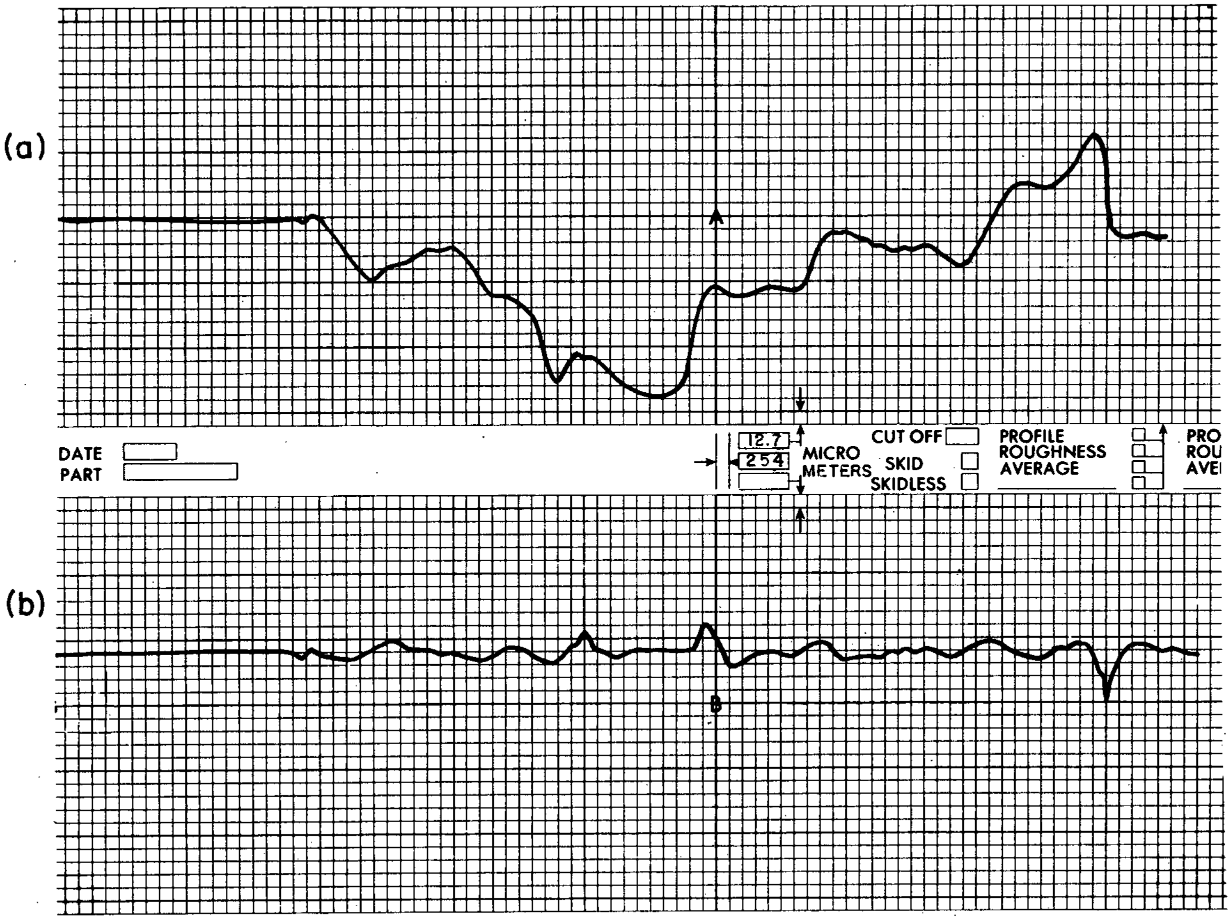

XBL 801-7843

Fig. 4.3 (a) Crater Depth Profile along the Major Axis

(b) Surface Roughness Reference

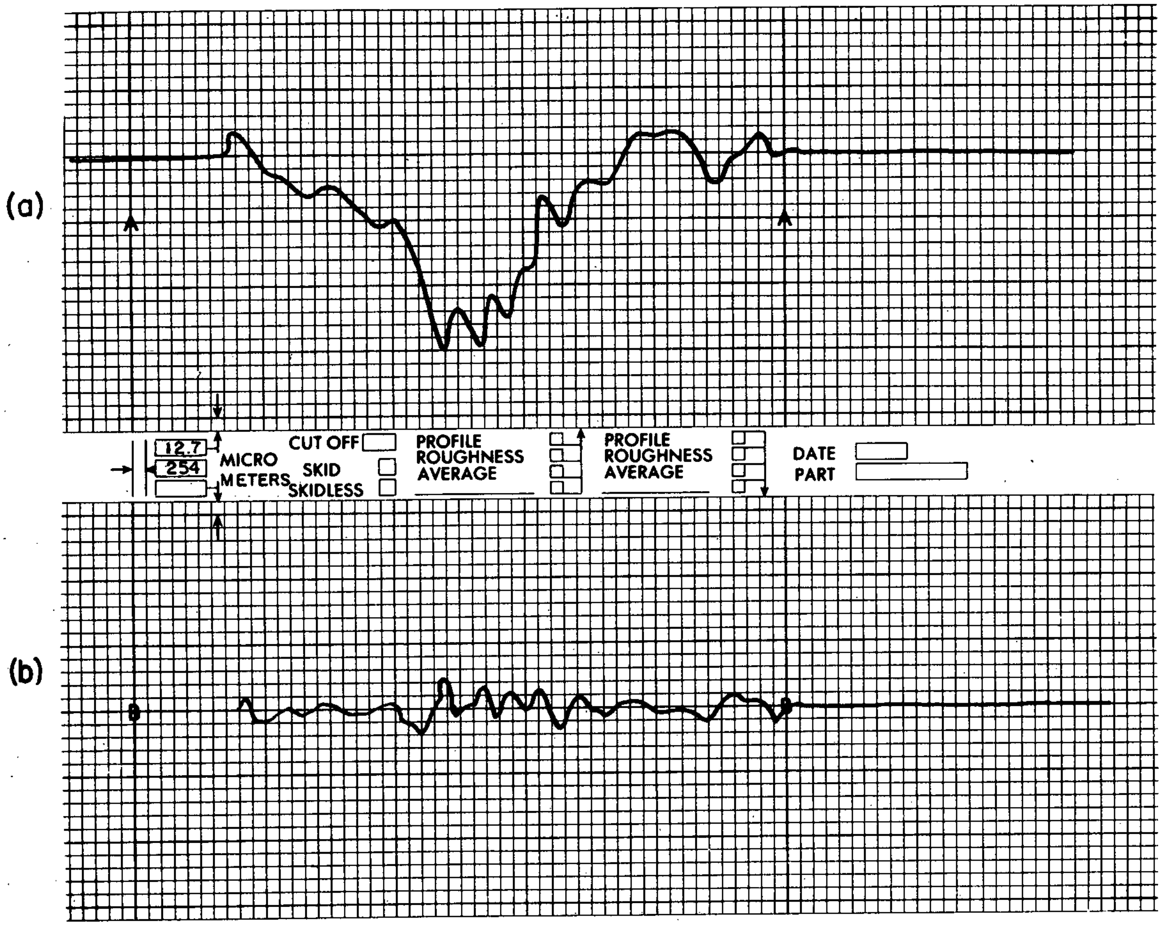

XBL 801-7842

Fig. 4.4 (a) Crater Depth Profile along the Minor Axis

(b) Surface Roughness Reference

IV.3 VAPOR YIELD MEASUREMENT

A radioactive tracer technique was used by Varsi *[59]* for the measurement of the amount of material ablated by high intensity laser radiation as well as the angular distribution of the particles emitted from a copper single crystal. The same idea was applied here, except that, instead of using a radioactive tracer, collected uranium (with 0.715% natural abundance of uranium 235) was activated in the TRIGA Reactor and the yield obtained by γ counting of fission product radioactive decay.

As shown in Fig. 4.5a, b and c, two arrays of small teflon* disks and aluminum disks were placed around the target by a collector assembly mounted in the y-z plane ("out-of-plane" Fig. 4.5b) in run #A-1 and in the x-y plane (containing the laser beam and the target normal, or "in-plane" Fig. 4.5c) in run #A-2 to collect part of the ejected UO_2 from laser-heated spot. The collector disks were half inches diameter, arranged in arrays of about 10° angular resolution. The collector assembly was 3 inches away from the target. UO_2 target was subject to five laser shots of energy 28 joules each in run #A-1, and two shots of 26 joules each in run #A-2.

The teflon disks were irradiated in the Berkeley Research Reactor** and the amount of UO_2 was determined by counting the fission products radioactivity with a 3" by 3" NaI(Tl) scintillation detector and a 1024 multichannel analyzer. Calibrated standards consisting of known amount of uranium from uranyl nitrate solution deposited on teflon disks were used to determine the absolute magnitude of the quantity of uranium deposited on the disks by the laser vaporization process. Prior to assembling the stack of disks and the standards in the reactor capsule, the disks were sprayed with a plastic coating to prevent loss of uranium by abrasion or loss of neutron-induced radioactivity by recoil from the thin uranium layer. By this technique, not only could the angular distribution be determined but also the total amount of UO_2 vaporized in one pulse. The results are shown in Table 4.1.

---

*Teflon was employed to minimize the background due to activation of the disk proper. A "blank" teflon was also irradiated with the samples to obtain the background counts, which came out to be less than 1% of the sample counts.

**Two hours of irradiation under flux of 5×10^{12} n/sec—cm^2 at 1 MW full power and one week cooling before counting.

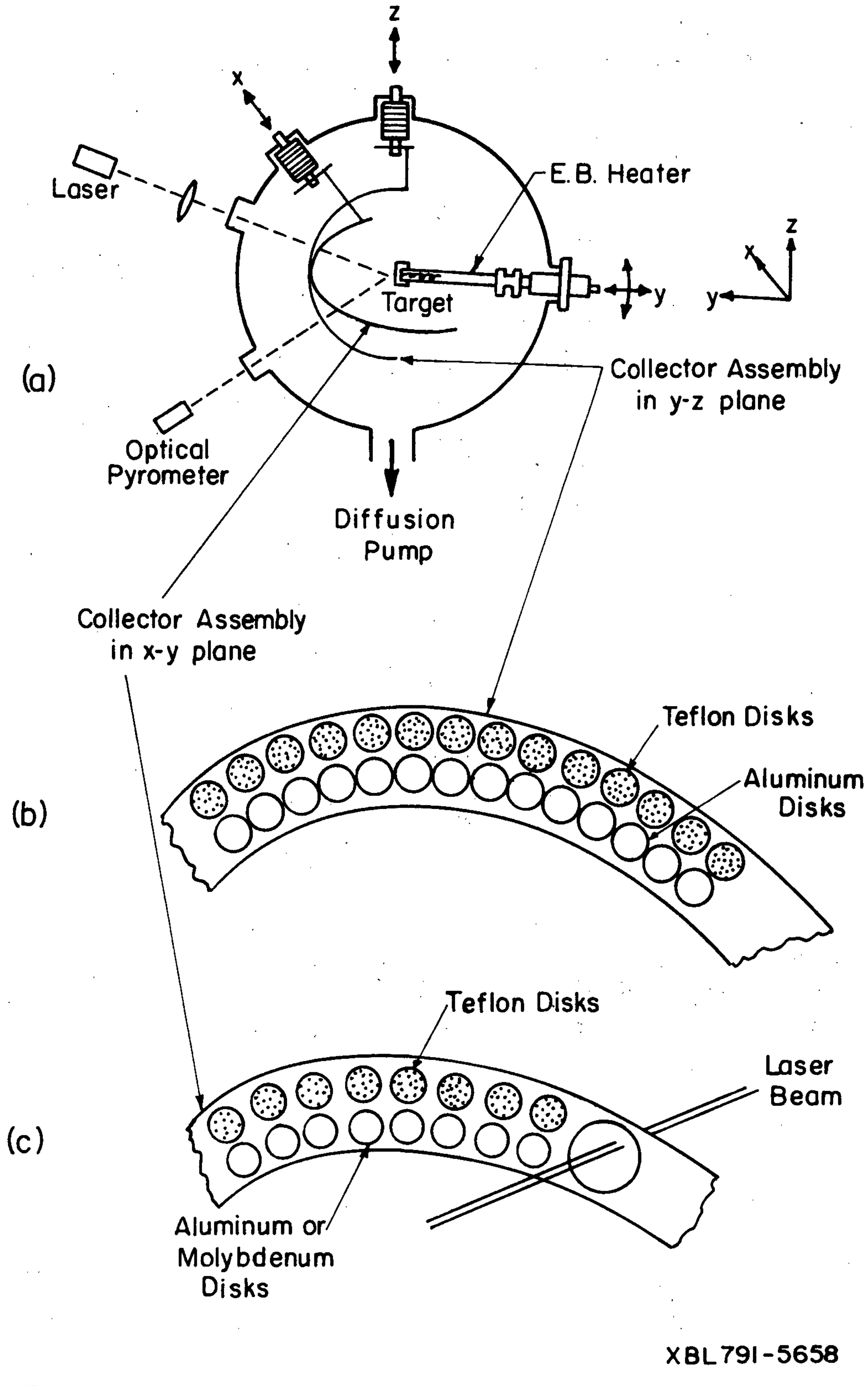

Fig. 4.5 The Collector Assembly for Angular Distribution Measurement and Liquid Droplet Collection Inspection

TABLE 4.1

The Amount of UO_2 Collected from Neutron Activation Analysis

Angle (deg)	Run #A-1 m(μg)	Run #A-2 m(μg)
85	16.85	5.82
75	20.58	8.06
65	23.26	9.75
55	26.06	-
45	32.69	-
35	36.51	-
25	42.11	22.47
15	49.95	27.66
5	55.79	32.68
0	60.39	33.75
5	53.06	32.34
15	46.49	29.76
25	46.23	24.27
35	47.07	19.75
45	42.65	16.55
55	32.87	12.93
65	29.10	11.07
75	26.07	8.37
85	19.64	5.67
M_{tot}**	8.8	4.2

* m_o is the amount of UO_2 collected on the disk at a direction normal to the surface (zero degree); m_o = 60.39 μg for run #A-1 and 33.75 μg for run #A-2.

** M_{tot} (in mg) is the total mass after integrating over a hemisphere.

The amount of UO_2 collected in each teflon disk (m) ranged from 5 μg to 60 μg, which corresponds to about 40 Å to 480 Å thicknesses of UO_2 if uniformly deposited. Table 4.1 shows that even the disks at angles close to 90° from the surface normal collected significant amounts of UO_2. This phenomenon, which would not occur for a cosine angular distribution is usually called "tails" of the distribution and is believed to be due to collisional effects*[60]*.

From the geometry of the collection disks system and the angular distribution of emitted UO_2 determined, integration over the hemisphere gives the total quantity of UO_2 vaporized by the laser pulse.

$$M_{tot}(exp) = \frac{2\pi L^2}{\pi a^2} \int_0^{\pi/2} m(\theta)\sin\theta d\theta \tag{4-1}$$

where $m(\theta)$ is the collected vapor mass on the disk at angle θ with respect to the surface normal (presumably axisymmetric), L is the distance between the disk and the vaporization surface and a is the disk radius.

Total amounts of UO_2 evaporated can also be theoretically calculated based upon the Langmuir vaporization formuula and the surface temperature radial profiles as follows:

$$M_{tot}(theory) = \int_0^{\infty} \int_0^{a} \Phi(r) 2\pi r dr dt \tag{4-1a}$$

where $\Phi(r)$ is the mass evaporation rate ($= \frac{(1-\beta)p(T_s)\sqrt{M_{UO_2}}}{\sqrt{2\pi RT_s(r)}}$ ing/cm^2—sec) and $T_s(r)$ is calculated from the STAR code with laser radial profile measured in Sec. III.2.1.2.

From the mass distribution in Table 4.1, Eq. (4-1) gives the amounts of UO_2 evaporated as 8.8 mg in run #A-1 and 4.2 mg in run #A-2, compared to the theoretical calculation of 7.9 mg and 3.9 mg in each run, respectively, from Eq. (4-1a). The results are quite consistent except that the measured values are about 10% higher.

The angular distributions normalized with respect to the total amounts of material evaporated ($M_{tot}(exp)$) are shown in Fig. 4.6. Also shown for comparison are $\cos\theta$ and $\cos^2\theta$ distributions suggested for Knudsen effusion and supersonic free-jet expansion respectively. This figure shows that the mass flux angular distribution can be approximated by $\cos^n\theta$ distribution

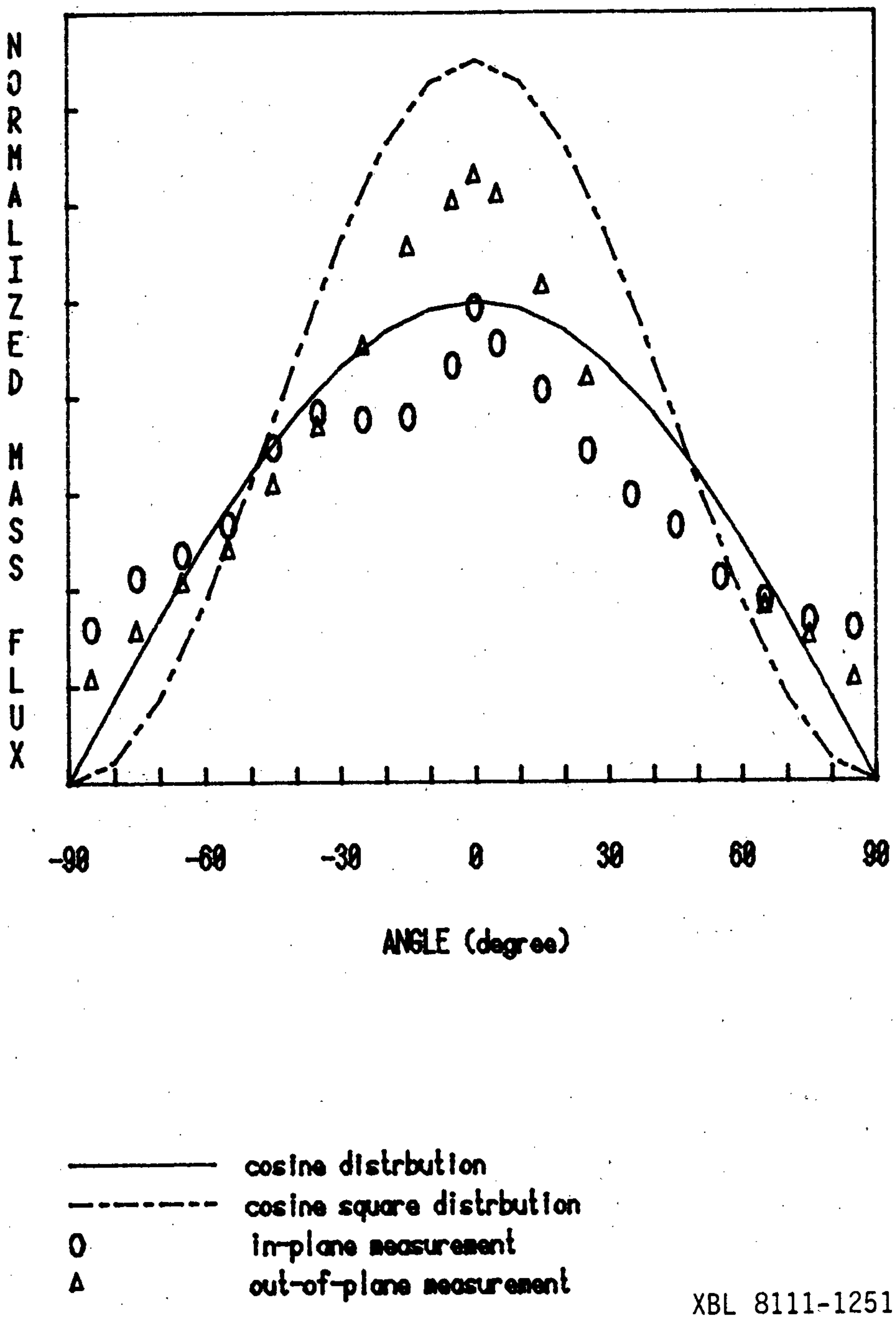

XBL 8111-12515

Fig. 4.6 . Angular Distribution of the Laser Blow-off

where n is between 1 and 2. It suggests that the flow might have gone through a transition to collision dominated flow(see Appendix E).

The second set of aluminum disks shown in Fig. 4.5 collected some of the vapor plume for scanning electron microscope examination. This test was intended to determine whether the vapor blowoff consisted solely of a molecular vapor or also contained a condensed phase. Figs. 4.7 and 4.8 show scanning electron micrographs of the aluminum disks in run A-1 and A-2, respectively. It is evident that there is condensed-phase agglomerates of UO_2 on the disks, some with donut shape and some spherical -- suggesting that they were liquid globules before striking the disks. The radii of the frozen droplets range from ~ 1 μm to 15 μm. Elemental analysis (EDAX) results, shown in Figs. 4.7c and Fig. 4.8b,c, show large peaks of uranium on the particulate phase and little uranium on the matrix (from condensed vapor). The particles on the surface are principally uranium, most likely in the form of UO_2. Two interpretations of this result are possible: either (a) UO_2 liquid-droplet ejection directly from the melt occurs, or (b) liquid droplets are formed by condensation in the highly superasturated vapor plume. The mass of UO_2 as particles was calculated from their size and spacing on the collector surfaces. The mass associated with the particles (estimated from the optical microscope observation) is at most 1% of the total UO_2 collected on each disk. Therefore, the formation of liquid droplets does not affect the angular distribution measurement, nor the interpretation of the vaporization as a molecular process. However, further investigation of droplet formation may help in understanding the vaporization and vapor expansion processes.

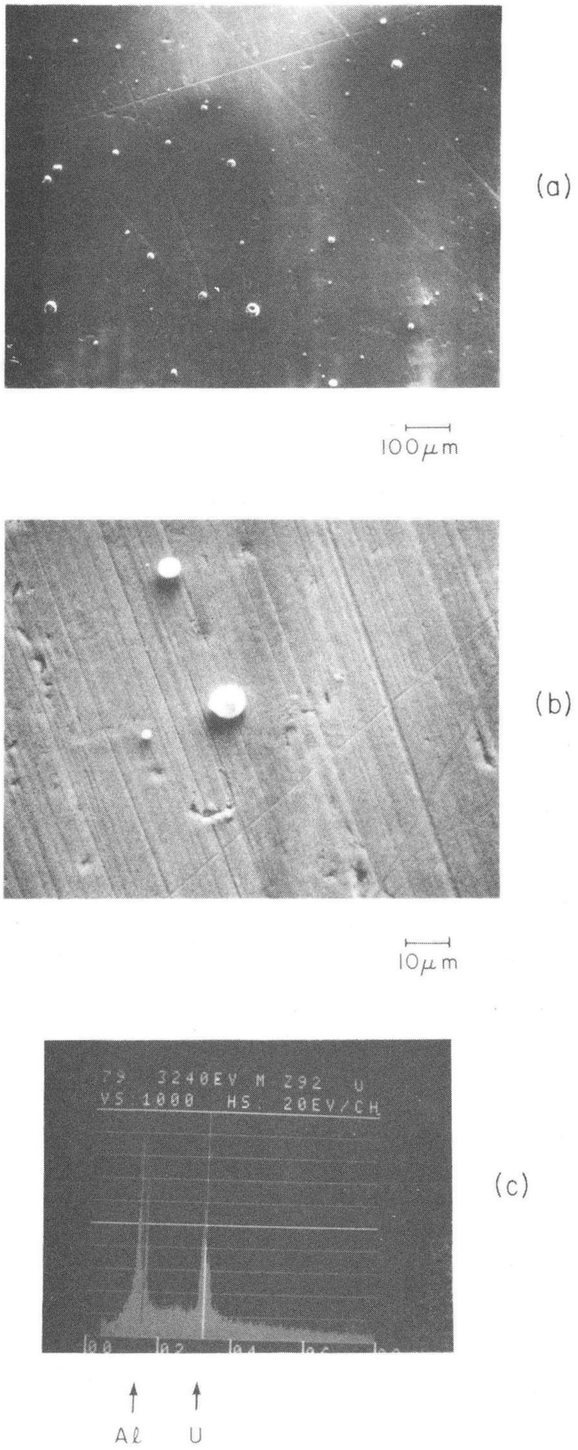

XBB 792-1497

Fig. 4.7 Aluminum Disk Collector Surface following Run #A-1
(a) & (b) Scanning Electron Microphotographs
(c) EDAX Analysis of the white spot

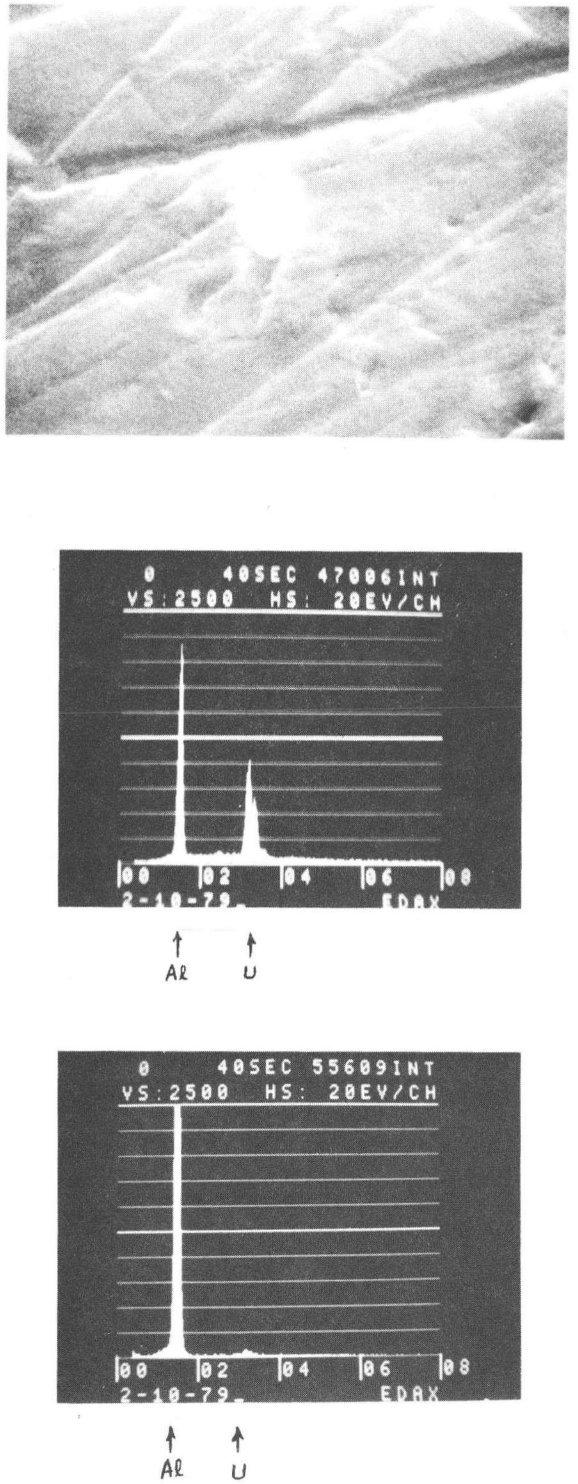

XBB 801-351

Fig. 4.8 Aluminum Disk Collector Surface following Run #A-2
(a) Scanning Electron Microphotograph
(b) EDAX Analysis of the white spot in (a)
(c) EDAX Analysis of gray surface

IV.4 FREE-JET PHOTOGRAPHY

The high Mach number* shock waves have been observed and investigated for years. When a relatively low pressure atmosphere experiences a sudden compression from a high pressure wave, a compression wave is formed and propagates along the streamline. It finally reaches the boundary where a density discontinuity (shock wave) occurs. The nozzle jet expansion is a typical example. The shock wave structure, characterized by the barrel shock boundary and the normal shock (or Mach disc) boundary, has been shown to be related to the flow properties (e.g. the pressure jump, Mach number) of the jet. By photographing** the shock structure created by the laser-induced free jet, one can measure the saturation total vapor pressure of the materials evaporated by laser pulse. This method has been found quite successful in measuring the high temperature vapor pressure of graphite*[60]*. The same apparatus was used for UO_2.

IV.4.1 Experimental Apparatus

A sketch of the apparatus set up is shown in Fig. 4.9. The solid sample is heated by a normal mode Nd-glass laser pulse of msec duration to develop the visible shock structure. The background gas pressure is varied from shot to shot at levels between 1 atm and a few microns, in order to get the best image of Mach disc geometry on the pictures. It is found that the result is independent of the type of ambient gas used, air or Argon. A conventional camera is used to obtain time-integrated images of the evaporating UO_2 free-jet structure. The barrel shock and the normal shock (Mach disc) appear as well-defined boundaries on the photos. The analogy of laser induced flow to the free-jet expansion from a sonic orifice is supported not only by the similarity of the shock characteristics observed, but also confirmed by a molecular velocity measurement with a time-of-flight mass spectrometer*[61]*.

The surface temperature transient was measured by a pre-calibrated wide-band silicon

---

*Mach number is defined by the ratio of the fluid velocity to the sound velocity.

**The self-luminosity of the jet is believed to be caused by emission from excited molecular species in the flow.

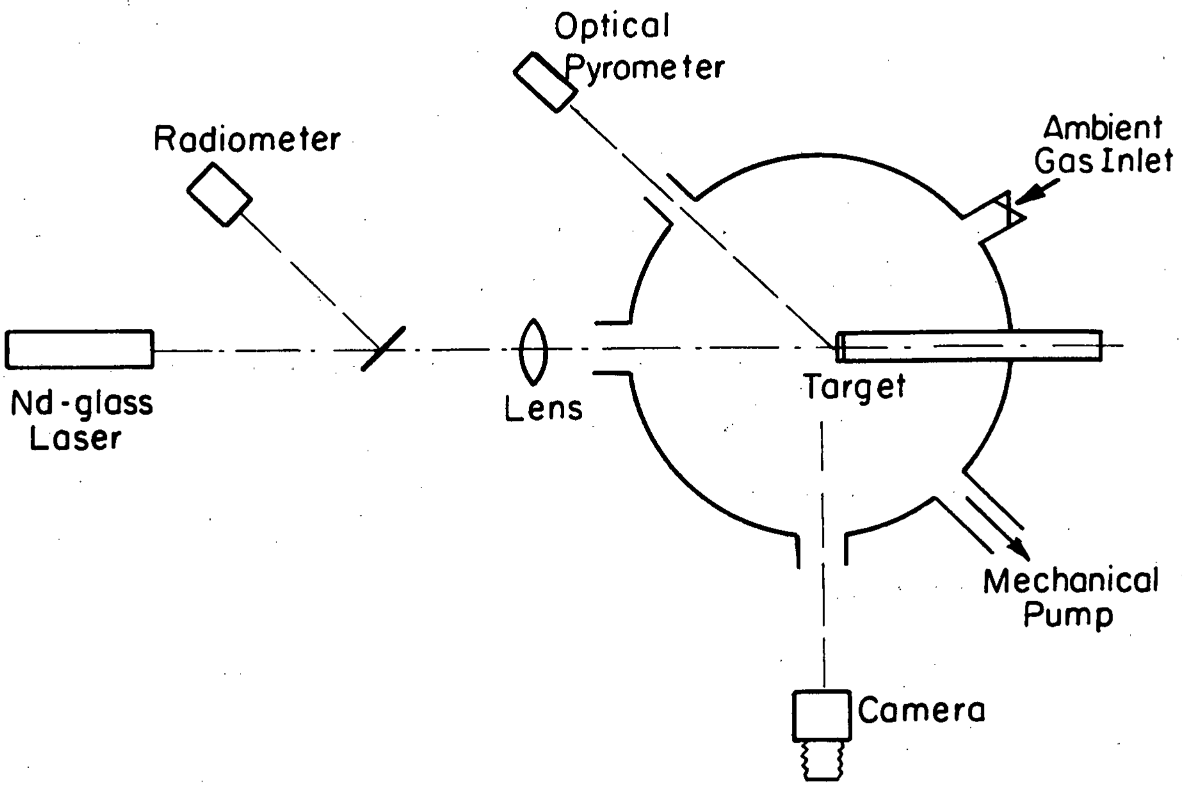

XBL 7712-6606

Fig. 4.9 Experimental Apparatus Setup for Mach Disk Photographic Measurement photodetector pyrometer. The maximum displacement of the standing normal shock from the vaporizing surface (i.e., the position of the outer boundary of the Mach disc image) corresponding to the time at which peak surface temperature and pressure occur. This has been justified by time-resolved photographs framing camera*[60]*. The maximum total vapor pressure is then interpreted from the Mach disc formula*[60]* by analogy with a free jet expansion from a sonic orifice (see Appendix F):

$$\frac{x}{d} = 0.67 \left(\frac{p_o}{p_\infty}\right)^{1/2} \tag{4-2}$$

where x is the axial distance between the Mach disc and the orifice, d is the sonic orifice diameter, p_0 is the total (reservior) pressure, and p_∞ is the ambient (background) pressure.

In applying Eq. (4-2) to laser pulsing of solids, the following identifications are made: (i) the "orifice diameter" is the spot size on the solid illuminated by the laser, and (ii) the "reservior" pressure is the total vapor pressure on the solid surface.

IV.4.2 Results and Discussion

Fig. 4.10 shows the barrel shock and Mach disc typical of this type of laser-generated aerodynamic flow. Table 4.2 shows the results deduced from the photos and Eq. (4-2) as well as the temperatures measured by the pyrometer and the temperatures calculated by the computer code "STAR" described in chapter II. The total energy of the laser pulse and its temporal shape are obtained from a radiometer signal, and are then used as the input for the computer code. A uniformly distributed power profile on the target was assumed. The vapor pressures plotted against temperatures are shown in Fig. 4.11, compared with extrapolations of low temperature measurements (see Appendix A). The discrepancy of about a factor of 2 to 4 deviation for temperatures above 4000 K is believed to be due to nonequilibrium radiation from the hot UO_2 vapor in the plume, which is apparently very rich in excited gaseous species emitted from the surface. This emission has been observed spectroscopically by side-viewing a rapid scanning spectrometer onto the vapor alone. It is also doubtful that the "reservior" pressure in the Mach disc formula represents the total vapor pressure on the surface. In accordance with

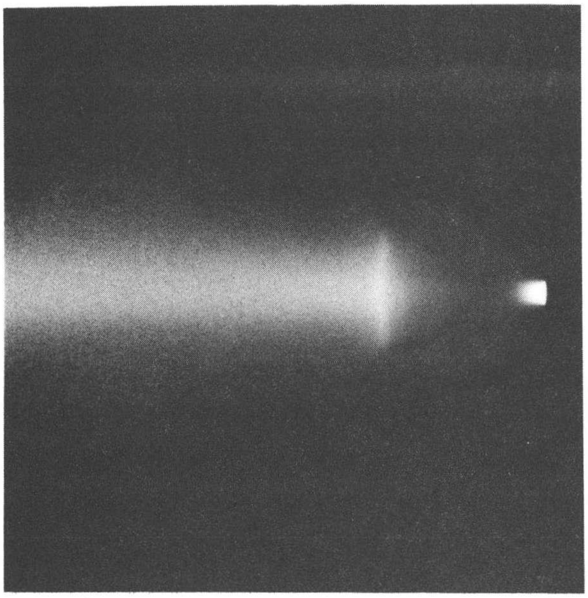

$$\frac{X}{D} = 0.67\left(\frac{P_o}{P_1}\right)^{1/2}$$

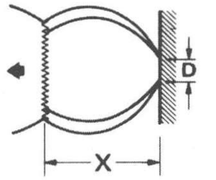

XBB 770-12666

Fig.4.10 Typical Photograph of UO_2 Vapor Plume Structure.

TABLE 4.2

The Total Vapor Pressure of UO_2 by Free-Jet Photography Method

Shot #	Pulse Energy E_i (J)	Peak Power Density* ($10^5 W/cm^2$)	Maximum Temperature (K)		O/U** at Max Temp	Vapor Pressure (atm)	
			T_{exp}	T_{calc}**		P_{exp}	P_{calc}**
47	3.65	0.60	3396	3390	1.976	0.16	0.22
50	4.49	0.74	3643	3640	1.958	0.38	0.54
53	4.90	0.81	3766	3730	1.948	0.48	0.75
55	6.78	1.12	3984	3980	1.896	0.74	1.5
61	17.53	2.89	4926	4690	1.337	2.1	6.2
67	38.71	6.39	5764	5250	1.133	3.2	13.0
68	43.83	7.24	5917	5290	1.110	3.6	13.8

* Peak power density is given by $Q_p = P_{max}(1-R)/A$, where P_{max} = peak power = $E_i/5.074\times10^{-4}$, R = reflectivity of UO_2 to Nd-glass laser = 0.05 and A = evaporation surface area = 0.113 cm^2.

** From computer code "STAR", allowing for oxygen depletion at the surface. The pressure is that at the maximum temperature of all uranium-bearing species over UO_{2-x}, where 2-x is the O/U ratio of the surface at the time of the maximum temperature.

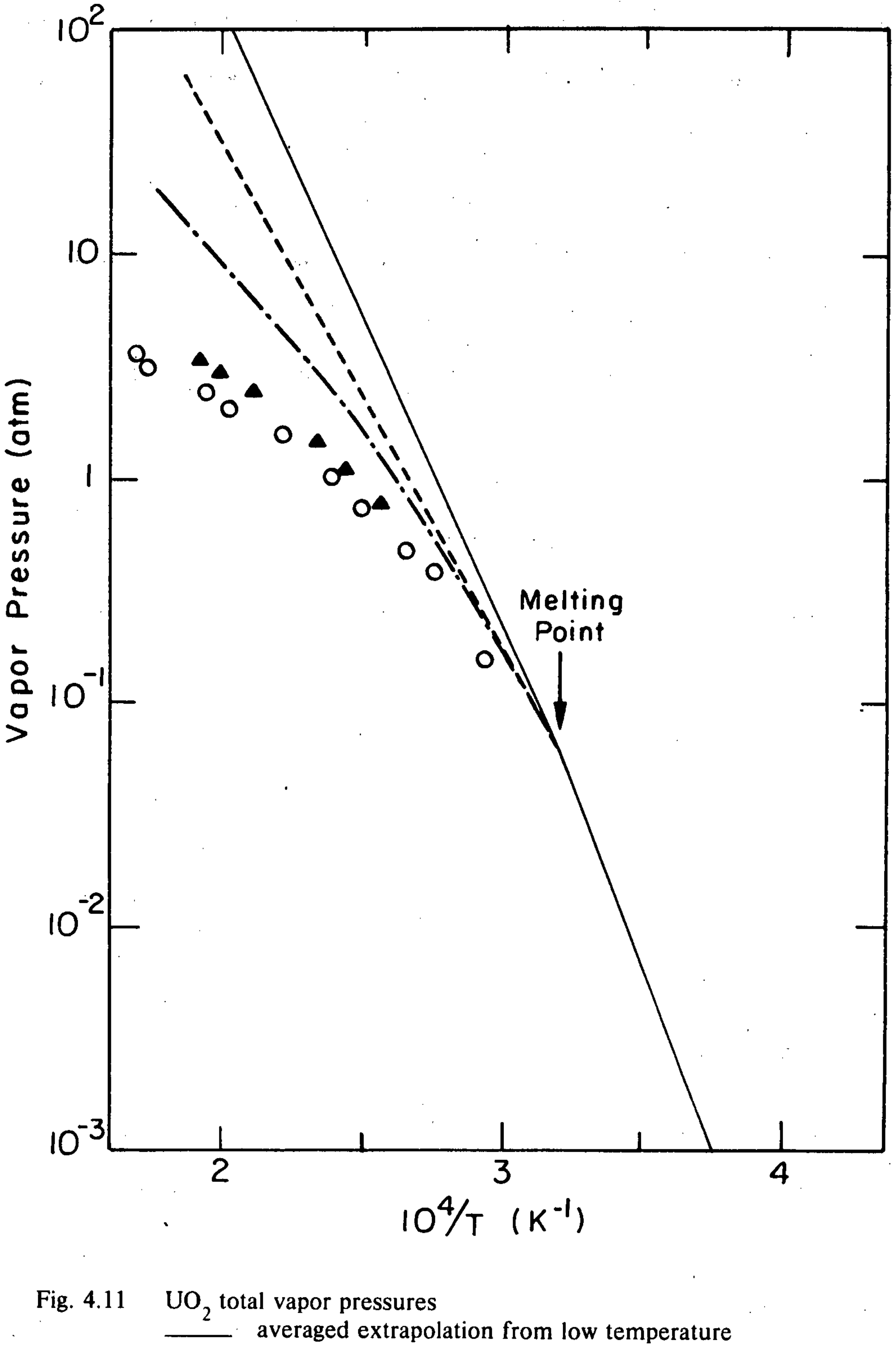

Fig. 4.11 UO_2 total vapor pressures

——— averaged extrapolation from low temperature
------- equilibrium total vapor pressure of $UO_{2.00}$ from *[82]*
—·— vapor pressure from *[82]* including O/U depletion
○ photographic measurements
Δ photographic measurements with calculated temperatures

Anisimov's model*[34]*, a nonequilibrium layer exists between the surface and the zone when continuum flow starts. The pressure drops about a factor of 5 across this layer of a few mean free paths thickness before the vaporizing molecules can accelerate to the local velocity of sound and reach hydrodynamic equilibrium.

The same type of experiment has been recently carried out by Ohse*[62]*, in which the orifice diameter was corrected by an effective area considering the radial evaporation flux distribution and the pressure was also corrected assuming an adiabatic expansion process. The results are about a factor of 5 higher than the values reported here, and this discrepancy is relatively insensitive to the temperature. The influence of the light from the hot vapor on the measured temperature was also reported in Ref. 62, in which the pyrometrically measured temperature increases with background pressure for a constant laser energy.

IV.5 TEMPERATURE MEASUREMENT

The surface temperature of each experiement is measured by a automatic optical pyrometer operated in the transient mode. The time response of the photomultiplier at this mode is normally in the nanosecond range; however, the external RC time constant connected to this optical unit is in tenth of millisecond range, the same order as the temperature transient, so the raw temperature trace has to be corrected for the external RC circuit.

For a current source connecting to a RC circuit with resistance R and capacitance C, the relation between the input current I(t) and the output voltage V(t) is the following:

$$I(t) = C \frac{dV(t)}{dt} + \frac{V(t)}{R} \tag{4-3}$$

In our case, the resistance R is the input resistance of the transient recorder, 1 MΩ, and the capacitance C is the summation of the input capacitance of the transient recorder, 25 pf, and the line capacitance, ~275 pf. After this correction, the voltage R×I(t) is used to obtain the temperature transient through Fig. 3.7. Fig. 4.12 shows a typical temperature trace with time. The solid line and dashed line are the temperature before and after correction for RC time constant, respectively. Also shown in the figure is the surface temperature calculated from the computer program STAR for that particular experimental run. The maximum surface temperature of the experiment and the calculation agree quite well but they show different time characteristics. The measured temperature tends to rise faster than the calculation, while they both cool at the same rate. Fig. 4.13 shows a comparison of the maximum surface temperatures of experiment and calculation as function of input laser total energy.

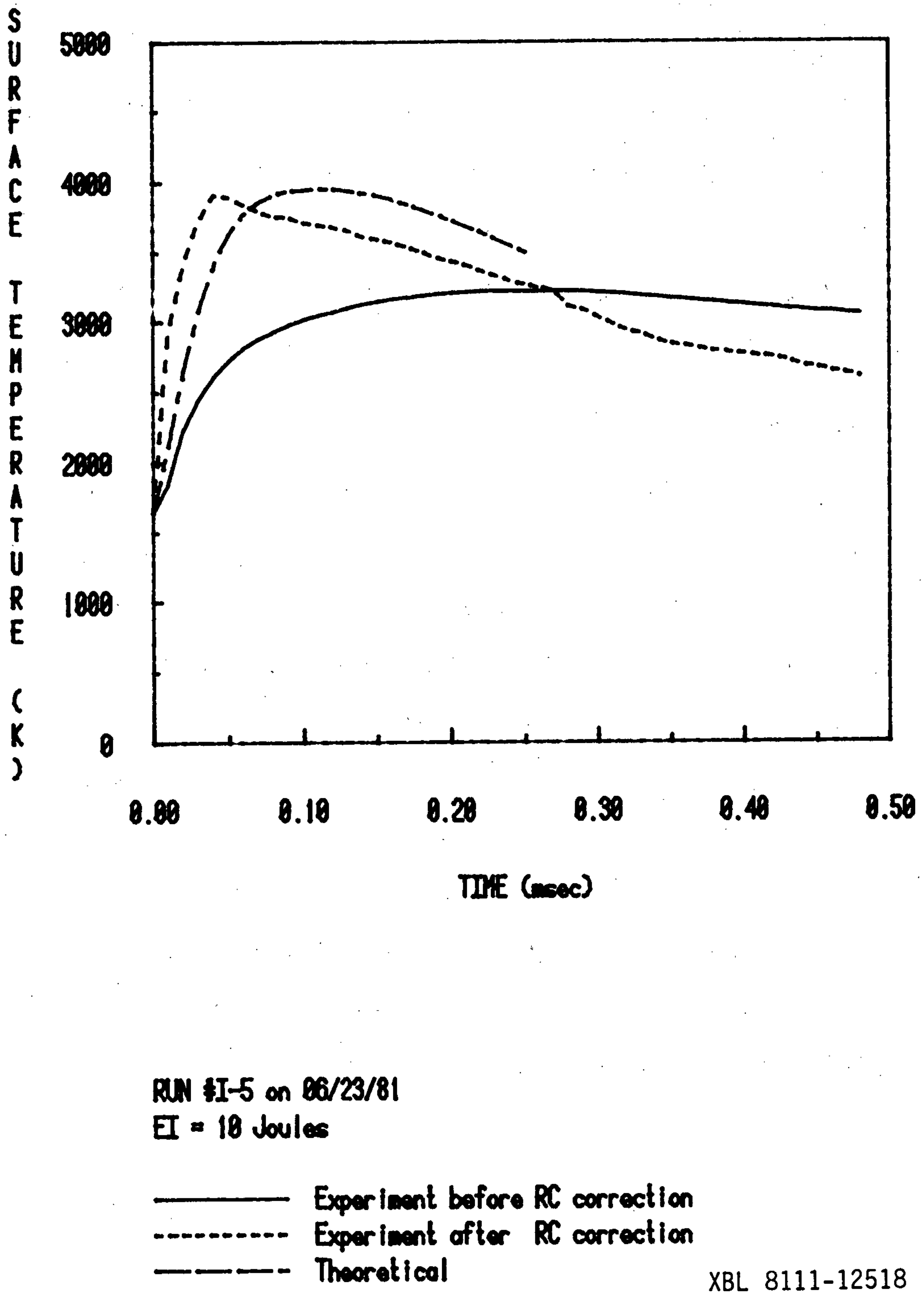

XBL 8111-12518

Fig. 4.12 Surface Temperature Transient for 10 J Laser Pulse

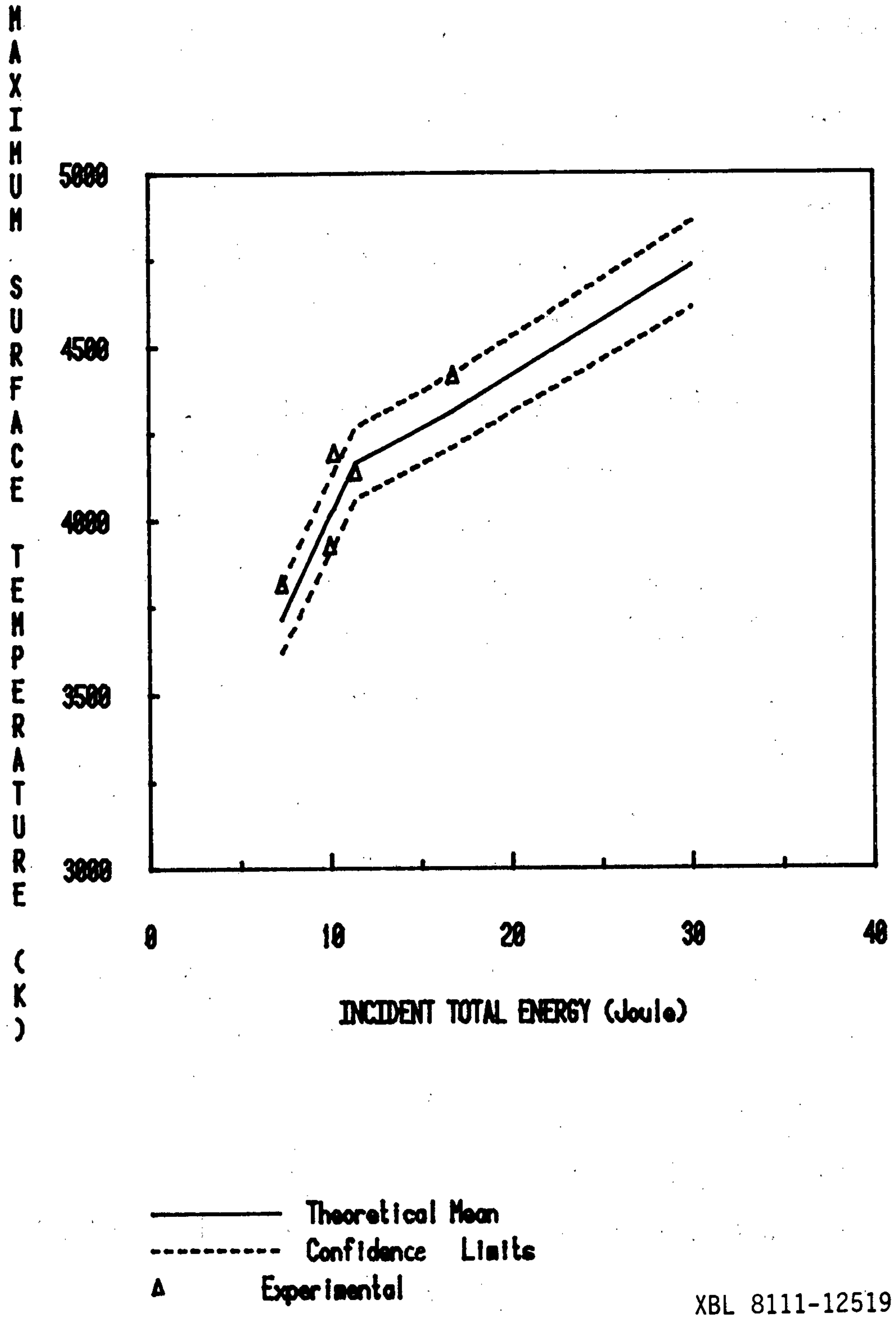

XBL 8111-12519

Fig. 4.13 Calculated and Measured Maximum Surface Temperature

IV.6 MASS SPECTROMETER MEASUREMENT

IV.6.1 Molecular Density in the Ionizer

IV.6.1.1 Theory:

The molecular density in the ionizer from a vaporizing surface of transient surface temperature $T_s(t)$ is derived by Olstad*[48]*:

$$n(t) = \frac{\alpha(1-\beta) l A_s}{k} \left(\frac{m}{2\pi k}\right)^{3/2} \int_0^t \frac{p(T_s)}{T_s^{5/2}(t-\tau)^4} \exp\left(\frac{-ml^2}{2kT_s(t-\tau)^2}\right) d\tau \qquad (4\text{-}4)$$

where α = condensation coefficient (assumed = 1)

β = backscattering coefficient due to the collisions between the vaporizing molecules (= 18% based on Anisimov's calculation*[34]*)

l = distance from source to the ionizer (= 40 cm)

A_s = surface area viewed by mass spectrometer ($\approx 0.79\ cm^2$)

k = Boltzmann constant

m = mass of the molecule detected

p = partial pressure of the molecule detected at temperature T_s

T_s = the surface temperature

τ = time of emission of the molecule from the source surface

t = time of arrival of the molecule at the ionizer at distance l.

The calculation was based on the assumptions:

(1) the vapor is in thermal equilibrium with the vaporizing surface,

(2) the vaporization is Hertz-Langmuir; or, the rate of vaporization is given by Eq. (2-19) assuming unit vaporization (condensation) coefficient,

(3) the velocity distribution of the vaporizing molecules is Maxwellian,

(4) the angular distribution is cosine,

(5) the expansion of the molecular flow from source to the ionizer is free of collisions, or free molecular flow.

(6) the collisional effect is taken into account through the backscattering factor β.

The verification of these assumptions will be discussed later with the experimental results.

For the steady state condition such as that used in the mass spectrometer calibration (section III.2.3), the steady state density is:

$$n = \frac{\alpha(1-\beta)A_s p(T)}{4\pi l^2 kT} \tag{4-5}$$

Comparing with Eq. (3-16), we have the unit conversion factor $K_u = 7.32\times10^{21}$ molecules/cm^3-K/atm and the geometric constant $K_g = \frac{A_s}{4\pi l^2} = 3.9\times10^{-5}$ with unity condensation coefficient.

IV.6.1.2 Experimental Interpretation:

Since the sweep frequency of the mass filter for sweep mode operation is limited by the transit time of the ions through the quadrupole structure, the mass control is tuned to monitor one mass at each laser shot. Fig. 4.14 shows a typical measured raw UO_2^+ signal by the mass spectrometer when it is tuned for mass 270. Therefore, in order to obtain the informations for each laser energy and temperature transient, four separate shots are needed to detect the four uranium bearing species, namely, U, UO, UO_2 and UO_3. After recording the output voltage signals of all the species, the following steps should be taken to yield the molecular densities of the measured neutral species in the ionizer:

(1) Correction for the RC time constant of the external circuitry:

Beginning with the voltage measured as a function of time by the transient recorder $V_{ms}(t)$, and given the external circuit as shown in Fig. 4.15, the current $I_{emp}(t)$ out of the electron multiplier is given by:

$$I_{emp}(t) = (C_l + C_b)\frac{dV_{ms}(t)}{dt} + \frac{V_{ms}(t)}{R_b} \tag{4-6}$$

where C_l = the capacitance of the cable lines

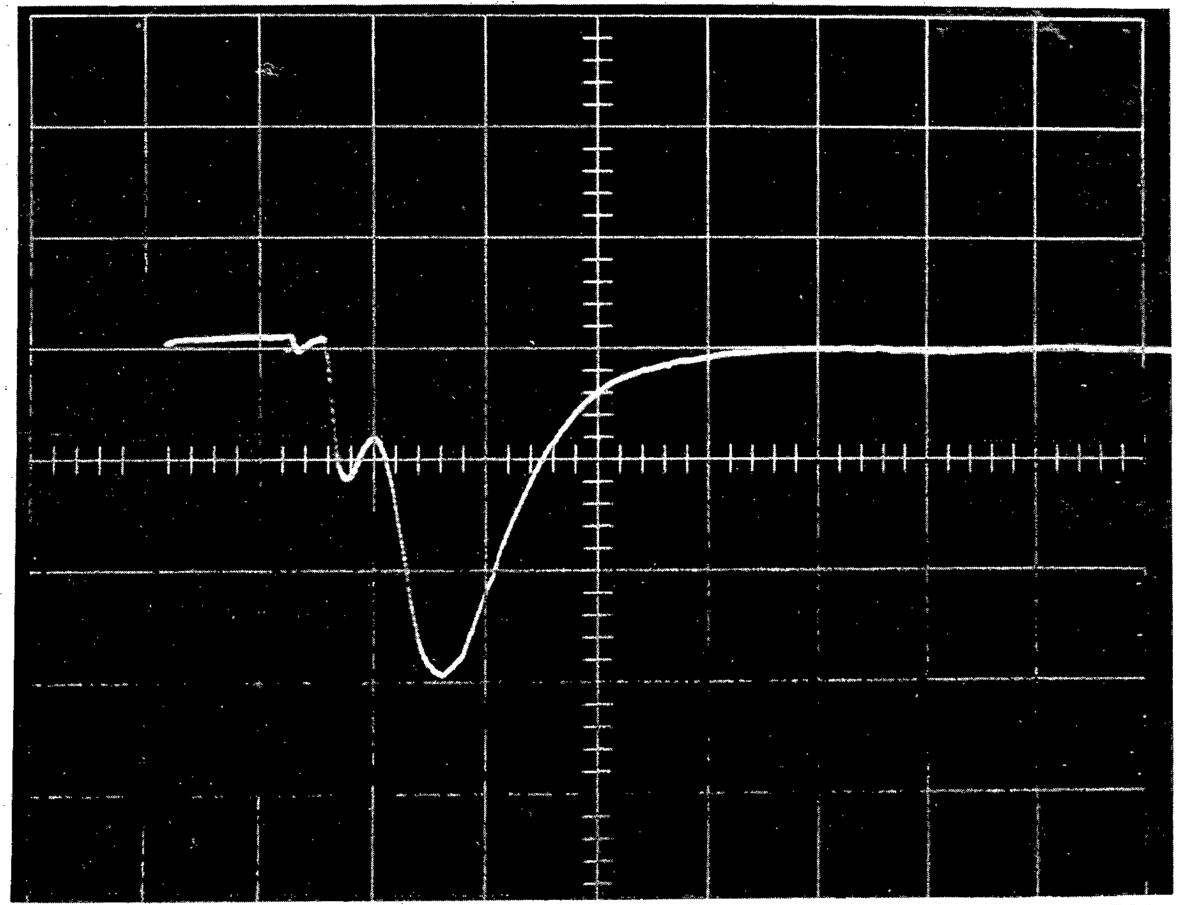

XBB 810-10735

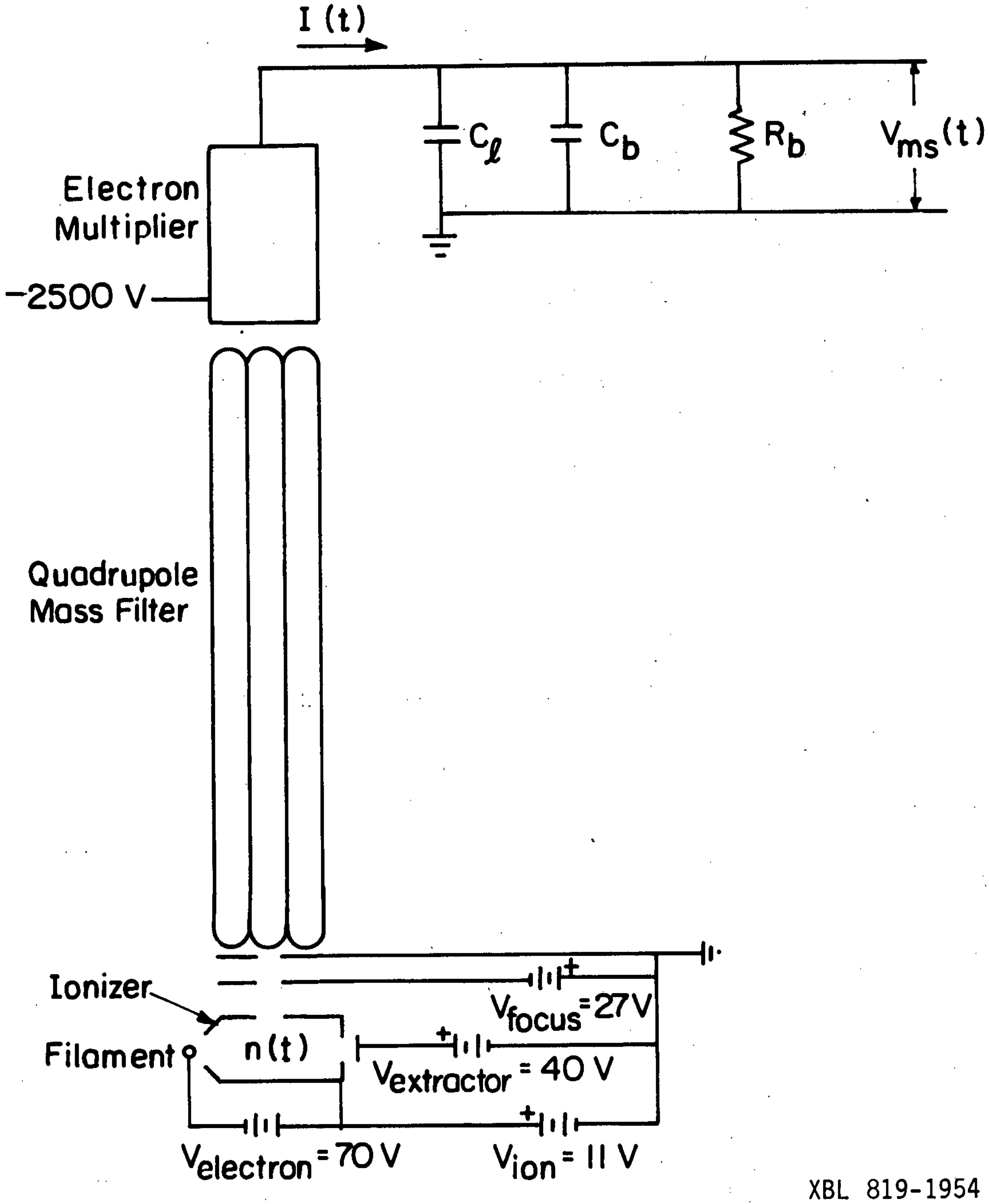

XBL 819-1954

Fig. 4.15 Electrical Circuit of Mass Spectrometer Ionizer and External Circuit for Signal Recording

C_b = the input capacitance of the transient recorder

R_b = the input resistance of the transient recorder.

(2) Correction for the electron multiplier efficiency:

The rate of the ion collected by the first dynode of the electron multiplier I_{fd} is given by

$$I_{fd}(t) = \frac{I_{emp}(t)}{G\gamma} \tag{4-7}$$

where G = electron multiplier gain

γ = number of secondary electrons emitted at the first dynode for each ion collected.

(3) Correction for the ion drift time and efficiency of the quadrupole structure:

The ions produced in the ionizer per unit time I_{ion} is given by

$$I_{ion}(t) = \frac{I_{fd}\,(t + t_d)}{F_q} \tag{4-8}$$

where t_d = drift time of ions from ionizer through quadrupole

(acceleration time before quadrupole is neglected)

F_q = the fraction of ions reaching the electron multiplier

compared to the total ions produced in the ionizer.

The drift time t_d can be calculated from the ion kinetic energy entering the quadrupole eV_{ion}:

$$eV_{ion} = \frac{1}{2}\, m\, (\frac{L_q}{t_d})^2 \tag{4-9}$$

where V_{ion} = ion potential relative to the ionizer

e = ion charge

m = ion mass

L_q = length of quadrupole structure (= 14 cm)

Solving for t_d gives

$$t_d = L_q\,(\frac{m}{2eV_{ion}})^{1/2} \tag{4-10}$$

or

$$t_d = 1.01 \times 10^{-5} \left(\frac{M}{11}\right)^{1/2} \qquad (4\text{-}11)$$

in which t_d is in second and M is the molecular weight in g/mole.

In UO_2 system, t_d = 0.0468 msec for U^+ (mass 238)

= 0.0484 msec for UO^+ (mass 254)

= 0.0499 msec for UO_2^+ (mass 270)

= 0.0513 msec for UO_3^+ (mass 286).

(4) Correction for the ionization cross section and the fragmentation pattern:

For UO_2 vaporization where UO_3, UO_2, UO and U neutral species are present in the vapor and cracking fragmentation occurs by electron impact, the ions produced in the ionizer are attributed to the sum of the ionization of the neutrals of the same mass and the fragments from the neutrals of higher mass.

Similar to the section III.2.3 for steady state condition, the production rate of the ions i^+ from step (3) I_{i^+} is given by:

$$I_{i^+}(t) = [\sigma_i F_{ii} n_i(t) + \sum_{k>i}^{3} \sigma_k F_{ki} n_k(t)]\, I_e L \qquad (4\text{-}12)$$

where $\sigma_i(\sigma_k)$ = total ionization cross section of i(k) neutral

F_{ii} = fraction of i^+ ions from i neutral

F_{ki} = fraction of i^+ ions from k neutral ($m_k > m_i$)

$n_i(n_k)$ = molecular density of i(k) neutral in the ionizer.

I_e = emission electron current of ionizer filament

L = length of the electron sheet

Combining step (1) to (4) yields:

$$\frac{1}{G\gamma_i F_q}[(C_l+C_b)\frac{dV_i(t+t_d)}{dt}+\frac{V_i(t+t_d)}{R_b}]=[\sigma_i F_{ii} n_i(t)+\sum_{k>i}^{3}\sigma_k F_{ki} n_k(t)]I_e L \qquad (4\text{-}13)$$

Rearranging Eq. (4-13) gives, for each species i,

$$V'_i(t)=\tau_{RC}\frac{dV_i(t+t_{di})}{dt}+V_i(t+t_{di})=K_{MS}\sigma_2\gamma_i R_b[C_i F_{ii} n_i(t)+\sum_{k>i}^{3} C_k F_{ki} n_k(t)] \qquad (4\text{-}14)$$

where $\tau_{RC} = R_b\ (C_l+C_b)$

$K_{MS} = I_eLF_qG$ = mass spectrometer instrumental constant

σ_2 = ionization cross section of UO_2

C_i = relative total ionization cross section of i neutral to that of UO_2 ($= \sigma_i/\sigma_2$)

γ_i = first dynode efficiency for i^+ ion.

For UO_2 vaporization, the measured voltage signals from the transient recorder $V_i(t)$ ($i=0$, 1, 2, 3) determine the molecular densities of the neutral molecules U, UO, UO_2, and UO_3 at any time t by the numerical solutions of the following equations:

$$V'_3(t) = \tau_{RC}\frac{dV_3(t+t_{d3})}{dt}+V_3(t+t_{d3})$$
$$= K_{MS}\sigma_2\gamma_3R_b[C_3F_{33}n_3(t)] \tag{4-15}$$
$$V'_2(t) = \tau_{RC}\frac{dV_2(t+t_{d2})}{dt}+V_2(t+t_{d2})$$
$$= K_{MS}\sigma_2\gamma_2R_b[C_2F_{22}n_2(t)+C_3F_{32}n_3(t)] \tag{4-16}$$
$$V'_1(t) = \tau_{RC}\frac{dV_1(t+t_{d1})}{dt}+V_1(t+t_{d1})$$
$$= K_{MS}\sigma_2\gamma_1R_b[C_1F_{11}n_1(t)+C_2F_{21}n_2(t)+C_3F_{31}n_3(t)] \tag{4-17}$$
$$V'_0(t) = \tau_{RC}\frac{dV_0(t+t_{d0})}{dt}+V_0(t+t_{d0})$$
$$= K_{MS}\sigma_2\gamma_0R_b[C_0F_{00}n_0(t)+C_1F_{10}n_1(t)+C_2F_{20}n_2(t)+C_3F_{30}n_3(t)] \tag{4-18}$$

For each time t, Eqs. (4-15) - (4-18) are solved for V'_0, V'_1, V'_2, and V'_3. Then n_0, n_1, n_2 and n_3 are determined from the second equalities in these equations. The instrumental constant $K_{MS}\sigma_2\gamma_2$ is determined from the steady state calibration (Sect. III.2.3).

IV.6.1.3 Results:

Fig. 4.16 shows the comparison of the raw mass spectrometer signal V(t) with the result of the RC time constant and drift time correction V'(t) in Eq. (4-14). The signal shows two time peaks; the first one is attributed to the fast ions with 11 eV energy (to be discussed in a later section), while the second one is due to thermal molecules. In solving for the transient molecular densities by means of Eqs. (4-15) to (4-18), the first peaks are not included in V'(t) since the ions are not created in the ionizer by electron impact. In the correction, the transient

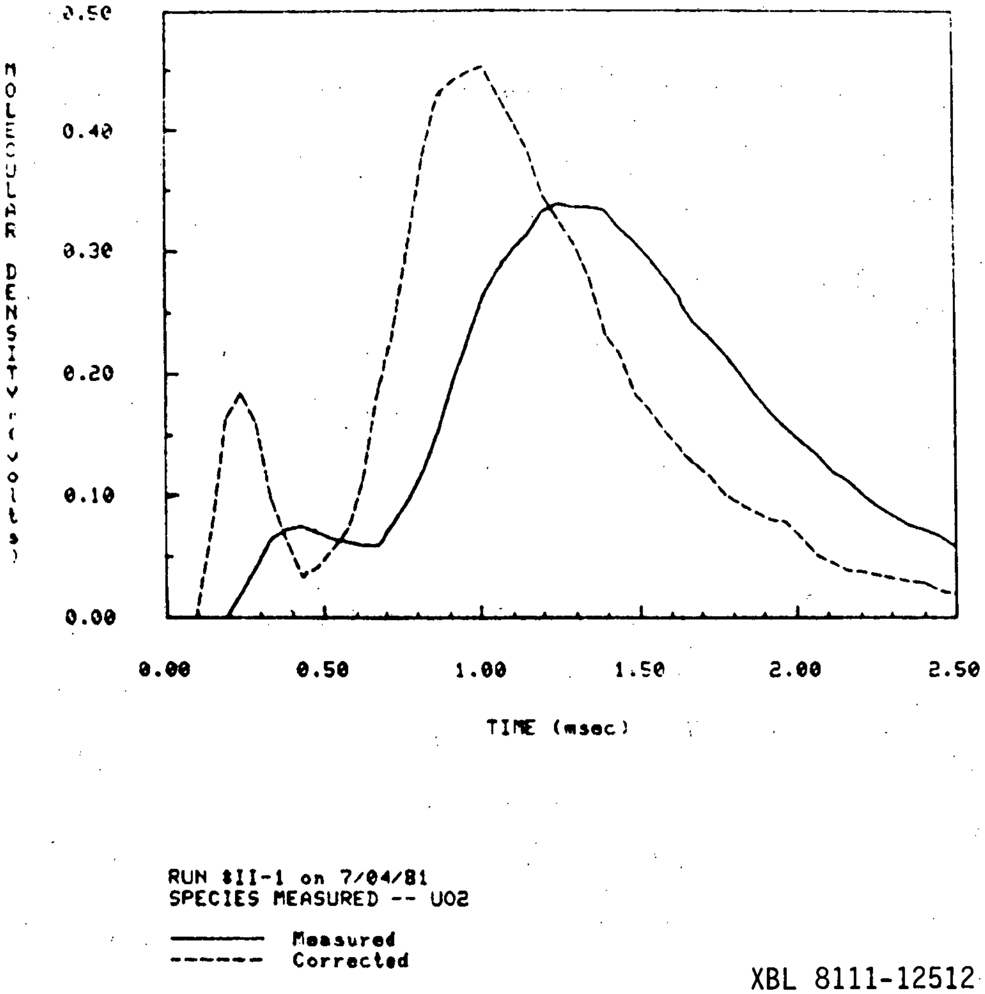

XBL 8111-12512

Fig. 4.16 A Measured UO_2^+ Signal before and after correction for RC time constant and ion drift time recorder input resistance is 1 MΩ, the transient recorder input capacitance is 25 pf and the line capacitance is about 175 pf, so the RC time constant for the mass spectrometer signals is about 0.2 msec. The drift time for the ions are given in Eq. (4-11). The fragment ratios F_{ij}'s, relative ionization cross section C_i, relative electron multiplier gain γ_i are from section III.2.3.

Six sets of experiments were carried out for mass spectrometric measurement. Table 4.3 shows the measured maximum molecular density of the uranium bearing species. Also shown are the calculations by Eq. (4-4) based on Blackburn's equilibrium model for the partial pressures and the calculated temperature transients by STAR code. Because of the uncertainties of the fragmentation pattern, the results for the species U, UO, UO_3 are relatively unreliable compared to UO_2. For example, U mostly comes from the fragmentation of UO_2, which has 4 orders of magnitude higher theoretical density. Moreover, the results for n_{UO_3} are relatively reliable compared to those of n_{UO} and n_U because UO_3 ions are always parent ions. Fig. 4.17 shows\a typical UO_2 molecular density with time compared to the theoretical calculation. Aside a time shift of about 0.25 msec, the experimental result has very similar time response with the theoretical one. Also shown in Fig. 4.17 is an arrow of theoretical time of maximum molecular density if the flow is collision-dominated hydrodynamic flow*[63]*. The time response will also be narrower for hydrodynamic flow*[63]*. Therefore, it is concluded that the free-molecular flow is the adequate one to describe the gasdynamic flow expansion in the problem of interest.

Table 4.4 shows the ratio of $n_{UO_3}^{max}$ to $n_{UO_2}^{max}$, and n_{UO}^{max} to $n_{UO_3}^{max}$ from experiments compared with the calculations based upon the partial pressures from three different theoretical models*[81,82,109]*. The calculations from Blackburn*[82]* and Breitung*[81]* are consistent with the experiments. The sensitivity of calculated $n_{UO_3}^{max}/n_{UO_2}^{max}$ and $n_{UO}^{max}/n_{UO_3}^{max}$ to the uncertainties of material properties is estimated to be ~±50% from the sensitivity study described in section II.4.3. The error of measured $n_{UO_3}^{max}/n_{UO_2}^{max}$ ratio is estimated to be ~±50%, while the error of measured $n_{UO}^{max}/n_{UO_3}^{max}$ ratio may be more than 100% due to fragmentation.

Table 4.5 shows the time of maxima of the UO_2 and UO_3 signals compared with the theoretical calculation based on Blackburn's model. The measured time of maxima are bigger

TABLE 4.3

Maximum Molecular Density of Experiment compared with Theory

RUN#	E_i	Theory*					Experiment				
		T_s^{max}	$n_{UO_3}^{max}$	$n_{UO_2}^{max}$	n_{UO}^{max}	n_U^{max}	T_s^{max}	$n_{UO_3}^{max}$	$n_{UO_2}^{max}$	n_{UO}^{max}	n_U^{max}
	(J)	(K)	$(\times 10^{-11})$	$(\times 10^{-12})$	$(\times 10^{-10})$	$(\times 10^{-9})$	(K)	$(\times 10^{-11})$	$(\times 10^{-12})$	$(\times 10^{-10})$	$(\times 10^{-9})$
I	10.6	4016	.2699	.2047	.4283	.0218	3913	.1959	.1893	.5541	.2336
II	10.25	3983	.2475	.1746	.3302	.0151	3769	.1969	.1282	.4759	.5215
VI	11.4	3963	.2799	.1985	.3756	.0172	4115	.2131	.1653	.2143	.5441
VII	16.8	4225	.4333	.4238	1.3300	.1047	4412	.2193	.3198	.4866	2.4630
VIII	7.32	3684	.1373	.0683	.0722	.0018	3813	.0988	.0454	.0563	.4435
IX	10.2	3971	.2497	.1750	.3259	.0146	4088	.1969	.1714	.5551	.2893

* Theoretical Calculation is based on Blackburn's calculation *[82]* for partial pressures of each species.

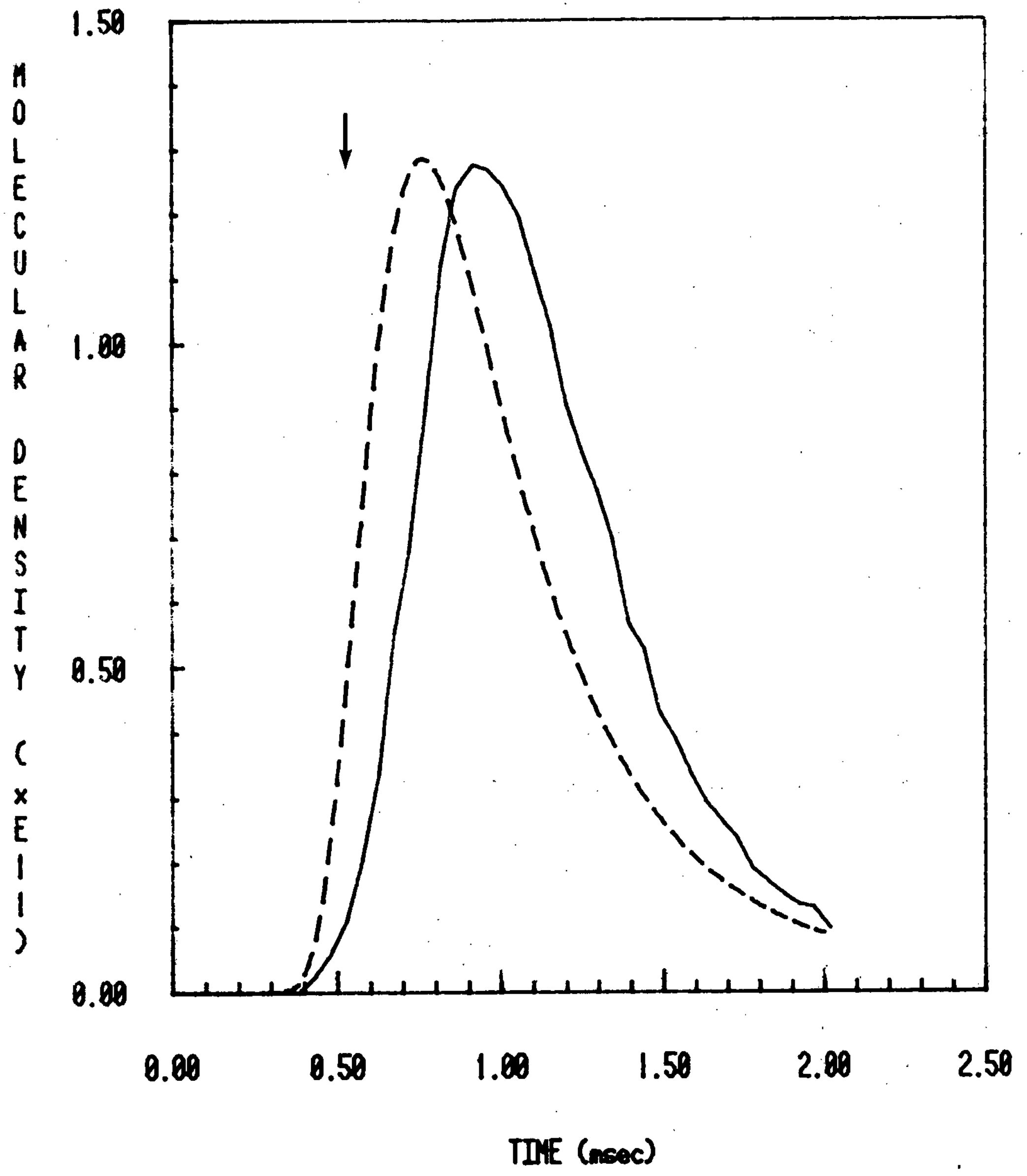

XBL 8110-12285

Fig. 4.17 The UO_2 Molecular Density from Mass Spectrometer Signal — compared to the free-molecular flow calculation

(The arrow shows the time of maximum density from gasdynamic expansion model.)

TABLE 4.4

The Ratios of Maximum UO_3 Density to UO_2 and Maximum UO Density to UO_3

RUN#	E_i (J)	$n^{max}_{UO_3}/n^{max}_{UO_2}$				$n^{max}_{UO}/n^{max}_{UO_3}$			
		Theory(1)	Theory(2)	Theory(3)	Experiment	Theory(1)	Theory(2)	Theory(3)	Experiment
I	10.6	.132	.294	.967	.103	.159	.224	.0079	.283
II	10.25	.142	.319	1.004	.154	.133	.194	.0072	.242
VI	11.4	.141	.296	.953	.129	.134	.221	.0079	.100
VII	16.8	.102	.215	.748	.069	.307	.493	.015	.222
VIII	7.32	.201	.381	1.161	.218	.053	.108	.0039	.057
IX	10.2	.143	.313	.992	.115	.131	.199	.0072	.282

* Theory(1): Blackburn's Calculation [82]

Theory(2): Breitung's Calculation [81]

Theory(3): Leibowitz's Calculation [109]

TABLE 4.5

Time of Maximum of UO_2 and UO_3 Signals

RUN#	E_i (J)	Time of Max of n_{UO_2}		Time of Max of n_{UO_3}		Ratio of Time of Max	
		Theory	Experiment	Theory	Experiment	Theory	Experiment
I	10.6	0.74	1.25	0.76	1.30	0.97	0.96
II	10.25	0.73	1.01	0.75	1.10	0.97	0.92
VI	11.4	0.76	1.10	0.78	1.35	0.97	0.82
VII	16.8	0.75	1.30	0.78	1.45	0.97	0.90
VIII	7.32	0.77	1.05	0.79	1.30	0.97	0.81
IX	10.2	0.74	1.15	0.76	1.30	0.97	0.89

* $\left(\frac{M_{UO_2}}{M_{UO_3}}\right)^{1/2} = \left(\frac{270}{286}\right)^{1/2} = 0.97$

than calculation as pointed out earlier. However, the ratio of the two is quite consistent with a calculation based on the square root of the mass ratio.

IV.6.2 Gas Phase Composition

The gas phase composition can be calculated from the partial pressures of the vapor species by the following equation:

$$(O/U)_{gas} = \frac{p_O + 2p_{O_2} + p_{UO} + 2p_{UO_2} + 3p_{UO_3}}{p_U + p_{UO} + p_{UO_2} + p_{UO_3}} \tag{4-19}$$

In estimating the vapor composition from experiment, we assume that the vapor composition of the vapor adjacent to the target surface can be approximated by the vapor composition in the ionizer (within ±5% estimated error), which is further approximated by the following equation:

$$(O/U)_{ionizer} = \frac{n_{UO} + 2n_{UO_2} + 3n_{UO_3}}{n_U + n_{UO} + n_{UO_2} + n_{UO_3}} \tag{4-20}$$

The contributions of oxygen atoms and oxygen molecules were estimated to be not more than 5%. The result is shown in Table 4.6.

IV.6.3 Fast Ions

As seen in Fig. 4.14, there are two time maxima detected for all the species except UO_3, for which the concentration is probably too small to be measurable. The first peak is believed to arise from hot ions emmited with the vapor cloud. The qualitative justification comes from the following observations: (i) Only the first peak is measured when the filament current in the ionizer is turned off, (ii) A huge signal is measured by the ion probe described in section III.1.3. The quantitative interpretation is difficult because the biased acceleration of ions by the collecting plate alters the random motion flux-density relation in the ejected vapor cloud.

The calculation by Karow*[64]* based on Sha's equation and effective "un-isolated" ionization potential shows that the degree of ionization due to thermal effects is 2.8% at 4500 K. The partially ionized gas does not attain plasma characteristics (quasi-neutrality and collective

TABLE 4.6

The Oxygen-to-Uranium Ratio in the Gas Phase

RUN#	E_i (J)	Theory		Experiment	
		T_s^{max}	$(O/U)_{gas}$*	T_s^{max}	$(O/U)_{gas}$**
I	10.6	4016	2.146	3913	2.063
II	10.25	3983	2.152	3769	2.091
VI	11.4	3963	2.141	4115	2.096
VII	16.8	4225	2.105	4412	2.035
VIII	7.32	3684	2.192	3813	2.150
IX	10.2	3971	2.148	4088	2.069

* Calculated from Eq. (4-19) and based on Blackburn's partial pressure calculation.

** Estimated from Eq. (4-20).

behavior) at temperatures less than 5000 K. The absorption of the laser energy by a partially ionized vapor is dominated by the inverse Bremsstrahlung process of the interaction between the laser photons and the free electrons in the vapor*[65]*. According to the Bremsstrahlung absorption theory*[66]*, assuming all the ions are singly charged, and that ionization is 2.8% at 4500 K, the absorption coefficient is 0.0328 cm^{-1} for 1.06 μm Nd-glass laser and 0.0076 cm^{-1} for 0.65 μm optical pyrometer. Assuming an absorbing layer of 0.5 mm*[23]*, the absorption of 1.06 μm laser light is 0.16% and that of 0.65 μm radiation is 0.04%. Therefore the interference of the partially ionized vapor with the laser or with the optical pyrometer measurement is not likely to be important. However, Karow*[30]* proposed that, instead of the inverse Bremsstrahlung absorption which is usually in the eV range, bound-bound absorption in the visible spectral range is the mechanism responsible for the interference of the ionized vapor with the thermal radiation. According to his calculation, based on a smeared quasi-continuous energy spectrum for the vapor molecules, the uranium oxide vapor becomes optically thick and the pyrometric temperature measurement becomes unreliable when the temperature is higher than 4200 K*[30,53]*.

From the double-maxima mass spectrometer signals, we can estimate the degree of ionization of the hot vapor. The relative magnitude of the raw signals does not directly reflect this percentage of thermonic emission because the mass spectrometer does not have the same detection efficiency for the ions and the neutral molecules. This difference is attributed to the following two factors: (i) The neutral molecules need to be ionized in order to be detected, while the ions do not, and (ii) The mass spectrometer has different extraction efficiencies (defined as the percentage of ions passing through the entry of the quadrupole structure compared to the total number of ions in the ionizer) for two groups of ions due to different velocity distributions.

The absolute ionization cross sections of uranium-bearing species have not been measured. However, the ionization efficiency of most of the molecules is in the order of 10^{-3} to 10^{-4}. The ionization efficiency of the ions is of course equal to one. In order to estimate the extraction efficiency of ions, one has to consider the forces exerted on the ions in the ionizer. There are two principal forces from the electric potential difference in the ionizer*[110]*: one is due to the electric field between the filament and the electron collector (see Fig. 4.15), which tends to divert lower speed ions from a trajectory to extraction hole and results in lower extraction probabilty for low speed ions; the other one is due to the electric field set up by the electric potential difference between the focus electrode and the ionizer cage, which gives slow ions higher extraction efficiency than fast ones*[110]*. This extraction efficiency, or bias function as it is called, has been determined experimentally in Ref. 110, and the effect of the beam temperature due to the fact that the mass spectrometer is optimized at lower temperature was treated in Appendix B of the cited reference. The temperature of the neutral molecules is assumed equal to the surface temperature, which is in the range of 3600 to 4300 K. The "temperature" of the thermal ions is represented by the mean energy of the ions. It has been found*[111,65]* that thermal ion energies increase with increasing laser power density in proportion to approximately the 0.33 power for high atomic mass materials. From ion energy measurement given in Ref. 65, it is estimated that the thermal ions have a mean energy of approximately 30 eV. Taking into account the deceleration of the ions due to the ionizer cage relative to ground, the average ion energy in the ionizer is about 19 eV. According to Ref. 110, the extraction efficiency for ions from 4000 K neutral molecules is about 80% and about 1% for 19 eV thermonic ions.

Combining factors (i) and (ii), the degree of ionization of UO_2 gas in the partially ionized vapor is shown in Table 4.7. Also shown in the Table is the degree of ionization calculated by Karow*[64]*.

Because of the 11 eV potential imposed on the ionizer cage, the ions detected by the mass filter should have energies slightly higher or equal to 11 eV. This expectation is consistent with the observation that the times of maxima for the first peaks of U^+, UO^+ and UO_2^+ signals have the same ratio as that of the square root of the masses. Also, it is shown in Fig. 4.18 that the normalized ion signal follows quite well the shape of the normalized laser pulse, and the time of maximum differs for 0.14 msec, which is exactly the transit time of UO^+ ions from the tar-

TABLE 4.7

The Estimated Degree of Ionization from Mass Spectrometer Signals

RUN#	E_i	T_s^{max}	UO_2 Signal		% of Ionization*	% of Ionization
			ion peak	neutral peak	estimated	calc*[64]*
I	10.6	4016	0.05	0.68	0.8	1.82
II	10.25	3983	0.18	0.45	4.1	1.78
VI	11.4	3963	0.18	0.56	3.2	1.76
VII	16.8	4225	0.34	1.24	2.7	2.28
VIII	7.32	3684	0.08	0.17	4.6	1.32
IX	10.2	3971	0.31	0.61	5.0	1.77

* Ionization fraction for neutral molecules in the ionizer is assumed to be 10^{-4}.

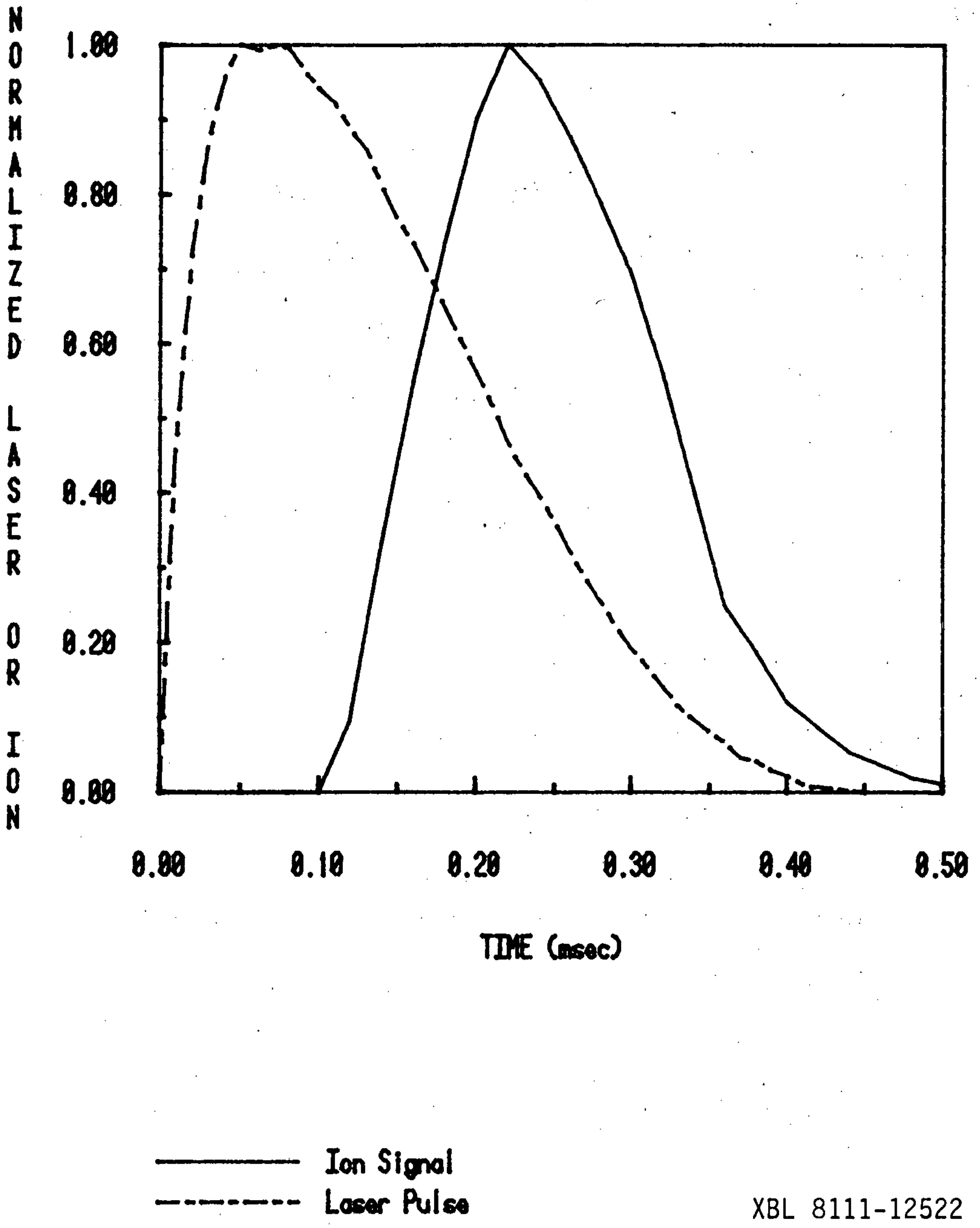

XBL 8111-12522

Fig. 4.18 The Mass Spectrometer Signal with zero Ionizer Filament Current compared to the Laser Pulse (species measured: UO_2^+)

get surface to the ionizer with 11 eV energy. Consequently, although the thermionic fast ions have an energy distribution as reported in Ref. 65, because of the filtering effect of ion potential the fast ions will not disturb the measurement of the neutrals. This filtering effect justifies the interpretation procedures described in the last section by simply eliminating the first peak from thermionic emission.

IV.6.3 Dimers

The mass spectrometer is tuned to mass 540 for $(UO_2)_2$ and 508 for $(UO)_2$ to examine the dimer formation. No signal was measured at either mass even when the resolution was reduced to cover a mass range of about ±20 a.m.u.

IV.7 VAPOR PRESSURE - TEMPERATURE RELATION

In reactor safety application, the format of the material equation of states is usually expressed in the form of either pressure - energy relation or pressure - temperature relation. A pressure - temperature relation for the total pressure of UO_2 is recommended as*[67]*:

$$\log p = 29.65 - 34933/T - 5.641 \log T \qquad (4\text{-}21)$$

where p is in atm and T is in K.

Therefore, the same kind of relation as:

$$\log p = A + B/T + C \log T \qquad (4\text{-}22)$$

is assumed to fit the experiment results for the parameters A, B and C. In doing the fitting, Eq. (4-4) is used to calculate the maximum UO_2 molecular density and then compared with the experimental values as shown in Table 4.3.

Depending on the temperature transients used in Eq. (4-4), the following relations prove to be the best fit for the partial pressure of UO_2:

$$\log p = 26.81 - 26089/T - 5.594 \log T \qquad (4\text{-}23)$$

provided that the temperature transients calculated from the computer program STAR described in Chapter II is used, and

$$\log p = 24.22 - 24238/T - 5.033 \log T \qquad (4\text{-}24)$$

provided that the temperature transients measured by optical pyrometer is used. The results are shown in Fig. 4.19. About 50% discrepancy between two equations results from the difference in the temporal shape of the temperature transients as shown in Fig. 4.12.

Also shown in the figure are the calculation based on Blackburn's model for the temperature and oxygen-to-uranium ratio calculated from STAR code, and a band of limits recommended in Ref. 67 from assessing the published theoretical calculations and measurements in the literature. Notice that the limits given are for total pressures. The relation given in Eq. (4-23) is in good agreement with the calculation based on Blackburn's model. Both of the fitted equations fall inside the limits. The results of the Mach disk photographic measurement (Sect. IV.4) is also shown in Fig. 4.19 for comparison.

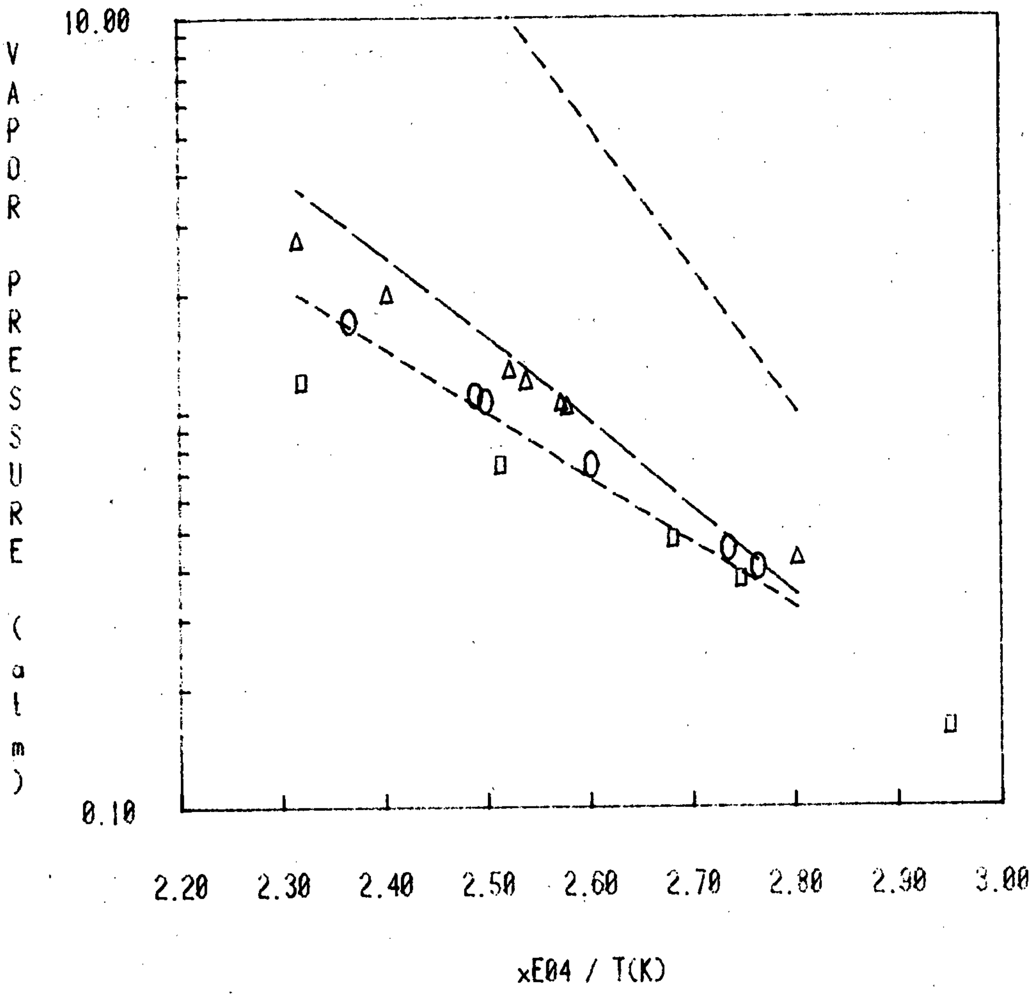

Fig. 4.19 The Pressure - Temperature Relation for UO_2

— — — Blackburn's Model for UO_2 partial pressure

----- recommended limits of total vapor pressure in Ref. *[67]*

Δ This work fitted to eq. (4-23) for UO_2 partial pressure (calculated temp)

○ This work fitted to eq. (4-24) for UO_2 partial pressure (measured temp)

□ Mach disk Photographic measurments for total pressure (measured temp)

V. CONCLUSION

A computer code was developed to simulate the laser heating process and calculate the surface temperature transient. The sensitivity study of the effect of uncertainties of the high temperature material properties resulted in about 3% variance for the surface temperature calculation and about 40% variance for surface O/U ratio depletion. The uncertainties in the thermal conductivity and the heat of vaporization have the greatest effect on the thermal response, while the O/U ratio is principally controlled by the diffusion coefficient.

The pyrometrically measured temperatures are in good agreement with the calculation in the mass spectrometric experiment, while in the photographic technique, the measured temperatures are higher than the calculation for temperatures above 4000 K. The excessively high temperature in the photographic measurement is believed to be due to the radiation contribution from the hot vapor when an ambient gas is present. It is concluded that the pyrometric temperature measurement is feasible up to 4000 K in ambient pressure and at least 4225 K in vacuum.

The Mach disk photographic measurement of total vapor pressure showed good agreement with theoretical prediction in temperatures below 4000 K, but a factor of 2 to 4 lower than theory above that. The low vapor pressure is partly attributed to the excessively high measured temperatures and probably partly from the wrong interpretation of "reservoir" pressure in applying the sonic orifice analogy to the vaporization process.

The mass spectrometric technique is the only way of identifying different vapor species from vaporization of solids, measuring the evaporation rate of each of them, and deducing the vapor composition. Thus it is the only way of directly checking whether vaporization is an equilibrium process. The results of the vapor pressure and the vapor composition deduced from the experiments favor the Blackburn's model for calculating the equilibrium partial pressure of each species compared to the other calculations in the literature. It also suggests that the equilibrium vaporization, after taking into account the oxygen depletion on the surface, successfully describes the vaporization process in the sub-millisecond transient, and the transient calculation presented here is more suitable than either the congruent or the "forced congruent" calculations.

The measured time-of-arrival and the width of the mass spectrometric signals compared to the free molecular model (collisionless expansion) and hydrodynamic model (collision-dominated continuum flow) suggest that the free molecular expansion best represents the expansion process in vacuum. The fact that no dimers of any species were measured also suggests that collisions are negligible in the expansion into vacuum. On the other hand, the Mach disk structure observed in pulse vaporization under ambient background pressure is well represented by the supersonic flow expansion model.

A time delay is observed from the mass spectrometric signals compared to the theoretical calculation based upon free molecular model. However, the fact that the ratio of time of maximum of UO_2 signal to UO_3 signal is in satisfactory agreement with the square root of the mass ratio suggests that the time delay is not due to the expansion process or the detector. Therefore, the possibility of a time delay due to the surface processes, such as surface diffusion, formation of compound molecules, etc., which are not considered in the theoretical calculation, should be considered.

The mass spectrometric measurement also provides a way of measuring the degree of ionization of the high temperature gas ejected from the surface. The result is in good agreement with the thermonic calculation based on Sha's equilibrium model.

APPENDIX A: THEORETICAL EXTRAPOLATIONS OF UO_2 VAPOR PRESSURE

Simple direct extrapolation according to the second law is not reliable because of the scatter of the measured values of the heat of sublimation and the multispecies nature of UO_2 vaporization. There are, however, three theoretical approaches to predict the thermodynamic equation of state in the temperature range where no experimental data are available from well-established information in the low temperature range. These theories are the Principle of the Corresponding States (PCS), the Significant Structure Theory of Liquids (SST) and the Law of Mass Action (LMA). A brief description of each of the approach and a summary of the calculations on UO_2 are presented here.

In dealing with the first two approaches one should keep in mind that, although the critical region of UO_2 is not of interest for HCDA analysis, critical point data are useful in establishing a thermodynamically consistent set of data in the temperature range of interest (4000 K - 5000 K).

A.1 Principle of Corresponding States:

The basis of the theory states that the thermodynamic properties of fluids are universal functions of the "reduced" variables of state+ (such as pressure, volume, temperature, internal energy, enthalpy etc.). The concept was originally proposed by Hirschfelder et, al *[68]* after examing the equations of state of a number of fluids in the neighborhood of their critical points. The idea of applying this principle is that the critical constants may be estimated on the basis of experimental data from a region remote from the critical point. These predicted critical constants are then used to predict the equation of state in the intermediate range where experimental data are not available. More specifically, if the pressure, volume and temperature of a mole of material are denoted by P, V and T respectively, and their values at the critical point are P_c, V_c and T_c, the reduced quantities are:

$$P_r = \frac{P}{P_c} \; ; \; V_r = \frac{V}{V_c} \; ; \; T_r = \frac{T}{T_c} \qquad \text{(A-1)}$$

+The "reduced" variable of state is defined as the ratio of the variable to its value at the critical point.

The Principle of Corresponding States has been generalized by Riedel*[69]* by stating that the compressibility factor Z defined as $\frac{PV}{RT}$ should be a universal function of V_r, T_r and α, where α is defined as the slope of the reduced vapor pressure-temperature curve at the critical point, or $\alpha = (\frac{dP_r}{dT_r})_{T_r=1}$; that is

$$Z = \frac{PV}{RT} = Z(V_r,T_r,\alpha) \tag{A-2}$$

and the proposed critical compressibility factor Z_c is:*[69]*

$$Z_c = \frac{P_cV_c}{RT_c} = 1/(1.90+0.26\alpha) \tag{A-3}$$

The reduced saturated vapor pressure of a fluid is a universal empirical function of reduced temperature T_r:*[69]*

$$\ln P_r = \alpha \ln T_r - 0.0838(\alpha-3.75)(36/T_r - 35 - T_r^6 + 42\ln T_r) \tag{A-4}$$

Menzies*[70]* and Meyer and Wolfe*[71]* have applied Eqs. (A-3) and (A-4) and the fitted empirical vapor pressure-temperature relation in the low temperature range is:

$$\ln P(\text{atm}) = 83.804 - 76800/T - 4.34\ln T \tag{A-5}$$

by assuming 0.27 and 0.272, respectively for Z_c in Eq. (A-3).

The values of P_c, V_c, T_c and Z_c are listed in Table A.1.

This method is basically equivalent to extrapolating the measured vapor pressure over solid (Eq. (A-5)) by many orders of magnitude to the critical region. The weakness of direct extrapolation remains. Kapil*[72]* has proposed another method of determing critical constants, hoping to avoid the large extrapolations and to obtain a single set of critical constants which would be consistent with all the available low temperature data. This method is based on the universal relation of reduced density versus reduced temperature for a given Z_c as tabulated form from Hougen, Watson and Ragatz*[68]* and the measured (i) melting temperature (ii) volume expansion coefficient of liquid (iii) liquid densty at melting temperature from Christiansen*[73]* to iterate and obtain a self-consistent set of critical constants (V_c,P_c,T_c). Using various values of Z_c and the corresponding critical constants along with Riedel's vapor pressure equation (A-4), a vapor pressure equation can be written and then "extrapolated down" to the low temperature region where experimental data are available. Finally, by comparing to the experimental data (from either Ohse*[7]* or Tetenbaum and Hunt*[5]*) a specific set of critical constants is proposed, as shown in Table A.1.

According to Kapil, since the low temperature experimental data is used strictly within the range in which it is measured, in contrast to the large extrapolations of this data in the earlier methods, the chosen set of critical constants is practically insensitive to the source of data used. In addition, the major uncertainty in the use of the Principle of Corresponding States arises from the lack of a good estimate of the critical compressibility Z_c of the material, and it is explicitly "solved" in this method, while it is arbitrarily guessed in the earlier methods.

By adopting Booth's scheme*[74]*, Browning, Gillan and Potter*[75]* proposed another method which combines Eqs. (A-3) and (A-4) with the law of rectilinear diameters:

$$\frac{\rho_l+\rho_v}{2} = AT+B \qquad \text{(A-6)}$$

where values of A and B are determined from measured values of liquid density and expansion coefficient at the melting point, assuming ρ_v to be negligible. From Christiansen's*[73]* liquid UO_2 data, A and B are calculated -4.5885×10^{-4} and 5.8076 respectively.

With reduced volume and temperature, Eq. (A-6) becomes

$$\frac{1}{V_r^l} + \frac{1}{V_r^v} = (\frac{CT_c}{V_c})T_r + \frac{D}{V_c} \qquad \text{(A-7)}$$

The liquid density is given by Guggenheim*[76]*

$$\frac{1}{V_r^l} = 1+0.85(1-T_r)+(0.53+0.2\alpha)(1-T_r)^{1/3} \qquad \text{(A-8)}$$

By iterating Eqs. (A-3), (A-4), (A-7) and (A-8), starting with an estimated critical temperature and using the measured vapor pressure and liquid densty at the melting temperature*[75]*, P_c, V_c, T_c and Z_c are solved, as listed in Table A.1.

Browning, Gillan and Potter*[75]* have also examined the effect of Ohse's*[7]* and Tetenbaum and Hunt's*[5]* vapor pressure data and the results (as shown in Table A.1) concluded that the effect of changing the vapor pressure data is rather small.

After having the critical quantities, the saturation vapor pressure-temperature relation below the critical point can be obtained by Eq. (A-4). Fig. A.1 shows the results from the sources listed in Table A.1.

A.2 Significant Structures Theory of Liquids:

The assumption of this theory, which was originally proposed by Eyring*[77]*, is that the thermodynamic partition function for the liquid may be expressed as an average of the partition functions for the solid and the gas. The theory has been quite successful for materials similar to UO_2 (e.g. alkali halides NaF etc.) *[78]*. According to the theory, each molecule in the liquid is partly in a solid-like and partly in a gas-like environment and the partition function $Z_l(V,T)$ for a mole of liquid at temperature T and volume V can be written as a weighted geometrical mean of partition functions for the solid Z_s and for the gas Z_g, i.e.

$$Z_l(V,T) = Z_s^{NV_s/V} Z_g^{N(V-V_s)/V} \qquad \text{(A-9)}$$

where N is the Avogadro's number and V_s and V are respectively the molar volume of the solid at the melting point and of the liquid in the state of interest.

The partition function for the "solid-like" molecules in the liquid can be written as*[78]*

$$Z_s = \exp(-\frac{E_s(V/V_s)^\gamma}{kT})[1+n_h\exp(\frac{aE_s}{n_hkT})](\frac{kT}{h\nu_s})^{3\mu} \qquad \text{(A-10)}$$

where E_s is the binding energy per molecule, $n_h=n(V-V_s)/V$ is the number of additional quasi-equilibrium positions of solid-like molecule in the liquid than in the solid, ν_s is a mean vibrational frequency, μ is the number of atoms per molecule (=3 for stoichiometric UO_2) and γ, n, a are three free parameters in this model.

The partition function of the "gas-like" molecules is given by the product of translational, vibrational, rotational and electronic partition functions as:

$$Z_g = Z_g^{tr} Z_g^{vib} Z_g^{rot} Z_g^{elec} \qquad \text{(A-11)*}$$

---

*In Ref. A.13, Gillan did not take into account the partition function for electronic states which was then in-where $Z_g^{tr} = (2\pi mkT)^{3/2}\frac{eV}{Nh^3}$

$$Z_g^{vib} = \prod_i \exp(-\frac{h\nu_i}{2kT})/[1-\exp(-\frac{h\nu_i}{kT})]$$

$$Z_g^{rot} = 8\pi IkT/h^2\sigma \quad \text{(for linear molecules)}$$

and $Z_g^{elec} = g_0+g_1\exp(-\frac{E_1}{kT})$

Having constructed the partition functions for the liquid, the Helmholtz free energy is given by

$$F(V,T) = -kT\ln Z_l(V,T) = -NkT\ [(V_s/V)\ln Z_s+((V-V_s)/V)\ln Z_{g]} \qquad \text{(A-12)}$$

All the other thermodynamic functions can then be found from F by applying standard formulae to Eq. (A-12).

Browning, Gillan and Potter*[75]* have applied this theory on UO_2. In determing the binding energy E_s and the mean vibrational frequency ν_s of "solid-like" molecules, they used both low temperature vapor pressure data of Ohse*[7]* and Tetenbaum and Hunt*[5]*. The three free-parameters were determined by matching the available data associated with the melting transition: melting temperature, volume change on fusion and entropy of fusion with the experimental values. The critical constants were then estimated by the measured liquid expansion coefficient together with the law of rectilinear diameters. The result is also listed in Table A.1 for comparison with the Principle of Corresponding States. They concluded that (i) the Significant Structures results are much more sensitive to the vapor pressure data than those from the theory of Corresponding States (ii) the critical volumes are uniformly greater by about 50% (iii) the values of Z_c are about 25% higher. The vapor pressure-temperature relation for liquid UO_2 by taking the derivative of Helmholtz free energy (Eq. A-12) with volume is shown in Fig. A.2.

Fischer et al.*[79]* have also applied Significant Structures theory to predict the critical constants, based on Ohse's low temperature data. They included an excess enthalpy (assumed to

---

cluded in a later publication Ref. A.10.

be due to Frenkel defects) in the solid-like partition function and assumed non-linear UO_2 molecules with higher electronic entropy. Furthermore, they used the vapor pressure and the liquid volume at the melting temperature, and the heat of fusion to determine the three free parameters. The result are shown in Table A.1 in the form of critical constants and in Fig. A.2 as the vapor pressure-temperature relation.

A.3 Law of Mass Action:

The basic assumption of applying the Law of Mass Action on the vaporization process is thermodynamic equilibrium at the phase boundary; that is, the vaporizing gaseous species from a condensed phase is in thermodynamic equilibrium with the condensed phase. For instance, the general vaporization reaction from a solid or liquid metal oxide is:

$$MO_A(\mathrm{cond}) + \frac{B-A}{2}O_2(g) \rightarrow MO_B(g) \tag{A-13}$$

This reaction includes also the vaporization of pure metals (A=B=0). For thermodynamic equilibrium the law of mass action gives

$$\Delta G_T = \Delta G^o_{f,T}[MO_A] + RT\ln\frac{P_{MO_B}}{a_{MO_A}P_{O_2}^{(B-A)/2}} = 0 \tag{A-14}$$

where P_{MO_B} = vapor pressure of gaseous MO_B

a_{MO_A} = activity of the metal oxide in the condensed phase MO_A

$\Delta G^o_{f,T}[MO_A]$ = free energy of formation of the condensed MO_A at temperature T

$\Delta G^o_{f,T}[MO_B]$ = free energy of formation of the gaseous MO_B at temperature T

With $\Delta\overline{G_{O_2}}$ = oxygen potential = $RT\ln P_{O_2}$, the relation

$$RT\ln P_{MO_B} = RT\ln a_{MO_A} + \Delta G^o_{f,T}[MO_A] - \Delta G^o_{f,T}[MO_B] + \frac{B-A}{2}\Delta\overline{G_{O_2}} \tag{A-15}$$

is then used to calculate the vapor pressure of each of the gaseous species MO_B.

Breitung, following Rand and Markin's technique *[80]*, has applied this method to calculate the equilibrium partial pressures of $UO_3(g)$, $UO_2(g)$, $UO(g)$, $U(g)$, $O(g)$ and $O_2(g)$ for vaporization of condensed $UO_{2\pm x}$ *[81]* and to estimate the tolerable uncertainty of the equation of state of liquid UO_2 *[21]* due to the scatter of the free energy of formation of the gaseous species.

Blackburn*[82]* has also applied this model, although in a slightly different way, to perform the same calculation.

In both calculations, the oxygen potential as a function of stoichiometry and temperature are required. This is also calculated by the law of mass action for the equilibrium reactions among the cations and anions in the condensed phase with oxygen gas. The equilibrium conditions near stoichiometric UO_2 are used to solve for the oxygen potential.

Fig. A.3 shows the two calculations for stoichiometric UO_2. The difference between the two is attributed to the use of different thermodynamic functions of the gaseous species*[83]*. Also shown in Fig. A.3 are the results of both calculations based on Breitung's forced congruent vaporization model*[31]*, assuming depletion of surface stoichiometry due to preferential vaporization of oxygen compared to uranium and eventual "congruent" vaporization at a given steady state temperature when the gas composition is identical to the bulk composition.

A.4 Discussion:

The basic assumptions for the Priciple of the Corresponding States concerning the microscopic behavior of the materials are (i) the potential energy of two particals is a function only of their separation i.e. the Lennard-Jone type of potential, (ii) the potential energy of entire N-partical system is the sum of the potential energy of all possible pairs of particles and (iii) the partition functions are evaluated by classical statistical mechanics. However, UO_2 is believed to be ionic and the intermolecular forces do not quite meet the assumptions stated. Therefore the prediction by the Corresponding States seems to lack the necessary theoretical foundation for application to UO_2.

The results of the Significant Structures Theory have the disadvantage of strong dependence of the input low temperature data, as shown in Table A.1. Since all the vapor pressure measurements in low temperature region agree quite well, a model which effectively magnifies this small discrepancy is not considered to be acceptable. Nevertheless, by comparing the results of Gillan*[78]* and Potter*[75]* in which the only difference was the inclusion of the electronic term in gas partition function, it seems reasonable to say that because the latter has smaller inconsistency with different low temperature data, more accurate informations on gas properties might compensate for this weakness in the theory.

The results from the Law of Mass Action show very strong effects of the gaseous thermodynamic data used. As shown in Table A.2, a linear temperature dependence of the free energy of formation is assumed. Due to the scatter of these data, this method is not reliable until more measurements in the higher temperature region are available. By comparing Fig. A.2 and Fig. A.3, it is found that Blackburn's result agrees suprisingly well with Gillan's and Potter's SST calculations and with Tetenbaum and Hunt vapor pressure data, while Breitung's calculation is much higher than any other calculation. The Breitung's calculation with forced congruent model (Fig. A.3) exhibits positive curvature while negative curvature is expected as the critical point is approached.

By comparing the results of three different methods applied to UO_2, the following conclusions can be drawn:

(1) The application of the Principle of Corresponding States is the least feasible due to the lack of theoretical foundation.

(2) Z_c values of 0.27 is valid only for Van der Waals bonded organic compounds. From the results of the alkali halides*[78]*, which have the same ionic structure as UO_2, the higher value of 0.31 from the Significant Structures Theory seems to be acceptable.

(3) The importance of the electronic excitation state of UO_2 is not only involved in the heat capacity, but in the vapor pressure assessment as well.

(4) Although the Law of Mass Action may have the strongest theoretical basis of the three, it is not reliable unless more precise gaseous thermodynamic data is available. In view of the ease of application in the vaporization problem we are dealing with, this medel is strongly preferred.

(5) In the future applications, the effect of change in stoichiometry and the addition of fission products can be included in the Significant Structures Theory and the Law of Mass Action, but not in the Principle of Corresponding States.

(6) In reassessing the theoretical models, liquid UO_2 properties just above the melting points need to be reconfirmed and more precisely determined.

(7) None of the theoretical models at this moment give satisfactory predictions.

(8) The theoretical calculation in the present stage plays two roles: (i) as preliminary information required in the HCDA analysis until the direct measurement becomes available, (ii) to accompany the direct measurements for a reliable data basis for final analysis. In the ultimate stage, due to the experimental difficulties, the complete equation-of-state will not rely on the direct measurement; therefore, direct measurement plays a role by helping to assess the validity of the theoretical models and enventally, to produce an appropriate and more reliable model for use in HCDA analyses.

TABLE A.1

Critical Constants of UO_2 Using the Principle of Corresponding States and the Significant Structures Theory of Liquid

Auther(s)	Ref	Model	Low Temp Data	Critical Constants			
				T_c(K)	V_c(cm^3/mol)	P_c(atm)	Z_c
Menzies *(1966)*	*70*	PCS	Ackermann	8000	89.8	2000	0.27
Meyer & Wolfe *(1964)*	*71*	PCS	Ackermann	7300	85.5	1900	0.272
Booth *(1968)*	*74*	PCS	Ohse	6723	98.7	1404	0.2513
Kapil *(1976)*	*72*	PCS	Ohse	6744	98.5	1404	0.25
Potter *(1977)*	*75*	PCS	Ohse	6723	98.7	1404	0.2513
			T & H	6820	98.4	1380	0.2426
Gillan *(1975)*	*78*	SST	Ohse	6960	164	1070	0.308
			T & H	9332	163	1450	0.308
Fischer *(1976)*	*79*	SST	Ohse	7560	166	1210	0.316
Potter *(1977)*	*75*	SST	Ohse	7320	152	1256	0.318
			T & H	8840	158	1424	0.310

TABLE A.2

Thermodynamic Properties of Gaseous Uranium Oxides

Species	Formation Reaction	Free Energy $\Delta G^{o}_{f,T}$(J/mol)	Reference
$UO_{3(g)}$	$U_{(l)}+\frac{3}{2}O_{2(g)}=UO_{3(g)}$	-830920+79.53T	Ackermann[84]
		-845910+87T	Alexander[85]
		-920380+113.65T	Rand & Markin[80]
		-837200+81.21T	Ackermann[86]
		-873800+93.56T	Bober[21]
		-836800+81.17T	Leibowitz[87]
$UO_{2(g)}$	$U_{(l)}+O_{2(g)}=UO_{2(g)}$	-508600+17.75T	Ackermann[84]
		-516550+23.86T	Rand & Markin[80]
		-508600+22.81T	Ackermann[88]
		-486830+2.09T	Ackermann[88]
		-483480+7.95T	Ackermann[88]
		-124900+21.86T-116.2logT	Bober[21]
		-486600+2.09T	Leibowitz[87]
$UO_{(g)}$	$U_{(l)}+\frac{1}{2}O_{2(g)}=UO_{(g)}$	-43325-48.56T	Ackermann[84]
		-45500-46.97T	Rand & Markin[80]
		-36840-43.12T	Blackburn[82]
		-18420-65.30T	Ackermann[88]
		-32650-57.77T	Ackermann[88]
		-32640-57.74T	Bober[21],Leibowitz[87]
$U_{(g)}$	$U_{(l)}=U_{(g)}$	488920-112.2T	Pattoret[89]
		482650-109.25T	Rand & Markin[80]
		497170-112.3T	Ackermann[88]
		491855-113.02T	Ackermann[88]
		447060-109.2T	Blackburn[82]
		491620-113T	Bober[21],Leibowitz[87]
$O_{(g)}$	$\frac{1}{2}O_{2(g)}=O_{(g)}$	256370-67.27T	Ackermann[88]
		250300-66.8T	Hultgren[90]
		257400-67.6T	Bober[21]
		256250-67.24T	Leibowitz[87]

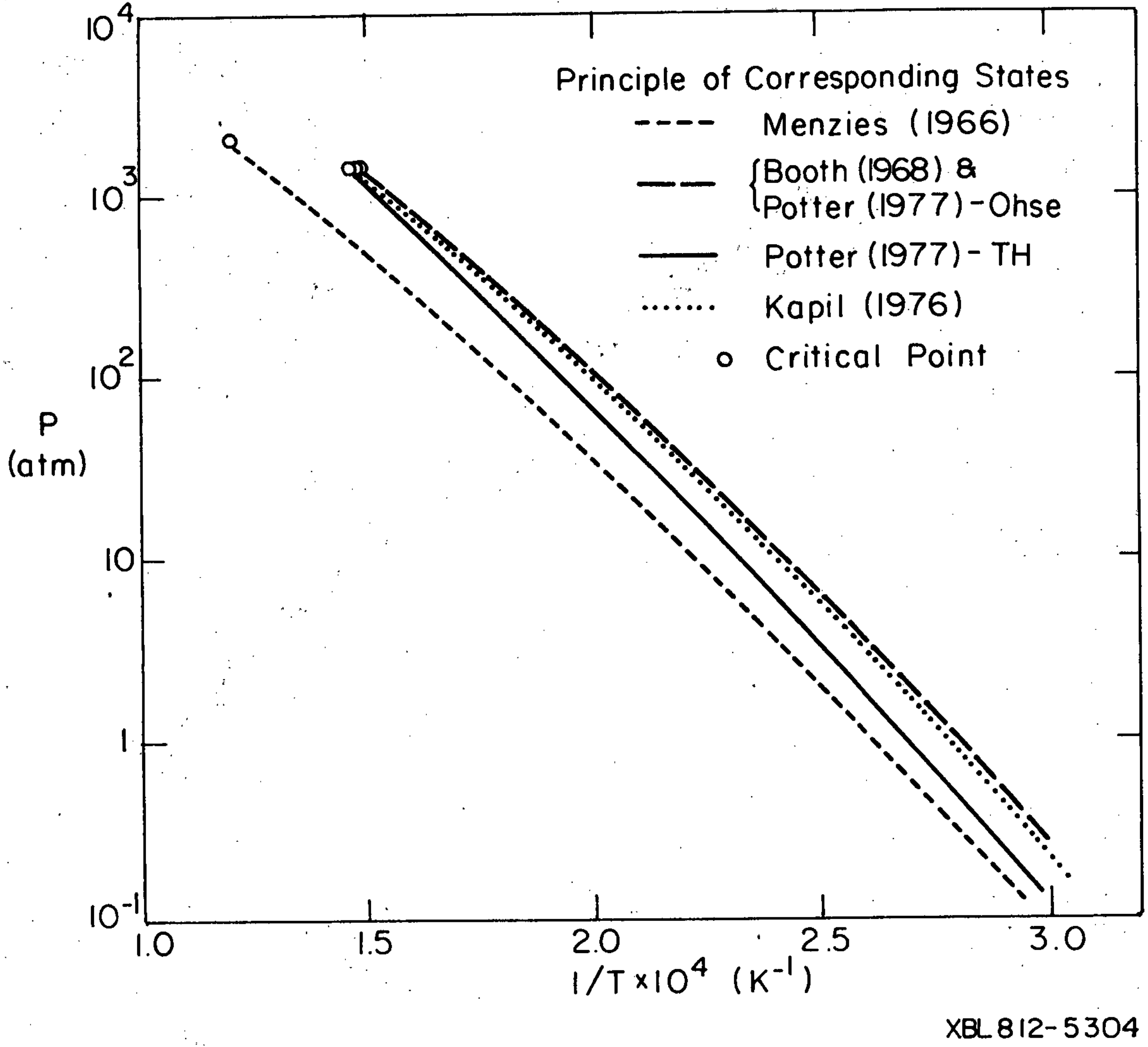

Fig. A.1 Vapor Pressure - Temperature relation based on the Principle of Corresponding States

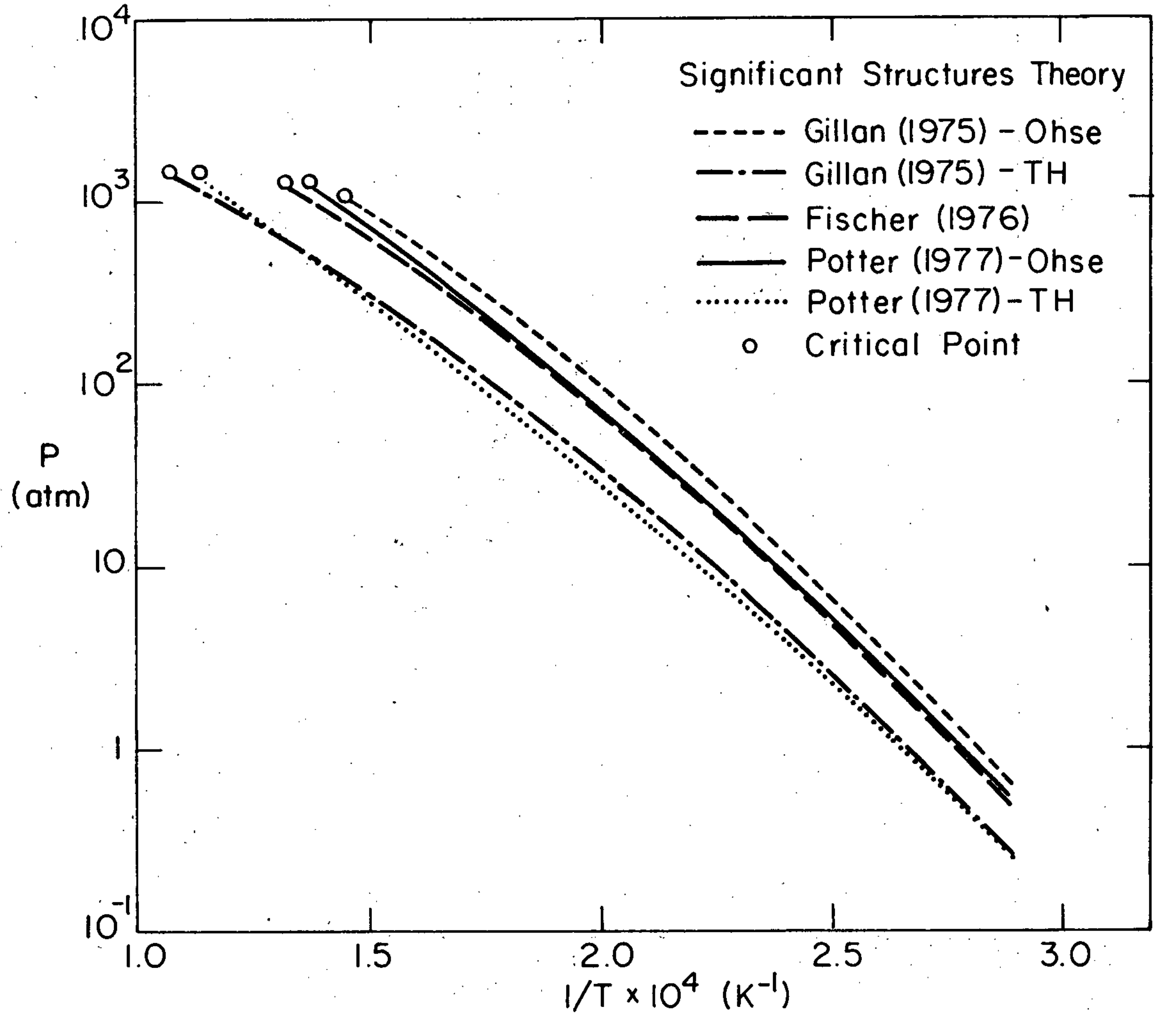

XBL 812-5305

Fig. A.2 Vapor Pressure - Temperature relation based on Significant Structures Theory

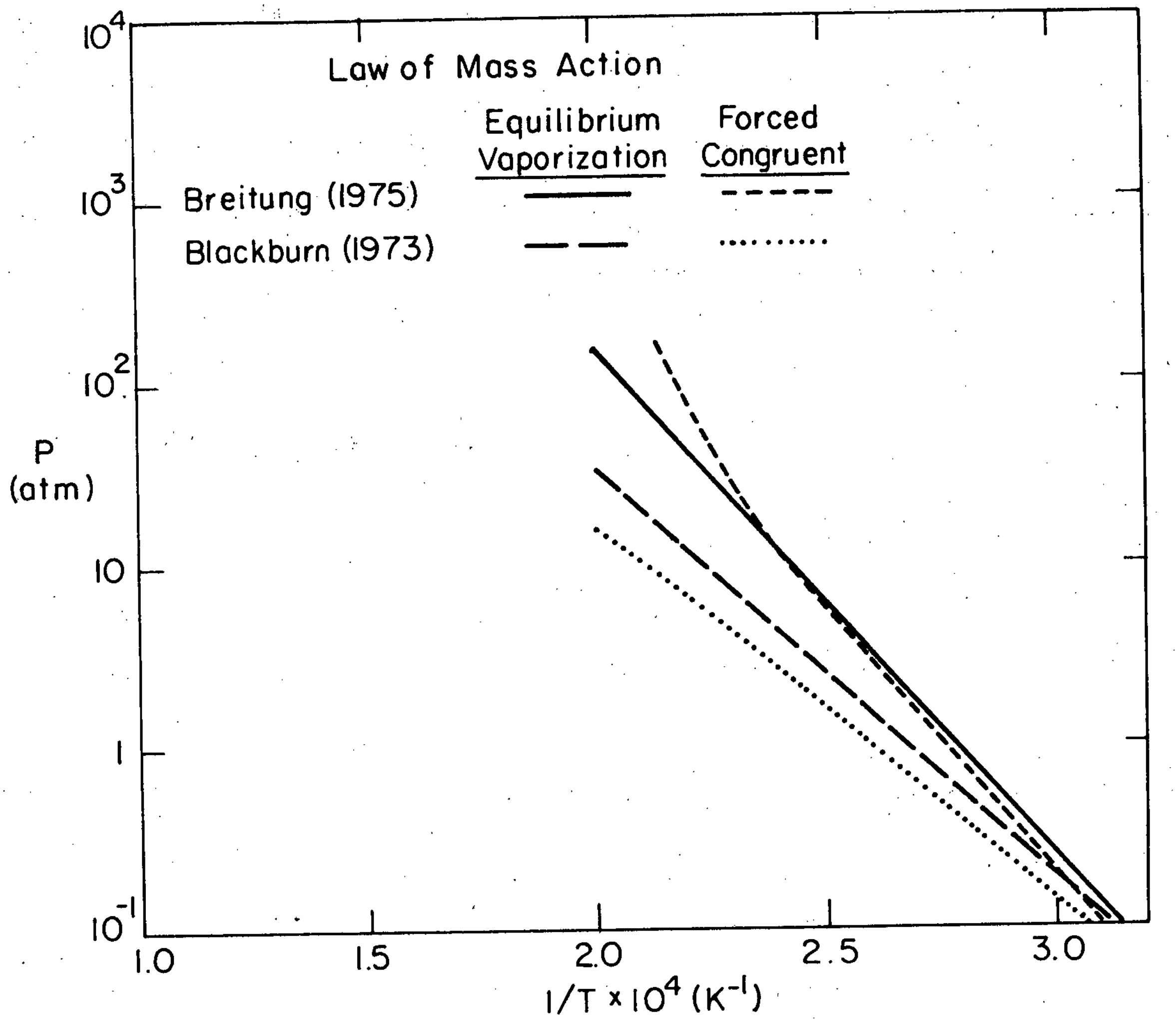

XBL 812-5306

Fig. A.3 Vapor Pressure - Temperature relation based on the Law of Mass Action

APPENDIX B: NUMERICAL SOLUTION METHOD

B.1 Non-dimensionalization of Conservation Equations

Because of the non-linearity of the governing differential equations (2-32) and (2-33) and the boundary condition equations (2-35), (2-36) and (2-37), analytical solution is not possible. Before the numerical methods are applied, Eqs. (2-32) - (2-38) are non-dimensionalized. By introducing appropriate characteristic composition $\tilde{r}$, characteristic temperature $\tilde{T}$, characteristic time $\tilde{t}$ and characteristic length $\tilde{x}$, we can define:

$$Y = \frac{r}{\tilde{r}} \; ; \; \Theta = \frac{T}{\tilde{T}} \; ; \; \tau = \frac{t}{\tilde{t}} \; ; \; \chi = \frac{x}{\tilde{x}} \tag{B-1}$$

In the problem formulated in the beginning of the section, especially for UO_2, the characteristic quantities were taken as:

$$\tilde{r} = r_o \; ; \; \tilde{T} = T_o \; ; \; \tilde{t} = t_{pul} \; ; \; \tilde{x} = (\frac{k}{\rho C_p})_m^{1/2} (t_{pul})^{1/2} \tag{B-2}$$

where r_o = initial oxygen-to-uranium ratio

T_o = initial temperature, K

t_{pul} = effective laser power pulse width = $\int P(t)dt/P_{max} = E/P_{max}$, sec

E = incident laser energy, Joules

P_{max} = maximum laser power, Watts

and "m" means that the properties are evaluated at the melting temperature.

After the introduction of dimensionless quantities and re-arrangement, there results:

$$\begin{aligned} \frac{\partial^2\Theta}{\partial\chi^2} &= A_1\frac{\partial\Theta}{\partial\tau} - A_2\frac{\partial\Theta}{\partial\chi} - A_3(\frac{\partial\Theta}{\partial\chi})^2 - A_4 \\ &= A_1\frac{\partial\Theta}{\partial\tau} + \Psi_T(\tau,\chi,\Theta,\partial\frac{\Theta}{\partial}\chi) \end{aligned} \tag{B-3}$$

$$\begin{aligned} \frac{\partial^2 Y}{\partial\chi^2} &= B_1\frac{\partial Y}{\partial\tau} - B_2\frac{\partial Y}{\partial\chi} - B_3(\frac{\partial Y}{\partial\chi})(\frac{\partial\Theta}{\partial\chi}) \\ &= B_1\frac{\partial Y}{\partial\tau} + \Psi_r(\tau,\chi,\Theta,Y,\partial\frac{\Theta}{\partial}\chi,\partial\frac{Y}{\partial}\chi) \end{aligned} \tag{B-4}$$

$$\text{I.C.: } \Theta(\chi,0) = 1 \text{ and } Y(\chi,0) = 1 \tag{B-5}$$

$$\text{B.C.: } (\frac{\partial\Theta}{\partial\chi})_{\chi=0} = \eta_T \tag{B-6}$$

$$(\frac{\partial Y}{\partial\chi})_{\chi=0} = \eta_r \tag{B-7}$$

$$\Theta(\infty,\tau) = 1 \quad \text{and} \quad Y(\infty,\tau) = 1 \tag{B-8}$$

where

$$A_1 = \left(\frac{k}{\rho C_p}\right)_m / \left(\frac{k}{\rho C_p}\right) \tag{B-9}$$

$$A_2 = v\sqrt{t_{pul}}\left(\frac{k}{\rho C_p}\right)_m^{\frac{1}{2}} / \left(\frac{k}{\rho C_p}\right) \tag{B-10}$$

$$A_3 = \frac{T_o}{k}\,\frac{dk}{dT} \tag{B-11}$$

$$A_4 = \left(\frac{k}{\rho C_p}\right)_m \frac{t_{pul}}{kT_o} Q_v \tag{B-12}$$

$$B_1 = \left(\frac{k}{\rho C_p}\right)_m / D_o \tag{B-13}$$

$$B_2 = v\sqrt{t_{pul}}\left(\frac{k}{\rho C_p}\right)_m^{\frac{1}{2}} / D_o \tag{B-14}$$

$$B_3 = \frac{T_o}{D_o}\,\frac{dD_o}{dT} \tag{B-15}$$

η_T = dimensionless surface temperature gradient

$$= \frac{\sqrt{t_{pul}}\left(\frac{k}{\rho C_p}\right)_m^{\frac{1}{2}}}{k_s} T_o[j_{tot}\Delta H_{vap} + \epsilon_t\sigma(T_s^4 - T_b^4) - (1-R)q_p(t)] \tag{B-16}$$

and eta$_r$ = dimensionless surface composition gradient

$$= \frac{-\sqrt{t_{pul}}\left(\frac{k}{\rho C_p}\right)_m^{\frac{1}{2}}}{D_o^s r_o}\left[\frac{j_o^g}{C_U} + vr_s\right] \tag{B-17}$$

B.2 Crank-Nicolson Finite Difference Approximation

The Crank-Nicolson finite difference method is an implicit technique in which truncated Taylor series expansions are used to approximate the derivatives in the governing differential equations. The space and time derivatives are then replaced by second order correct finite difference representations.

Let $W_{i,n}$ and $U_{i,n}$ denote the approximate solutions of the dimensionless temperature Θ and the dimensionless oxygen-to-uranium ratio Y at space (dimensionless) grid χ_i (called "grid" hereafter) and time (dimensionless) step τ_n (called "step" hereafter) respectively. The Crank-Nicolson method assumes that *[40]*:

$$\frac{\partial^2 W_{i,n+\frac{1}{2}}}{\partial \chi^2} = \frac{1}{2}\left(\frac{\partial^2 W_{i,n+1}}{\partial \chi^2} + \frac{\partial^2 W_{i,n}}{\partial \chi^2}\right) + O((\Delta\tau)^2)$$

$$= \frac{1}{2}\Delta_\chi^2(W_{i,n+1}+W_{i,n}) + O((\Delta\chi)^2+(\Delta\tau)^2) \tag{B-18}$$

$$\begin{aligned}\frac{\partial^2 U_{i,n+\frac{1}{2}}}{\partial\chi^2} &= \frac{1}{2}\left(\frac{\partial^2 U_{i,n+1}}{\partial\chi^2}+\frac{\partial^2 U_{i,n}}{\partial\chi^2}\right) + O((\Delta\tau)^2)\\ &= \frac{1}{2}\Delta_\chi^2(U_{i,n+1}+U_{i,n}) + O((\Delta\chi)^2+(\Delta\tau)^2)\end{aligned} \tag{B-19}$$

$$\frac{\partial W_{i,n+\frac{1}{2}}}{\partial\tau} = \frac{W_{i,n+1}-W_{i,n}}{\Delta\tau} + O((\Delta\tau)^2) \tag{B-20}$$

$$\frac{\partial U_{i,n+\frac{1}{2}}}{\partial\tau} = \frac{U_{i,n+1}-U_{i,n}}{\Delta\tau} + O((\Delta\tau)^2) \tag{B-21}$$

$$\frac{\partial W_{i,n+\frac{1}{2}}}{\partial\chi} = \frac{1}{2}\Delta_\chi(W_{i,n+1}+W_{i,n}) + O((\Delta\chi)^2) \tag{B-22}$$

$$\frac{\partial U_{i,n+\frac{1}{2}}}{\partial\chi} = \frac{1}{2}\Delta_\chi(U_{i,n+1}+U_{i,n}) + O((\Delta\chi)^2) \tag{B-23}$$

where $\Delta_\chi^2 W_{i,n}$ = second order correct centered second difference of $W_{i,n}$

$\Delta_\chi^2 U_{i,n}$ = second order correct centered second difference of $U_{i,n}$

$\Delta_\chi W_{i,n}$ = second order correct centered first difference of $W_{i,n}$

$\Delta_\chi U_{i,n}$ = second order correct centered first difference of $U_{i,n}$

By utilizing these finite difference operators, the differential equations (B-3) and (B-4) can be approximated by the following difference equations: (for $i \geqslant 2$)

$$\begin{aligned}\frac{1}{2}\Delta_\chi^2(W_{i,n+1}+W_{i,n}) &= A_1\frac{W_{i,n+1}-W_{i,n}}{\Delta\tau}\\ &\quad -A_2[\frac{1}{2}\Delta_\chi(W_{i,n+1}+W_{i,n})]-A_3[\frac{1}{2}\Delta_\chi(W_{i,n+1}+W_{i,n})]^2-A_4\end{aligned} \tag{B-24}$$

$$\begin{aligned}\frac{1}{2}\Delta_\chi^2(U_{i,n+1}+U_{i,n}) &= B_1\frac{U_{i,n+1}-U_{i,n}}{\Delta\tau}-B_2[\frac{1}{2}\Delta_\chi(U_{i,n+1}+U_{i,n})]\\ &\quad -B_3[\frac{1}{2}\Delta_\chi(W_{i,n+1}+W_{i,n})]\ [\frac{1}{2}\Delta_\chi(U_{i,n+1}+U_{i,n})]\end{aligned} \tag{B-25}$$

where the coefficients $A_1, A_2, A_3, A_4, B_1, B_2$ and B_3 are, in general, functions of $[\chi_i, \tau_{n+\frac{1}{2}}, \frac{1}{2}(W_{i,n+1}+W_{i,n})]$ and $\tau_{n+\frac{1}{2}} = \frac{1}{2}(\tau_{n+1}+\tau_n)$.

B.3 Second Order Correct Centered Finite Difference Operators

There are several ways of expressing the finite difference operators Δ_{chi}, Δ_χ^{2}, $\cdots$ of different degree of order of accuracy, depending on the truncated error from the Taylor series expansion. In this section, the second order correct centered finite difference operators are discussed.

For the case of constant increment in χ, denoted by ξ, the Taylor series expansion of F_{i+1} around F_i is:

$$F_{i+1} = F_i + \xi \dot{F}_i + \frac{\xi^2}{2} \ddot{F}_i + O(\xi^3) \tag{B-26}$$

The Taylor series expansion of F_{i-1} around F_i is:

$$F_{i-1} = F_i - \xi \dot{F}_i + \frac{\xi^2}{2} \ddot{F}_i + O(\xi^3) \tag{B-27}$$

Let us approximate the first derivative $\dot{F}_i$ by the finite difference operator $\Delta_\chi F_i$. Then $\Delta_\chi F_i$ can be solved from the equations:

$$F_{i+1} = F_i + \xi (\Delta_\chi F_i) + \frac{\xi^2}{2} \ddot{F}_i \tag{B-28}$$

$$F_{i-1} = F_i - \xi (\Delta_\chi F_i) + \frac{\xi^2}{2} \ddot{F}_i \tag{B-29}$$

These two equations yields:

$$\Delta_\chi F_i = \frac{F_{i+1} - F_{i-1}}{2\xi} \tag{B-30}$$

which is correct to order of $\xi^3/\xi = \xi^2$.

Similarly, the second dfference operator $\Delta_\chi^2 F_i$ can be solved from the two equations:

$$F_{i+1} = F_i + \xi \dot{F}_i + \frac{\xi^2}{2} (\Delta_\chi^2 F_i) + \frac{\xi^3}{6} \dddot{F}_i \tag{B-31}$$

$$F_{i-1} = F_i - \xi \dot{F}_i + \frac{\xi^2}{2} (\Delta_\chi^2 F_i) - \frac{\xi^3}{6} \dddot{F}_i \tag{B-32}$$

which yields:

$$\Delta_\chi^2 F_i = \frac{F_{i+1} - 2F_i + F_{i-1}}{\xi^2} \tag{B-33}$$

which is correct to order of $\xi^4/\xi^2 = \xi^2$.

Rather than using a constant ξ (as is usually the case), in this program ξ increases geometrically into the bulk of the solid according to the relation:

$$\xi_i = \epsilon \xi_{i-1} = \epsilon^{i-1} \xi_1 \tag{B-34}$$

where ϵ = a constant, taken to be 1.035

ξ_i = grid increment following ith grid plane

ξ_1 = the first grid increment at the surface

The second order correct differences are considerably more complicated; however, the method of deriving the finite difference operators from the truncated Taylor series expansions is exactly the same.

From the following third-order truncated expansions:

$$F_{i+1} = F_i + \xi_1\epsilon^{i-1}(\Delta_x F_i) + \frac{(xi_1\epsilon^{i-1})^2}{2}\ddot{F}_i \tag{B-35}$$

$$F_{i-1} = F_i - \xi_1\epsilon^{i-2}(\Delta_x F_i) + \frac{(xi_1\epsilon^{i-2})^2}{2}\ddot{F}_i \tag{B-36}$$

Solving for $(\Delta_x F_i)$, we have:

$$\Delta_x F_i = \frac{1}{\xi_1\epsilon^{i-1}}[\frac{-\epsilon^2}{1+\epsilon}F_{i-1}+(\epsilon-1)F_i+\frac{1}{1+\epsilon}F_{i+1}] \tag{B-37}$$

which is correct to second order.

From the following fourth order truncated expansions:

$$F_{i+2} = F_i+(\epsilon+1)\xi_i\dot{F}_i+\frac{\xi_i^2(1+\epsilon)^2}{2}(\Delta_x^2F_i)+\frac{\xi_i^3(1+\epsilon)^3}{6}\dddot{F}_i \tag{B-38}$$

$$F_{i+1} = F_i+\xi_i\dot{F}_i+\frac{\xi_i^2}{2}(\Delta_x^2F_i)+\frac{\xi_i^3}{6}\dddot{F}_i \tag{B-39}$$

$$F_{i-1} = F_i-\frac{\xi_i}{\epsilon}\dot{F}_i+\frac{\xi_i^2}{2\epsilon^2}(\Delta_x^2F_i)-\frac{\xi_i^3}{6\epsilon^3}\dddot{F}_i \tag{B-40}$$

where $\xi_i = \epsilon^{i-1}\xi_1$.

Solving for $(\Delta_x^2F_i)$, we have:

$$\Delta_x^2F_i = \frac{2}{(xi_1\epsilon^{i-1})^2}[\frac{\epsilon^3(2+\epsilon)}{(1+\epsilon+\epsilon^2)(1+\epsilon)}F_{i-1}-\frac{\epsilon^2+2\epsilon-1}{1+\epsilon}F_i + \frac{\epsilon^2+\epsilon-1}{\epsilon(1+\epsilon)}F_{i+1}-\frac{\epsilon-1}{\epsilon(1+\epsilon)(1+\epsilon+\epsilon^2)}F_{i+2}] \tag{B-41}$$

Applying these formulae to the variables W and U yields:

$$\Delta_x W_{i,n} = \frac{1}{\xi_1\epsilon^{i-1}}[\frac{-\epsilon^2}{1+\epsilon}W_{i-1,n}+(\epsilon-1)W_{i,n}+\frac{1}{1+\epsilon}W_{i+1,n}] \tag{B-42}$$

$$\Delta_x^2W_{i,n} = \frac{2}{(\xi_1\epsilon^{i-1})^2}[\frac{\epsilon^3(2+\epsilon)}{(1+\epsilon+\epsilon^2)(1+\epsilon)}W_{i-1,n}-\frac{\epsilon^2+2\epsilon-1}{1+\epsilon}W_{i,n} + \frac{\epsilon^2+\epsilon-1}{\epsilon(1+\epsilon)}W_{i+1,n}-\frac{\epsilon-1}{\epsilon(1+\epsilon)(1+\epsilon+\epsilon^2)}W_{i+2,n}] \tag{B-43}$$

$$\Delta_\chi U_{i,n} = \frac{1}{\xi_1 \epsilon^{i-1}}[\frac{-\epsilon^2}{1+\epsilon}U_{i-1,n}+(\epsilon-1)U_{i,n}+\frac{1}{1+\epsilon}U_{i+1,n}] \tag{B-44}$$

$$\Delta_\chi^2 U_{i,n} = \frac{2}{(\xi_1 \epsilon^{i-1})^2}[\frac{\epsilon^3(2+\epsilon)}{(1+\epsilon+\epsilon^2)(1+\epsilon)}U_{i-1,n}-\frac{\epsilon^2+2\epsilon-1}{1+\epsilon}U_{i,n}$$

$$+\frac{\epsilon^2+\epsilon-1}{\epsilon(1+\epsilon)}U_{i+1,n}-\frac{\epsilon-1}{\epsilon(1+\epsilon)(1+\epsilon+\epsilon^2)}U_{i+2,n}] \tag{B-45}$$

B.4 Initial and Boundary Conditions

In the notation of the approximate solutions, the finite difference approximation to the initial conditions (B-5) are:

$$W_{i,1}=1 \text{ and } U_{i,1}=1 \text{ for all } \chi_i \text{ at } \tau_1(=0) \tag{B-46}$$

The finite difference approximation to the boundary conditions (B-6) - (B-8) are: (for i=1)

$$W'_{1,n+1} = \eta_T(tau_{n+1}, W_{1,n+1}, U_{1,n+1}) \tag{B-47}$$

$$U'_{1,n+1} = \eta_r(tau_{n+1}, W_{1,n+1}, U_{1,n+1}) \tag{B-48}$$

where $W'_{1,n+1}$ = second order correct forward first differrence of $W_{1,n+1}$

$U'_{1,n+1}$ = second order correct forward first difference of $U_{1,n+1}$

(The boundary conditions do not have to be evluated at $\tau_{n+\frac{1}{2}}$ as do the governing equations, because time derivatives are involved in the latter but not in the former.)

For the case of constant ξ, the second order correct forward difference can be solved from the two truncated equations:

$$F_{i+2} = F_i+2\xi F'_i+\frac{(2\xi)^2}{2}\ddot{F}_i \tag{B-49}$$

$$F_{i+1} = F_i+\xi F'_i+\frac{\xi^2}{2}\ddot{F}_i \tag{B-50}$$

here F'_i denotes the second order correct forward first difference instead of exact first derivative.

Eliminating $\xi^2\ddot{F}_i$ from the above equations, we have:

$$F'_i = \frac{1}{2\xi}(-3F_i+4F_{i+1}-F_{i+2}) \tag{B-51}$$

Similarly, for the case of varying ξ according to Eq. (B-34), the second order forward first difference can be solved from the two truncated equations:

$$F_{i+2} = F_i+(\xi_i+\xi_{i+1})F'_i+\frac{(\xi_i+\xi_{i+1})^2}{2}\ddot{F}_i \tag{B-52}$$

$$F_{i+1} = F_i+\xi_i F'_i+\frac{\xi_i^2}{2}\ddot{F}_i \tag{B-53}$$

where $\xi_i = \epsilon^{i-1}\xi_1$.

The solution is:

$$F'_i = \frac{1}{\xi_i}[-\frac{\epsilon+2}{\epsilon+1}F_i+\frac{\epsilon+1}{\epsilon}F_{i+1}-\frac{1}{\epsilon(\epsilon+1)}F_{i+2}] \tag{B-54}$$

For i=1:

$$F'_1 = \frac{1}{\xi_1}[-\frac{\epsilon+2}{\epsilon+1}F_1+\frac{\epsilon+1}{\epsilon}F_2-\frac{1}{\epsilon(\epsilon+1)}F_3] \tag{B-55}$$

Applying these results to the variables W and U yields:

$$W'_{1,n+1} = \frac{1}{\xi_1}[\frac{-(2+\epsilon)}{1+\epsilon}W_{1,n+1}+\frac{1+\epsilon}{\epsilon}W_{2,n+1}-\frac{1}{\epsilon(1+\epsilon)}W_{3,n+1}] \tag{B-56}$$

$$U'_{1,n+1} = \frac{1}{\xi_1}[\frac{-(2+\epsilon)}{1+\epsilon}U_{1,n+1}+\frac{1+\epsilon}{\epsilon}U_{2,n+1}-\frac{1}{\epsilon(1+\epsilon)}U_{3,n+1}] \tag{B-57}$$

B.5 Solutions of Finite Difference Equations

The step-by-step method is used to take care of the time (dimensionless) variation. At each step, Eqs. (B-24), (B-25), (B-47) and (B-48) comprise a set of nonlinear equations that are to be solved for $W_{i,n+1}$ and $U_{i,n+1}$ for all i. Only an iterative technique can be used to solve a set of nonlinear equations. The Newton-Raphson's method adopted in this study to carry out the iterations was found to be quite powerful and converges well. Adoption of the predictor-corrector scheme for finding good starting values for the iterations also helps to retain both efficency and convergency of the program with reasonable time steps.

B.5.1 Predictor-corrector Method

The idea of the predictor-corrector method is as follows. Instead of using the results from previous step as the first guess to start the iteration, the approximate solution at half of the time step is solved by the simpler linear equations (called "predictor") which needs only the informations at previous step. Then the "corrector" is used to obtain an approximate solution for the current step as the first guess for the following iteration involving more complicated nonlinear equations.

If the difference equation has the form:

$$\frac{1}{2}\Delta_\chi^2(F_{i,n+1}+F_{i,n}) - A_1\frac{F_{i,n+1}-F_{i,n}}{\Delta\tau} = \Psi_f[\chi_i,\tau_{n+\frac{1}{2}},\frac{1}{2}(F_{i,n+1}+F_{i,n}),\frac{1}{2}\Delta_\chi(F_{i,n+1}+F_{i,n})] \tag{B-58}$$

then the predictor is:*[41]*

$$\frac{1}{2}\Delta_\chi^2(F_{i,n+\frac{1}{2}}+F_{i,n}) - A_1\frac{F_{i,n+\frac{1}{2}}-F_{i,n}}{\Delta\tau} = \Psi_f(\chi_i,\tau_{n+\frac{1}{2}},F_{i,n},\Delta_\chi F_{i,n}) \tag{B-59}$$

which becomes a linear algebraic problem, because unknowns only appear in the left hand side in linear form.

After solving for $F_{i,n+\frac{1}{2}}$ from Eq. (B-59), the following equation for the corrector is solved:*[41]*

$$\frac{1}{2}\Delta_\chi^2(F_{i,n+1}+F_{i,n}) - A_1\frac{F_{i,n+1}-F_{i,n}}{\Delta\tau} = \Psi_f(\chi_i,\tau_{n+\frac{1}{2}},F_{i,n+\frac{1}{2}},\Delta_\chi F_{i,n+\frac{1}{2}}) \tag{B-60}$$

which is also a linear problem. The solution for the corrector, denoted by $F_{i,n+1}^{(o)}$, is then used as the first guess for the iteration:

$$\frac{1}{2}\Delta_\chi^2(F_{i,n+1}^{(k)}+F_{i,n}) - A_1\frac{F_{i,n+1}^{(k)}-F_{i,n}}{\Delta\tau} = \Psi_f[\chi_i,\tau_{n+\frac{1}{2}},\frac{1}{2}(F_{i,n+1}^{(k-1)}+F_{i,n}),\frac{1}{2}\Delta_\chi(F_{i,n+1}^{(k-1)}+F_{i,n})] \tag{B-61}$$

where $k=1,2,\ldots,$ with repeated iteration, if necessary, to obtain the final solution.

B.5.2 Iteration Procedure by Newton-Raphson's Method

Let us multiply Eqs. (B-6) & (B-7) by ξ_1 and rewrite them in the form:

$$f_1(\vec{W}_{n+1}) = [W'_{1,n+1}-\eta_T(\tau_{n+1},W_{1,n+1})]\xi_1 = 0 \tag{B-62}$$

$$g_1(\vec{U}_{n+1}) = [U'_{1,n+1}-\eta_r(\tau_{n+1},U_{1,n+1})]\xi_1 = 0 \tag{B-63}$$

Let us also multiply Eqs. (B-3) & (B-4) by $2\xi_1^2$ and rewrite them in the form:

$$f_i(\vec{W}_{n+1}) = \{\Delta_\chi^2(W_{i,n+1}+W_{i,n})-2A_1\frac{W_{i,n+1}-W_{i,n}}{\Delta\tau_n}$$

$$+A_2[\Delta_\chi(W_{i,n+1}+W_{i,n})]+\frac{A_3}{2}[\Delta_\chi(W_{i,n+1}+W_{i,n})]^2+2A_4\}\xi_1^2 = 0 \tag{B-64}$$

$$g_i(\vec{U}_{n+1}) = \{\Delta_\chi^2(U_{i,n+1}+U_{i,n})-2B_1\frac{U_{i,n+1}-U_{i,n}}{\Delta\tau_n}+B_2[\Delta_\chi(U_{i,n+1}+U_{i,n})]$$

$$+\frac{B_3}{2}[\Delta_\chi(W_{i,n+1}+W_{i,n})]\ [\Delta_\chi(U_{i,n+1}+U_{i,n})]\}\xi_1^2 = 0 \tag{B-65}$$

where $\vec{W}_{n+1}$ is the vector $[W_{1,n+1},W_{2,n+1},\ldots,W_{m,n+1}]$,

$\vec{U}_{n+1}$ is the vector $[U_{1,n+1},U_{2,n+1},\ldots,U_{m,n+1}]$,

and m is the number of grid beyond which the profiles are essentially constant.

Therefore, we have a set of 2m nonlinear equations to be solved for $\vec{W}_{n+1}$ and $\vec{U}_{n+1}$.

$$\left\{\begin{array}{l} f_1(\vec{W}_{n+1}) = 0 \\ f_2(\vec{W}_{n+1}) = 0 \\ \cdot \\ \cdot \\ \cdot \\ f_m(\vec{W}_{n+1}) = 0 \\ g_1(\vec{U}_{n+1}) = 0 \\ g_2(\vec{U}_{n+1}) = 0 \\ \cdot \\ \cdot \\ \cdot \\ g_m(\vec{U}_{n+1}) = 0 \end{array}\right. \tag{B-66}$$

To do so, we have to start with an initial guesses $\vec{W}_{n+1}^{(o)}$ and $\vec{U}_{n+1}^{(o)}$, from predictor-corrector scheme described in the last section, and then find the successive approximate solutions following the procedure:

(i) For the first iteration of W, $W_{i,n+1}$ and $U_{i,n+1}$ in the coefficient terms of Eqs. (B-62) - (B-65) are approximated by $W_{i,n+1}^{(o)}$ and $U_{i,n+1}^{(o)}$ and the following linear equation is solved:*[42]*

$$\vec{\vec{J}}(\vec{W}_{n+1}^{(o)},\vec{h})\,(\vec{W}_{n+1}^{(1)}-\vec{W}_{n+1}^{(o)}) + \vec{F}(\vec{W}_{n+1}^{(o)}) = 0 \tag{B-67}$$

where $\vec{\vec{J}}$ is an m × m matrix with elements $\Delta_{ij}=(\frac{\partial f_i}{\partial W_{j,n+1}})_{\vec{W}_{n+1}^{(o)}}$ if the derivative can be obtained analytically; otherwise, the derivative is approximated by Steffenson's method*[42]*, $\Delta_{ij} = \frac{f_i(\vec{W}_{n+1}^{(o)}+h_j\vec{e}_j)-f_i(\vec{W}_{n+1}^{(o)})}{h_j}$

$h_j = f_j(\vec{W}_{n+1}^{(o)})$

$\vec{h} = [h_1, h_2, \ldots, h_m]$

and $\vec{F}(\vec{W}^{(o)}_{n+1}) = [f_1(\vec{W}^{(o)}_{n+1}), f_2(\vec{W}^{(o)}_{n+1}), \ldots, f_m(\vec{W}^{(o)}_{n+1})]$

The equation is then solved for $\vec{W}^{(1)}_{n+1}$ by the Gaussian elimination method.

(ii) For the first iteration of U, every $W_{i,n+1}$ is approximated by $W^{(1)}_{i,n+1}$ and $U_{i,n+1}$ in B_1, B_2, B_3 and η_r is approximated by $U^{(o)}_{i,n+1}$, and the following linear equation is solved:

$$\vec{\vec{L}}(\vec{U}^{(o)}_{n+1}, \vec{q})(\vec{U}^{(1)}_{n+1} - \vec{U}^{(o)}_{n+1}) + \vec{G}(\vec{U}^{(o)}_{n+1}) = 0 \tag{B-68}$$

where $\vec{\vec{L}}$ is an m × m matrix with elements $\Omega_{ij} = \left(\frac{\partial g_i}{\partial U_{j,n+1}}\right)_{U^{(o)}_{n+1}}$ if the derivative can be obtained analytically; otherwise, the derivative is approximated by Steffenson's method,

$$\Omega_{ij} = \frac{g_i(\vec{U}^{(o)}_{n+1} + q_j \vec{e}_j) - g_i(\vec{U}^{(o)}_{n+1})}{q_j}$$

$q_j = g_j(\vec{U}^{(o)}_{n+1})$

$\vec{q} = [q_1, q_2, \ldots, q_m]$

and $\vec{G}(\vec{U}^{(o)}_{n+1}) = [g_1(\vec{U}^{(o)}_{n+1}), g_2(\vec{U}^{(o)}_{n+1}), \ldots, g_m(\vec{U}^{(o)}_{n+1})]$

The equation is again solved for $\vec{U}^{(1)}_{n+1}$ by the Gaussian elimination method.

(iii) The approximate solutions $W^{(1)}_{i,n+1}$ and $U^{(1)}_{i,n+1}$ from the first iteration are then used to calculate solutions for the second iteration.

(iv) The process is repeated until the successive iterations are sufficiently close to each other; then the calculations go on to the next step after determination of the next step size.

B.5.3 Gaussian Elimination Method

The predictor-corrector method and Newton-Raphson's method are linearization process as which deals with a nonlinear problem. After linearization, the Gaussian elimination back-substitution is found to be a very easy and efficient way to solve the system of linear equations.

To solve Eqs. (B-59), (B-60) in section B.5.1 and (B-67), (B-68) in section B.5.2, we must deal with a set of equations with the following format:

$$
\begin{aligned}
&b_1\delta_1+c_1\delta_2+d_1\delta_3 &&= e_1\\
&a_2\delta_1+b_2\delta_2+c_2\delta_3+d_2\delta_4 &&= e_2\\
&\qquad a_3\delta_2+b_3\delta_3+c_3\delta_4+d_3\delta_5 &&= e_3\\
&\qquad \cdots\cdots\cdots\cdots &&\\
&\qquad\qquad a_i\delta_{i-1}+b_i\delta_i+c_i\delta_{i+1}+d_i\delta_{i+2} &&= e_i\\
&\qquad\qquad \cdots\cdots\cdots\cdots\cdots\cdots &&\\
&\qquad\qquad\qquad a_{m-1}\delta_{m-2}+b'_{m-1}\delta_{m-1}+c'_{m-1}\delta_m &&= e_{m-1}\\
&\qquad\qquad\qquad\qquad a'_m\delta_{m-1}+b'_m\delta_m &&= e_m
\end{aligned}
\qquad \text{(B-69)}
$$

where δ_i denotes either the variables $W_{i,n+\frac{1}{2}}$, $U_{i,n+\frac{1}{2}}$ in (B-59), $W_{i,n+1}$, $U_{i,n+1}$ in (B-60) or $(\vec{W}^{(k)}_{n+1}-\vec{W}^{(k-1)}_{n+1})$ in (B-67), $(\vec{U}^{(k)}_{n+1}-\vec{U}^{(k-1)}_{n+1})$ in (B-68), a_i, b_i, c_i, d_i denote either the coefficients in (B-59), (B-60) with Eqs. (B-42) - (B-45), and (B-56), (B-57), or the elements of Jacobin matrixes $\vec{\vec{J}}$, $\vec{\vec{L}}$ in (B-67), (B-68), and e_i denotes the known quantities from either the previous step in Eqs. (B-59) and (B-60) or the previous iteration in Eqs. (B-67) and (B-68).

The primes in b'_{m-1}, c'_{m-1}, a'_m and b'_m are introduced because we have approximated δ_{m+1} and δ_{m+2} by a linear extrapolation of δ_{m-1} and δ_m in order to reduce the number of unknowns to m,

$$
\begin{cases}
b'_{m-1} = b_{m-1} - d_{m-1}\epsilon\\
c'_{m-1} = c_{m-1} + d_{m-1}(1+\epsilon)\\
a'_m = a_m - c_m\epsilon - d_m\epsilon(1+\epsilon)\\
b'_m = b_m + c_m(1+\epsilon) + d_m(1+\epsilon+\epsilon^2)
\end{cases}
\qquad \text{(B-70)}
$$

The system of equations (B-69) can be cast in the matrix form:

$$\vec{\vec{\mathbf{M}}}\vec{\mathbf{\Delta}} = \vec{\mathbf{E}} \qquad \text{(B-71)}$$

where $\vec{\mathbf{\Delta}}$ is the column vector $\delta_1, \delta_2, \ldots, \delta_m$

$\vec{\mathbf{E}}$ is the column vector $e_1, e_2, \ldots, e_m$

and $\vec{\vec{\mathbf{M}}}$ is an m × m quad-diagonal matrix since all elements are zero except those on the principal diagonal, one below and one and two above the principal diagonal.

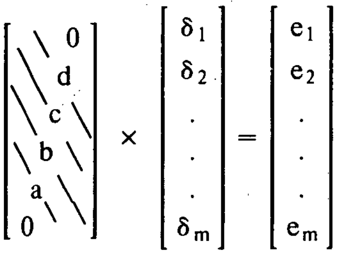

(B-72)

The idea behind the Gaussian elimination method is to remove the unknowns in a systematic way; the first equation can be used to eliminate δ_1 from the second equation, the new second equation used to eliminate δ_2 from the third equation, and so on, until finally, the new next-to-last equation can be used to eliminate δ_{m-1} from the last equation, giving one equation with one unknown δ_m. The unknowns δ_i can then be found in turn by back-substitution.*[42]*

Generally, after i-2 eliminations ($i \geqslant 2$), we obtain the following two equations for the next elimination:

$$\begin{cases} \alpha_{i-1}\delta_{i-1} + \beta_{i-1}\delta_i + d_{i-1}\delta_{i+1} = S_{i-1} \\ a_i\delta_{i-1} + b_i\delta_i + c_i\delta_{i+1} + d_i\delta_{i+2} = e_i \end{cases} \tag{B-73}$$

where $\alpha_1 = b_1$, $\beta_1 = c_1$, $S_1 = e_1$.

Eliminating δ_{i-1} leads to:

$$\begin{aligned} (b_i - \frac{a_i\beta_{i-1}}{\alpha_{i-1}})\delta_i + (c_i - \frac{a_i d_{i-1}}{\alpha_{i-1}})\delta_{i+1} + d_i\delta_{i+2} \\ = e_i - \frac{a_i S_{i-1}}{\alpha_{i-1}} \end{aligned} \tag{B-74}$$

i.e. $\alpha_i\delta_i + \beta_i\delta_{i+1} + d_i\delta_{i+2} = S_i$ (B-75)

with the recursion relations:

$$\begin{cases} \alpha_i = b_i - \dfrac{a_i\beta_{i-1}}{\alpha_{i-1}} \\ \beta_i = c_i - \dfrac{a_i d_{i-1}}{\alpha_{i-1}} \qquad \text{when} 1 \leqslant i \leqslant m-2 \\ S_i = e_i - \dfrac{a_i S_{i-1}}{\alpha_{i-1}} \end{cases} \tag{B-76}$$

After m-3 eliminations, the last three equations are:

$$\begin{cases} \alpha_{m-2}\delta_{m-2} + \beta_{m-2}\delta_{m-1} + d_{m-2}\delta_m = S_{m-2} \\ a_{m-1}\delta_{m-2} + b'_{m-1}\delta_{m-1} + c'_{m-1}\delta_m = e_{m-1} \\ a'_m\delta_{m-1} + b'_m\delta_m = e_m \end{cases} \tag{B-77}$$

Eliminating δ_{m-2} from the first two equations yields:

$$\begin{cases} \alpha'_{m-1}\delta_{m-1} + \beta'_{m-1}\delta_m = S_{m-1} \\ a'_m\delta_{m-1} + b'_m\delta_m = e_m \end{cases} \tag{B-78}$$

where $\alpha'_{m-1} = b'_{m-1} - \dfrac{a_{m-1}\beta_{m-2}}{\alpha_{m-2}}$

$$\beta'_{m-1} = c_{m-1} - \frac{a_{m-1}d_{m-2}}{\alpha_{m-2}}$$

$$S_{m-1} = e_{m-1} - \frac{a_{m-1}S_{m-2}}{\alpha_{m-2}}$$

Eliminating δ_{m-1} from (B-78) yields:

$$\alpha'_m\delta_m = S'_m \tag{B-79}$$

$$\text{where}\quad \alpha'_m = b'_m - \frac{a'_m\beta'_{m-1}}{\alpha'_{m-1}}$$

$$S'_m = e_m - \frac{a'_m S_{m-1}}{\alpha'_{m-1}}$$

Therefore, the solutions are:

$$\begin{cases} \delta_m = \dfrac{S'_m}{\alpha'_m} \\ \delta_{m-1} = \dfrac{S_{m-1} - \beta'_{m-1}\delta_m}{\alpha'_{m-1}} \\ \cdot \\ \cdot \\ \cdot \\ \delta_i = \dfrac{1}{\alpha_i}(S_i - \beta_i\delta_{i+1} - d_i\delta_{i+2}) \quad 1 \leqslant i \leqslant m-1 \end{cases} \tag{B-80}$$

B.6 Determination of the Time Increment

The step-by-step techniques as described above can be applied to either one-step methods or multi-step methods, depending upon whether the informations from previous steps is used in formulating the next step. The multi-step methods are more efficient in the sense that they generally require fewer evaluations of the difference operators to achieve a given acccuracy. The greater efficiency of the multi-step methods is obtained at the cost of introducing special provisions for changing the step size. Considering the fact that the general shape of the solutions can be closely estimated and powerful iteration method are used, the multi-step method is used, the step size is determined as follows:

Define the ratio of the truncated second order term to the first order term as:

$$d_f = \frac{|(\Delta\tau)^2\ddot{f}|}{(\Delta\tau)|\dot{f}|} = \frac{\Delta\tau|\ddot{f}|}{|\dot{f}|} \tag{B-81}$$

where f is either T or r, $\dot{f}$ and $\ddot{f}$ are first and second order derivative of f, respectively.

In the present physical problem, the composition changes much slower than the temperature, so the time increment is determined by the truncated error ratio for W:

$$d_W \approx \frac{|\Delta(\frac{\Delta W}{\Delta\tau})|}{|\frac{\Delta W}{\Delta\tau}|} = \frac{|(\frac{\Delta W}{\Delta\tau})_{n+1} - (\frac{\Delta W}{\Delta\tau})_n|}{|(\frac{\Delta W}{\Delta\tau})_{n+1}|} = \frac{|\frac{W_{n+1}-W_n}{\Delta\tau_n} - \frac{W_n-W_{n-1}}{\Delta\tau_{n-1}}|}{|\frac{W_{n+1}-W_n}{\Delta\tau_n}|} \tag{B-82}$$

And the criterion is that $\Delta\tau$ is increased when d_W is less than 10%, while $\Delta\tau$ is decreased when d_W is larger than 10%. A maximum change of three times the previous step size is permitted. Both upper and lower bounds for the permissible step size are set based on considerations of the convergence and efficiency.

APPENDIX C: USER'S MANUAL FOR COMPUTER PROGRAMS

The programs STAR and SURFT have been developed based on the numerical scheme described in Appendix B and are coded in FORTRAN IV language. A flow chart for STAR and SURFT is shown in Fig. C.1. Variable dimensioning is used to make optimum usage of the available storage and flexible capacity controllable by the user.

The program SURFT was tested by comparing the results with two analytic solutions assuming no ablation of the surface ($v=0$, $j=0$), no radiation heat loss ($\epsilon=0$) and constant properties rho, C_p and k. The heat source was assumed either rectangular or triangular. The numerical solutions are in good agreement with the analytic solutions, differing by no more than 0.1% in the calculated temperature distribution.

C.1 Program Input Data Cards

(1) PROGRAM INITIATION AND TITLE (2(A5,5x),6A5,5x,2A5) - One card, read in by subroutine TLCDE.

Column	Variable	Description
1-5	MODE	Problem initiation flag; "START" for initiation and "STOP" for termination
6-10	--	Blank
11-15	MTYPE	Problem type; "SURFT" for heat conduction only and "STAR" for conduction and diffusion
16-20	--	Blank
21-50	HED	Problem title for labeling output (an array of dimension 6)
51-55	--	Blank
56-65	DATE	Date of the run

(2) DIMENSION SPECIFICATION (2I5) - One card, read in by subroutine TLCDE.

Column	Variable	Description
1-5	NPDE	Number of partial differential equations to solve; 1 for "SURFT" and 2 for "STAR"
6-10	NGMAX	Estimated maximum number of grid points needed for space variable (normally 300)

(3) MATERIAL PROPERTIES - read in by subroutine PROP.

(i) ATOMIC WEIGHTS (2F10.0)

Column	Variable	Description
1-10	WA(1)	Atomic weight of component 1 (g/g-atom)

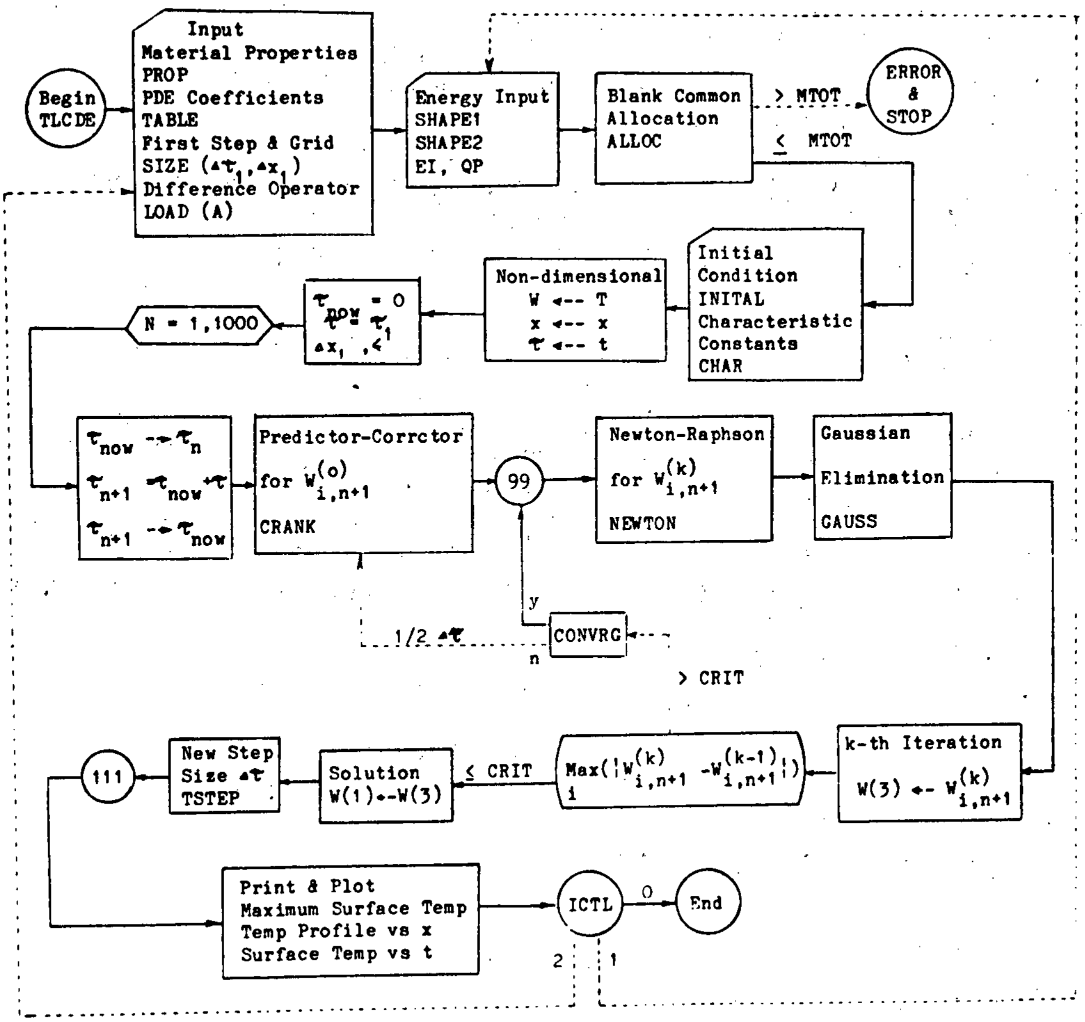

XBL 8111-12523

Fig.C.1 The Flow Diagram of the Computer Program **STAR** and **SURFT**

11-20	WA(2)	Atomic weight of component 2 (g/g-atom); zero or blank for single component materials or congruently vaporizing materials

(ii) OTHER PROPERTIES (4F10.0,E10.0)

Column	Variable	Description
1-10	TM	Melting temperature (K)
11-20	HSUB	Heat of sublimation of solid phase (J/g)
21-30	HFUS	Heat of fusion (J/g)
31-40	EMISS	Total normal thermal emissivity
41-50	A3RM	Coefficient A3 (1/k dk/dT) of heat conduction equation at room temperature

(iii) DIFFUSION COEFFICIENT (2(F10.0,E10.0)) - Blank for "SURFT".

Column	Variable	Description
1-10	EH	Diffusion activation energy / Gas constant of the mobile component above TM
11-20	EHEX	Pre-exponential factor of diffusion coefficient of the mobile component above temperature TM
21-30	EL	Diffusion activation energy / Gas constant of the mobile component below temperature TM
31-40	ELEX	Pre-exponential factor below temperature TM

(4) LASER PARAMETERS (F10.0,E10.0,E10.0) - One card, read in by subroutine PROP.

Column	Variable	Description
1-10	R	Reflectivity of target material to the laser light
11-20	TPUL	Effective laser pulse width (sec)
21-30	AEFF	Effective surface area (cm^2) of laser exposure spot

(5) CONTROL CARDS FOR NUMERICAL STABILITY - Two cards, read in by subroutine SIZE.

(i) STEP AND GRID SIZES (2E10.0,F10.0)

Column	Variable	Description
1-10	DT1	First time step size (dimensionless); also the lower limit of the following step sizes
11-20	DX1	First space grid size (dimensionless); grid sizes are geometrically increasing
21-30	EPS	Geometric factor for increasing grid sizes; a constant greater than 1 (normally 1.035)

(ii) ITERATION CONTROL (I10,E10.0)

Column	Variable	Description
1-10	ITMAX	Maximum number of iterations allowed
11-20	CRIT	Error tolerance for iteration termination

(6) TABULATED LASER PULSE

(i) SIZE AND DIVISION OF TABULATION - One card, read in by subroutine SHAPE1.

Column	Variable	Description
1-10	SDT	Step size of tabulation
11-20	LSPUL	Number of divisions of tabulation

(ii) NORMALIZED LASER PULSE SHAPE (7F10.0) - As many cards as needed to specify the tabulated normalized pulse shape (LSPUL/7 or LSPUL/7+1), read in by subroutine SHAPE2.

Column	Variable	Description
1-10	SS(I)	Normalized digital pulse shape
...	...	. . .

(7) TERMINATION OF STEP DO LOOP (2E10.0) - One card, read in by the main program.

Column	Variable	Description
1-10	TSTOP	Time to stop the time step DO loop (sec)
11-20	TCYCL	Time of a cycle for repetitive pulse (sec); Default (if zero or blank) for single pulse source is set to 1.E10 which is supposed to be approximately infinite

(8) INCIDENT TOTAL ENERGY (F10.0) - One card, read in by the main program.

Column	Variable	Description
1-10	EI	Incident total laser energy (J)

(9) INITIAL CONDITIONS (F10.0) - NPDE cards, read in by subroutine INITAL.

Column	Variable	Description
1-10	WO(I)	Initial condition for ith partial differential equation; e.g. WO(1) - initial temperature and WO(2) - initial composition

(10) RESTART OR TERMINATION CARD (I1) -One card, read in by the main program.

Column	Variable	Description
1	ICTL	Control character; 0 or blank: STOP 1: same material, another run for different laser energy 2: different material, start from the right beginning

An example of the input cards for STAR is given in Table C.1.

C.2 Subroutines to be Supplied by the User

(1) BNDRY: Gives the surface condition(s) of the problem. Input the surface value(s) and output the surface gradient(s).

(2) ACALC: Supplies the coefficients of the partial differential equation(s) and the forms of the function(s) PHAI (Ψ_T in Eq. (B-3) or/and Ψ_r in Eq. (B-4)).

(3) TABLE: Tabulates the coefficients of the partial differential equation(s).

(4) INITAL: Supplies the initial condition(s).

(5) CHAR: Provides the characteristic quantities for the non-dimensionalization of the boundary value problem.

(6) MFLUX: The calculation of the convective term (due to moving boundry) and the surface heat loss due to surface recession. Also, some printout formats are provided.

(7) A function library providing the physical properties, such as RHO (density), SPHT (specific heat), COND (thermal conductivity), DIF (diffusion coefficient), etc.

C.3 Program Capacity

The total blank common block storage MTOT has to be greater than

$$NGMAX*(NPDE*7+11)+LSPUL*(3+NPDE)+NPDE*15$$

An error message will be generated and the run will be aborted if MTOT is set too small.

Table C.1

An Example of The Input Deck for "STAR"

```
Card #
(1)    START     STAR      UO2 SURF TEMP AND COMP CALC        12/03/80
(2)        2  300
(3)           16.      238.
(4)         3133.     2234.      275.      0.83  -.190E-2
(5)         5033.  2.22E-02    28550.   .115E01
(6)          0.05 0.1685E-3  4.964E-1
(7)       1.0E-03     .2E-1     1.035
(8)             5    1.0E-4
(9)        1.0E-5        41
(10)          0.0     0.481     0.721     0.859     0.992     1.000     0.978
(11)        0.973     0.955     0.917     0.862     0.829     0.789     0.728
(12)        0.688     0.649     0.589     0.526     0.483     0.432     0.381
(13)        0.349     0.309     0.261     0.226     0.202     0.155     0.131
(14)        0.121     0.080     0.056     0.040     0.032     0.032     0.016
(15)        0.003     0.002     0.001     0.001     0.001       0.0
(16)      0.25E-3
(17)        1.0E1
(18)        1645.
(19)         2.00
(20)      (blank)
```

C.4 Program Listing

```
      PROGRAM STAR(INPUT,OUTPUT,TAPE5=INPUT,TAPE6=OUTPUT,TAPE99)
C
C ********************************************************************
C * THIS PROGRAM CALCULATES THE TRANSIENT HEAT CONDUCTION AND MASS     *
C * TRANSPORT PROBLEMS OF A COMPOUND SUBJECT TO LASER IRRADIATIONS     *
C * BY SOLVING COUPLED ONE DIMENSIONAL TIME DEPENDENT HEAT CONDUCTION  *
C * AND DIFFUSION EQUATIONS SIMULTANEOUSLY CONSIDERING MELTING,        *
C * ABLATING MOVING BOUNDARY, AND RADIATION.                           *
C * THE INCONGRUENT VAPORIZATION IS CONSIDERED.                        *
C * THIS PROGRAM ALLOWS EITHER THE PENETRATION OF LASER RADIATION      *
C * (VOLUMETRIC HEATING) OR ABSORBING SURFACE (SURFACE HEATING).       *
C * THE NUMERICAL METHODS USED ARE CRANK-NICOLSON FINITE DIFFERENCE    *
C * METHOD WITH VARIABLE GRID SPACE INCREMENT AND SELF-ADJUSTABLE      *
C * TIME INCREMENT, NEWTON-RAPHSON AND GAUSSIAN ELIMINATION BACK       *
C * SUBSTITUTION METHODS.                                              *
C * THE PREDICTOR-CORRECTOR SCHEME IS USED FOR FINDING BETTER INITIAL  *
C * GUESS AND FASTER CONVERGENCE.                                      *
C *                                                                    *
C * DEVELOPED BY C. H. TSAI, JUNE 1980.                                *
C * UNIVERSITY OF CALIFORNIA - BERKELEY                                *
C ********************************************************************
C
      COMMON/BLOCK/MTOT
      COMMON/DIM  /NPDE,NGMAX,LSPUL
      COMMON/DMAIN/N1,N2,N3,N4,N5,N6,N7,N8,N9,N10,N11,N12,N13
      COMMON/CHART/XCH,TCH
      COMMON/LASER/EI,QP,R,TPUL,AEFF
      COMMON/STEP /DT1
      COMMON C(8000)
C
      MTOT=8000
C
C     **********************************************
C     BLANK       COMMON       STORAGE       ALLOCATION
C         ARRAY   ------- DESCRIPTION ------   DIMENSION
C     N1  W       DIMENSIONLESS SOLUTION      NGMAX*3*NPDE
C     N2  A       DIFFER OPERATOR COEFF       NGMAX*7
C     N3  SS      NORMALIZED PULSE SHAPE      LSPUL
C     N4  TT      TIME INCRE FOR SS (DIM)     LSPUL
C     N5  PP      PEAK POWER DENSITY AT TT    LSPUL
C     N6  WCH     CHART QUANTITY FOR W (DIM) NPDE
C     N7  WS      SURFACE W AT TNOW           NPDE
C     N8  WSURF   SURF W AS FUNC OF TT (DIM) LSPUL*NPDE
C     N9  WX      W PRFLE AS FUNC OF X (DIM) NGMAX*NPDE
C     N10 X       SPACE GRID FOR PRFLE WX     NGMAX
C     N11 WO      INITIAL VALUE OF W (DIM)    NPDE
C     N12 WOLD    SURFACE W AT TOLD (DIMLSS) NPDE
C     N13 WLAST   WS OF LAST ITERATION        NPDE
C     **********************************************
C
C  INITIATE OR STOP THE PROGRAM
C  READ NPDE,NGMAX
   99 CALL FLCUE
C
C  INPUT THE MATERIAL PROPERTIES AND LASER CHARACTERISTICS
      CALL PROP
C  GENERATION OF COEFFICIENT TABLES
      CALL TABLE
C
C  STEP AND GRID SIZES FOR NUMERICAL STABILITY
      CALL SIZE
C
      CALL SHAPE1
C
C  DEFINE COMMON BLOCK ALLOCATION
      CALL ALLOC
C
C  INPUT LASER NORMALIZED PULSE SHAPE
      CALL SHAPE2(C(N3),C(N4),LSPUL)
C
C  LOAD CONSTANT VECTORS A'S FOR DIFFERENCE OPERATORS
      CALL LOAD(C(N2),NGMAX)
C
C  CALCULATION TO BE ENDED AT TSTOP (IN SEC)
      READ (5,9) TSTOP,TCYCL
    9 FORMAT(2E10.0)
      IF(TSTOP.GT.C(N5-1)) TSTOP=C(N5-1)
C  DEFAULT OF TCYCL FOR SINGLE PULSE IS 100.,
C  WHICH IS ASSUMED TO BE INFINITIVE.
      IF(TCYCL.EQ.0.0) TCYCL=100.
C
C  INPUT LASER ENERGY
   88 READ (5,8) EI
    8 FORMAT(E10.0)
      IF(EI.EQ.0.0) CALL EXIT
      QP=EI/(TPUL*AEFF)
      DO 1 I=1,LSPUL
      IM=I-1
    1 C(N5+IM)=QP*C(N3+IM)*(1.-R)
C
C  LOAD INITIAL CONDITIONS
      CALL INITAL(C(N1),C(N11),NPDE,NGMAX)
C  CHARACTERISTIC CONSTANTS FOR NON-DIMENSIONALIZATION
      CALL CHAR(C(N11),C(N6),NPDE)
C
      TNOW =0.0
      DT   =DT1
      IFLAG=0
      DO 2 I=1,NPDE
      IL=(I-1)*LSPUL
    2 C(N8+IL)=C(N11+I-1)
      TAME =0.0
      TSMAX=0.0
      AMULD=0.0
      NGMIN=20
      M    =NGMIN
      K    =2
C
```

```
STR109  C  STEP-BY-STEP NUMERICAL CALCULATION
STR110         DO 111 N=1,1000
STR111         TOLD=TNOW
STR112         IF(N.EQ.1) GOTO 11
STR113         DO 3 I=1,NPDE
STR114     3   C(N12+I-1)=C(N1+(I-1)*3*NGMAX)
STR115     11  CALL NUMCAL(C(N1),TNOW,DT,C(N6),M,C(N2),C(N5),LSPUL,
STR116        1                N,IFLAG,DWS,C(N7),C(N13),NPDE,NGMAX)
STR117         TIME=TNOW*TCH
STR118         TS=C(N7)*C(N6)
STR119  C
STR120  C  TOTAL AMOUNT OF MATERIAL EVAPORATED
STR121         RS=C(N7+1)*C(N6+1)
STR122         CALL MFLUX(TIME,TS,RS,AME,AME1,AME2,IFLAG)
STR123         DAMDT=(AME-AMOLD)/(DT*TCH)
STR124         AMOLD=AME
STR125         AMEDT=AME*DT*AEFF*TCH
STR126         TAME=TAME+AMEDT
STR127         FRAC=AMEDT/TAME
STR128  C
STR129  C  DETERMINE NEXT TIME STEP SIZE
STR130         CALL TSTEP(DT,DWS,N)
STR131  C
STR132  C  MAXIMUM SURFACE TEMPERATURE
STR133         IF(TS.LT.TSMAX) GOTO 20
STR134         TSMAX=TS
STR135         RTMAX=RS
STR136         TIMAX=TIME*1.0E3
STR137         LM=M+2
STR138         DO 10 I=1,NPDE
STR139         IM=(I-1)*NGMAX
STR140         DO 10 J=1,LM
STR141         JI=IM+J-1
STR142         JJ=IM*3+J-1
STR143     10  C(N9+JI)=C(N1+JJ)*C(N6+I-1)
STR144  C
STR145     20  IF(TIME.LT.C(N4+K-1)) GOTO 111
STR146  C
STR147         DO 30 I=1,NPDE
STR148         IM=(I-1)*LSPUL
STR149     30  C(N8+IM+K-1)=(C(N12+I-1)+(C(N4+K-1)/TCH-TOLD)*(C(N1+3*(I-1)*
STR150        1                  NGMAX)-C(N12+I-1))/(TNOW-TOLD))*C(N6+I-1)
STR151         IF(C(N4+K-1).GE.TSTOP) GOTO 40
STR152         K=K+1
STR153     111 CONTINUE
STR154  C
STR155     40  KK=K
STR156  C
STR157  C  TEMP AND COMP PROFILE AT THE TIME WHEN SURF TEMP IS MAX
STR158         CALL PRFLE(TSMAX,TIMAX,C(N9),C(N10),LM,NPDE,NGMAX)
STR159         DO 4 I=1,LM
STR160     4   C(N10+I-1)=C(N10+I-1)*1.E4
STR161         IFRM=0
STR162         CALL PLOTTX(C(N10),C(N9),LM,IFRM)
STR163         CALL PLOTRX(C(N10),C(N9+NGMAX),LM,IFRM)
STR164  C
STR165  C  TOTAL AMOUNT OF MATERIAL EVAPORATED
STR166         IFLAG=1
STR167         CALL MFLUX(TIMAX/1.E-3,TSMAX,RTMAX,AMET,AMET1,AMET2,IFLAG)
STR168         IF(DAMDT.GE.0.0) GOTO 41
STR169         TEND=TIME-AME/DAMDT
STR170         GOTO 42
STR171    41   TEND=TIME
STR172    42   CONTINUE
STR173         IF(TEND.GT.TCYCL) TEND=TCYCL
STR174         TAME1=TAME+AME*AEFF*(TEND-TIME)
STR175         TAME2=AMET*TPUL*AEFF
STR176         WRITE (6,103) TAME,FRAC,TAME2
STR177         WRITE (6,104) TCYCL,TEND,TAME1
STR178  C
STR179  C  SURFACE TEMPERATURE AND COMPOSITION RATIOS
STR180  C
STR181    50   WRITE (6,100)
STR182         WRITE (6,101) EI,QP
STR183         WRITE (6,102)
STR184         DO 70 I=1,KK
STR185         IF(I.GT.2) GOTO 60
STR186         IFLAG=IFLAG+1
STR187    60   CALL MFLUX(C(N4+I-1),C(N8+I-1),C(N8+LSPUL+I-1),FLUX,F1,F2,IFLAG)
STR188    70   CONTINUE
STR189  C
STR190         DO 5 I=1,KK
STR191     5   C(N4+I-1)=C(N4+I-1)*1.E3
STR192         CALL PLOTTS(C(N4),C(N8),KK,IFRM)
STR193  C
STR194    100 FORMAT(1H1,10X,88(1H*))
STR195    101 FORMAT(1H ,13X,66HTHE SURFACE TEMPERATURES AND COMPOSITION RATIOS
STR196       1WITH TIME FOR EI =,E10.3,9H (JOULES)/
STR197       2            18X,4HQP =,E10.3,8H (W/CM2))
STR198    102 FORMAT(1H ,10X,88(1H*)/)
STR199    103 FORMAT(1H0,6X,64HTHE TOTAL AMOUNT OF MATERIAL EVAPORATED FROM TIME
STR200       1 INTEGRATION IS,E13.6,6H GRAMS/
STR201       2        26X,45HFRACTION OF THE MASS OF TIME STEP TO TOTAL IS,E13.6/
STR202       3        7X,75HTHE TOTAL AMOUNT OF MATERIAL EVAPORATED FROM MAX SURF
STR203       4 TEMP AND TPUL CALC IS,E13.6,6H GRAMS)
STR204    104 FORMAT(1H0,6X,7HTCYCL =,E13.6,15H SEC AND TEND =,E13.6,4H SEC/
STR205       1        7X,86HTHE TOTAL AMOUNT OF MATERIAL EVAPORATED TAKING ACCOUN
STR206       2T THE AMOUNT FROM TIME TO TEND IS,E13.6,6H GRAMS)
STR207  C
STR208         READ (5,200) ICTL
STR209         IF(ICTL.EQ.0.OR.ICTL.GT.2) IFRM=1
STR210         CALL PLOTRS(C(N4),C(N8+LSPUL),KK,IFRM)
STR211         DO 51 I=1,KK
STR212    51   C(N4+I-1)=C(N4+I-1)/1.E3
STR213         IF(ICTL.EQ.1) GOTO 88
STR214         IF(ICTL.EQ.2) GOTO 99
STR215    200 FORMAT(I1)
STR216         STOP
STR217         END
```

```
TLC001        SUBROUTINE TLCDE
TLC002  C
TLC003  C  READ CONTROL STATEMENT FOR PROBLEM INITIATION
TLC004  C  (NOT PROBLEM NOR MATER DEPENT)
TLC005  C
TLC006        COMMON/DIM  /NPDE,NGMAX,LSPUL
TLC007        DIMENSION HED(6),DATE(2)
TLC008        DIMENSION MOD(2)
TLC009        DATA MOD/5HSTART,5HSTOP /
TLC010  C
TLC011     10  READ (5,100) MODE,MTYPE,HED,DATE
TLC012        IF(MODE.EQ.MOD(2)) STOP
TLC013        IF(MODE.EQ.MOD(1)) GOTO 20
TLC014        WRITE (6,300)
TLC015        GOTO 10
TLC016  C  READ NO OF PARTIAL DIFFERENTIAL EQUATIONS,
TLC017  C  AND DIMENSION OF MAXIMUM GRID POINTS
TLC018     20  READ (5,101) NPDE,NGMAX
TLC019        IF(NGMAX.GT.0) GOTO 30
TLC020        WRITE (6,301)
TLC021     30  WRITE (6,200) HED,DATE
TLC022        WRITE (6,201) NPDE,NGMAX
TLC023  C
TLC024     100 FORMAT(2(A5,5X),6A5,5X,2A5)
TLC025     101 FORMAT(2I5)
TLC026     200 FORMAT(1H1,5(1H*),2X,6A5,2X,5(1H*)/1X,5(1H*),12X,2A5,12X,5(1H*)//)
TLC027     201 FORMAT(1H0,40HTHE NUMBER OF DIFFERENTIAL EQUATIONS IS ,I2/
TLC028        1           1X,37HTHE MAXIMUM NUMBER OF GRID PLANES IS ,I5//)
TLC029     300 FORMAT(//48H **ERROR**  DATA DECK MUST BEGIN WITH START CARD)
TLC030     301 FORMAT(//46H **ERROR**  NO. OF GRID PLANES MUST BE GT ZERO)
TLC031  C
TLC032        RETURN
TLC033        END


AL0001        SUBROUTINE ALLOC
AL0002  C
AL0003  C  DEFINE COMMON BLOCK STORAGE ALLOCATION FOR
AL0004  C  THE MAIN PROGRAM AND SUBROUTINES
AL0005  C
AL0006        COMMON/BLOCK/MTOT
AL0007        COMMON/DIM  /NPDE,NGMAX,LSPUL
AL0008        COMMON/DMAIN/N1,N2,N3,N4,N5,N6,N7,N8,N9,N10,N11,N12,N13
AL0009        COMMON/DCRAN/M1,M2,M3,M4,M5,M6,M7,M8,M9,M10,M11,M12,M13
AL0010        COMMON/DNEWT/L1,L2,L3,L4,L5,L6,L7,L8,L9,L10,L11,L12,L13,L14,
AL0011       1                L15,L16,L17
AL0012  C
AL0013  C  PARTITION OF BLANK COMMON FOR MAIN PROGRAM
AL0014        N1 =1
AL0015        N2 =N1 +NGMAX*3*NPDE
AL0016        N3 =N2 +NGMAX*7
AL0017        N4 =N3 +LSPUL
AL0018        N5 =N4 +LSPUL
AL0019        N6 =N5 +LSPUL
AL0020        N7 =N6 +NPDE
AL0021        N8 =N7 +NPDE
AL0022        N9 =N8 +LSPUL*NPDE
AL0023        N10=N9 +NGMAX*NPDE
AL0024        N11=N10+NGMAX
AL0025        N12=N11+NPDE
AL0026        N13=N12+NPDE
AL0027        NLAST=N13+NPDE
AL0028        IF(NLAST.GT.MTOT) CALL ERROR(NLAST-MTOT)
AL0029  C
AL0030  C  PARTITION OF BLANK COMMON FOR SUBROUTINE CRANK
AL0031        M1 =NLAST
AL0032        M2 =M1 +NGMAX*NPDE
AL0033        M3 =M2 +NGMAX*NPDE
AL0034        M4 =M3 +NGMAX*NPDE
AL0035        M5 =M4 +NPDE
AL0036        M6 =M5 +NPDE
AL0037        M7 =M6 +NPDE
AL0038        M8 =M7 +NPDE
AL0039        M9 =M8 +NPDE
AL0040        M10=M9 +NPDE
AL0041        M11=M10+NPDE
AL0042        M12=M11+NPDE
AL0043        M13=M12+NGMAX
AL0044        IF(M13.GT.MTOT) CALL ERROR(M13-MTOT)
AL0045  C
AL0046  C  PARTITION OF BLANK COMMON FOR SUBROUTINE NEWTON
AL0047        L1 =NLAST
AL0048        L2 =L1 +NGMAX
AL0049        L3 =L2 +NGMAX
AL0050        L4 =L3 +NGMAX
AL0051        L5 =L4 +NPDE
AL0052        L6 =L5 +NPDE
AL0053        L7 =L6 +NPDE
AL0054        L8 =L7 +NPDE
AL0055        L9 =L8 +NPDE
AL0056        L10=L9 +NPDE
AL0057        L11=L10+NGMAX*NPDE
AL0058        L12=L11+NGMAX*NPDE
AL0059        L13=L12+NPDE
AL0060        L14=L13+NPDE
AL0061        L15=L14+NPDE
AL0062        L16=L15+NPDE
AL0063        L17=L16+NGMAX
AL0064        IF(L17.GT.MTOT) CALL ERROR(L17-MTOT)
AL0065  C
AL0066        RETURN
AL0067        END


SZE001        SUBROUTINE SIZE
SZE002  C
SZE003  C  SET STEP AND GRID SIZES FOR NUMERICAL STABILITY
SZE004  C  (NOT PROBLEM NOR MATER DEPENT)
```

```
SZE005   C
SZE006          COMMON/GRID /DX1,EPS,EPS1,EPS2
SZE007          COMMON/ITER /ITMAX,CRIT
SZE008          COMMON/STEP /DT1
SZE009   C
SZE010          READ (5,100) DT1,DX1,EPS
SZE011          WRITE (6,200) DT1,DX1,EPS
SZE012          READ (5,101) ITMAX,CRIT
SZE013          WRITE (6,201) ITMAX,CRIT
SZE014   C
SZE015      100 FORMAT(2E10.0,F10.0)
SZE016      101 FORMAT(I10,E10.0)
SZE017      200 FORMAT(1H0,23HTHE NUMERICAL CONSTANTS/
SZE018        1              5X,21HTHE FIRST STEP SIZE =,E9.3/
SZE019        2              5X,21HTHE FIRST GRID SIZE =,E9.3/
SZE020        3              5X,21HGRID INCRE FACTOR   =,F9.3)
SZE021      201 FORMAT(5X,21HMAX NO OF ITERATION =,I9/
SZE022        1          5X,21HERROR TOLERANCE     =,E9.3)
SZE023   C
SZE024          RETURN
SZE025          END


LOD001          SUBROUTINE LOAD(A,NGMAX)
LOD002   C
LOD003   C  LOAD CONSTANT VECTORS FOR DIFFERENCE OPERATORS
LOD004   C  (NOT PROBLEM NOR MATER DEPENT)
LOD005   C
LOD006          COMMON/GRID /DX1,EPS,EPS1,EPS2
LOD007          DIMENSION A(NGMAX,7)
LOD008   C
LOD009          EPS1=1.+EPS
LOD010          EPS2=1.+EPS+EPS**2
LOD011          I=2
LOD012          A(I,1)=2.*EPS*(2.+EPS)/(EPS1*EPS2)
LOD013          A(I,2)=-2.*(EPS**2+2.*EPS-1.)/(EPS**2*EPS1)
LOD014          A(I,3)=2.*(EPS**2+EPS-1.)/(EPS1*EPS**3)
LOD015          A(I,4)=2.*(1.-EPS)/(EPS**3*EPS1*EPS2)
LOD016          A(I,5)=-EPS/EPS1
LOD017          A(I,6)=(EPS-1.)/EPS
LOD018          A(I,7)=1./(EPS*EPS1)
LOD019          DO 1 J=1,4
LOD020          DO 1 I=3,NGMAX
LOD021     1    A(I,J)=A(I-1,J)/EPS**2
LOD022          DO 2 J=5,7
LOD023          DO 2 I=3,NGMAX
LOD024     2    A(I,J)=A(I-1,J)/EPS
LOD025          I=1
LOD026          A(I,1)=0.0
LOD027          A(I,2)=-(EPS+2.)/EPS1
LOD028          A(I,3)=EPS1/EPS
LOD029          A(I,4)=-1./(EPS*EPS1)
LOD030          RETURN
LOD031          END
```

```
SAP101          SUBROUTINE SHAPE1
SAP102   C
SAP103   C  READ SDT AND LSPUL
SAP104   C
SAP105          COMMON/DIM  /N(2),LSPUL
SAP106          COMMON/PULS /SDT
SAP107   C
SAP108          READ (5,100) SDT,LSPUL
SAP109          WRITE (6,200) SDT,LSPUL
SAP110      100 FORMAT(E10.1,I10)
SAP111      200 FORMAT(1H0,25HTEMP PRINT OUT PARAMETERS/
SAP112        1              5X,4HSDT=,E7.2,4H SEC,5X,6HLSPUL=,I3)
SAP113   C
SAP114          RETURN
SAP115          END


SAP201          SUBROUTINE SHAPE2(SS,TT,LSPUL)
SAP202   C
SAP203   C  LASER NORMALIZED PULSE SHAPE
SAP204   C  (NOT PROBLEM NOR MATER DEPENT)
SAP205   C
SAP206          COMMON/PULS /SDT
SAP207          DIMENSION SS(LSPUL),TT(LSPUL)
SAP208   C
SAP209          DO 1 I=1,LSPUL
SAP210     1    TT(I)=SDT*FLOAT(I-1)
SAP211          READ (5,101) (SS(I),I=1,LSPUL)
SAP212          WRITE (6,201)
SAP213          WRITE (6,202)
SAP214          WRITE (6,203)
SAP215          WRITE (6,204) (I,TT(1),I,SS(I),I=1,LSPUL)
SAP216   C
SAP217      101 FORMAT(7F10.3)
SAP218      201 FORMAT(1H1,55(1H*))
SAP219      202 FORMAT(1H ,1X,53HHISTOGRAM OF TEMPORAL SHAPE OF PULSE FROM POWER T
SAP220        1RACE)
SAP221      203 FORMAT(1H ,55(1H*)/)
SAP222      204 FORMAT(1H ,10X,3HTT(,I2,3H) =,E8.2,5X,3HSS(,I2,3H) =,F6.3)
SAP223   C
SAP224          RETURN
SAP225          END


SRC001          FUNCTION SOURCE(TIME,FF,LSPUL)
SRC002   C
SRC003   C  TEMPORAL SHAPE FROM LASER POWER TRACE
SRC004   C
SRC005          COMMON/PULS /SDT
SRC006          DIMENSION FF(LSPUL)
SRC007   C
SRC008          XI=TIME/SDT
SRC009     2    I=XI
SRC010          IF(I.GE.LSPUL-1) GOTO 1
```

```
SRC011        SOURCE=FF(I+1)+(XI-I)*(FF(I+2)-FF(I+1))
SRC012        RETURN
SRC013     1  SOURCE=0.0
SRC014        RETURN
SRC015        END


CRG001        SUBROUTINE CONVRG(W,WLAST,NIT,M,MRESET,DT.NPDE,NGMAX)
CRG002  C
CRG003  C  TEST THE CONVERGENCY OF ITERATIONS
CRG004  C  (NOT PROBLEM NOR MATER DEPENT)
CRG005  C
CRG006        DIMENSION W(NGMAX,3.NPDE),WLAST(NPDE)
CRG007  C
CRG008        IF(NIT.EQ.0) GOTO 2
CRG009        DO 10 I=1,NPDE
CRG010        RATIO=ABS((W(1,3,I)-W(1,2,I))/(W(1,2.I)-WLAST(I)))
CRG011        IF(RATIO.GE.1.) GOTO 1
CRG012    10  CONTINUE
CRG013        GOTO 2
CRG014  C  IF NOT CONVERGE, DT WAS TOO LARGE
CRG015  C  DT REDUCED TO HALF
CRG016     1  DT=DT/2.
CRG017        M=MRESET
CRG018        NIT=0
CRG019        RETURN
CRG020  C  IF CONVERGE, (I,3) TRANSFER TO (I,2), ITERATION GOES ON
CRG021     2  CONTINUE
CRG022        DO 20 I=1,NPDE
CRG023    20  WLAST(I)=W(1,2,I)
CRG024        L1=M+2
CRG025        DO 3 I=1,NPDE
CRG026        DO 3 J=1,L1
CRG027        W(J,2,I)=W(J,3,I)
CRG028     3  CONTINUE
CRG029        NIT=NIT+1
CRG030        RETURN
CRG031        END


TSTP01        SUBROUTINE TSTEP(DT,DWS,N)
TSTP02  C
TSTP03  C  DETERMINATION OF TIME INCREMENT BY COMPARING SUCCESIVE TIME
TSTP04  C  DERIVATIVE OF SURFACE TEMPERATURE (NOTE THAT ONLY TEMP IS USED)
TSTP05  C  (NOT PROBLEM NOR MATER DEPENDENT)
TSTP06  C
TSTP07        DTOLD=DT
TSTP08        DWDT=DWS/DTOLD
TSTP09        IF(N.EQ.1) GOTO 1
TSTP10        DDWDT=ABS(DWDT-DWDTO)/ABS(DWDT)
TSTP11        DT=DT*0.1/DDWDT
TSTP12  C  10% OF D(DWDT) TOLERANCE
TSTP13        IF(DT.GT.3.0*DTOLD) DT=3.0*DTOLD
TSTP14        IF(DT.GT.50.*DT1)    DT=50.*DT1
TSTP15        IF(DT.LT.DT1)        DT=DT1
TSTP16        K1=0
TSTP17    10  K1=K1+1
TSTP18        POWER=10.**K1
TSTP19        IF(AINT(DT*POWER).EQ.0) GOTO 10
TSTP20        DT=AINT(DT*POWER+.5)/POWER
TSTP21     1  DWDTO=DWDT
TSTP22        IF(N.GT.1) RETURN
TSTP23        DT1=DT
TSTP24        RETURN
TSTP25        END


EOR001        SUBROUTINE ERROR(N)
EOR002  C
EOR003        WRITE (6,1) N
EOR004     1  FORMAT(//31H**ERROR**  STORAGE EXCEEDED BY ,I6)
EOR005        STOP
EOR006        END


NCL001        SUBROUTINE NUMCAL(W,TNOW,DT,WCH,M,A,FF,LSPUL,N.IFLAG,
NCL002       1                  DWS,WS,WLAST,NPDE,NGMAX)
NCL003  C
NCL004  C  NUMERICAL CALCULATION OF PARTIAL DIFFERENCIAL EQUATION AT SOME
NCL005  C  TIME STEP 'TNOW' WITH CRANK-NICOLSON FINITE DIFFERENCE METHOD.
NCL006  C  PREDICTOR-CORRECTOR SCHEME FOR THE FIRST GUESS, NEWTON-RAPHSON
NCL007  C  METHOD FOR ITERATION AND GAUSSIAN ELIMINATION METHOD FOR SOLVING
NCL008  C  LINEARIZED EQUATIONS.
NCL009  C  (NOT PROBLEM NOR MATER DEPENDENT)
NCL010  C
NCL011        COMMON/ITER /ITMAX,CRIT
NCL012        DIMENSION W(NGMAX,3,NPDE)
NCL013        DIMENSION A(NGMAX,7)
NCL014        DIMENSION WS(NPDE),WCH(NPDE)
NCL015        DIMENSION WLAST(NPDE)
NCL016        DIMENSION FF(LSPUL)
NCL017  C
NCL018        TOLD=TNOW
NCL019        MRESET=M
NCL020     1  NIT=0
NCL021        T=TOLD+DT/2.
NCL022        TNOW=T+DT/2.
NCL023  C
NCL024  C  PREDICTOR
NCL025        NFLAG=0
NCL026        CALL CRANK(W,T,DT/2.,WCH,M,A,FF,LSPUL,NFLAG,NPDE,NGMAX)
NCL027  C
NCL028  C  CORRECTOR
NCL029        NFLAG=1
NCL030        CALL CRANK(W,TNOW,DT,WCH,M,A,FF,LSPUL,NFLAG,NPDE,NGMAX)
NCL031  C
NCL032        L1=M+2
NCL033        DO 11 I=1.NPDE
```

```
NCL034         DO 11 J=1,L1
NCL035      11  W(J,2,I)=W(J,3,I)
NCL036    C
NCL037    C  ITERATIONS
NCL038         NFLAG=2
NCL039      99  CONTINUE
NCL040    C
NCL041         DO 12 I=1,NPDE
NCL042      12  CALL NEWTON(W,TNOW,DT,WCH,NIT,M,A,FF,LSPUL,I,NFLAG,NPDE,NGMAX)
NCL043    C
NCL044         I=NPDE
NCL045     100 IF(ABS(W(1,3,I)-W(1,2,I)).GT.CRIT) GOTO 101
NCL046         IF(I.EQ.1) GOTO 102
NCL047         I=NPDE-1
NCL048         GOTO 100
NCL049    C
NCL050    C  BEFORE FURTHER ITERATION, CONVERGENCY IS CHECKED.
NCL051     101 CALL CONVRG(W,WLAST,NIT,M,MRESET,DT,NPDE,NGMAX)
NCL052         IF(NIT.EQ.0) GOTO 1
NCL053         IF(NIT.GT.ITMAX) GOTO 102
NCL054         GOTO 99
NCL055    C
NCL056    C  ITERATIONS COMPLETED, W(J,3,I) BECOME FINAL SOLUTIONS OF THE
NCL057    C  CURRENT TIME STEP AND ARE TRANSFERED TO W(J,1,I) AND GO ON
NCL058    C  TO THE NEXT TIME STEP.
NCL059     102 DWS=W(1,3,1)-W(1,1,1)
NCL060         DO 14 I=1,NPDE
NCL061         DO 13 J=1,M
NCL062         W(J,1,I)=W(J,3,I)
NCL063      13  W(J,2,I)=W(J,3,I)
NCL064         J=1
NCL065      14  WS(I)=W(J,1,I)
NCL066    C
NCL067         RETURN
NCL068         END


CNK001         SUBROUTINE CRANK(W,T,DT,WCH,M,A,FF,LSPUL,NFLAG,NPDE,NGMAX)
CNK002    C
CNK003    C  CRANK-NICOLSON FINITE DIFFERENCE
CNK004    C  GAUSSIAN ELIMINATION BACK-SUBSTITUTION
CNK005    C  (NOT PROBLEM NOR MATER DEPENT)
CNK006    C
CNK007         COMMON/GRID /DX1,EPS,EPS1,EPS2
CNK008         COMMON/DCRAN/N1,N2,N3,N4,N5,N6,N7,N8,N9,N10,N11,N12,N13
CNK009         COMMON C(1)
CNK010         DIMENSION W(NGMAX,3,NPDE)
CNK011         DIMENSION A(NGMAX,7)
CNK012         DIMENSION WCH(NPDE)
CNK013         DIMENSION FF(LSPUL)
CNK014    C
CNK015    C    *********************************************
CNK016    C    BLANK       COMMON      STORAGE       ALLOCATION
CNK017    C        ARRAY  ----- DESCRIPTION -----   DIMENSION
```

```
CNK018    C      N1  ALPHA  COEFF OF I FROM ELIM      NGMAX*NPDE
CNK019    C      N2  BETA   COEFF OF I+1 FROM ELIM    NGMAX*NPDE
CNK020    C      N3  S      RECUR SUM AFTER ELIM      NGMAX*NPDE
CNK021    C      N4  BC     BNDRY GRADIENTS           NPDE
CNK022    C      N5  FLNR   BNDRY LNR CORR TERM       NPDE
CNK023    C      N6  FD     BNDRY LNR TERM AFT CORR   NDPE
CNK024    C      N7  DDX    SEC CORR CE FRST DIFF     NPDE
CNK025    C      N8  A1     COEFF OF TIME DER TERM    NPDE
CNK026    C      N9  PHAI   PDE SPACE DEPENT TERMS    NPDE
CNK027    C      N10 WS     SURF VALUE OF W           NPDE
CNK028    C      N11 WJ     W VALUE AT J-TH GRID      NPDE
CNK029    C      N12 WGS    SOLUTION FROM GAUSS ELIM NGMAX
CNK030    C      ********************************************
CNK031    C
CNK032           N=NFLAG+1
CNK033           J=1
CNK034           DO 10 I=1,NPDE
CNK035           II=(I-1)*NGMAX
CNK036           C(N2+II)=A(J,3)
CNK037      10   C(N10+I-1)=W(J,N,I)
CNK038           CALL BNDRY(C(N10),WCH,T,FF,LSPUL,C(N4),V,C(N5),C(N6),
CNK039          1               NPDE)
CNK040           DO 11 I=1,NPDE
CNK041           IM=I-1
CNK042           II=IM*NGMAX
CNK043           C(N1+II)=A(J,2)-C(N5+IM)*DX1
CNK044           C(N6+IM)=C(N6+IM)*DX1
CNK045      11   C(N3+II)=C(N6+IM)
CNK046      1    J=J+1
CNK047           DO 12 I=1,NPDE
CNK048           IM=I-1
CNK049           C(N7+IM)=(A(J,5)*W(J-1,N,I)+A(J,6)*W(J,N,I)+A(J,7)*W(J+1,N,I))/
CNK050          1             DX1
CNK051      12   C(N11+IM)=W(J,N,I)
CNK052           CALL ACALC(C(N11),WCH,T,V,C(N7),C(N8),C(N9),DDD,1,NFLAG,NPDE)
CNK053           DO 13 I=1,NPDE
CNK054           IM=I-1
CNK055           FJ=-A(J,1)*W(J-1,1,I)-A(J,2)*W(J,1,I)-A(J,3)*W(J+1,1,I)-A(J,4)*W(J
CNK056          1    +2,1,I)-2.*(C(N8+IM)*W(J,1,I)/DT+C(N9+IM))*DX1**2
CNK057           JI=IM*NGMAX+J-1
CNK058           C(N1+JI)=A(J,2)-C(N2+JI-1)*A(J,1)/C(N1+JI-1)-2.*C(N8+IM)/DT*DX1**
CNK059          1          2
CNK060           C(N2+JI)=A(J,3)-A(J-1,4)*A(J,1)/C(N1+JI-1)
CNK061      13   C(N3+JI)=FJ-A(J,1)*C(N3+JI-1)/C(N1+JI-1)
CNK062           IF(J.LT.M) GOTO 1
CNK063           IF(NFLAG.GT.0) GOTO 2
CNK064    C  IN THE BEGINNING OF EACH TIME STEP TO DETERMINE THE NEW M VALUE FOR
CNK065    C  THE CURRENT TIME STEP
CNK066           MFLAG=0
CNK067           DO 14 I=1,NPDE
CNK068           JI=(I-1)*NGMAX+J-1
CNK069           W(J+3,1,I)=W(J+2,1,I)*EPS1-W(J+1,1,I)*EPS
CNK070           IF(W(J+3,1,I).LT.1.) W(J+3,1,I)=1.
CNK071           W(J+3,2,I)=W(J+3,1,I)
```

```
CNK072          IF(J.EQ.NGMAX-3) GOTO 14
CNK073          CON1=(C(N1+JI)+C(N2+JI)+A(J,4))/C(N3+JI)-(C(N1+JI-1)+C(N2+JI-1)
CNK074         1     +A(J-1,4))/C(N3+JI-1)
CNK075          CON2=(C(N2+JI)+2.*A(J,4))/C(N3+JI)+(C(N1+JI-1)-A(J-1,4))/C(N3+JI
CNK076         1     -1)
CNK077          IF(ABS(CON1/CON2).GT.0.002) MFLAG=1
CNK078       14 CONTINUE
CNK079          IF(MFLAG.NE.0) GOTO 1
CNK080          M=J
CNK081    C  BACK SUBSTITUTION
CNK082        2 L1=M+2
CNK083          DO 15 I=1,NPDE
CNK084          II=(I-1)*NGMAX
CNK085          CALL GAUSS(C(N1+II),C(N2+II),C(N3+II),A(1,4),C(N12),M)
CNK086          DO 3 J=1,L1
CNK087        3 W(J,N+1,I)=C(N12+J-1)
CNK088       15 CONTINUE
CNK089          RETURN
CNK090          END


NWT001          SUBROUTINE NEWTON(W,T,DT,WCH,NIT,M,A,FF,LSPUL,IEQN,NFLAG,NPDE,
NWT002         1                      NGMAX)
NWT003    C
NWT004    C  NEWTON-RAPHSON METHOD
NWT005    C  (NOT PROBLEM NOR MATER DEPENT)
NWT006    C
NWT007          COMMON/GRID /DX1,EPS,EPS1,EPS2
NWT008          COMMON/DNEWT/N1,N2,N3,N4,N5,N6,N7,N8,N9,N10,N11,N12,N13,N14,
NWT009         1                N15,N16,N17
NWT010          COMMON C(1)
NWT011          DIMENSION W(NGMAX,3,NPDE)
NWT012          DIMENSION A(NGMAX,7)
NWT013          DIMENSION WCH(NPDE)
NWT014          DIMENSION FF(LSPUL)
NWT015    C
NWT016    C     ***********************************************
NWT017    C     BLANK       COMMON      STORAGE       ALLOCATION
NWT018    C          ARRAY  ------- DESCRIPTION -------  DIMENSION
NWT019    C     N1   ALPHA  COEFF OF I FROM ELIM         NGMAX
NWT020    C     N2   BETA   COEFF OF I+1 FROM ELIM       NGMAX
NWT021    C     N3   S      RECUR SUM AFTER ELIM         NGMAX
NWT022    C     N4   BC     BNDRY GRADIENTS              NPDE
NWT023    C     N5   PBC    PERTURBED BNDRY GRAD         NPDE
NWT024    C     N6   FLNR   DUMMY VARIALBE               NPDE
NWT025    C     N7   FO     DUMMY VARIALBE               NPDE
NWT026    C     N8   FFO    DUMMY VARIABLE               NPDE
NWT027    C     N9   DDX    SEC CORR CE FRST DIFF        NPDE
NWT028    C     N10  DDXO   DDX OF LAST TIME STEP        NGMAX*NPDE
NWT029    C     N11  D2DXO  LAST SEC CORR CE SEC DIFF    NGMAX*NPDE
NWT030    C     N12  A1     COEFF OF TIME DER TERM       NPDE
NWT031    C     N13  PHAI   PDE SPACE DEPENT TERMS       NPDE
NWT032    C     N14  WS     SURF VALUE OF W              NPDE
NWT033    C     N15  WJ     W VALUE AT J-TH GRID         NPDE
NWT034    C     N16  WGS    SOLUTION FROM GAUSS ELIM   NGMAX
NWT035    C     ***********************************************
NWT036    C
NWT037          IF(NIT.GT.0.OR.IEQN.GT.1) GOTO 20
NWT038          DO 9 I=1,NPDE
NWT039          IM=I-1
NWT040          JI=IM*NGMAX
NWT041          C(N10+JI)=0.0
NWT042          C(N11+JI)=0.0
NWT043          DO 10 J=2,M
NWT044          JI=IM*NGMAX+J-1
NWT045          C(N10+JI)=(A(J,5)*W(J-1,1,I)+A(J,6)*W(J,1,I)+A(J,7)*W(J+1,1,I))/
NWT046         1           DX1
NWT047       10 C(N11+JI)=A(J,1)*W(J-1,1,1)+A(J,2)*W(J,1,I)+A(J,3)*W(J+1,1,I)
NWT048         1           +A(J,4)*W(J+2,1,I)
NWT049        9 CONTINUE
NWT050    C
NWT051       20 J=1
NWT052          IEM=IEQN-1
NWT053          C(N2)=A(J,3)
NWT054          DO 11 I=1,NPDE
NWT055          IM=I-1
NWT056          IF(I.LE.IEM) GOTO 12
NWT057          C(N14+IM)=W(J,2,I)
NWT058          GOTO 11
NWT059       12 C(N14+IM)=W(J,3,I)
NWT060       11 CONTINUE
NWT061          CALL BNDRY(C(N14),WCH,T,FF,LSPUL,C(N4),V,C(N6),C(N7),NPDE)
NWT062          FJ=A(J,2)*W(J,2,IEQN)+A(J,3)*W(J+1,2,IEQN)+A(J,4)*W(J+2,2,IEQN)-C
NWT063         1   (N4+IEM)*DX1
NWT064          C(N14+IEM)=C(N14+IEM)+FJ
NWT065          CALL BNDRY(C(N14),WCH,T,FF,LSPUL,C(N5),FV,C(N6),C(N8),NPDE)
NWT066          C(N14+IEM)=C(N14+IEM)-FJ
NWT067          C(N1-1+J)=A(J,2)-(C(N5+IEM)-C(N4+IEM))/FJ*DX1
NWT068          C(N3-1+J)=-FJ
NWT069        1 J=J+1
NWT070          DO 13 I=1,NPDE
NWT071          IM=I-1
NWT072          IF(I.LE.IEM) GOTO 14
NWT073          C(N15+IM)=(W(J,2,I)+W(J,1,I))/2.
NWT074          C(N9+IM)=(A(J,5)*W(J-1,2,I)+A(J,6)*W(J,2,I)+A(J,7)*W(J+1,2,I))/
NWT075         1           DX1
NWT076          GOTO 13
NWT077       14 C(N15+IM)=(W(J,3,I)+W(J,1,I))/2.
NWT078          C(N9+IM)=(A(J,5)*W(J-1,3,I)+A(J,6)*W(J,3,I)+A(J,7)*W(J+1,3,I))/
NWT079         1           DX1
NWT080       13 C(N9+IM)=(C(N9+IM)+C(N10+IM*NGMAX+J-1))/2.
NWT081          CALL ACALC(C(N15),WCH,T,V,C(N9),C(N12),C(N13),DPHAI,IEQN,NFLAG,
NWT082         1            NPDE)
NWT083          D2DX=A(J,1)*W(J-1,2,IEQN)+A(J,2)*W(J,2,IEQN)+A(J,3)*W(J+1,2,IEQN)+
NWT084         1     A(J,4)*W(J+2,2,IEQN)
NWT085          FJ=D2DX+C(N11+IEM*NGMAX+J-1)-2.*(C(N12+IEM)*(W(J,2,IEQN)-
NWT086         1  W(J,1,IEQN))/DT-C(N13+IEM))*DX1**2
NWT087          AK=A(J,1)+A(J,5)*DPHAI*DX1
```

```
NWT088        BK=A(J,2)+A(J,6)*DPHAI*DX1-2.*C(N12+IEM)/DT*DX1**2
NWT089        CK=A(J,3)+A(J,7)*DPHAI*DX1
NWT090        C(N1-1+J)=BK-C(N2+J-2)*AK/C(N1+J-2)
NWT091        C(N2-1+J)=CK-A(J-1,4)*AK/C(N1+J-2)
NWT092        C(N3-1+J)=-FJ-AK*C(N3+J-2)/C(N1+J-2)
NWT093        IF(J.LT.M) GOTO 1
NWT094  C  BACK-SUBSTITUTION
NWT095        CALL GAUSS(C(N1),C(N2),C(N3),A(1,4),C(N16),M)
NWT096        L1=M+2
NWT097        DO 2 J=1,L1
NWT098     2  W(J,3,IEQN)=C(N16+J-1)+W(J,2,IEQN)
NWT099        RETURN
NWT100        END


GUS001        SUBROUTINE GAUSS(ALPHA,BETA,S,D,WGS,M)
GUS002  C
GUS003  C  BACK-SUBSTITUTION AFTER GAUSSIAN ELIMINATION
GUS004  C
GUS005        COMMON/GRID /DX1,EPS,EPS1,EPS2
GUS006        DIMENSION WGS(1)
GUS007        DIMENSION ALPHA(1),BETA(1),S(1),D(1)
GUS008  C
GUS009        AM1=ALPHA(M-1)-D(M-1)*EPS
GUS010        BM1=BETA(M-1)+D(M-1)*EPS1
GUS011        AMM=ALPHA(M)+BETA(M)*EPS1+D(M)*EPS2
GUS012        BMM=-BETA(M)*EPS-D(M)*EPS*EPS1
GUS013        WGS(M)=(S(M)-BMM*S(M-1)/AM1)/(AMM-BMM*BM1/AM1)
GUS014        WGS(M-1)=(S(M-1)-BM1*WGS(M))/AM1
GUS015        WGS(M+1)=WGS(M)*EPS1-WGS(M-1)*EPS
GUS016        WGS(M+2)=WGS(M+1)*EPS1-WGS(M)*EPS
GUS017        L=M-1
GUS018        DO 100 J=2,L
GUS019    100 WGS(M-J)=(S(M-J)-BETA(M-J)*WGS(M-J+1)-D(M-J)*WGS(M-J+2))/
GUS020       1          ALPHA(M-J)
GUS021        RETURN
GUS022        END


BDY001        SUBROUTINE BNDRY(WS,WCH,TAU,FF,LSPUL,BC,V,FLNR,FO,NPDE)
BDY002  C
BDY003  C  BOUNDARY CONDITION(S)
BDY004  C  (PROBLEM DEPENDENT BUT NOT MATER DEPENT)
BDY005  C
BDY006        COMMON/CHART/XCH,TCH
BDY007        COMMON/LASER/EI,QP,R,TPUL,AEFF
BDY008        COMMON/MATP /TM,HSUB,HFUS,EMISS,A3RM
BDY009        COMMON/MOLW /WM(5,5)
BDY010        DIMENSION WS(NPDE),BC(NPDE),FLNR(NPDE),FD(NPDE)
BDY011        DIMENSION WCH(NPDE)
BDY012        DIMENSION FF(LSPUL)
BDY013  C
BDY014        TEMP=WS(1)*WCH(1)
BDY015        OU=WS(2)*WCH(2)
```

```
BDY016        T=TAU*TCH
BDY017        IFLAG=4
BDY018        CALL MFLUX(T,TEMP,OU,FLUX,FLUX1,FLUX2,IFLAG)
BDY019        HVAP=HSUB
BDY020        IF(TEMP.GE.TM) HVAP=HVAP-HFUS
BDY021        C=XCH/(WCH(1)*COND(TEMP))
BDY022        QV=FLUX*HVAP*C
BDY023        QR=EMISS*(TEMP**4-298.2**4)*5.6686E-12*C
BDY024        QI=SOURCE(T,FF,LSPUL)*C
BDY025        BC(1)=QV+QR-QI
BDY026        FLNR(1)=QV/WS(1)+QR/WS(1)
BDY027        FO(1)=-QI
BDY028        V=WM(3,2)/WM(1,2)*FLUX2/RHO(TEMP)*TCH/XCH
BDY029        BC(2)=(WM(3,2)*FLUX1/(WM(2,1)*RHO(TEMP))-V*XCH/TCH*OU)*XCH/
BDY030       1(DIF(TEMP)*WCH(2))
BDY031        FLNR(2)=BC(2)/WS(2)
BDY032        FO(2)=0.0
BDY033        RETURN
BDY034        END


ACL001        SUBROUTINE ACALC(WJ,WCH,T,V,DDX,A1,PHAI,DPHAI,IEQN,NFLAG,NPDE)
ACL002  C
ACL003  C  COEFFICIENTS IN CONDUCTION AND DIFFUSION EQUATIONS
ACL004  C  (PROBLEM DEPENDENT BUT NOT MATER DEPENT)
ACL005  C
ACL006        COMMON/CHART/XCH,TCH
ACL007        COMMON/DIFFE/EH,EHEX,EL,ELEX
ACL008        COMMON/MATP /TM,HSUB,HFUS,EMISS,A3RM
ACL009        COMMON/TAB  /SCON(500),SA1(500),SA3(500)
ACL010        DIMENSION WJ(NPDE),WCH(NPDE)
ACL011        DIMENSION A1(NPDE),DDX(NPDE),PHAI(NPDE)
ACL012  C
ACL013        TEMP=WJ(1)*WCH(1)
ACL014        OU=WJ(2)*WCH(2)
ACL015        IF(IEQN.GT.1) GOTO 2
ACL016        IF(TEMP.LT.300.0.OR.TEMP.GE.TM) GOTO 10
ACL017        XI=TEMP/10.0-29.0
ACL018        I=XI
ACL019        A1(1)=SA1(I)+(XI-I)*(SA1(I+1)-SA1(I))
ACL020        A1(1)=A1(1)*XCH**2/TCH
ACL021        A3=SA3(I)+(XI-I)*(SA3(I+1)-SA3(I))
ACL022        A3=A3*WCH(1)
ACL023        GOTO 20
ACL024     10 A1(1)=SPHT(TEMP)/COND(TEMP)*RHO(TEMP)*XCH**2/TCH
ACL025        A3=0.0
ACL026     20 A2=V*A1(1)
ACL027        A4=0.0
ACL028        PHAI(1)=A2*DDX(1)+A3*DDX(1)**2+A4
ACL029        IF(NFLAG.GT.1) GOTO 100
ACL030      2 CONTINUE
ACL031        IF(TEMP.GE.TM) GOTO 30
ACL032        A3=EL/TEMP**2*WCH(1)
ACL033        GOTO 40
```

```
ACL034    30  A3=EH/TEMP**2*WCH(1)
ACL035    40  A1(2)=XCH**2/TCH/DIF(TEMP)
ACL036        A2=V*A1(2)
ACL037        A4=0.0
ACL038        PHAI(2)=A2*DDX(2)+A3*DDX(2)*DDX(1)+A4
ACL039   100  CONTINUE
ACL040        DPHAI=A2+A3/FLOAT(IEQN)*DDX(1)*2.
ACL041        RETURN
ACL042        END


PFL001        SUBROUTINE PRFLE(TS,TIME,WX,X,M,NPDE,NGMAX)
PFL002   C
PFL003   C  WRITE AND PLOT PROFILES WX AT TIME
PFL004   C  (NOT PROBLEM NOR MATER DEPENDENT)
PFL005   C  (FORMAT EASY TO MODIFY IF DESIRED)
PFL006   C
PFL007        COMMON/CHART/XCH,TCH
PFL008        COMMON/GRID /DX1,EPS,EPS1,EPS2
PFL009        COMMON/LASER/EI,QP,R,TPUL,AEFF
PFL010        DIMENSION WX(NGMAX,NPDE)
PFL011        DIMENSION X(NGMAX)
PFL012   C
PFL013        WRITE (6,100)
PFL014        WRITE (6,101) TS,TIME,EI,QP
PFL015        WRITE (6,102)
PFL016        WRITE (6,103)
PFL017        DX=DX1*XCH
PFL018        X(1)=0.0
PFL019        DO 20 J=2,M
PFL020    20  X(J)=X(J-1)+EPS**(J-2)*DX
PFL021        WRITE (6,104) (X(J),(WX(J,I),I=1,NPDE),J=1,M)
PFL022   C
PFL023   100 FORMAT(1H1,11X,105(1H*))
PFL024   101 FORMAT(1H0,14X,60HTEMPERATURE AND COMPOSITION PROFILES AT MAXIMUM
PFL025       1SURFACE TEMP,F7.1,13H DEG AT TIMAX,F7.4,5H MSEC/
PFL026       2             26X,8HFOR EI =,F7.3,14H (JOULES) QP =,E10.3,8H (W/CM2))
PFL027   102 FORMAT(1H0,11X,105(1H*)/)
PFL028   103 FORMAT(3(15X,5HX(CM),4X,7HTEMP(K),5X,4HCOMP))
PFL029   104 FORMAT(3(7X,E15.4,F9.1,F9.4))
PFL030   C
PFL031        RETURN
PFL032        END


PTS001        SUBROUTINE PLOTTS(X,Y,N,IFRM)
PTS002   C
PTS003   C, PLOT SURFACE TEMPERATURE VS TIME
PTS004   C
PTS005        DIMENSION SPECS(30),X(1),Y(1)
PTS006        DIMENSION SIDEX(3),SIDEY(3)
PTS007        DIMENSION BUFX(500),BUFY(500)
PTS008   C
PTS009   C  SET XDIST, YDIST (IN INCHES)
PTS010        SPECS(1)=1.5
PTS011        SPECS(2)=1.5
PTS012   C  SET XRIGHT, XLEFT, YTOP, YBOT
PTS013        SPECS(3)=0.5
PTS014        SPECS(4)=0.0
PTS015        SPECS(5)=5000.
PTS016        SPECS(6)=0.0
PTS017   C  SET XLNGTH, YLNGTH (IN INCHES)
PTS018        SPECS(7)=5.0
PTS019        SPECS(8)=5.0
PTS020   C  SET NO. OF DIVISIONS
PTS021        SPECS(9)=10.
PTS022        SPECS(10)=10.
PTS023   C  SPECIFY TOOL
PTS024        SPECS(11)=1.0
PTS025   C  SPECIFY INTERMEDIATE FILE NO.
PTS026        SPECS(12)=99.
PTS027        CALL AXLILI(SPECS)
PTS028   C  SPECIFY NO. OF DATA POINTS
PTS029        SPECS(13)=FLOAT(N)
PTS030   C  SET XSKIPS, YSKIPS
PTS031        SPECS(14)=1.
PTS032        SPECS(15)=1.
PTS033   C  SET FONTB,FONTH,SPACER,ROTATE,FONTNO
PTS034   C  FONT 2 FOR CHARACTERS OTHER THAN GRAPH TITLE
PTS035        SPECS(17)=0.08
PTS036        SPECS(18)=0.12
PTS037        SPECS(19)=0.04
PTS038        SPECS(20)=0.0
PTS039        SPECS(21)=2.0
PTS040   C  SET ZONES
PTS041        SPECS(24)=0.1
PTS042        SPECS(26)=0.05
PTS043   C  ANNOTATE HORIZONTAL AXIS
PTS044        SPECS(28)=2.0
PTS045        SPECS(29)=2.0
PTS046        SPECS(9)=5.0
PTS047        CALL NODLIB(SPECS)
PTS048   C  ANNOTATE VERTICAL AXIS
PTS049        SPECS(28)=1.0
PTS050        SPECS(29)=4.0
PTS051        SPECS(10)=10.0
PTS052        CALL NODLIL(SPECS)
PTS053   C  CONSTRUCT TITLE FOR X-AXIS
PTS054        CALL TITLEB(11HTIME (MSEC),SPECS)
PTS055   C  CONSTRUCT TITLE FOR Y-AXIS
PTS056        CALL TITLEL(23HSURFACE TEMPERATURE (K),SPECS)
PTS057   C  CONSTRUCT ANNOTATION OF GRAPH TITLE
PTS058   C  ALSO USE FONT 2
PTS059   C  SPECIFY XSTART, YSTART (INCHES)
PTS060        SPECS(22)=2.5
PTS061        SPECS(23)=4.0
PTS062        RULE=1.0
PTS063        CALL TITLEG(RULE,27HSURFACE TEMPERATURE VS TIME,SPECS)
```

```
PTS064        SPECS(23)=SPECS(23)-0.3
PTS065        CALL TITLEG(RULE,18HFOR EI =     JOULES,SPECS)
PTS066  C  PLOT DATA POINTS WITH SOLID LINE
PTS067        CALL PFLILI(X,Y,BUFX,BUFY,SPECS)
PTS068  C  PLOT LINES FOR TOP AND RIGHT EDGES OF PLOT AREA
PTS069        SIDEX(1)=SPECS(4)
PTS070        SIDEY(1)=SPECS(5)
PTS071        SIDEX(2)=SPECS(3)
PTS072        SIDEY(2)=SPECS(5)
PTS073        SIDEX(3)=SPECS(3)
PTS074        SIDEY(3)=SPECS(6)
PTS075        SPECS(13)=3.0
PTS076        CALL SLLILI(SIDEX,SIDEY,SPECS)
PTS077  C
PTS078  C  FINISH PLOT IF IT IS THE LAST ONE;
PTS079  C  OTHERWISE, CALL NEXT FRAME
PTS080        IF(IFRM.EQ.1) GOTO 1000
PTS081        CALL NXTFRM(SPECS)
PTS082        RETURN
PTS083   1000 CALL GDSEND(SPECS)
PTS084        RETURN
PTS085        END


PTX001        SUBROUTINE PLOTTX(X,Y,N,IFRM)
PTX002  C
PTX003  C  PLOT TEMPERATURE PROFILE VS SPACE
PTX004  C
PTX005        DIMENSION SPECS(30),X(1),Y(1)
PTX006        DIMENSION SIDEX(3),SIDEY(3)
PTX007        DIMENSION BUFX(500),BUFY(500)
PTX008  C
PTX009  C  SET XDIST, YDIST (IN INCHES)
PTX010        SPECS(1)=1.5
PTX011        SPECS(2)=1.5
PTX012  C  SET XRIGHT, XLEFT, YTOP, YBOT
PTX013        SPECS(3)=50.
PTX014        SPECS(4)=0.0
PTX015        SPECS(5)=5000.
PTX016        SPECS(6)=0.0
PTX017  C  SET XLNGTH, YLNGTH (IN INCHES)
PTX018        SPECS(7)=5.0
PTX019        SPECS(8)=5.0
PTX020  C  SET NO. OF DIVISIONS
PTX021        SPECS(9)=10.
PTX022        SPECS(10)=10.
PTX023  C  SPECIFY TOOL
PTX024        SPECS(11)=1.0
PTX025  C  SPECIFY INTERMEDIATE FILE NO.
PTX026        SPECS(12)=99.
PTX027        CALL AXLILI(SPECS)
PTX028  C  SPECIFY NO. OF DATA POINTS
PTX029        SPECS(13)=FLOAT(N)
PTX030  C  SET XSKIPS, YSKIPS
PTX031        SPECS(14)=1.
PTX032        SPECS(15)=1.
PTX033  C  SET FONTB,FONTH,SPACER,ROTATE,FONTNO
PTX034  C  FONT 2 FOR CHARACTERS OTHER THAN GRAPH TITLE
PTX035        SPECS(17)=0.08
PTX036        SPECS(18)=0.12
PTX037        SPECS(19)=0.04
PTX038        SPECS(20)=0.0
PTX039        SPECS(21)=2.0
PTX040  C  SET ZONES
PTX041        SPECS(24)=0.1
PTX042        SPECS(26)=0.05
PTX043  C  ANNOTATE HORIZONTAL AXIS
PTX044        SPECS(28)=0.0
PTX045        SPECS(29)=2.0
PTX046        SPECS(9)=5.0
PTX047        CALL NODLIB(SPECS)
PTX048  C  ANNOTATE VERTICAL AXIS
PTX049        SPECS(28)=1.0
PTX050        SPECS(29)=4.0
PTX051        SPECS(10)=10.0
PTX052        CALL NODLIL(SPECS)
PTX053  C  CONSTRUCT TITLE FOR X-AXIS
PTX054        CALL TITLEB(11HX (MICRONS),SPECS)
PTX055  C  CONSTRUCT TITLE FOR Y-AXIS
PTX056        CALL TITLEL(15HTEMPERATURE (K),SPECS)
PTX057  C  CONSTRUCT ANNOTATION OF GRAPH TITLE
PTX058  C  ALSO USE FONT 2
PTX059  C  SPECIFY XSTART, YSTART (INCHES)
PTX060        SPECS(22)=3.0
PTX061        SPECS(23)=5.0
PTX062        RULE=1.0
PTX063        CALL TITLEG(RULE,19HTEMPERATURE PROFILE,SPECS)
PTX064        SPECS(23)=SPECS(23)-0.3
PTX065        CALL TITLEG(RULE,19HAT MAX SURFACE TEMP,SPECS)
PTX066        SPECS(23)=SPECS(23)-0.3
PTX067        CALL TITLEG(RULE,18HFOR EI =     JOULES,SPECS)
PTX068  C  PLOT DATA POINTS WITH SOLID LINE
PTX069        CALL PFLILI(X,Y,BUFX,BUFY,SPECS)
PTX070  C  PLOT LINES FOR TOP AND RIGHT EDGES OF PLOT AREA
PTX071        SIDEX(1)=SPECS(4)
PTX072        SIDEY(1)=SPECS(5)
PTX073        SIDEX(2)=SPECS(3)
PTX074        SIDEY(2)=SPECS(5)
PTX075        SIDEX(3)=SPECS(3)
PTX076        SIDEY(3)=SPECS(6)
PTX077        SPECS(13)=3.0
PTX078        CALL SLLILI(SIDEX,SIDEY,SPECS)
PTX079  C
PTX080  C  FINISH PLOT IF IT IS THE LAST ONE;
PTX081  C  OTHERWISE, CALL NEXT FRAME
PTX082        IF(IFRM.EQ.1) GOTO 1000
PTX083        CALL NXTFRM(SPECS)
PTX084        RETURN
```

```
PTX085   1000 CALL GDSEND(SPECS)
PTX086        RETURN
PTX087        END

PRS001        SUBROUTINE PLOTRS(X,Y,N,IFRM)
PRS002   C
PRS003   C  PLOT SURFACE COMPOSITION VS TIME
PRS004   C
PRS005        DIMENSION SPECS(30),X(1),Y(1)
PRS006        DIMENSION SIDEX(3),SIDEY(3)
PRS007        DIMENSION BUFX(500),BUFY(500)
PRS008   C
PRS009   C  SET XDIST, YDIST (IN INCHES)
PRS010        SPECS(1)=1.5
PRS011        SPECS(2)=1.5
PRS012   C  SET XRIGHT, XLEFT, YTOP, YBOT
PRS013        SPECS(3)=0.5
PRS014        SPECS(4)=0.0
PRS015        SPECS(5)=2.0
PRS016        SPECS(6)=1.5
PRS017   C  SET XLNGTH, YLNGTH (IN INCHES)
PRS018        SPECS(7)=5.0
PRS019        SPECS(8)=5.0
PRS020   C  SET NO. OF DIVISIONS
PRS021        SPECS(9)=10.
PRS022        SPECS(10)=10.
PRS023   C  SPECIFY TOOL
PRS024        SPECS(11)=1.0
PRS025   C  SPECIFY INTERMEDIATE FILE NO.
PRS026        SPECS(12)=99.
PRS027        CALL AXLILI(SPECS)
PRS028   C  SPECIFY NO. OF DATA POINTS
PRS029        SPECS(13)=FLOAT(N)
PRS030   C  SET XSKIPS, YSKIPS
PRS031        SPECS(14)=1.
PRS032        SPECS(15)=1.
PRS033   C  SET FONTB,FONTH,SPACER,ROTATE,FONTNO
PRS034   C  FONT 2
PRS035        SPECS(17)=0.08
PRS036        SPECS(18)=0.12
PRS037        SPECS(19)=0.04
PRS038        SPECS(20)=0.0
PRS039        SPECS(21)=2.0
PRS040   C  SET ZONES
PRS041        SPECS(24)=0.1
PRS042        SPECS(26)=0.1
PRS043   C  ANNOTATE HORIZONTAL AXIS
PRS044        SPECS(28)=2.0
PRS045        SPECS(29)=2.0
PRS046        SPECS(9)=5.0
PRS047        CALL NODLIB(SPECS)
PRS048   C  ANNOTATE VERTICAL AXIS
PRS049        SPECS(28)=4.0
PRS050        SPECS(29)=5.0
PRS051        SPECS(10)=5.0
PRS052        CALL NODLIL(SPECS)
PRS053   C  CONSTRUCT TITLE FOR X-AXIS
PRS054        CALL TITLEB(11HTIME (MSEC),SPECS)
PRS055   C  CONSTRUCT TITLE FOR Y-AXIS
PRS056        CALL TITLEL(19HSURFACE COMPOSITION,SPECS)
PRS057   C  CONSTRUCT ANNOTATION OF GRAPH TITLE
PRS058   C  FONT 2 ALSO
PRS059   C  SPECIFY XSTART, YSTART (INCHES)
PRS060        SPECS(22)=3.0
PRS061        SPECS(23)=3.5
PRS062        RULE=1.0
PRS063        CALL TITLEG(RULE,27HSURFACE COMPOSITION VS TIME,SPECS)
PRS064        SPECS(23)=SPECS(23)-0.3
PRS065        CALL TITLEG(RULE,18HFOR EI =     JOULES,SPECS)
PRS066   C  PLOT DATA POINTS WITH SOLID LINE
PRS067        CALL PFLILI(X,Y,BUFX,BUFY,SPECS)
PRS068   C  PLOT LINES FOR TOP AND RIGHT EDGES OF PLOT AREA
PRS069        SIDEX(1)=SPECS(4)
PRS070        SIDEY(1)=SPECS(5)
PRS071        SIDEX(2)=SPECS(3)
PRS072        SIDEY(2)=SPECS(5)
PRS073        SIDEX(3)=SPECS(3)
PRS074        SIDEY(3)=SPECS(6)
PRS075        SPECS(13)=3.0
PRS076        CALL SLLILI(SIDEX,SIDEY,SPECS)
PRS077   C  FINISH PLOT IF IT IS THE LAST,
PRS078   C  OTHERWISE, CALL NEXT FRAME
PRS079        IF(IFRM.EQ.1) GOTO 1000
PRS080        CALL NXTFRM(SPECS)
PRS081        RETURN
PRS082   1000 CALL GDSEND(SPECS)
PRS083        RETURN
PRS084        END

PRX001        SUBROUTINE PLOTRX(X,Y,N,IFRM)
PRX002   C
PRX003   C  PLOT COMPOSITION PROFILE VS SPACE
PRX004   C
PRX005        DIMENSION SPECS(30),X(1),Y(1)
PRX006        DIMENSION SIDEX(3),SIDEY(3)
PRX007        DIMENSION BUFX(500),BUFY(500)
PRX008   C
PRX009   C  SET XDIST, YDIST (IN INCHES)
PRX010        SPECS(1)=1.5
PRX011        SPECS(2)=1.5
PRX012   C  SET XRIGHT, XLEFT, YTOP, YBOT
PRX013        SPECS(3)=50.
PRX014        SPECS(4)=0.0
PRX015        SPECS(5)=2.0
PRX016        SPECS(6)=1.5
PRX017   C  SET XLNGTH, YLNGTH (IN INCHES)
```

```
      SPECS(7)=5.0
      SPECS(8)=5.0
C  SET NO. OF DIVISIONS
      SPECS(9)=10.
      SPECS(10)=10.
C  SPECIFY TOOL
      SPECS(11)=1.0
C  SPECIFY INTERMEDIATE FILE NO.
      SPECS(12)=99.
      CALL AXLILI(SPECS)
C  SPECIFY NO. OF DATA POINTS
      SPECS(13)=FLOAT(N)
C  SET XSKIPS, YSKIPS
      SPECS(14)=1.
      SPECS(15)=1.
C  SET FONTB,FONTH,SPACER,ROTATE,FONTNO
C  FONT 2
      SPECS(17)=0.08
      SPECS(18)=0.12
      SPECS(19)=0.04
      SPECS(20)=0.0
      SPECS(21)=2.0
C  SET ZONES
      SPECS(24)=0.1
      SPECS(26)=0.1
C  ANNOTATE HORIZONTAL AXIS
      SPECS(28)=0.0
      SPECS(29)=2.0
      SPECS(9)=5.0
      CALL NODLIB(SPECS)
C  ANNOTATE VERTICAL AXIS
      SPECS(28)=4.0
      SPECS(29)=5.0
      SPECS(10)=5.0
      CALL NODLIL(SPECS)
C  CONSTRUCT TITLE FOR X-AXIS
      CALL TITLEB(11HX (MICRONS),SPECS)
C  CONSTRUCT TITLE FOR Y-AXIS
      CALL TITLEL(11HCOMPOSITION,SPECS)
C  CONSTRUCT ANNOTATION OF GRAPH TITLE
C  FONT 2 ALSO
C  SPECIFY XSTART, YSTART (INCHES)
      SPECS(22)=3.0
      SPECS(23)=5.0
      RULE=1.0
      CALL TITLEG(RULE,19HCOMPOSITION PROFILE,SPECS)
      SPECS(23)=SPECS(23)-0.3
      CALL TITLEG(RULE,19HAT MAX SURFACE TEMP,SPECS)
      SPECS(23)=SPECS(23)-0.3
      CALL TITLEG(RULE,18HFOR EI =      JOULES,SPECS)
C  PLOT DATA POINTS WITH SOLID LINE
      CALL PFLILI(X,Y,BUFX,BUFY,SPECS)
C  PLOT LINES FOR TOP AND RIGHT EDGES OF PLOT AREA
      SIDEX(1)=SPECS(4)
      SIDEY(1)=SPECS(5)
      SIDEX(2)=SPECS(3)
      SIDEY(2)=SPECS(5)
      SIDEX(3)=SPECS(3)
      SIDEY(3)=SPECS(6)
      SPECS(13)=3.0
      CALL SLLILI(SIDEX,SIDEY,SPECS)
C  FINISH PLOT IF IT IS THE LAST,
C  OTHERWISE, CALL NEXT FRAME
      IF(IFRM.EQ.1) GOTO 1000
      CALL NXTFRM(SPECS)
      RETURN
 1000 CALL GDSEND(SPECS)
      RETURN
      END


      SUBROUTINE PROP
C
C  THE MATERIAL PROPERTIES AND LASER CHARACTERISTICS
C  (NOT PROBLEM NOR MATER DEPENT)
C
      COMMON/DIFFE/EH,EHEX,EL,ELEX
      COMMON/LASER/EI,QP,R,TPUL,AEFF
      COMMON/MATP /TM,HSUB,HFUS,EMISS,A3RM
      COMMON/MOLW /WM(5,5)
      DIMENSION WA(2)
C
C  (MAX NO OF COMPONENTS      = 2
C   MAX NO OF ATOMS OF EACH
C   COMPONENT IN MOLECULE     = 4)
C  (FOR CONGRUENT VAPORIZATION, GIVE
C   WA(1) = WM AND WA(2) = 0)
C
C  MATERIAL PROPERTIES
      READ (5,100) (WA(I),I=1,2)
      WRITE (6,200) (WA(I),I=1,2)
      READ (5,101) TM,HSUB,HFUS,EMISS,A3RM
      WRITE (6,201) TM,HSUB,HFUS,EMISS,A3RM
      READ (5,102) EH,EHEX,EL,ELEX
      IF(EH.EQ.0.) GOTO 10
      WRITE (6,202) EH,EHEX,EL,ELEX
C
C  LASER CHARACTERISTICS
  10  READ (5,110) R,TPUL,AEFF
      WRITE (6,210) R,TPUL,AEFF
C
C  MOLECULAR WEIGHTS
      DO 1 N=1,5
      DO 1 M=1,5
      WM(N,M)=FLOAT(N-1)*WA(1)+FLOAT(M-1)*WA(2)
  1   CONTINUE
C
  100 FORMAT(2F10.0)
```

```
PRP038     101 FORMAT(4F10.0,E10.0)
PRP039     102 FORMAT(2(F10.0,E10.0))
PRP040     110 FORMAT(F10.0,2(E10.0))
PRP041     200 FORMAT(1H0,23HTHE MATERIAL PROPERTIES/
PRP042        1             5X,25HATOMIC WEIGHT OF COMP 1 =,F9.2/
PRP043        2             5X,25HATOMIC WEIGHT OF COMP 2 =,F9.2)
PRP044     201 FORMAT(1H0,4X,3HTM=,F5.0,5X,5HHSUB=,F5.0,5X,5HHFUS=,F5.0,
PRP045        1             5X,6HEMISS=,F5.3,5X,14HA3(ROOM TEMP)=,E10.3)
PRP046     202 FORMAT(1H0,4X,3HEH=,F7.0,5X,5HEHEX=,E9.2,5X,3HEL=,F7.0,
PRP047        1             5X,5HELEX=,E9.2)
PRP048     210 FORMAT(1H0,21HLASER CHARACTERISTICS/
PRP049        1             5X,2HR=,F5.3,5X,5HTPUL=,E10.4,4H SEC,
PRP050        2             5X,5HAEFF=,E10.4,4H CM2)
PRP051   C
PRP052          RETURN
PRP053          END

TBL001          SUBROUTINE TABLE
TBL002   C
TBL003   C  TABULATED A1, A3 AND COND BELOW MELTING TEMP
TBL004   C  (PROBLEM DEPENT BUT NOT MATER DEPENT)
TBL005   C
TBL006          COMMON/MATP /TM,HSUB,HFUS,EMISS,A3RM
TBL007          COMMON/TAB  /SCON(500),SA1(500),SA3(500)
TBL008   C
TBL009          IS=AINT((TM-300.)/10.)+2
TBL010          DO 1 I=1,IS
TBL011          TEMP=300.+10.*FLOAT(I-1)
TBL012          SCON(I)=COND(TEMP)
TBL013   C  SPHT CORRECTED WITH MELTING BY TREATING HFUS AS DELTA FUNCTION
TBL014          ARG=((TEMP-TM)/50.)**2
TBL015          IF(ARG.LT.20.) GOTO 11
TBL016          CPP=0.0
TBL017          GOTO 12
TBL018     11   CPP=HFUS/(SQRT(3.14159)*50.)*EXP(-ARG)
TBL019     12   SA1(I)=RHO(TEMP)*(SPHT(TEMP)+CPP)/SCON(I)
TBL020          IF(I.EQ.1) GOTO 13
TBL021          SA3(I)=(SCON(I)-SCON(I-1))/(10.*SCON(I))
TBL022          GOTO 1
TBL023   C  THE VALUE OF A3 AT ROOM TEMP (300 K)
TBL024     13   SA3(I)=A3RM
TBL025     1    CONTINUE
TBL026          RETURN
TBL027          END

ITL001          SUBROUTINE INITAL(W,WO,NPDE,NGMAX)
ITL002   C
ITL003   C  INITIAL CONDITIONS
ITL004   C  (PROBLEM DEPENT BUT NOT MATER DEPENT)
ITL005   C
ITL006          DIMENSION W(NGMAX,3,NPDE)
ITL007          DIMENSION WO(NPDE)
ITL008   C
ITL009          READ (5,100) (WO(I),I=1,NPDE)
ITL010          WRITE (6,200)
ITL011          WRITE (6,201) (I,WO(I),I=1,NPDE)
ITL012          DO 1 K=1,NPDE
ITL013          DO 1 I=1,NGMAX
ITL014          W(I,1,K)=1.0
ITL015          W(I,2,K)=1.0
ITL016          W(I,3,K)=1.0
ITL017     1    CONTINUE
ITL018          WRITE (6,300)
ITL019          WRITE (6,201) (I,W(1,1,I),I=1,NPDE)
ITL020   C
ITL021     100 FORMAT(F10.0)
ITL022     200 FORMAT(1H1,40HTHE INITIAL QUANTITY (WITH DIMENSION) OF/)
ITL023     201 FORMAT(11X,27HPARTIAL DIFFERENTIAL EQN NO,I2,2H =,F10.4)
ITL024     300 FORMAT(1H0,40HTHE INITIAL QUANTITY (DIMENSIONLESS)  OF/)
ITL025   C
ITL026          RETURN
ITL027          END

CHR001          SUBROUTINE CHAR(WO,WCH,NPDE)
CHR002   C
CHR003   C  DEFINE THE CHARACTERISTIC TERMS
CHR004   C  (PROBLEM DEPENT AND MAYBE MATER DEPENT)
CHR005   C
CHR006          COMMON/CHART/XCH,TCH
CHR007          COMMON/LASER/EI,QP,R,TPUL,AEFF
CHR008          COMMON/MATP /TM,H(4)
CHR009          DIMENSION WCH(NPDE),WO(NPDE)
CHR010   C
CHR011   C  THERMAL DIFFUSIVITY AT MELTING TEMPERATURE
CHR012          TDIFM=COND(TM)/(RHO(TM)*SPHT(TM))
CHR013   C
CHR014          TCH=TPUL
CHR015          XCH=SQRT(TDIFM*TCH)
CHR016          DO 1 I=1,NPDE
CHR017     1    WCH(I)=WO(I)
CHR018          WRITE (6,100)
CHR019          WRITE (6,200) TCH,XCH,(I,WCH(I),I=1,NPDE)
CHR020   C
CHR021     100 FORMAT(1H2,34HTHE CHARACTERISTIC QUANTITIES ARE:/)
CHR022     200 FORMAT(11X,29HCHARACTERISTIC TIME            =,E10.4,4H SEC/
CHR023        1        11X,29HCHARACTERISTIC DISTANCE        =,E10.4,4H  CM/
CHR024        2       (11X,25HCHARAC QUANTITY OF PDE NO,I2,2H =,F10.4))
CHR025          RETURN
CHR026          END

MFX001          SUBROUTINE MFLUX(TIME,T,R,F,F1,F2,IFLAG)
MFX002   C
MFX003   C  CALCULTION OF THE EVAPORATED MASS FLUXES (G/CM2-SEC)
MFX004   C  (PROBLEM AND MATERIAL DEPENDENT)
```

```
MFX005  C
MFX006        COMMON/MOLW /WM(5,5)
MFX007        DIMENSION P(5,5)
MFX008  C
MFX009        DO 9 N=1,5
MFX010        DO 9 M=1,5
MFX011      9 P(N,M)=0.
MFX012        CALL ROOT(T,R,P(3,1),P(2,1),P(1,2),P(2,2),P(3,2),P(4,2))
MFX013        PTOT=0.
MFX014        S0=0.
MFX015        S1=0.
MFX016        S2=0.
MFX017        DO 10 N=1,5
MFX018        DO 10 M=1,5
MFX019        IF(N.EQ.1.AND.M.EQ.1) GOTO 10
MFX020        PTOT=PTOT+P(N,M)
MFX021        S0=S0+SQRT(WM(N,M))*P(N,M)
MFX022        S1=S1+FLOAT(N-1)*P(N,M)/SQRT(WM(N,M))
MFX023        S2=S2+FLOAT(M-1)*P(N,M)/SQRT(WM(N,M))
MFX024     10 CONTINUE
MFX025        C=44.2/SQRT(T)*0.82
MFX026  C  44.2 = 3.5E22*760/6.023E23 - FLUX IN G/CM2-SEC
MFX027        F=C*S0
MFX028        F1=C*WM(2,1)*S1
MFX029        F2=C*WM(1,2)*S2
MFX030        IF(IFLAG.LT.1.OR.IFLAG.GT.3) RETURN
MFX031        GOTO (1,2,3),IFLAG
MFX032  C
MFX033      1 CONTINUE
MFX034        WRITE (6,100)
MFX035        WRITE (6,101) P(4,2),P(3,2),P(2,2),P(1,2),P(3,1),P(2,1),PTOT
MFX036        RETURN
MFX037  C
MFX038      2 CONTINUE
MFX039        WRITE (6,200)
MFX040  C
MFX041      3 CONTINUE
MFX042        WRITE (6,300) TIME,T,R,P(4,2),P(3,2),P(2,2),P(1,2),P(3,1),P(2,1),
MFX043       1              PTOT,F
MFX044  C
MFX045    100 FORMAT(1H2,6X,66HTHE EQUILIBRIUM VAPOR PRESSURES AT MAXIMUM SURFAC
MFX046       1E TEMPERATURE ARE//
MFX047       2              10X,5HP-UO3,5X,5HP-UO2,6X,4HP-UO,7X,3HP-U,6X,4HP-O2,
MFX048       3               7X,3HP-O,3X,7HP-TOTAL)
MFX049    101 FORMAT(1H ,4X,7(E10.3))
MFX050    200 FORMAT(1H ,5X,6HT(SEC),3X,5HTS(K),6X,3HO/U,5X,5HP-UO3,5X,5HP-UO2,
MFX051       1               6X,4HP-UO,7X,3HP-U,6X,4HP-O2,7X,3HP-O,
MFX052       2               3X,7HP-TOTAL,7X,4HFLUX)
MFX053    300 FORMAT(1H ,E11.3,F8.0,F9.4,7(E10.3),E11.3)
MFX054  C
MFX055        RETURN
MFX056        END
```

```
U02001        SUBROUTINE ROOT(TEMP,OU,PO2,PO,PU,PUO,PUO2,PUO3)
U02002  C
U02003  C  CALCULATION OF PARTIAL VAPOR PRESSURES OF URANIUM-OXYGEN
U02004  C  SYSTEM BASED ON BLACKBURN'S MODEL.
U02005  C  MODIFIED FROM SUBROUTINE DEVELOPED BY BLACKBURN FOR MIXED OXIDE
U02006  C
U02007        COMMON/CC/A1,A2,A3,A4,A5,A6,A7
U02008  C
U02009        Y=OU-2.0
U02010        IF(Y.LT.0.) Y=0.0
U02011        OOH=SQRT(OU)
U02012        OU2=OU**2
U02013        TM=3133.0
U02014  C
U02015  C  THERMODYNAMIC DATA
U02016        IF(TEMP.GT.TM) GOTO 60
U02017        DD=EXP(78260./TEMP-13.6)
U02018        EE=EXP(16350./TEMP-4.96-54.0*Y*Y)
U02019        FF=EXP(47000./TEMP-11.25)
U02020        GG=EXP(25100./TEMP-4.92)
U02021        CUC=EXP(-187200./TEMP+33.6)
U02022        CUOC=EXP(-128700./TEMP+27.3)
U02023        CUO2C=EXP(-72600./TEMP+20.3)
U02024        CUO3C=EXP(-28500./TEMP+10.5)
U02025        GOTO 70
U02026     60 DD=EXP((78260.-1.51*TM)/TEMP-12.066)
U02027        EE=EXP((16500.-1.006*TM)/TEMP-4.19-54.0*Y*Y)
U02028        FF=EXP((47000.-.755*TM)/TEMP-10.455)
U02029        GG=EXP((25100.-.755*TM)/TEMP-4.065)
U02030        CUC=EXP(-167900./TEMP+27.3)
U02031        CUOC=EXP(-108600./TEMP+20.8)
U02032        CUO2C=EXP(-51500./TEMP+13.4)
U02033        CUO3C=EXP(-5100./TEMP+2.8)
U02034  C
U02035     70 DEF=DD*EE*FF
U02036        FG=FF*GG
U02037        HH=DEF*GG/OU2*(3.0/OU-1.0)
U02038        PP=DEF/OU**1.5*(3.0/OU-1.0)
U02039        QQ=DD/OU*(3.0*EE/OU+2.0*FG/OU)+DD/OU*(-EE-FG)
U02040        RR=DD*FF/OOH*(2.0/OU-1.0)
U02041        SS=FG/OU+DD*(2.0/OU)+(-DD-FG)
U02042        TT=(1.0/OOH-OOH)*FF
U02043        A1=HH
U02044        A2=PP
U02045        A3=QQ
U02046        A4=RR
U02047        A5=SS
U02048        A6=TT
U02049        A7=1.0-OU
U02050  C
U02051        G=0.0
U02052        GTEST=G
U02053        G1=GTEST
U02054        DO 20 I=1,40
```

```
      DO 10 J=1,5
      FN=F(G1)
      FD=FP(G1)
      GS=G1-FN/FD
      G1=GS
      IF(G1.LT.0.0) G1=10.0
   10 CONTINUE
      G2=G1*G1
      G=G1
      U2=1.0/(1.0+G2*DD/OU+G2*G2*DD*EE/OU2)
      U4=U2*G2*DD/OU
      U6=U4*G2*EE/OU
      OM=U2+2.0*U4+3.0*U6
      ERELO=(OU-OM)/OU
      TESTO=ABS(ERELO)
      IF(TESTO.LT.1.0E-6) GOTO 50
      GOTO 20
   50 IF(G.LT.0.0) GOTO 40
      OMCK=OM
      GOTO 100
   20 CONTINUE
   40 PRINT 2
    2 FORMAT(90X,21HROOT DID NOT CONVERGE)
  100 PO2=G**4
      PO=SQRT(PO2)*EXP(-30103./TEMP+8.036)
      PU=U4/PO2*CUC
      PUO=U4/SQRT(PO2)*CUOC
      PUO2=U4*CUO2C
      PUO3=U4*SQRT(PO2)*CUO3C
      RETURN
      END


      FUNCTION F(X)
      COMMON/CC/A1,A2,A3,A4,A5,A6,A7
      F=(((((A1*X+A2)*X+A3)*X+A4)*X+A5)*X+A6)*X+A7
      RETURN
      END


      FUNCTION FP(X)
      COMMON/CC/A1,A2,A3,A4,A5,A6,A7
      FP=((((6.0*A1*X+5.0*A2)*X+4.0*A3)*X+3.0*A4)*X+2.0*A5)*X+A6
      RETURN
      END


      FUNCTION RHO(TEMP)
C
C  DENSITY OF UO2 IN G/CM3
C  GIVEN BY CHASANOV(1973) AND LEIBOWITZ(1976)
C
      DATA A,B,C,D/9.0E-6,6.0E-9,3.0E-12,10.98/
      DATA T1,A1,B1/3133.,10.658,-6.3609E-4/
      IF(TEMP.GE.T1) GOTO 1
      T=TEMP-273.
      RHO=D/(1.+A*T+B*T**2+C*T**3)
      RETURN
    1 RHO=A1+B1*TEMP
      RETURN
      END

      FUNCTION SPHT(TEMP)
C
C  SPECIFIC HEAT OF UO2 IN J/G-K
C  GIVEN BY KERRISK AND CLIFTON (1972) - BELOW TM
C    AND BY LEIBOWITZ (1971) - ABOVE TM
C
      DATA S,ED,A1,A2,A3/535.285,1.578E5,0.2968,1.217E-5,8.750E-8/
      DATA T1/3133./
      T=TEMP
      IF(T.GE.T1) GOTO 1
      R=8.314
      B=EXP(S/T)-1.
      CV=A1*S**2*EXP(S/T)/T**2/B**2
      SPHT=CV+2.*A2*T+A3*ED*EXP(-ED/(R*T))/(R*T**2)
      RETURN
    1 SPHT=0.503
      RETURN
      END


      FUNCTION COND(TEMP)
C
C  THERMAL CONDUCTIVITY OF UO2 IN W/CM-K
C  GIVEN BY SCHMIDT(1971) - BELOW TM
C  ASSUMED CONSTANT VALUE ABOVE TM
C
      DATA A,B/10.80,0.0218/
      DATA X,CVO,TO/2.00E-5,.299,2050./
      DATA T1,T2/1200.,2860./
      T=TEMP-273.
      IF(T.GE.T1) GOTO 1
      COND=1./(A+B*T)
      RETURN
    1 IF(T.GE.T2) GOTO 2
      F=(SPHT(TEMP)-X*T-CVO)/CVO
      Y=((T+TO)-(T-TO)*TANH(T-TO))/2.
      COND=(1./(A+B*Y))*(1.+F)
      RETURN
    2 COND=0.037
      RETURN
      END


      FUNCTION DIF(TEMP)
C
C  OXYGEN DIFFUSIVITY IN UO2 IN CM2/SEC
C  COEFFICIENTS READ FROM SUBROUTINE PROP
C
      COMMON/DIFFE/EH,EHEX,EL,ELEX
      IF(TEMP.GE.3133.) GOTO 1
      DIF=ELEX*EXP(-EL/TEMP)
      RETURN
    1 DIF=EHEX*EXP(-EH/TEMP)
      RETURN
      END
```

APPENDIX D: THERMODYNAMIC DATA AND MATERIAL PROPERTIES OF UO_2

D.1 Density

The density of solid UO_2 is given by Chasanov et al*[91]* as:

$$\rho = (10.98)/[1+9\times10^{-6}(T-273)+6\times10^{-9}(T-273)^2+3\times10^{-12}(T-273)^3] \quad \text{for } T<3140 \text{ K} \qquad \text{(D-1)}$$

The density of liquid UO_2 is given by Leibowitz et al*[92]* as:

$$\rho = 10.658 - 6.3609\times10^{-4}\,T \quad \text{for } T>3140 \text{ K} \qquad \text{(D-2)}$$

where ρ is in g/cm^3 and T is in K.

D.2 Specific Heat

The specific heat of solid UO_2 is given by Kerrisk and Clifton*[93]* as:

$$C_p = \frac{K_1\theta^2 e^{\theta/T}}{T^2(e^{\theta/T}-1)^2} + 2K_2T + \frac{K_3E_D}{RT^2}\, e^{-E_D/RT} \quad \text{for } T<3140 \text{ K} \qquad \text{(D-3)}$$

where θ = 535.285 K

$E_D = 1.578\times10^5$ J/mole

$K_1 = 0.2968$ J/g-K

$K_2 = 1.217\times10^{-5}$ J/g-K^2

$K_3 = 8.750\times10^{-8}$ J/g

R = 8.314 J/mole-K

and C_p is in J/g-K and T is in K.

The specific heat of liquid UO_2 is given by Leibowitz*[32]* as:

$$C_p = 0.503 \text{ J/g-K} \quad \text{for } T>3140 \text{ K} \qquad \text{(D-4)}$$

At the melting point, the enthalpy increment exhibits a discontinuity due to the phase change. This enthalpy of the phase transition is handled by an effective heat capacity term in the vicinity of the melting temperature.*[48]*

The molar enthalpy of a material at temperature T can be expressed in terms of the heat of fusion and the molar heat capacity at constant pressure C_p as follows:

$$H^{o}(T) = \begin{cases} H^{o}_{298}+\int_{298}^{T} C_p dT' & \text{if } T<T_{mp} \\ H^{o}_{298}+\Delta H_f+\int_{298}^{T} C_p dT' & \text{if } T>T_{mp} \end{cases} \tag{D-5}$$

Define an apparent molar heat capacity $\tilde{c}_p$:

$$\tilde{c}_p(T) = C_p(T) + \Delta H_f \delta(T-T_{mp}) \tag{D-6}$$

so that

$$H^{o}(T) = H^{o}_{298} + \int_{298}^{T} \tilde{c}_p(T')dT' \quad \text{for all } T \tag{D-7}$$

Since discontinuities in material properties are not desirable in the numerical solution of the conduction equation, the heat capacity is approximated by a continuous function of temperature; instead of using a delta function to account for the heat of fusion, a Gaussian function of finite width centered at the melting point is used. Thus $C_{pp} \equiv \Delta H_f \delta(T-T_{mp})$ is approximated by a function of Gaussian form:

$$C_{pp} = \frac{\Delta H_f}{\sqrt{\pi}\sigma_1} \exp^{-(\frac{T-T_{mp}}{\sigma_1})^2} \tag{D-8}$$

where ΔH_f = heat of fusion of UO_2 = 274.4 J/g*[94]*

T_{mp} = 3140 K*[95]*

σ_1 = half width of the heat of fusion peak = 50 K (arbitrary)

The apparent specific heat is:

$$\tilde{C}_p(T) = C_p(T) + C_{pp}(T) \tag{D-9}$$

D.3 Thermal Conductivity

The thermal conductivity of solid UO_2 is given by Schmidt*[96]* as:

$$k = 1/[10.80 + 0.0218(T-273)] \quad \text{for } T<1473 \text{ K} \tag{D-10}$$

$$k = (1+F)/(10.80 + 0.0218\,\theta) \quad \text{for } 1473 \text{ K}<T<3140 \text{ K} \tag{D-11}$$

$$\theta = [T+1777-(T-273)\tanh(T-2323)]/2$$

$$F = [C_p-2\times10^{-5}(T-273)-0.299]/0.299$$

where k is in W/cm-K, T is in K, and C_p is in J/g-K. The thermal conductivity of liquid UO_2 is assumed constant value (at melting temperature) of 0.037 W/cm-K with ±20% standard deviation.

D.4 Vapor Pressure

A computer subroutine following Blackburn's model*[82]*, "ROOT", is used to calculate the partial pressure of each vapor species as a function of both compos tion and temperature.

D.5 Heat of Vaporization

The heat of vaporization is assumed constant below the melting temperature:

$$\Delta H_{vap} = 2234 \text{ J/g} \qquad \text{for } T<3140 \text{ K} \tag{D-12}$$

given by Bogensberger et al*[98]* in which the averaged vapor pressure curve of Ohse*[7]* and Tetenbaum and Hunt*[5]* was fitted to the Claysius-Clapeyton equation.

Given the heat of fusion, 274.4 J/g, from Leibowitz, et al.*[99]*, the heat of vaporization above the melting point is:

$$\Delta H_{vap} = 2234 - 274.4 = 1959.6 \text{ J/g} \quad \text{for } T>3140 \text{ K} \tag{D-13}$$

D.6 Diffusion Coefficient of Oxygen

For T<3140 K, the diffusion coefficient of oxygen in solid UO_2 is given by Belle*[100]* as:

$$D_o = 1.15 \exp(-28550/T) \qquad \text{for } T<3140 \text{ K} \tag{D-14}$$

Since the diffusion coefficient of oxygen in molten UO_{2-x} is not available, estimates of upper and lower limits are made in this calculation. An upper estimate can be arrived at with the aid of kinetic gas theory*[81]*. In a ideal gas the diffusion coefficient is $D = \frac{1}{3}\bar{l}\,\bar{v}$, where $\bar{l}$ is the mean free path and $\bar{v}$ is the mean velocity of the gas molecules. If the interionic distance in the oxide melt (~10 Å) is introduced for $\bar{l}$, then $D_o = 7.4\times10^{-3}$ cm^2/sec at 3140 K and 1.1×10^{-2} cm^2/sec at 7560 K (the critical temperature estimated by Ohse*[79]*). In this case, D_o is approximately

$$(D_o)_{max} = 1.6\times10^{-2} \exp(-2500/T) \quad \text{for } T>3140 \text{ K} \tag{D-15}$$

where $(D_o)_{max}$ is in cm^2/sec and T is in K. This sets up an upper limit of diffusion coefficient at the temperature of interest, since the ions in the oxide melt cannot move unimpeded between collisions in the same way as gas molecules. Instead, molecules in the liquid migrate from one potential ste to an adjacent one, remaining in each site for a certain time. A lower estimate is based upon the fact that the diffusion coefficient in the liquid oxide is higher than that in the solid.

$$(D_o)_{min} = 3.0\times10^{-1}\exp(-25000/T) \quad \text{for } T>3140 \text{ K} \qquad \text{(D-16)}$$

This equation was obtained by taking $D_o = 1.1\times10^{-4}$ cm^2/sec from Belle*[100]* at 3140 K and 1.1×10^{-2}cm^2/sec at 7560 K.

D.7 Optical Emissivity

The spectral emissivity at λ = 6500 Å is given by Held and Wilder*[101]* as:

$$\epsilon_{\lambda=6500\text{Å}} = 0.83 \qquad \text{(D-17)}$$

which is found insensitive to the temperature over a wide temperature range (450 - 2400 K). It is proposed*[92]* that $\epsilon_{\lambda=6500\text{Å}}$ be constant up to the melting point.

Above the melting point $\epsilon_{\lambda=6500\text{Å}}$ is measured by Bober*[53]* as:

$$\epsilon_{\lambda=6500\text{Å}} = 0.81 \text{ to } 0.87 \quad \text{for } 3140 \text{ K}<T<3700 \text{ K} \qquad \text{(D-18)}$$

No data is available on the total hemispherical emissivity of UO_2, so an average value of 0.83 at all temperatures is adopted.

APPENDIX E: CALCULATION OF THE TRANSITION FROM FREE MOLECULE TO COLLISIONAL FLOW IN THE VAPOR PLUME

E.1 Introduction

In previous investigations, the free molecular flow model has been assumed in the interpretation of the mass spectrometer measurement to obtain the rate of vaporization, and ultimately the saturation vapor pressure*[48]*. In this model, it is assumed that the gas molecules ejected from the vaporizing surface will not undergo any collision or the collision probability is so low that the molecules are simply freely expanding into the vacuum and the molecular density decreases as the inverse of the square of the distance. It has been pointed out*[102]*, however, that at high temperatures the vapor near the surface is so dense that the blowoff is dominated by collisional interactions of the vapor molecules. It is then experimentally verified that molecular flow breaks down at pressures exceeding 10^{-4} atm*[11]*. It is attempted in this appendix to provide a simple method of estimating the transition from free molecular flow to collision-dominated flow.

E.2 Model

The calculation is based on the test particle method. Basically, a test particle is chosen and the escape probability defined as the probability that the test particle does not undergo collision along the path to the ionizer of the mass spectrometer some distance away from the vaporizing source.

The assumptions of the model are:

(i) The heated area is a circular spot of radius R over which the temperature is uniform. The vaporizing molecules (both the "test" molecule and the "background" molecules in the plume) are from the same source and posess the temperature of the surface at the time they were evaporated.

(ii) All molecules emitted at time t are of the same speed equal to the mean speed of the Maxwellian velocity distribution characteristic of the evaporation temperature at time t.

(iii) The vaporizing molecules have a cosine angular distribution with respect to the surface normal.

Three cases in increasing order of complexity are considered:

(A) *Steady state evaporation source with the mean free path calculated by the hard sphere model*

Let

$$\lambda(z) = [\sqrt{2}\pi\sigma^2 n(z)]^{-1} \tag{E-1}$$

be the mean free path at distance z from the surface along the centerline, σ the collision diameter (i.e. $\pi\sigma^2$ is the collision cross section), and n the molecular density of the vapor plume at distance z.

The molecular density from a cosine disk source of radius R with temperature T_0 and equilibrium vapor pressure $P^o(T_0)$ along the centerline is

$$n(z) = \frac{P^o(T_0)}{2kT_0}\left[1 - \frac{z}{\sqrt{R^2+z^2}}\right] \tag{E-2}$$

where an evaporation coefficient of unity is assumed.

The escape probability is

$$\begin{aligned} P_e &= \exp[-\int_0^L \frac{dz}{\lambda(z)}] \\ &= \exp\{-\frac{\sqrt{2}\pi\sigma^2 P^o(T_0)}{2kT_0}(L+R-\sqrt{L^2+R^2})\} \end{aligned} \tag{E-3}$$

When L>>R

$$P_e \approx \exp\{-\frac{\sqrt{2}\pi\sigma^2 P^o(T_0)}{2kT_0} R(1-\frac{R}{2L})\} \tag{E-4}$$

(B) *Unsteady state source with the mean free path given by the hard sphere model*

This case better simulates laser pulse vaporization than case (A); the surface temperature $T_S(t)$ is a known function of time, but is constant at any time over the surface area. The escape probability $P_e(t)$ of the test particle coming from the surface at t is

$$P_e(t) = \exp[-\int_0^L \sqrt{2}\pi\sigma^2 n(z,t')dz] \tag{E-5}$$

where n(z,t') is the molecular density of the plume at distance z along the centerline at time t' when the test particle (having been evaporated at time t) arrives at z; in other words, t and t' are related by:

$$t' = t + \frac{z}{v_{tp}} = t + \frac{z}{\beta\sqrt{T_s(t)}} \tag{E-6}$$

where v_{tp} is the velocity of the test particle, taken as the root mean square velocity in equilibrium with T_s, so that β is equal to $(\frac{8k}{\pi m})^{1/2}$.

To calculate n(z,t'), consider a molecule contributing to n(z,t') coming from radius r' on the surface; this molecule was evaporated at time τ, which is related to r' and t' by

$$t'-\tau = \frac{\sqrt{r'^2+z^2}}{\beta\sqrt{T_s(\tau)}} \tag{E-7}$$

The number of molecules leaving a surface ring element dA'=2πr'dr' at radius r' per unit time at time τ and contributing to a unit area at z is

$$\Phi(r',z,\tau)dA' = \frac{P^o[T_s(\tau)]}{kT_s(\tau)}\,\beta\sqrt{T_s(\tau)}\,\frac{z2\pi r'dr'}{(z^2+r'^2)^{1/2}}\,\frac{1}{4\pi(z^2+r'^2)} \tag{E-8}$$

So the contribution of the surface ring element dA' to the molecular density n(z,t') is

$$dn = \sum_i \frac{P^o[T_s(\tau_i)]}{2kT_s(\tau_i)}\,\frac{zr'dr'}{(z^2+r'^2)^{3/2}} \tag{E-9}$$

where τ_i's are the roots of Eq. (E-7). In solving the roots τ_i's, note that t' in Eq. (E-7) is related to t and z through Eq. (E-6).

Integrating dn over the heated surface yields:

$$n(z,t') = \int_0^R \sum_i \frac{P^o[T_s(\tau_i)]}{2kT_s(\tau_i)}\,\frac{zr'dr'}{(z^2+r'^2)^{3/2}} \tag{E-10}$$

Therefore, the escape probability from Eq. (E-5) is:

$$P_e(t) = \exp\{-\int_0^L \sqrt{2}\pi\sigma^2\int_0^R \sum_i \frac{P^o[T_s(\tau_i)]}{2kT_s(\tau_i)}\,\frac{zr'dr'}{(z^2+r'^2)^{3/2}}\,dz\} \tag{E-11}$$

Define dimensionless variables:

$$\eta = \frac{z}{L}; \quad \xi = \frac{r'}{R} \tag{E-12}$$

Then Eq. (E-11) becomes:

$$P_e(t) = \exp\{-C_b \int_0^1\int_0^1 \sum_i \frac{P^o[T_s(\tau_i)]}{T_s(\tau_i)} \frac{\eta\xi}{(\eta^2+\frac{R^2}{L^2}\xi^2)^{3/2}} d\xi d\eta\} \tag{E-13}$$

where the coefficient C_b is equal to $\frac{\sqrt{2}\pi\sigma^2R^2}{2kL}$. Eq. (E-13) can be solved numerically. Note that in the evaluation of the integrand, when η and ξ are given, T_s can be evaluated at time τ_i for a given t where the former can be solved iteratively from the equation:

$$t + \frac{\eta L}{\beta\sqrt{T_s(t)}} = \tau_i + \frac{\sqrt{\eta^2L^2+\xi^2R^2}}{\beta\sqrt{T_s(\tau_i)}} \tag{E-14}$$

In solving Eq. (E-13), it is found profitable to transform the variable from ξ to τ. These two are related by Eq. (E-14). Rearranging Eq. (E-14), we have:

$$\sqrt{\xi^2R^2+\eta^2L^2} = \beta\sqrt{T_s(\tau)}\ [t - \tau + \frac{\eta L}{\beta\sqrt{T_s(t)}}] \tag{E-15}$$

or,

$$\xi^2 = -\eta^2\frac{L^2}{R^2} + \frac{\beta^2 T_s(\tau)}{R^2}\ [t - \tau + \frac{\eta L}{\beta\sqrt{T_s(t)}}] \tag{E-16}$$

Taking the derivative with respect to τ:

$$\frac{d\xi^2}{d\tau} = \frac{\beta^2}{R^2}\frac{dT_s(\tau)}{d\tau}\ [t-\tau+\frac{\eta L}{\beta\sqrt{T_s(t)}}]^2 - \frac{\beta^2 T_s(\tau)}{R^2}\ 2[t-\tau+\frac{\eta L}{\beta\sqrt{T_s(t)}}] \tag{E-17}$$

or,

$$d\xi^2 = \frac{\beta^2}{R^2}\ [t-\tau+\frac{\eta L}{\beta\sqrt{T_s(t)}}]\ \{[t-\tau+\frac{\eta L}{\beta\sqrt{T_s(t)}}]\ \frac{dT_s(\tau)}{d\tau} - 2T_s(\tau)\}d\tau \tag{E-18}$$

Since $d\xi^2 = 2\xi d\xi$, the integral in Eq. (E-13) becomes:

$$\sum_i \int_0^1\int_0^1 \frac{P^o[T_s(\tau_i)]}{T_s(\tau_i)} \frac{\eta\xi}{(\eta^2+\frac{R^2}{L^2}\xi^2)^{3/2}} d\xi d\eta$$

$$= \sum_i \int_0^1\int_0^1 \frac{1}{2} \frac{P^o[T_s(\tau_i)]}{T_s(\tau_i)} \frac{\eta}{(\eta^2+\frac{R^2}{L^2}\xi^2)^{3/2}} d\xi^2 d\eta$$

$$= \sum_i \int_0^1 \int_{b_i}^{a_i} \frac{N(\eta,\tau)}{[D(\eta,\tau)]^{3/2}} d\tau d\eta \tag{E-19}$$

where

$$D(\eta,\tau) = \frac{\beta^2 T_s(\tau)}{L^2} [t - \tau + \frac{\eta L}{\beta\sqrt{T_s(t)}}]^2$$

$$N(\eta,\tau) = \frac{\eta}{2} \frac{P^o[T_s(\tau)]}{T_s(\tau)} \frac{\beta^2}{R^2} [t-\tau+\frac{\eta L}{\beta\sqrt{T_s(t)}}] \{2T_s(\tau) - \frac{dT_s(\tau)}{d\tau}[t-\tau+\frac{\eta L}{\beta\sqrt{T_s(t)}}]\}$$

and a_i, b_i are function of η and are the roots of Eq. (E-14) when $\xi=1$ and $\xi=0$ respectively.

Furthermore, the integrand can be reduced to:

$$\frac{N(\eta,\tau)}{[D(\eta,\tau)]^{3/2}} = \frac{L^3}{\beta R^2} \frac{\dfrac{2T_s(\tau)}{t-\tau+\dfrac{\eta L}{\beta\sqrt{T_s(t)}}} - \dfrac{dT_s(\tau)}{d\tau}}{T_s(\tau)^{3/2}[t-\tau+\dfrac{\eta L}{\beta\sqrt{T_s(t)}}]} \tag{E-20}$$

Therefore, the escape probability of test particle evaporated at time t will be:

$$P_e(t) = \exp\{-C_B \sum_i \int_0^1 \int_{a_i}^{b_i} \frac{\eta}{2} \frac{P^o[T_s(\tau)]}{T_s(\tau)^{5/2}} \frac{\dfrac{2T_s(\tau)}{t-\tau+\dfrac{\eta L}{\beta\sqrt{T_s(t)}}} - \dfrac{dT_s(\tau)}{d\tau}}{t-\tau+\dfrac{\eta L}{\beta\sqrt{T_s(t)}}} d\tau d\eta\} \tag{E-21}$$

where $C_B = \dfrac{\sqrt{2}\pi\sigma^2 L^2}{2k\beta}$.

Note that, after replacing surface temperature $T_s(\tau)$ with a constant temperature T_o, Eq. (E-21) reduces to Eq. (E-3), showing the consistency of the model. The numerical calculation was also checked with constant temperature and compared with the analytical result in case (A).

(C) *Corrections of the mean free path formula by the relative speed of collision:*

The mean free path in Eq. (E-1) assumes that the molecules in collision are randomly moving in all directions; however, in the problem considered here, this is not the case. Consider a "probe" molecule A moving through a gas of stationary molecules B of density n. In one second, the A molecule moves a total path length of v_A and in so doing, it will collide with any B molecule in the volume $\pi\sigma^2 v_A$. So the collisions of probe molecule A per second is $\pi\sigma^2 v_A n$. Now if B molecules are moving with a vector velocity $\vec{v}_B$, the above derivation of collision frequency with stationary B molecules will be recovered if the relative velocity $g=|\vec{v}_A-\vec{v}_B|$ is used instead of v_A; that is, the number of collisions per second of probe molecule of velocity $\vec{v}_A$ with B molecules of velocity $\vec{v}_B$ is $\pi\sigma^2 gn$, where $g=[v_A^2+v_B^2-2v_A v_B \cos\theta]^{1/2}$ is the relative speed. Since the distance moved by the A molecule per second is v_A, the collisions of molecule A with B molecules per unit path length of A molecule is $\pi\sigma^2 gn/v_A$ and so the mean free path of a test molecule moving in z direction in our problem will be

$$\lambda(z) = [(\frac{g}{v_{tp}})\pi\sigma^2 n(z)]^{-1} \tag{E-22}$$

Here it is still assumed that all the background molecules in n(z) are moving in the same direction with the same velocity so that they have the same relative velocity g with the test particle.

To account for the fact that the molecules in n(z) are in fact not moving with same velocity, let us start over again from dn in Eq. (E-9), which gives the contribution of molecules from a surface ring element dA' of radius r' evaporated at the same time τ_i. The relative velocity of these molecules with respect to the test particle is:

$$g^2 = v_{tp}^2+v^2-2v_{tp}v\cos\theta \tag{E-23}$$

$$\text{where} \quad \cos\theta = \frac{z}{\sqrt{z^2+r'^2}}; \quad v_{tp} = \beta\sqrt{T_s(t)}; \quad v = \beta\sqrt{T_s(\tau)} \tag{E-24}$$

Applying Eqs. (E-9) and (E-16) to the mean free path Eq. (E-15) yields:

$$\begin{aligned} \frac{1}{\lambda(z)} &= \int (\frac{g}{v_{tp}})\pi\sigma^2 dn \\ &= \pi\sigma^2\int_0^R \sum_i [1+\frac{v^2}{v_{tp}^2}-2\frac{v}{v_{tp}} \frac{z}{\sqrt{z^2+r'^2}}]^{1/2} \frac{P^o[T_s(\tau_i)]}{2kT_s(\tau_i)} \frac{zr'dr'}{(z^2+r'^2)^{3/2}} \\ &= \frac{\pi\sigma^2}{2k}\int_0^R \sum_i [1+\frac{T_s(\tau_i)}{T_s(t)}-2\sqrt{\frac{T_s(\tau_i)}{T_s(t)}} \frac{z}{\sqrt{z^2+r'^2}}]^{1/2} \frac{P^o[T_s(\tau_i)]}{T_s(\tau_i)} \frac{zr'dr'}{(z^2+r'^2)^{3/2}} \end{aligned} \tag{E-25}$$

Therefore, the escape probability

$$P_e(t) = \exp[-\int_0^L \frac{dz}{\lambda(z)}]$$

$$= \exp\{-\frac{\pi\sigma^2}{2k}\int_0^L\int_0^R \sum_i [1+\frac{T_s(\tau_i)}{T_s(t)}-2\sqrt{\frac{T_s(\tau_i)}{T_s(t)}}\frac{z}{\sqrt{z^2+r'^2}}]^{1/2} \frac{P^o[T_s(\tau_i)]}{T_s(\tau_i)}\frac{zr'}{(z^2+r'^2)^{3/2}}dr'dz\} \tag{E-26}$$

Substituting with dimensionless variables in Eq. (E-12), we have:

$$P_e(t) = \exp\{-C_c\int_0^1\int_0^1 \sum_i [1+\frac{T_s(\tau_i)}{T_s(t)}-2\sqrt{\frac{T_s(\tau_i)}{T_s(t)}}\frac{\eta}{\sqrt{\eta^2+\frac{R^2}{L^2}\xi^2}}]^{1/2} \frac{P^o[T_s(\tau_i)]}{T_s(\tau_i)}\frac{\xi\eta}{(\eta^2+\frac{R^2}{L^2}\xi^2)^{3/2}}d\xi d\eta\} \tag{E-27}$$

where the coefficient C_c is equal to $\frac{\pi\sigma^2R^2}{2kL}$.

Having made the same variable transformation as in case B, the escape probability of the test particle evaporated at time t considering relative velocity will be:

$$P_e(t) = \exp\{-C_C\sum_i\int_0^1\int_{a_i}^{b_i} [1+\frac{T_s(\tau)}{T_s(t)}-2\sqrt{\frac{T_s(\tau)}{T_s(t)}}\frac{\eta}{\frac{\beta\sqrt{T_s(\tau)}}{L}[t-\tau+\frac{\eta L}{\beta\sqrt{T_s(t)}}]}]^{1/2} \frac{\eta}{2}\frac{P^o[T_s(\tau)]}{T_s(\tau)^{5/2}}\frac{\frac{2T_s(\tau)}{t-\tau+\frac{\eta L}{\beta\sqrt{T_s(t)}}}-\frac{dT_s(\tau)}{d\tau}}{t-\tau+\frac{\eta L}{\beta\sqrt{T_s(t)}}}d\tau d\eta\} \tag{E-28}$$

where $C_C = \frac{\pi\sigma^2L^2}{2k\beta}$, and a_i, b_i are given in Eq. (E-19).

E.3 Results

Assuming the surface temperature transients are generated by a triangular surface heat flux with the form:

$$q_s(t) = \begin{cases} \frac{q_p t}{\tau_1} & \text{for } 0 < t < \tau_1 \\ (\frac{\tau_2-t}{\tau_2-\tau_1})q_p & \text{for } \tau_1 < t < \tau_2 \\ 0 & \text{for } t > \tau_2 \end{cases} \tag{E-29}$$

where q_p = absorbed power density at the peak of the triangular pulse

τ_1 = time corresponding to the peak of the pulse

τ_2 = time of the end of the triangular pulse

and assuming that there is no ablation, radiation heat loss, and the thermal properties are not temperature dependent, the heat conduction problem can be solved analytically to give the surface temperature transient as:

$$T_s(t)-T_o = \frac{4q_p}{3k}\left(\frac{K}{\pi}\right)^{1/2}\left[\frac{t^{3/2}}{\tau_1} - \frac{\tau_2}{\tau_1}\,\frac{(t-\tau_1)^{3/2}}{(\tau_2-\tau_1)}\,H(t-\tau_1) + \frac{(t-\tau_2)^{3/2}}{\tau_2-\tau_1}\,H(t-\tau_2)\right] \qquad \text{(E-30)}$$

where k is the thermal conductivity, K is the thermal diffusivity, T_o is the initial temperature and

$$H(t-\tau_i) \begin{array}{ll} = 1 & \text{for } t > \tau_i \\ = 0 & \text{for } t < \tau_i \end{array} \qquad \text{(E-31)}$$

Numerical analyses were performed for the following parameters:

$\sigma = 3.7\times10^{-8}$ cm

$\alpha = 1$

$R = 0.40$ cm

$L = 40$ cm ($\approx\infty$)

$\kappa = 0.113$ W/cm-K

$K = 2.6\times10^{-2}$ cm^2/sec

$\tau_1 = 0.07\times10^{-3}$ sec

$\tau_2 = 0.192\times10^{-3}$ sec

$q_p = 5\times10^4$ to 2×10^5 W/cm^2

(corresponding to the peak power densities, the maximum surface temperature are 1980 to 3720 K).

Fig. E.1 shows the escape probability of each case in Sect. E.2 as a function of temperature (in cases B and C, P_e refers to the maximum temperature). The result shows that transition to collisional flow starts at about 2100 K and becomes collision-dominating from 2800 K in case A, 2900 K in case B and 3000 K in case C. The edge shifts to higher temperature as some of the simplifying assumptions are relaxed.

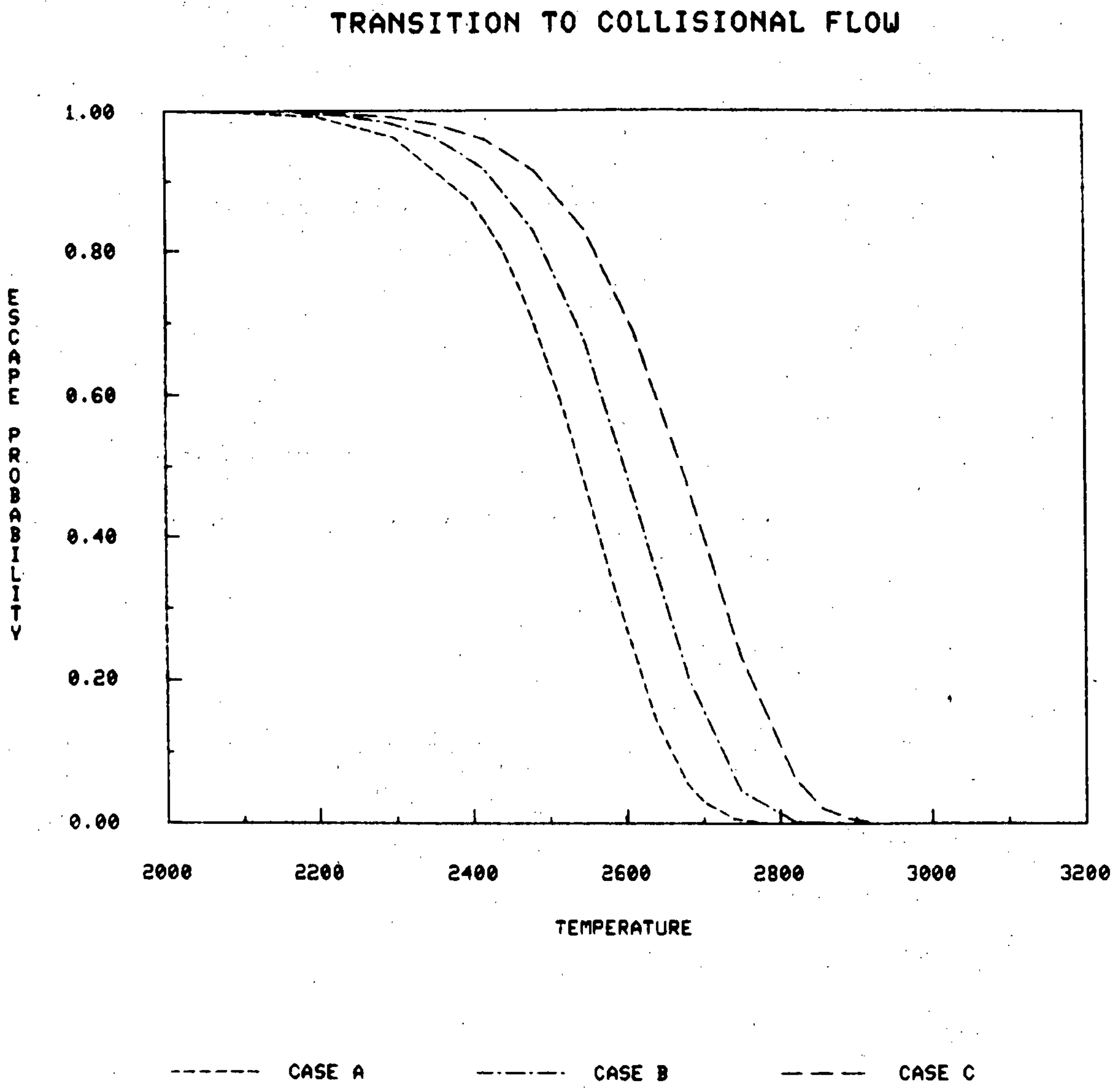

XBL 8110-12288

Fig. E.1 The escape probability of a test particle from a vaporizing surface to the mass spectrometer

APPENDIX F: MACH DISC FORMULA FOR THE FREE-JET FROM A SONIC ORIFICE

The Mach disc formula given by Eq. (4-2) has been derived semi-empirically for the type of shock structure shown in Fig. 4.10 using two different approaches: *[104]*

(I) *Pressure Matching at the normal shock front*:

Let us start with the conservation equations before and after the shock:

$$\rho_1 u_1 = \rho_2 u_2 \tag{F-1}$$

$$p_1 + \rho_1 u_1^2 = p_2 + \rho_2 u_2^2 \tag{F-2}$$

$$\frac{1}{2}u_1^2 + \frac{\gamma}{\gamma-1}\frac{p_1}{\rho_1} = \frac{1}{2}u_2^2 + \frac{\gamma}{\gamma-1}\frac{p_2}{\rho_2} \tag{F-3}$$

where ρ, u and p are the density, velocity and pressure respectively, subscripts 1 and 2 represent the quantities before and after the normal shock, and γ is the specific heat ratio (or adiabatic exponent).*

Defining the Mach numbers as:

$$M = \text{the Mach number before the shock} = \frac{u_1}{c_1} = \frac{u_1}{\sqrt{\gamma p_1/\rho_1}} \tag{F-4}$$

$$M_2 = \text{the Mach number after the shock} = \frac{u_2}{c_2} = \frac{u_2}{\sqrt{\gamma p_2/\rho_2}}, \tag{F-5}$$

where $c_i = \sqrt{\gamma p_i/\rho_i}$ is the sonic velocity.

Then Eqs. (F-1) to (F-3) become:

$$M\sqrt{p_1\rho_1} = M_2\sqrt{p_2\rho_2} \tag{F-6}$$

$$p_1(1+\gamma M^2) = p_2(1+\gamma M_2^2) \tag{F-7}$$

$$\frac{p_1}{\rho_1}\left(\frac{1}{2}M^2 + \frac{1}{\gamma-1}\right) = \frac{p_2}{\rho_2}\left(\frac{1}{2}M_2^2 + \frac{1}{\gamma-1}\right) \tag{F-8}$$

From Eq. (F-7), we obtain the ratio of the pressure before and after the shock in terms of Mach numbers:

$$\frac{p_1}{p_2} = \frac{1+\gamma M_2^2}{1+\gamma M^2} \tag{F-9}$$

---

*Without considering the energy mode relaxation in the free-jet expansion, γ is assumed constant for the entire process.

The ratio of the densities is determined from (F-6) as:

$$\frac{\rho_1}{\rho_2} = \frac{M_2^2 p_2}{M^2 p_1} = \frac{M_2^2}{M^2}\,\frac{1+\gamma M^2}{1+\gamma M_2^2} \tag{F-10}$$

After applying Eqs. (F-9) and (F-10) into Eq. (F-8), it can be shown that the Mach number after the shock can be related to the Mach number before the shock by the following relation:

$$M_2^2 = \frac{1+\frac{\gamma-1}{2}M^2}{\gamma M^2 - \frac{\gamma-1}{2}} \tag{F-11}$$

In most free-jet applications the Mach number M is usually much greater than unity at the normal shock, so Eq. (F-11) can be approximated by

$$M_2^2 \approx \frac{\frac{\gamma-1}{2}M^2}{\gamma M^2} = \frac{\gamma-1}{2\gamma} \tag{F-12)*$$

The impact pressure p_i behind the shock is the sum of the static pressure and the dynamic pressure:

$$p_i = p_2 + \frac{1}{2}\rho_2 u_2^2 = p_2(1+\frac{\gamma}{2}M_2^2) \tag{F-13}$$

From Eq. (F-12), p_i can be approximated by

$$p_i \approx p_2(1+\frac{\gamma}{2}\,\frac{\gamma-1}{2\gamma}) = \frac{\gamma+3}{4}\,p_2 \tag{F-14}$$

The pressure match downstream of the normal shock requires:

$$p_2 = p_\infty \tag{F-15}$$

where p_∞ is the background pressure far down-stream.

Therefore the impact pressure is related to the background pressure by:

$$p_i \approx \frac{\gamma+3}{4}\,p_\infty \tag{F-16}$$

The method-of-characteristics calculation*[105]*, which was experimentally confirmed by Ashkenas and Sherman*[106]*, yields for large x/D,

---

*Note that since the specific heat ratio γ is always greater than 1, M_2^2 is always a positive number less than 1, which means that the velocity change across a normal shock must be from supersonic to subsonic.

$$\frac{p_{ib}}{p_o} \approx \left(\frac{\gamma-1}{2}\right)^{-\frac{\gamma}{\gamma-1}} \left(\frac{\gamma}{2}\right) A^{-\frac{2}{\gamma-1}} \left(\frac{x}{d}\right)^{-2} \qquad \text{(F-17)}$$

where p_{ib} is the impact pressure before shock, p_o is the reservior pressure, x is the distance between the sonic orifice and the normal shock boundary, d is the orifice diameter and A is a fitted constant depending on γ.

To relate the impact pressure after the shock p_i and that after the shock p_{ib}, use is made of:

$$p_i = p_2 + \frac{1}{2}\rho_2 u_2^2 = p_2(1+\frac{\gamma}{2}M_2^2) \qquad \text{(F-18)}$$

$$p_{ib} = p_1 + \frac{1}{2}\rho_1 u_1^2 = p_1(1+\frac{\gamma}{2}M^2) \qquad \text{(F-19)}$$

So, the ratio of p_{ib} to p_i is

$$\frac{p_i}{p_{ib}} = \frac{p_2}{p_1}\,\frac{1+\frac{\gamma}{2}M_2^2}{1+\frac{\gamma}{2}M^2} = \frac{1+\gamma M^2}{1+\frac{\gamma}{2}M^2}\,\frac{1+\frac{\gamma}{2}M_2^2}{1+\gamma M_2^2} \qquad \text{(F-20)}$$

For large M >> 1 and from Eq. (F-12):

$$\frac{p_i}{p_{ib}} \approx 2\,\frac{1+\frac{\gamma-1}{4}}{1+\frac{\gamma-1}{2}} = \frac{\gamma+3}{\gamma+1} \qquad \text{(F-21)}$$

Combining with Eq. (F-17), we obtain:

$$\frac{p_i}{p_o} \approx \left(\frac{\gamma-1}{2}\right)^{-\frac{\gamma}{\gamma-1}} \left(\frac{\gamma}{2}\right)\left(\frac{\gamma+3}{\gamma+1}\right) A^{-\frac{2}{\gamma-1}} \left(\frac{x}{d}\right)^{-2} \qquad \text{(F-22)}$$

Combining Eqs. (F-16) and (F-22) yields:

$$\frac{p_o}{p_\infty} = \left(\frac{\gamma-1}{2}\right)^{\frac{\gamma}{\gamma-1}} \left(\frac{\gamma+1}{2\gamma}\right) A^{\frac{2}{\gamma-1}} \left(\frac{x}{d}\right)^{2} \qquad \text{(F-23)}$$

Therefore,

$$\frac{x}{d} = C(\gamma)\left(\frac{p_o}{p_\infty}\right)^{1/2} \qquad \text{(F-24)}$$

where $C(\gamma)$ $= 0.75$ for $\gamma = 5/3$

$= 0.71$ for $\gamma = 7/5$

$= 0.68$ for $\gamma = 9/7$

Eq. (F-24) is eequivalent to Eq. (4-2), except that the proportional constant C is a weak function of γ here.

(II) *Entropy Balancing*.

From first law of thermodynamics it is easy to show that

$$\frac{dS}{R} = \frac{\gamma}{\gamma-1}\frac{dT}{T} - \frac{dp}{p} \tag{F-25}$$

where p, T, S represent the static pressure, static temperature and molar entropy respectively, R is the gas constant and γ is the specific heat ratio. Then, in general, the molar entropy change between an initial state i and a final state f can be expressed as

$$\frac{\Delta S_{i,f}}{R} = \ln[(\frac{p_i}{p_f})(\frac{T_f}{T_i})^{\frac{\gamma}{\gamma-1}}] \tag{F-26}$$

The free-jet expansion is divided into three flow regions:

(a) the jet core zone from the source to the upstream side of the Mach disc, in which the entropy production is denoted $\Delta S_{0,1}$,

(b) the normal shock jump across the upstream and downstream sides of the Mach disc, in which the entropy production is denoted $\Delta S_{1,2}$, and

(c) the mixing zone behind the Mach disc where the jet molecules are mixed with the background molecules, in which the entropy production is denoted $\Delta S_{2,\infty}$.

In region a, the entropy production inside the jet core depends on whether the flow is continuum or free molecular. In the former case, it is found that the flow can be approximated by an isentropic process, in which $\Delta S_{0,1} = 0$. On the other hand, if the background density is sufficiently low so that the jet core becomes partially rarefied at large distances, i.e. the flow becomes free molecular, then the entropy production due to "free" expansion (no collision) becomes significant. Apply the freezing model to this case and divide this jet core into two parts: (i) a continuum region (in which the entropy change is zero) from the jet source to the freezing plane where the flow becomes rarefied; (ii) a rarefied region from the freezing plane to the Mach disc, in which the static temperature and the hydrodynamic speed freeze and so the Mach number remains approminately constant (M_f), while the density continues to decrease as the inverse square of distance. To calculate the entropy production due to this "free expansion", set dT = 0 and dp/p = dn/n, then we have from Eq. (F-26):

$$\frac{\Delta S_{f,M}}{R} = -\ln \frac{n_M}{n_f} \tag{F-27}$$

where f and M represent the freezing plane and the Mach disc, respectively.

Since the density is inversely proportional to the square of the distance, we have

$$\frac{\Delta S_{f,M}}{R} = \ln \left(\frac{x}{x_f}\right)^2 \tag{F-28}$$

where x and x_f are the location of Mach disc and freezing plane, respectively.

In region b, the entropy production across the normal shock results from the viscous heating effect and heat transfer resulting from the temperature gradient across the shock boundary. It can be shown, from a jump condition calculation, that

$$\frac{\Delta S_{M,2}}{R} = \ln \left\{ \left[1+\frac{2\gamma}{\gamma+1}(M^2-1)\right]^{\frac{1}{\gamma-1}} \left[\frac{(\gamma+1)M^2}{(\gamma-1)M^2+2}\right]^{-\frac{\gamma}{\gamma-1}} \right\} \tag{F-29}$$

where M is the Mach number at the upstream side of the Mach disc.

For large Mach numbers, Eq. (F-29) can be written as:

$$\frac{\Delta S_{M,2}}{R} \approx \ln \left\{ \left(\frac{\gamma+1}{\gamma-1}\right)^{-\frac{\gamma}{\gamma-1}} \left(\frac{2\gamma}{\gamma+1}\right)^{\frac{1}{\gamma-1}} M^{\frac{2}{\gamma-1}} \right\} \tag{F-30}$$

To express the Mach number M, we have to consider the two different cases mentioned in region a. In the case of a continuum flow up to the Mach disc, the Mach number M at the Mach disc along the centerline was found empirically*[105]*, for large x,

$$M \approx A(\gamma)\left(\frac{x}{d}\right)^{\gamma-1} \tag{F-31}$$

where x is the location of Mach disc, d is the effective sonic diameter and A(γ) is a constant depending upon γ.

Substituting into Eq. (F-30), we have

$$\frac{\Delta S_{M,2}}{R} = \ln \left[\left(\frac{\gamma+1}{\gamma-1}\right)^{-\frac{\gamma}{\gamma-1}} \left(\frac{2\gamma}{\gamma+1}\right)^{\frac{1}{\gamma-1}} A^{\frac{2}{\gamma-1}} \left(\frac{x}{d}\right)^2 \right] \tag{F-32}$$

In the second case of a rarefied flow following the freezing plane, M is the Mach number at the freezing plane (after which the Mach number is "frozen"). From the same empirical relation as

Eq. (F-31), if x_f is large,

$$M = M_f \approx A(\gamma)\left(\frac{x_f}{d}\right)^{\gamma-1} \tag{F-33}$$

where x_f is the location of the freezing plane.

Substituting into Eq. (F-30) again, we have

$$\frac{\Delta S_{M,2}}{R} = \ln\left[\left(\frac{\gamma+1}{\gamma-1}\right)^{-\frac{\gamma}{\gamma-1}}\left(\frac{2\gamma}{\gamma+1}\right)^{\frac{1}{\gamma-1}} A^{\frac{2}{\gamma-1}}\left(\frac{x_f}{d}\right)^2\right] \tag{F-34}$$

In region c, the jet molecules mix with the background molecules at nearly constant pressure, or $dp = 0$, so Eq. (F-25) becomes

$$\frac{dS}{R} = \frac{\gamma}{\gamma-1}\frac{dT}{T} \tag{F-35}$$

Integrating over the whole region, we have the entropy change as:

$$\frac{\Delta S_{2,\infty}}{R} = \frac{\gamma}{\gamma-1}\int_{T_\infty}^{T_2}\frac{dT}{T} = \frac{\gamma}{\gamma-1}\ln\left(\frac{T_\infty}{T_2}\right) \tag{F-36}$$

where T_∞ is the temperature far downstream and T_2 is the temperature right behind the shock.

To get the temperature ratio, we use:

$$\frac{T_\infty}{T_2} = \left(\frac{T_\infty}{T_0}\right)\left(\frac{T_0}{T_1}\right)\left(\frac{T_1}{T_2}\right) \tag{F-37}$$

where the ratio of T_0 to T_1 is:

$$\frac{T_0}{T_1} = 1 + \frac{\gamma-1}{2}M^2 \tag{F-38}$$

where M can be the Mach number at the shock in case of continuum flow, or the Mach number at the freezing plane in case of rarefied flow (which is still equal to the Mach number at the shock because of the "frozen" Mach number), and the temperature ratio across the shock,

$$\frac{T_1}{T_2} = \left[1 + \frac{2(\gamma-1)}{(\gamma+1)^2}\frac{\gamma M^2+1}{M^2}(M^2-1)\right]^{-1} \tag{F-39}$$

then we have, for large Mach number at the shock,

$$\frac{T_\infty}{T_2} = \left(\frac{T_\infty}{T_0}\right)\frac{\left[1+\frac{\gamma-1}{2}M^2\right]}{\left[1+\frac{2(\gamma-1)}{(\gamma+1)^2}\frac{\gamma M^2+1}{M^2}(M^2-1)\right]} \approx \frac{(\gamma+1)^2}{4\gamma}\left(\frac{T_\infty}{T_0}\right) \tag{F-40}$$

Substituting into Eq. (F-36), yields:

$$\frac{\Delta S_{2,\infty}}{R} = \frac{\gamma}{\gamma-1} \ln \left[\frac{(\gamma+1)^2}{4\gamma}\left(\frac{T_\infty}{T_0}\right)\right] \qquad \text{(F-41)}$$

By combining the three regions, one finds the total entropy production:

$$\frac{\Delta S_{0,\infty}}{R} = \ln \left[A^{\frac{2}{\gamma-1}} 2^{-\frac{2\gamma-1}{\gamma-1}} (\gamma-1)^{\frac{\gamma}{\gamma-1}} \left(\frac{\gamma+1}{\gamma}\right)\left(\frac{T_\infty}{T_0}\right)^{\frac{\gamma}{\gamma-1}} \left(\frac{x}{d}\right)^2\right] \qquad \text{(F-42)}$$

no matter whether the flow remains continuum upstream of the Mach disc or the flow becomes rarefied before Mach disc.

Now, the Mach disc location formula can be obtained by equating Eqs. (F-26) and (F-42), after replacing i with 0 and f with ∞ in the former:

$$\ln\left[\left(\frac{p_0}{p_\infty}\right)\left(\frac{T_\infty}{T_0}\right)^{\frac{\gamma}{\gamma-1}}\right] = \ln \left[A^{\frac{2}{\gamma-1}} 2^{-\frac{2\gamma-1}{\gamma-1}} (\gamma-1)^{\frac{\gamma}{\gamma-1}} \left(\frac{\gamma+1}{\gamma}\right)\left(\frac{T_\infty}{T_0}\right)^{\frac{\gamma}{\gamma-1}} \left(\frac{x}{d}\right)^2\right] \qquad \text{(F-43)}$$

That is

$$\frac{x}{d} = C(\gamma)\left(\frac{p_o}{p_\infty}\right)^{1/2} \qquad \text{(F-44)}$$

where $C(\gamma) = 0.75$ for $\gamma = 5/3$

$= 0.71$ for $\gamma = 7/5$

$= 0.68$ for $\gamma = 9/7$

REFERENCES

1. W. T. Sha and T. H. Hughes, "VENUS: A Two-dimensional Coupled Neutronics-Hydrodynamics Computer Program for Fast-reactor Power Excursions," ANL-7701, Oct. 1970.
2. J. F. Jackson and R. B. Nicholson, "VENUS-II: An LMFBR Disassembly Program," ANL-7951, Sep. 1972.
3. S. Aoi, T. Sawada, M. Fukuda and T. Naganuma, "VENUS-PM: An Analytical Investigation of a Core Disassembly Process in Fast Reactors," SJ-206-76-25 Tr, JAPFNR-308, Oct. 1976.
4. C. A. Alexander, J. S. Ogden and G. W. Cunningham, BMI Report 1789 (1967).
5. M. Tetenbaum and P. D. Hunt, J. Nucl. Mater. **34** (1970) 86-91.
6. R. J. Ackermann, P. W. Gilles and R. J. Thorn, J. Chem. Phys. **25** (1956) 1089.
7. R. W. Ohse, J. Chem. Phys. **44** (1966) 1375.
8. V. E. Ivanov, IAEA Thermodynamics of Nuclear Materials, Vienna 1962.
9. A. Pattoret, IAEA Thermodynamics of Nuclear Materials, Vienna 1967, p.613.
10. G. T. Reedy and M. G. Chasanov, J. Nucl. Mater. **42** (1972) 341-344.
11. R. J. Ackermann, E. G. Rauh and M. H. Rand, IAEA Symposium on Thermodynamics of Nuclear Materials, Vol 1, Paper IAEA-SM-236/59, Julich, 29 Jan. - 2 Feb. 1979.
12. J. W. Shaner, G. R. Gathers, C. Minichino, High Temperatures - High Pressures **8** (1976) 425; Rev. Sci. Intru. **47** (1976) 471.
13. M. M. Martynyuk, O. G. Panteleichuk, High Temperature **14** (1976) 1075.
14. D. A. Benson, W. H. Buckalew, Trans. ANS **23** (1976) 325.
15. D. A. Benson, Report SAND-77-0429 (1977).
16. D. A. Benson, E. G. Bergeron, IAEA Symposium on Thermodynamics of Nuclear Materials, Vol 1, Paper IAEA-SM-236/60, Julich, 29 Jan. - 2 Feb. 1979.

17. K. O. Reil, Ph. D. Thesis, University of New Mexico, May 1977.

18. K. O. Reil, A. W. Cronenberg, Trans. ANS **27** (1977) 576.

19. M. Bober, H. U. Karow and K. Schretzmann, IAEA Symposium on Thermodynamics of Nuclear Materials, Paper IAEA-SM-190/34, Vienna Oct. 1974.

20. M. Bober, W. Breitung, H. U. Karow and K. Schretzmann, J. Nucl. Mater. **60** (1976) 20; KfK-2366 (1976).

21. M. Bober, W. Breitung, H. U. Karow, IAEA Specialists' Meeting on Equations of State of Materials of Relevance to the Analysis of Hypothetical Fast Breeder Reactor Accidents, IWGFR/26, p.8, Harwell, UK Jan. 1978; KfK-2689 (1976).

22. R. W. Ohse, P. G. Berrie, H. G. Bogensberger and E. A. Fischer, IAEA Symposium on Thermodynamics of Nuclear Materials, Paper IAEA-SM-190/8, Vienna Oct. 1974.

23. R. W. Ohse, P. G. Berrie, H. G. Bogensberger and E. A. Fischer, J. Nucl. Mater. **59** (1976) 112; KfK-2272 (1976).

24. J. F. Babelot, R. W. Ohse, H. Binder, IAEA Specialists' Meeting on Equations of State of Materials of Relevance to the Analysis of Hypothetical Fast Breeder Reactor Accidents, IWGFR/26, p.110, Harwell, UK Jan. 1978.

25. n. Asami, M. Michikawa and M. Tagnchi, IAEA Symposium on Thermodynamics of Nuclear Materials, Paper IAEA-SM-190/3, Vienna Oct. 1974.

26. C. H. Tsai, A. Covington and D. R. Olander, Lawrence Berkeley Lab. Report LBL-6016, UC-13, TID-4500-R65 (1976) p.188.

27. C. H. Tsai and D. R. Olander, Lawrence Berkeley Lab. Report LBL-8580, UC-13 (1978) p.202.

28. R. W. Ohse et al., J. Nucl. Mater. **80** (1979) 232-248.

29. F. W. Dabby and U-C Paek, IEEE J. Quan. Elec. Vol. QE-8, No.2, Feb. 1972.

30. H. U. Karow and M. Bober, IAEA Symp. on Thermodynamics of Nuclear Materials, Paper IAEA-SM-236/22, Julich, 29 Jan. - 2 Feb. 1979.

31. W. Breitung, KFK-2240, Jun. 1976.

32. R. A. Olstad and D. R. Olander, J. Appl. Phys. Vol. 46, No. 4, Apr. 1975, pp. 1499-1508.

33. R. A. Olstad and D. R. Olander, J. Appl. Phys. Vol. 46, No. 4, Apr. 1975, pp. 1509-1518.

34. S. I. Anisimov, Soviet Physics JETP, Vol. 27, No. 1, Jul. 1968, pp. 182-183.

35. Masahide Murakami and Koichi Oshima, 9th Int. Symp. on Rarefied Gas Dynamics, 1974, Vol. II, pp. F.6.1-F.6.9.

36. Tor Ytrehus, 10th Int. Symp. on Rarefied Gas Dynamics, Paper 28, July 1976.

37. H. S. Carslaw and J. C. Jaeger, "Conduction of Heat in Solids" Oxford University Press, London and N.Y. 1959.

38. R. D. Richtmyer and K. W. Morton, "Difference Methods for Initial Value Problems" 2nd edit., Interscience, N.Y. 1967.

39. G. E. Forsythe and W. R. Wason, "Finite Difference Methods for Partial Differential Equations" John Wiley, N.Y. 1960.

40. J. Douglas, Jr. "Survey of Numerical Methods for Parabolic Differential Equations" in Advances in Computers, Vol. 2 Academic Press, N.Y. 1961, pp. 1-54.

41. W. F. Ames, "Nonlinear Partial Differential Equations in Engineering", Academic Press, N.Y. 1965.

42. Germund Dahlquist and Ake Björck, "Numerical Methods", Series in Automatic Computation, Prentice-Hall, Inc., N.Y. 1974.

43. Instructional Manual for American Optical Model 30 Nd-glass Laser System, Southbridge, Massachusetts, 1968.

44. C. G. Young, Laser Focus, Laser Technology Section, July 1968, p.72.

45. D. R. Olander, "Fundamental Aspects of Nuclear Reactor Fuel Elements," ERDA Technical Information Center, Oak Ridge, Tennessee, Apr. 1976.

46. M. J. Davies, Ph. D. Thesis, Dept. of Inorganic and Structural Chemistry, University of Leeds, Jan. 1970.

47. Instructional Manual for PHOTO I Automatic Pyrometer Serial NO. A-164, The Pyrometer Instrument Co., Inc. 1973.

48. R. A. Olstad, Ph.D Thesis, University of California at Berkeley, Dec. 1972.

49. R. Depaula, M.S. Thesis, University of California at Berkeley, Dec. 1978.

50. P. J. Brannon et al., J. Appl. Phys. **46**, No. 8, Aug. 1975, pp. 3576-3579.

51. John Corcoran, Ampex Corp., Laser Focus, June 1973, p.61.

52. J. F. Ready, private communication, Sep. 1975.

53. M. Bober and H. U. Karow, 7th Symp. on Thermodynamical Properties, NBS Washington, D.C., 1977.

54. EAI Quadrupole Residual Gas Analyzer Operators and Maintenance Manual, Electronic Associates Inc., Palo Alto, CA., 1965, p.18.

55. A. Pattoret, Ph. D. Thesis, Université Libre de Bruxelles, 1969, pp. 30-36.

56. G. E. Blackburn and P. M. Danielson, J. Chem. Phys. **56** (1972) 6156.

57. J. Magill and R. W. Ohse, J. Nucl. Mater. **71** (1977) 191-193.

58. J. F. Ready, J. Apply. Phys. **36** (1965) 462.

59. G. Varsi, "Interaction of High Intensity Laser Radiation with Metallic Surface," Space Science Lab., Series 10, Issue 19, University of California, Berkeley, May 1969.

60. M. A. Covington, G. N. Liu and K. A. Lincoln, AIAA Paper no. 76-22, Jan. 1976.

61. K. A. Lincoln and M. A. Covington, Int. J. Mass Spectrometry & Ion Physics, **16** (1975) 191-208.

62. R. W. Ohse, et al., High Temp - High Pressure, **12** (1980) 537-548.

63. F. Tehranium, University of California at Berkeley, private communication.

64. H. U. Karow, KfK - 2390, Feb.1977; H. U. Karow, Rev. int. hautes Temper Refract Fr., Vol 15, 1978, pp. 347-354.

65. J. F. Ready, "Effect of High Power Laser Radiation," Academic press, 1971.

66. Ya.B. Zel'dovich and Yu P. Raizer, "Pysics of shock wave and high temperature hydrodynamic Phenomena," Vol I, Academic Prss, NY and Londen 1966.

67. IAEA Specialists' Meeting on Equations of State of Materials of Relevance to the Analysis of HCDA, IWGFR/26, June 1978.

68. O. A. Hougen and K. M. Watson, Chemical Process Principles, Pt. II, John Wiley and Sons, N. Y. 1947; see also, J. O. Hirschfelder, C. Curtiss, R. Bird, "Molecular Theory of Gases and Liquids", John Wiley, N. Y. 1954.

69. L. Riedel, Chem. Ing. Tech. **26** (1954) 83.

70. D. C. Menzies, UKAEA Report TRG-1119(D), 1966.

71. R. A. Meyer and B. E. Wolfe, High Temperature Equation of State of Uranium Dioxide, Trans. Amer. Nucl. Soc., June 1964.

72. S. K. Kapil, J. Nucl. Mater. **60** (1976) 158.

73. J. A. Christiansen, J. Am. Cerem. Soc. **46** (1963) 607; see also, Report HW-75148 (1962).

74. D. L. Booth, UKAEA Report TRG-1759 (1968), reprint 1974; TRG-1871(R/X) (1969).

75. P. Browning, M. J. Gillan and P. E. Potter, UKAEA Report AERA-R-8129, March 1977.

76. E. A. Guggenheim, J. Chem. Phys. **13** (1954) 253.

77. H. Eyring, M. S. Jhon, Significant Liquid Structures, Wiley, N. Y. 1969.

78. M. J. Gillan, Thermodynamics of Nucl. Mater., IAEA, Vienna 1975, Vol I. p.269.

79. E. A. Fischer, P. R. Kinsman and R. W. Ohse, J. Nucl. Mater. **59** (1976) 125-136.

80. M. H. Rand and T. L. Markin, UKAEA Report AERA-R-5560, 1967.

81. W. Breitung, KfK-2091, June 1975.

82. P. E. Blackburn, J. Nucl. Mater. **46** (1973) 244-252.

83. W. Breitung, private communication.

84. R. J. Ackermann, J. Phys. Chem. **64** (1960) 350.

85. C. A. Alexander, Ph. D. Dissertation 1961.

86. R. J. Ackermann, J. Chem. Thermo. **5** (1973) 873.

87. P. A. Finn, A. Sheth and L. Leibowitz, J. Nucl. Mater. **79** (1979) 14-19.

88. R. J. Ackermann, IAEA-SM-190/44 1974.

89. A. Pattoret, J. Chem. Phys. **42** (1965) 2629.

90. R. Hultgren, R. L. Orr, P. D. Anderson and K. K. Kelley, Selected Values of Thermodynamic Properties of Metals and Alloys, Wiley, N. Y. 1963.

91. M. G. Chasanov, L. Leibowitz and S. D. Gabelnick, J. Nucl. Mater. **49** (1973/74) 129-135.

92. L. Leibowitz et al, Report ANL-CEN-RSD-76-1, Mar. 1976.

93. J. F. Kerrisk and D. G. Clifton, Nucl. Tech. **16** (1972) 531.

94. L. Leibowitz, J. Nucl. Mater., **39** (1971) 115.

95. R. E. Latta and R. E. Fryxell, J. Nucl. Mater. **35** (1970) 195-210.

96. H. E. Schmidt, J. Nucl. Mater., **39** (1971) 234.

97. J. K. Fink, M. G. CChasanov and L. Leibowitz, ANL-CEN-RSD-81-3, June 1981.

98. H. G. Bogensberger, et al., GfK Report KfK-2272, May 1976.

99. L. Leibowitz, L. W. Mishler and M. G. Chasanov, J. Nucl. Mater., **29** (1969) 356.

100. J. Belle, "Properties of UO_2", 1962, p. 7.

101. P. C. Held and D. R. Wilder, J. Am. Cer. Soc., **52** (1969) 182-186.

102. M. Bober, K. U. Karow and K. Schretzmann, Nucl. Tech. **26** (1975) 237-241.

103. M. Bober, H. U. Karow and K. Muller, High Temp - High Pressure, **12** (1980) 161-168.

104. Wen S Young, the Physics of Fluids, Vol. 18, No. 11, Nov. 1975, pp. 1421-1425.

105. T. C. Adamson, Jr., and J. A. Nicholls, J. Aerospace Sci. **26** (1959) 16.

106. H. Ashkenas and F. S. Shermman, Rarefied Gas Dynamics, edited by J. H. deLeeuw (Academic, NY 1966) Vol. 2, p.84.

107. N. D. Cox, "A Report on a Sensitivity Study of the Response Surface Method of Uncertainty Analysis of a PWR Model," E G & G Idaho, Inc. Report no. RE-S-77-7, Jan. 1977.

108. S. O. Peck, "Code Development and Analysis Program," E G & G Idaho, Inc. Report no. CDAP-TR-78-024, July 1978.

109. D. W. Green and L. Leibowitz, ANL-CEN-RSD-81-1, June 1981.

110. W. J. Siekhaus, R. H. Jones and D. R. Olander, J. Appl. Phys. **41** (1970) 4392.

111. D. W. Gregg and S. J. Thomas, J. Appl. Phys. **37** (1966) 4313.

This report was done with support from the Department of Energy. Any conclusions or opinions expressed in this report represent solely those of the author(s) and not necessarily those of The Regents of the University of California, the Lawrence Berkeley Laboratory or the Department of Energy.

Reference to a company or product name does not imply approval or recommendation of the product by the University of California or the U.S. Department of Energy to the exclusion of others that may be suitable.

TECHNICAL INFORMATION DEPARTMENT
LAWRENCE BERKELEY LABORATORY
UNIVERSITY OF CALIFORNIA
BERKELEY, CALIFORNIA 94720